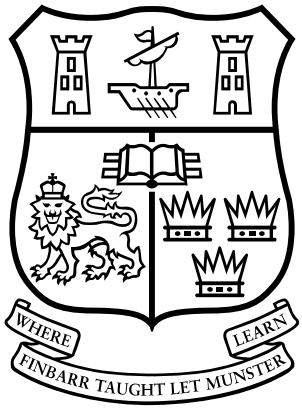

Magnetic Materials and Soft-Switched Topologies for High-Current DC-DC Converters

Marek S. Rylko M.Sc., B.E.

A thesis presented to the National University of Ireland for the degree of Doctor of Philosophy

January, 2011

Supervised by Dr. John G. Hayes and Dr. Michael G. Egan

Department of Electrical and Electronic Engineering
University College Cork
Ireland

A good scientist is a person with original ideas. A good engineer is a person who makes a design that works with as few original ideas as possible.

Freeman J. Dyson

Abstract

This thesis is focused on the comparison and selection of magnetic materials for high-power non-isolated dc-dc converters for industrial applications or electric, hybrid and fuel cell vehicles. The application of high-frequency bi-directional soft-switched dc-dc converters is also investigated.

The thesis initially outlines the motivation for an energy-efficient transportation system with minimum environmental impact and reduced dependence on exhaustible resources. This is followed by a general overview of the power system architectures for electric, hybrid and fuel cell vehicles. The vehicle power demand, power sources, and general dc-dc converter topologies are discussed. The dc-dc converter components are then discussed with emphasis on recent semiconductor advances.

A novel bi-directional soft-switched dc-dc converter with an auxiliary cell is introduced in this thesis. The soft-switching cell allows for the MOSFET's intrinsic body diode to operate in a half-bridge without reduced efficiency. A mode-by-mode analysis of the converter is performed and closed-form expressions are presented for the average current gain of the converter. The design issues are presented and circuit limitations are discussed.

Magnetic materials for the main dc-dc converter inductor are compared and contrasted. Novel magnetic material comparisons are introduced, which include the material dc bias capability and thermal conductivity.

An inductor design algorithm is developed and used to compare the various magnetic materials for the application. The area-product analysis is presented for the minimum inductor size and highlights the optimum magnetic materials.

Finally, the high-flux magnetic materials are experimentally compared. The practical effects of frequency, dc-bias, and converter duty-cycle for arbitrary shapes on flux density, air gap effects on core and winding, the winding shielding effect, and thermal configuration are investigated.

The thesis results have been documented at the IEEE EPE conference in 2007 and 2008, IEEE APEC in 2009 and 2010, and IEEE VPPC in 2010. A journal paper has been accepted for publication in 2011 by the IEEE Transactions on Power Electronics.

Acknowledgements

This thesis would not have been possible without the guidance and the help of several individuals who in one way or another contributed and extended their valuable assistance in the preparation and completion of this study.

First and foremost, I would like to thank my academic advisors Dr. John Hayes and Dr. Michael Egan for their encouragement, guidance, friendship, expertise, patience and enthusiasm over the last six years. I wish to thank Prof. Andrew Forsyth and Dr. Kevin McCarthy for examining my thesis.

I wish to thank Dr. Richard Kavanagh whose support made my study at UCC possible. The financial support of the EU Marie-Curie Fellowship programme and further technical and financial support of General Motors are greatly appreciated.

It is difficult to list all individuals who contributed to my work, but I wish to thank George Woody, John Hall, Steve Hulsey, Terry Ward and Dan Kowaleski in California for their motivation, valuable advices and friendship.

I am indebted to my many colleagues and the staff from Power Electronics Research Laboratory and UCC for support me through past years. Among the many contributors are Jason Hannon, Kevin Hartnett, Dr. Brendan Lyons, James Griffiths, Dr. Ray Foley, Dr. David Cashman, Donal Murray, Naveen Boggarapu, John Slowey, Dr. Richard Morrison, Daithi Power, Dr. Dara O'Sullivan, Judy Rea, Gerry McCarthy, Sarah Babbington, Geraldine Mangan, Rita Sarteschi, Tim Power and Michael O'Shea.

I wish to thank all Marie Curie Fellows for a great time together, support and valuable discussions.

The support of my family and friends has been ever so important to the success of my work. I want to thank Artur, Beata, Benjamin, Jana, Kasia and Hubert, Kinga, Krzysiek and Justyna, Magda, Monika, Nicole, Piotr. Please forgive me of not listing all of you.

Finally, I owe my deepest gratitude to my parents Zdzisław i Irena and brother Wojciech for their love, encouragement, continuous support and patience.

List of Publications

Journal Paper:

1. M.S. Rylko, B.J. Lyons, J.G. Hayes, M.G. Egan, "Revised magnetics performance factors and experimental comparison of high-flux materials for high-current dc-dc inductors," *IEEE Transactions on Power Electronics*, 2011, in press.

Conference Papers:

1. M.S. Rylko, J.G. Hayes, M.G. Egan, "Experimental investigation of high-flux density magnetic materials for high-current inductors in hybrid-electric vehicle dc-dc converters," *IEEE Vehicle Power and Propulsion Conference*, 2010, pp. 1-7 .
2. K.J. Hartnett, M.S. Rylko, J.G. Hayes, M.G. Egan, "A comparison of classical two phase (2L) and transformer — coupled (XL) interleaved boost converters for fuel cell applications," *IEEE Applied Power Electronics Conference*, 2010, pp. 787-793.
3. M.S. Rylko, K.J. Hartnett, J.G. Hayes, M.G. Egan, "Magnetic material selection for high power high frequency inductors in dc-dc converters," *IEEE Applied Power Electronics Conference*, 2009, pp. 2043-2049.
4. M.S. Rylko, B.J. Lyons, K.J. Hartnett, J.G. Hayes, M.G. Egan, "Magnetic material comparisons for high-current gapped and gapless foil wound inductors in high frequency dc-dc converters," *IEEE EPE-PEMC*, 2008, pp. 1249-1256.
5. M.S. Rylko, M.G. Egan, J.G. Hayes, D. Power, "A soft-switched bi-directional dc-dc converter," *IEEE European Conference on Power Electronics and Applications*, 2007, pp. 1-10

Table of Contents

Abstract…. V

Acknowledgements VII

List of Publications IX

Table of Contents XI

List of Tables XV

List of Figures XVII

Chapter 1 Introduction 1

1.1. Overview 3

1.2. Thesis Objectives 5

1.3. General Background 6

1.4. Electric Vehicle Propulsion Architecture 8

1.5. A DC-DC Interface For Electric Vehicle 11

1.5.1. DC-DC Converter 12

1.5.1.1. Hard Switching vs. Soft Switching 15

1.6. DC-DC Converter Components 16

1.6.1. Power Switch 16

1.6.2. Magnetic Component 19

1.6.3. Capacitor 19

1.7. Thesis Structure 20

Chapter 2 A Soft-Switched DC-DC Converter 21

2.1. Introduction 23

2.2. The Topology of Choice 24

2.3. Soft-Switching Converter Mode-by-Mode Analysis 25

2.4. Soft-Switching Converter Operation 31

2.5. Limitations 35

2.6. Auxiliary Transformer Turns Ratio Considerations 37
2.6.1. Damping Resistance Effect 38
2.6.2. Boundary Conditions Of Resonant Mode 40
2.6.3. Auxiliary Diodes Voltage Drop 41
2.6.4. Main Switch Anti-Parallel Diode Conduction Time Effect 42
2.6.5. The Autotransformer Turns Ratio 43
2.7. Converters Experimental Comparison 44
2.8. Conclusions on the Soft-Switched and Hard-Switched Converter 55
Chapter 3 Magnetic Material Comparison 57
3.1. Introduction 59
3.2. Magnetic Materials 60
3.3. Comparison of the Magnetic Materials 68
3.4. Conclusions on Performance Factor Materials Selection 79
Chapter 4 Inductor Size – Area Product Analysis 81
4.1. Inductor Design Flowchart 83
4.1.1. Gapped Inductor Design Flowchart 85
4.1.2. Gapless Inductor Design Flowchart 92
4.2. Area-Product Analysis 93
4.2.1. Current-Ripple Analysis 94
4.2.2. Efficiency and Inductor Size 96
4.2.3. Area Product Curves 98
4.3. Summary 100
Chapter 5 Experimental Comparison of High-Flux Magnetic Materials 101
5.1. Experimental Setup 103
5.2. Frequency Effect Analysis 105
5.2.1. Low to Medium Frequency 106
5.2.2. Medium to High Frequency 109
5.3. DC-Bias Effect on the Core Power Loss 112
5.4. Duty Cycle Effect on the Core Power Loss 117
5.5. Air Gap Effect 121
5.5.1. Air Gap Effect on the Core 121
5.5.2. Air Gap Effect on the Winding 125
5.6. Thermal Configuration 131
5.7. Summary 134

Chapter 6 Conclusions and Future Work 135
6.1. Thesis Summary 135
6.2. Future Work 138
Bibliography 140
Appendix A Soft-Switched DC-DC Converter 147
A.1. Transformer Current Transient Between Modes 5 and 6 147
A.2. Main Switch Turn-off Assisted by Soft-Switching Cell 149
A.3. PSpice Simulation Schematic of the Soft-Switching Converter 156
A.4. Resonant Cell ESR Effect on Transformers Voltage Ratio 157
A.5. TMS320F2808 Based Board Schematics 159
Appendix B Performance Factor 165
B.1. Steinmetz Parameters 165
Appendix C Area Product Analysis 168
C.1. 1 kW Area Product vs. Current Ripple 169
C.2. 10 kW Area Product vs. Current Ripple 172
C.3. Minimum Area Product Analysis 175
C.4. Efficiency Effect on the Inductor Size 178
Appendix D Experimental Analysis 180
D.1. Frequency Effect Analysis 180
D.2. DC-Bias Effect on the Core Power Loss 182
D.3. Duty Cycle Effect on the Core Power Loss 183
D.3.1. Modified Steinmetz Equation 183
D.3.2. Experimental Results 186
D.4. Air Gap Effect 186
D.5. Thermal Configuration 187

List of Tables

Table 2.1. Converters comparison 49
Table 2.2. Power loss breakdown at power of 1.25 kW 50
Table 2.3. Converters efficiency comparison 51
Table 3.1. Magnetic Materials Properties 61
Table 3.2. Magnetic Materials Properties 66
Table 5.1. List of experimental cores 104
Table 5.2. Investigated inductors details 105
Table 5.3. Losses and temperature rise for constant inductance in low to medium frequency range 107
Table 5.4. Losses and temperature rise for constant inductance in low to medium frequency range for single- and multi-cut amorphous metal-based inductors 108
Table 5.5. Losses and temperature rise for constant inductance in medium to high frequency range 110
Table 5.6. Losses and temperature rise for constant inductance in medium to high frequency range for single- and multi-cut amorphous metal-based inductors 111
Table 5.7. Inductance, Power losses and temperature rise for dc-bias analysis 116
Table 5.8. Power loss generated in the inductor and temperature rise for duty cycle effect analysis 120
Table 5.9. Power loss, temperature rise and inductance change in a relation to winding placement and air gap length 125
Table 5.10. FEA analysis model parameters 126
Table 5.11. FEA ac power loss in foil winding and inductance for various air gaps and distances between winding and core 128
Table 5.12. Temperature rise reduction due to multi gap core 130
Table 5.13. Conduction cooled inductor cores temperature rise 133
Table B.1. Steinmetz equation parameters 166
Table B.2. Steinmetz equation parameters 167

Table C.1. Minimum *AP* vs. frequency for gapped materials (1 kW, 99% efficient), convection-cooling and conduction-cooling 175

Table C.2. Minimum *AP* vs. frequency for gapped materials (10 kW, 99% efficient), convection-cooling and conduction-cooling 175

Table C.3. Minimum *AP* vs. frequency for gapless materials (1 kW, 99% efficient), convection-cooling and conduction-cooling 176

Table C.4. Minimum *AP* vs. frequency for gapless materials (10 kW, 99% efficient), convection-cooling and conduction-cooling 177

Table C.5. *AP* for 100 μH gapped inductor with and without efficiency restriction 178

Table C.6. *AP* for 100 μH gapless inductor with and without efficiency restriction 10 kW. 179

Table D.1. Experimental data for a low to medium frequency effect analysis 180

Table D.2. Experimental data for a low to medium frequency effect analysis on single- and multi-cut amorphous metal core 181

Table D.3. Experimental data for a medium to high frequency effect analysis 181

Table D.4. Experimental data for a medium to high frequency effect analysis on single- and multi-cut amorphous metal core 182

Table D.5. Experimental data for dc-bias analysis..... 182

Table D.6. Experimental data for duty cycle effect on the core power loss 186

Table D.7. Experimental data for air gap effect on the core 186

Table D.8. Experimental data for air gap effect on the winding 187

Table D.9. Experimental data for thermal configuration analysis 187

List of Figures

Figure 1.1. Temperature histories from paleoclimate compared to the history based on modern instruments. 6

Figure 1.2. Ultimate world crude oil production based upon initial reserves of 1250 billion barrels. 7

Figure 1.3. History of Illinois basin posted monthly crude oil prices 7

Figure 1.4. Traditional ICE-based powertrain. 8

Figure 1.5. Series hybrid electric powertrain. 9

Figure 1.6. Parallel hybrid electric powertrain. 9

Figure 1.7. Battery electric powertrain. 10

Figure 1.8. Fuel cell electric powertrain. 10

Figure 1.9. Output characteristic of: *(a)* fuel cell voltage and current vs. normalized power; (*b)* and lithium based battery voltage vs. state of charge. 11

Figure 1.10. Non-isolated dc-dc converter: *(a)* buck-boost, *(b)* cascade, *(c)* interleaved buck-boost. 13

Figure 1.11. Non-isolated dc-dc converter: *(a)* interleaved buck-boost with inter-phase coupling, *(b)* Z-source inverter. 13

Figure 1.12. Non-isolated dc-dc converter: *(a)* soft-switched buck-boost, *(b)* interleaved buck-boost with diode soft switching. 13

Figure 1.13. Non-isolated buck-boost with auxiliary soft-switching cell. 13

Figure 1.14. Hard-switched transistor operation. 16

Figure 1.15. Soft-switched transistor operation. 16

Figure 1.16. Application of various device types. 18

Figure 2.1. Bi-directional buck-boost converter: *(a)* conventional hard-switched, and *(b)* soft-switched. 24

Figure 2.2. Detailed converter modes, buck mode. 26

Figure 2.3. Operation waveforms, buck mode. 27

Figure 2.4. Volt-seconds loss due to soft-switching cell operation. 31

Figure 2.5. Idealised and predicted converter current gain characteristic for buck and boost modes. 34
Figure 2.6. Maximum power capability of the ideal soft-switched converter. 36
Figure 2.7. Maximum power capability of the non-ideal soft-switched converter. 36
Figure 2.8. Mode 2 cell resonant equivalent circuit for boost operation..... 38
Figure 2.9. Pole voltage resonant swing for various auxiliary voltage ratio and cell *ESR*: *(a)* ideal case, *(b)* overdamped voltage swing, *(c)* critical condition, *(d)* low transformers turns ratio. 39
Figure 2.10. Equivalent circuit for boundary conditions between Mode 1 and Mode 2..... 40
Figure 2.11. Equivalent circuit for diode voltage drop effect. 41
Figure 2.12. State-plane trajectory. 42
Figure 2.13. Experimental inductors 200 μH and 28 μH. 45
Figure 2.14. Soft-switched dc-dc converter. 45
Figure 2.15. Control board based on TMS320F2808..... 46
Figure 2.16. Experimental and theoretical inductor average current vs. duty cycle for soft-switched converter. 46
Figure 2.17. Low ripple *(a)* and high ripple *(b)* regime. 47
Figure 2.18. Efficiency vs. output power: *(a)* high current ripple (220 %) MOSFET based converter, *(b)* low current ripple (31%) hard-switched IGBT based converter, *(c)* current ripple (31 %) soft-switched MOSFET based converter. 48
Figure 2.19. Buck mode experimental waveform. 52
Figure 2.20. Boost mode experimental waveform. 52
Figure 2.21. Zero current crossing mode experimental waveform. 53
Figure 2.22. Converters pole voltage loss due to soft switching cell at 50 kHz. 54
Figure 2.23. Converters pole voltage loss due to soft switching cell at 100 kHz. 54
Figure 2.24. Experimental validation of the theoretical model at 100 kHz. 55
Figure 3.1. Volumetric power loss density vs. flux density amplitude at 20 kHz. 63
Figure 3.2. Volumetric power loss density vs. flux density amplitude at 100kHz. 63
Figure 3.3. Volumetric power density vs. frequency and flux density amplitude. 65
Figure 3.4. Pressed powder material power loss vs. permeability 65
Figure 3.5. Typical hysteresis loops and its corresponding dc bias characteristics with air gap. 67
Figure 3.6. Magnetization characteristic of μ60 powder cores. 68

Figure 3.7. JFE proposed material comparison at 20 kHz. 69

Figure 3.8. JFE proposed material comparison at 100 kHz. 69

Figure 3.9. 1-D heat conduction from the *(a)* external source and *(b)* internally generated. 71

Figure 3.10. Conduction cooled sample. 72

Figure 3.11. Gapped materials convection-cooled *PF* vs. freq. at P_V = 30 mW/cm^3 for *(a)* an ac inductor or transformer, and *(b)* an ac+dc inductor. 73

Figure 3.12. Gapped materials convection-cooled *PF* vs. freq. at P_V = 100 mW/cm^3 for *(a)* an ac inductor or transformer, and *(b)* an ac+dc inductor. 73

Figure 3.13. Gapped materials convection-cooled *PF* vs. freq. at P_V = 300 mW/cm^3 for *(a)* an ac inductor or transformer, and *(b)* an ac+dc inductor. 73

Figure 3.14. Gapless materials convection-cooled *PF* vs. freq. at P_V = 30 mW/cm^3 for *(a)* an ac inductor or transformer, and *(b)* an ac+dc inductor. 74

Figure 3.15. Gapless materials convection-cooled *PF* vs. freq. at P_V = 100 mW/cm^3 for *(a)* an ac inductor or transformer, and *(b)* an ac+dc inductor. 74

Figure 3.16. Gapless materials convection-cooled *PF* vs. freq. at P_V = 300 mW/cm^3 for *(a)* an ac inductor or transformer, and *(b)* an ac+dc inductor. 74

Figure 3.17. Gapped materials conduction-cooled *PF* vs. freq. with length h = 10 mm and max. temp. rise ΔT = 40 K for *(a)* an ac inductor or transformer, and *(b)* an ac+dc inductor. 75

Figure 3.18. Gapped materials conduction-cooled *PF* vs. freq. with length h = 30 mm and max. temp. rise ΔT = 40 K for *(a)* an ac inductor or transformer, and *(b)* an ac+dc inductor. 75

Figure 3.19. Gapped materials conduction-cooled *PF* vs. freq. with length h = 100 mm and max. temp. rise ΔT = 40 K for *(a)* an ac inductor or transformer, and *(b)* an ac+dc inductor. 75

Figure 3.20. Gapless materials conduction-cooled *PF* vs. freq. with length h = 10 mm and max. temp. rise ΔT = 40 K for *(a)* an ac inductor or transformer, and *(b)* an ac+dc inductor. 76

Figure 3.21. Gapless materials conduction-cooled *PF* vs. freq. with length h = 30 mm and max. temp. rise ΔT = 40 K for *(a)* an ac inductor or transformer, and *(b)* an ac+dc inductor. 76

Figure 3.22. Gapless materials conduction-cooled *PF* vs. freq. with length h = 100 mm and max. temp. rise ΔT = 40 K for *(a)* an ac inductor or transformer, and *(b)* an ac+dc inductor. 76

Figure 3.23. Convection-cooled inverted $PF_{ac+dc\ (conv)}$ vs. freq. at $P_V = 30$ mW/cm^3 for *(a)* gapped materials, and *(b)* gapless materials. 77

Figure 3.24. Convection-cooled inverted $PF_{ac+dc(conv)}$ vs. freq. at $P_V = 100$ mW/cm^3 for *(a)* gapped materials, and *(b)* gapless materials. 77

Figure 3.25. Convection-cooled inverted $PF_{ac+dc\ (conv)}$ vs. freq. at $P_V = 300$ mW/cm^3 for *(a)* gapped materials, and *(b)* gapless materials. 78

Figure 3.26. Conduction-cooled inverted $PF_{ac+dc\ (cond)}$ vs. freq. with length $h = 10$ mm and max. temp. rise $\Delta T = 40$ K for *(a)* gapped materials, and *(b)* gapless materials. 78

Figure 3.27. Conduction-cooled inverted $PF_{ac+dc\ (cond)}$ vs. freq. with length $h = 30$ mm and max. temp. rise $\Delta T = 40$ K for *(a)* gapped materials, and *(b)* gapless materials. 78

Figure 3.28. Conduction-cooled inverted $PF_{ac+dc\ (cond)}$ vs. freq. with length $h = 100$ mm and max. temp. rise $\Delta T = 40$ K for *(a)* gapped materials, and *(b)* gapless materials. 79

Figure 4.1. Design algorithm for *(a)* gapped and *(b)* gapless inductor. 84

Figure 4.2. Core and winding dimensions. 86

Figure 4.3. Air gap iteration loop. 87

Figure 4.4. Inductor section mounted on the cold-plate: *(a)* heat flow and *(b)* simplified 1D cooling model. 90

Figure 4.5. Winding cooling patch and its 1D equivalent model. 91

Figure 4.6. Local area product minima (1 kW 10JNHF600 design at 50 kHz). 91

Figure 4.7. *AP* vs. current ripple with frequency as a parameter (1 kW) for gapped amorphous metal design: *(a)* natural convection cooling, *(b)* cold-plate conduction cooling. 94

Figure 4.8. *AP* vs. current ripple with frequency as a parameter (10 kW) for gapped amorphous metal design: *(a)* natural convection cooling, *(b)* cold-plate conduction cooling. 95

Figure 4.9. Area Product vs. inductor efficiency for *(a)* 20 % and *(b)* 60 % and *(c)* 100 % current ripple. Gapped, amorphous metal (2605SA1) based inductor. 96

Figure 4.10. *AP* vs. frequency for a 100 μH gapped inductor (10 kW, 99% efficient): *(a)* convection-cooling and *(b)* conduction-cooling. 97

Figure 4.11. *AP* vs. frequency for a 100 μH gapped inductor (10 kW, no efficiency restriction): *(a)* convection-cooling and *(b)* conduction-cooling. 97

Figure 4.12. Convection-cooled Area Product vs. current ripple for frequency parameter (10 kW, 99% eff.): *(a)* 20 kHz and *(b)* 50 kHz and *(c)* 100 kHz and *(d)* 150 kHz. 98

Figure 4.13. Conduction-cooled Area Product vs. current ripple for frequency parameter (10 kW, 99% eff.): *a*) 20 kHz and *b*) 50 kHz and *c*) 100 kHz and *d*) 150 kHz. 99

Figure 4.14. Conduction-cooled 10 kW, 99% efficient inductor design at 20 kHz: *(a)* core power loss density vs. current ripple *(b*) and peak flux density vs. current ripple. 100

Figure 5.1. Hard switched dc-dc converter setup. 103

Figure 5.2. Single-cut Fe-based amorphous (left), multi-cut Fe-based amorphous (top), 6.5% Si-steel (right) and Fe-based powder core (bottom). 104

Figure 5.3. Drawing of core dimensions. 104

Figure 5.4. Inductor temperature rise vs. low to medium frequency range for constant inductance. 107

Figure 5.5. Multi-cut amorphous metal-based inductor temperature rise anomalies in low to medium frequency range for constant inductance. 108

Figure 5.6. Inductor temperature rise vs. medium to high frequency range for constant inductance. 110

Figure 5.7. Multi-cut amorphous metal-based inductor temperature rise anomalies in medium to high frequency range for constant inductance. 111

Figure 5.8. Amorphous metal based-inductor power loss and flux density vs. magnetizing dc-bias. 113

Figure 5.9. Amorphous metal based-inductor inductance and flux density vs. magnetizing dc-bias. 113

Figure 5.10. Silicon-steel 10JNHF600 based-inductor power loss and flux density vs. magnetizing dc-bias. 114

Figure 5.11. Silicon-steel 10JNHF600 based-inductor inductance and flux density vs. magnetizing dc-bias. 114

Figure 5.12. JFE prototype based-inductor power loss and flux density vs. magnetizing dc-bias. 115

Figure 5.13. JFE prototype based-inductor inductance and flux density vs. magnetizing dc-bias. 115

Figure 5.14. Magnetization curves. 117

Figure 5.15. Comparison between measurement and calculated temperature rise as a function of duty cycle for amorphous metal. 119

Figure 5.16. Comparison between measurement and calculated temperature rise as a function of duty cycle for silicon steel. 119

Figure 5.17. Comparison between measurement and calculated temperature rise as a function of duty cycle for powder material. 120

Figure 5.18. Air gap experimental inductors. Winding is far away from the air gap

(left), winding is shielding air gap (right)..... 122
Figure 5.19. Inductance change due to the winding position..... 123
Figure 5.20. Core temperature rise vs. shielded gap length for constant frequency 50 kHz. 124
Figure 5.21. Core temperature rise vs. unshielded gap length for constant frequency 50 kHz. 124
Figure 5.22. FEA of a single 3 mm inductor air gap per leg..... 126
Figure 5.23. FEA of distributed inductor air gap per leg (3 x 1mm). 126
Figure 5.24. FEA of gapless core inductor. 127
Figure 5.25. FEA foil winding ac power loss of distributed inductor air gap as function of the distance between the winding and the core..... 128
Figure 5.26. FEA inductance as a function of air gap and distance between the winding and the core. 129
Figure 5.27. Reduced core and winding temperature due to distributed air gaps. 130
Figure 5.28. Magnetic core segments. 131
Figure 5.29. Aluminium thermal jig. 132
Figure 5.30. Heat flow considerations. 133
Figure A.1. Mode 5 circuit operation..... 147
Figure A.2. Mode 5 resonant cell current. 148
Figure A.3. Switch open transient..... 148
Figure A.4. Cell current distribution in mode 6..... 149
Figure A.5. Buck mode main transistor turn-off initial conditions..... 150
Figure A.6. Buck mode transient circuit for the main transistor turn-off. 150
Figure A.7. Boost mode main transistor turn-off initial conditions. 151
Figure A.8. Boost mode transient circuit for the main transistor turn-off..... 151
Figure A.9. The capacitor voltage fall time as a function of the inductor current. 155
Figure A.10. Resonant mode equivalent circuit..... 157
Figure A.11. Main TMS320F2808 connection schematic. 159
Figure A.12. Power supply and decoupling capacitors..... 160
Figure A.13. PWM outputs with tranzistor drivrers. Upper 3 channels with a zero voltage detection..... 161
Figure A.14. PWM outputs with transistor drivers. Lower 3 channels with a zero voltage detection..... 162
Figure A.15. Communication interfaces, digital I/O, LCD interface, signal diodes, keyboard. 163

Figure A.16. Analog inputs: 6 voltage inputs, 2 voltage differential inputs, 2 high sensitivity current shunt inputs and 2 potentiometers. 164

Figure C.1. *AP* vs. current ripple with frequency as a parameter for 2605SA1 1 kW gapped inductor design: *(a)* natural convection-cooling, *(b)* cold-plate conduction-cooling. 169

Figure C.2. *AP* vs. current ripple with frequency as a parameter for 10JNHF600 1 kW gapped inductor design: *(a)* natural convection-cooling, *(b)* cold-plate conduction-cooling. 169

Figure C.3. *AP* vs. current ripple with frequency as a parameter for JFE Prototype 1 kW gapped inductor design: *(a)* natural convection-cooling, *(b)* cold-plate conduction-cooling. 169

Figure C.4. *AP* vs. current ripple with frequency as a parameter for Vitroperm 500F 1 kW gapped inductor design: *(a)* natural convection-cooling, *(b)* cold-plate conduction-cooling. 170

Figure C.5. *AP* vs. current ripple with frequency as a parameter for 3C93 1 kW gapped inductor design: *(a)* natural convection-cooling, *(b)* cold-plate conduction-cooling. 170

Figure C.6. *AP* vs. current ripple with frequency as a parameter for MPP 60 1 kW gapless inductor design: *(a)* natural convection-cooling, *(b)* cold-plate conduction-cooling. 170

Figure C.7. *AP* vs. current ripple with frequency as a parameter for High Flux 60 1 kW gapless inductor design: *(a)* natural convection-cooling, *(b)* cold-plate conduction-cooling. 171

Figure C.8. *AP* vs. current ripple with frequency as a parameter for KoolMu 60 1 kW gapless inductor design: *(a)* natural convection-cooling, *(b)* cold-plate conduction-cooling. 171

Figure C.9. *AP* vs. current ripple with frequency as a parameter for XFlux 60 1 kW gapless inductor design: *(a)* natural convection-cooling, *(b)* cold-plate conduction-cooling. 171

Figure C.10. *AP* vs. current ripple with frequency as a parameter for 2605SA1 10 kW gapped inductor design: *(a)* natural convection-cooling, *(b)* cold-plate conduction-cooling. 172

Figure C.11. *AP* vs. current ripple with frequency as a parameter for 10JNHF600 10 kW gapped inductor design: *(a)* natural convection-cooling, *(b)* cold-plate conduction-cooling. 172

Figure C.12. *AP* vs. current ripple with frequency as a parameter for JFE Prototype 10 kW gapped inductor design: *(a)* natural convection-cooling, *(b)* cold-plate conduction-cooling. 172

Figure C.13. *AP* vs. current ripple with frequency as a parameter for Vitroperm 500F 10 kW gapped inductor design: *(a)* natural convection-cooling, *(b)* cold-plate conduction-cooling. 173

Figure C.14. *AP* vs. current ripple with frequency as a parameter for 3C93 10 kW gapped inductor design: *(a)* natural convection-cooling, *(b)* cold-plate conduction-cooling. 173

Figure C.15. *AP* vs. current ripple with frequency as a parameter for MPP 60 10 kW gapless inductor design: *(a)* natural convection-cooling, *(b)* cold-plate conduction-cooling. 173

Figure C.16. *AP* vs. current ripple with frequency as a parameter for High Flux 60 10 kW gapless inductor design: *(a)* natural convection-cooling, *(b)* cold-plate conduction-cooling. 174

Figure C.17. *AP* vs. current ripple with frequency as a parameter for KoolMu 60 10 kW gapless inductor design: *(a)* natural convection-cooling, *(b)* cold-plate conduction-cooling. 174

Figure C.18. *AP* vs. current ripple with frequency as a parameter for XFlux 60 10 kW gapless inductor design: *(a)* natural convection-cooling, *(b)* cold-plate conduction-cooling. 174

Figure C.19. Minimum *AP* vs. frequency for gapless materials (1 kW, 99% efficient): *(a)* convection-cooling and *(b)* conduction-cooling. 176

Figure C.20. Minimum *AP* vs. frequency for gapless materials (10 kW, 99% efficient): *(a)* convection-cooling and *(b)* conduction-cooling. 177

Figure C.21. *AP* vs. frequency for a 100 μH gapless inductor (10 kW, 99% efficient): *(a)* convection-cooling and *(b)* conduction-cooling. 178

Figure C.22. *AP* vs. frequency for a 100 μH gapless inductor (10 kW, no efficiency restriction): *(a)* convection-cooling and *(b)* conduction-cooling. 179

Figure D.1. Triangular remagnetisation with varying duty cycle. 184

Figure D.2. Rising edge equivalent demagnetization waveform. 185

Figure D.3. Falling edge equivalent demagnetization waveform. 185

Chapter 1
Introduction

This chapter provides an overview of the research project background and outlines the thesis structure. The dc-dc soft-switched converter, magnetic material comparisons and inductor optimization flowchart presented in this thesis are intended for automotive or industrial use, where the size and cost are of prime importance. Thus, electric vehicle propulsion architectures are investigated and the roles of the dc-dc converter and its subcomponents in the vehicle powertrain are discussed.

1.1. Overview

Environmental concerns [1] and natural resource availability [2] are motivating drivers for technology advances in order to achieve greater energy efficiency. Drive for optimum efficiency at reasonable cost is common across the full spectrum of the power electronics industry, ranging from automotive powertrains to household appliances.

The internal combustion engine (ICE) vehicle suffers from low fuel efficiency during acceleration, and uses fuel while idling. The ICE process is irreversible and regenerative braking is impossible. On the other hand, fully electric, battery-operated vehicles suffer from limited range and long charging times. Car manufacturers are addressing these issues by merging these two approaches into hybrid electric vehicles (HEV) which combine the range of the ICE with the benefits of electric power support during acceleration, regenerative, and idling. The hybrid system can save up to 30% or more of the fuel in the urban driving cycle [5].

The battery electric vehicle (BEV) is pollution free at the point of use. However, the emissions are not eliminated, but transferred from the tailpipe into the power plant chimney [6]. The fuel cell vehicle (FCV) uses hydrogen and is often seen as the future for the on-board power plant.

Since HEV, BEV and FCV use batteries, dc-dc converters play a key role in the power system architecture as an interface between the battery and traction inverter. The task of the battery storage is very similar for the HEV and FCV and it is usually restricted to limited time periods of high-power demand such as acceleration or hill climbing; while the BEV operates solely on the battery power and the dc-dc converter, if present, operates continuously according to the power demand. The FCV may be equipped with a separate dc-dc converter as the fuel cell output voltage varies significantly with the load. The HEV, BEV and FCV architectures are discussed in [4].

Compact and efficient dc-dc converters are key components of the electric powertrain and several bi-directional topologies are already presented in [4][7]-[28]. The traction inverter dc-bus voltage may be up to 1 kV, which allows for high power and efficient operation. However, the resultant currents can still be high and are of the order of hundreds of amps. Large currents increase the electric and thermal stress on the component; thus, detailed optimization must be undertaken in order to satisfy the efficiency and size requirements. The system operating voltages must be considered as the battery and fuel cell voltages vary with load and may cause additional stress. The magnetic components should be carefully optimized to guarantee high partial-load and full-load efficiency and smallest overall size and cost.

The dc-dc converter design is constrained in a number of ways. The designer must select the optimum topology in order to satisfy the voltage and power requirements. The dc-dc converter may be low or high ripple, which is reflected in semiconductor selection. Also a hard- or soft-switching regime may be implemented according to the design philosophy. Interleaved discrete inductor or coupled inductors may be employed. Since the required inductor parameters are given by the chosen topology and semiconductor evaluation, the magnetic component may be optimized by the appropriate material selection, core geometry and cooling method.

1.2. Thesis Objectives

The thesis covers the wide area of power electronics in dc-dc conversion. The problem of the MOSFET body diode in the bi-directional dc-dc is addressed with a novel variation of the half-bridge non-isolated buck-boost converter with an auxiliary soft-switching cell. The soft-switching cell reduces the power loss during switching and allows for the MOSFET's intrinsic body-diode utilization without excess power loss. The high-frequency (100 kHz) dc-dc converter operation is investigated under low- and high-ripple regimes for hard- and soft-switching. The soft-switched dc-dc converter operation is analysed in detail and a full set of the equations is developed. The converter's operation analysis is validated by experimental results. Finally, the IGBT and MOSFET transistors operation under hard- and soft-switching is examined. The thesis provides a number of answers for the bi-directional converter operation at high-frequency regarding power limitations, advantages and frequency limits. The hard- and soft-switching regime is contrasted in order to aid the topology and semiconductor selection for the optimum dc-dc converter design.

The magnetic component is an essential part of the dc-dc converter. The inductor and transformer are traditional and well-established components of the power converter. Since the magnetic component depends on the magnetic material, the material selection is critical for an efficient design with maximized power density. In this thesis, a novel material selection approach is presented, which is suitable for dc inductors, both convection and conduction-cooled.

The magnetic material selection is verified by use of the dc-inductor design algorithm, which is developed in this thesis. The algorithm is a useful tool for inductor size investigation. The inductor design may be limited by a number of constraints, such as efficiency, maximum temperature rise, air gap length, number of turns and many more. Finally, the high-flux magnetic materials for high current dc-inductors are investigated. The study investigates the effects of frequency, dc-bias, extreme duty cycle, air gap, and thermal configuration.

1.3. General Background

We are living in a time with significant concern about climate change [31]. It is proven that global average temperatures have increased considerably in the last couple of decades.

In Earth's history before the Industrial Revolution, Earth's climate changed due to natural causes, generally not related to human activity. Most often, global climate has changed because of variations in sunlight. Tiny wobbles in the Earth's orbit altered when and where sunlight falls on the Earth's surface. Variations in the Sun itself have alternately increased and decreased the amount of solar energy reaching Earth. Volcanic eruptions have generated particles that reflect sunlight, brightening the planet and cooling the climate. Volcanic activity has also increased greenhouse gases over millions of years, contributing to episodes of global warming and cooling [31][32].

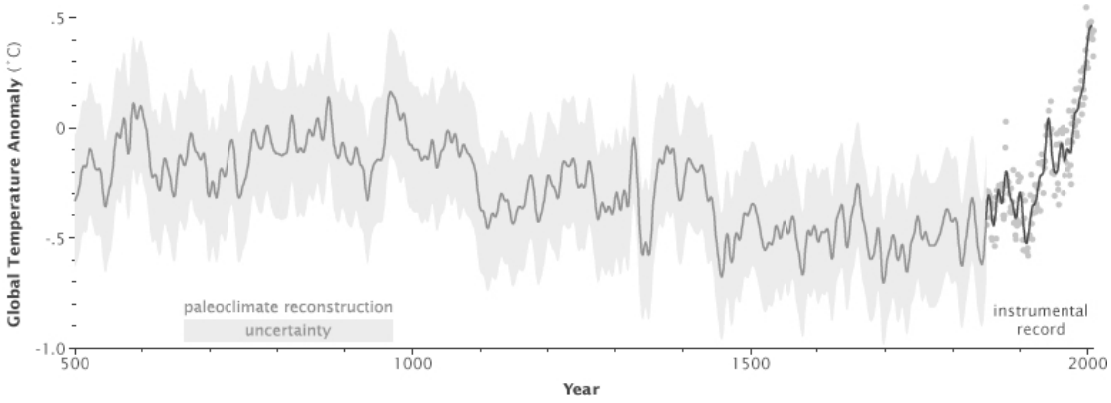

Figure 1.1. Temperature histories from paleoclimate data (green line) compared to the history based on modern instruments (blue line) suggest that global temperature is warmer now than it has been in the past 1,000 years, and possibly longer [31].

Models predict that Earth will warm between 2 and 6 degrees Celsius in the next century. While global warming has happened at various times in the past two million years, it has usually taken the planet about 5,000 years to warm 5 degrees. The predicted rate of warming for the next century is at least 20 times faster. This rate of change is extremely unusual [31].

Environmental concerns are not the only ones as the modern world is based on the availability of crude oil. The oil-fired transportation system is a major contributor to global greenhouse gas emissions, but limited resources of crude oil and increasing instability in the security of their supply diverts attention towards alternative technologies such as hybrid, electric, fuel cell, compressed air, and fly-wheel-based vehicles. The development of alternative and more efficient transport is essential for the economic and environmental sustainability.

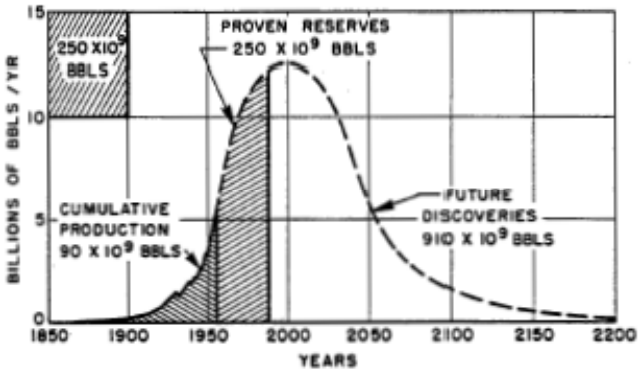

Figure 1.2. Ultimate world crude oil production based upon initial reserves of 1250 billion barrels [33].

The peak of production and world reserves for oil, as shown in Figure 1.2, were characterized by M. King Hubbert in 1956 [33] and is known as the Hubbert peak theory.

The crude oil price is strongly related to demand and supply as well as to the political situation and speculation [35]. Figure 1.3 shows the monthly averaged oil prices since 1946 adjusted for inflation in August 2010 dollars using the Consumer Price Index (CPI-U) as presented by the Bureau of Labour Statistics [36][37].

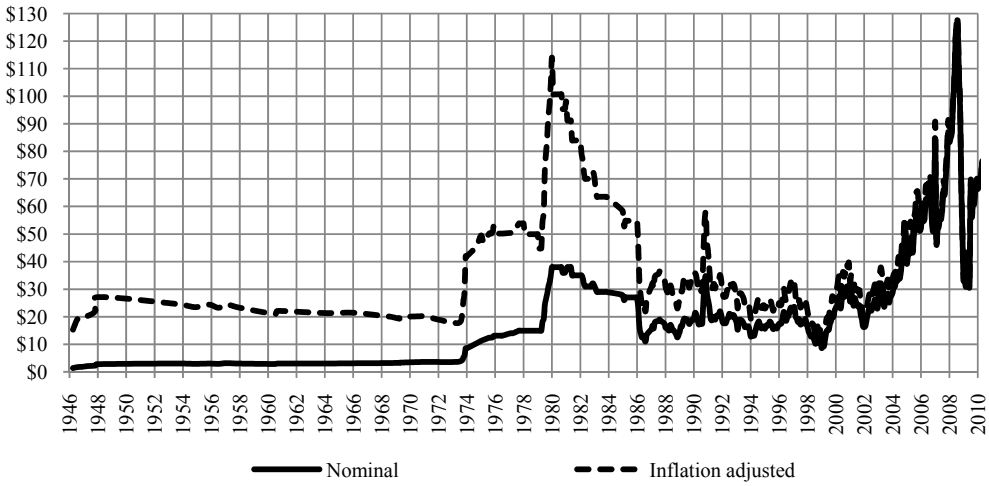

Figure 1.3. History of Illinois basin posted monthly crude oil prices [36][37] .

Note that the fall from the 1979 peak took until 1986 (7 years) to fall as much (percentage wise) as it lost in only six months in 2009. The absolute crude oil price peaked on the 11th of July 2008 reaching a record of $147.27.

The crude oil price does not reflect the real problem. Even a price of $100 or $200 per barrel would not increase crude oil resources nor stop people from filling up tanks. Thus, the development of alternative crude-oil-independent propulsion is essential for sustainability. The efficient and wise use of the crude oil resources would extend the oil era until a new energy source is fully developed.

1.4. Electric Vehicle Propulsion Architecture

The internal combustion engine (ICE) is an essential component of the modern vehicle propulsion system. It is the well known concept invented in 1876 by Nicolaus Otto. Since 1876 ICEs have been evolving and present ICEs are similar to the original prototype only by their operating principles. The modern ICE is a masterpiece of advanced technology. The ICE can be divided by ignition type: spark-ignited petrol engines and diesel engines. The classical ICEs are 2- or 4-stroke, which literally mean 1 or 2 crankshaft revolutions per working cycle. However, there are other types of ICEs which have been less popular in traditional powertrain system. The Wankel rotary piston engine is offered only in the Mazda RX-8. The Atkinson cycle engine is designed to provide high efficiency at the expense of lower power density and has found its place in hybrid electric vehicles such as the Toyota Prius and Ford Escape.

The main ICE vehicle elements are the ICE, gearbox, and transmission. A simplified ICE-based vehicle propulsion is presented in Figure 1.4. The ICE is predominantly fed by gasoline or diesel, but alternative solutions do exist and some cars are fed by CNG, LPG, or biofuels. A hydrogen-powered ICE was developed by BMW in the mid 90's, but it appears to be an expensive approach with marginal efficiency gains.

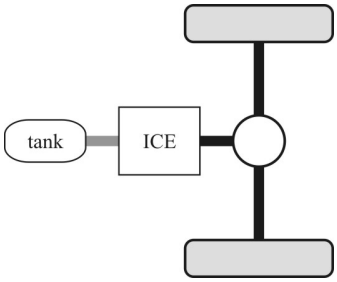

Figure 1.4. Traditional ICE-based powertrain.

The ICE vehicles produce significant tailpipe emissions and these gasses require significant treatment before they can be exhausted. The ICE's overall low drive cycle efficiency, poor transient efficiency, and idling energy loss are problem areas. Also, the braking energy cannot be recovered. The typical ICE vehicle efficiency is about 13 % according to [39].

The hybrid electric vehicle (HEV) combines the ICE with the electric motor and electric battery storage. The major challenges for HEV design are managing multiple energy sources, and are highly dependent on driving cycles, battery sizing, and battery management. HEVs take advantage of the electric drive to compensate for the inherent weaknesses of the ICE. The HEV electric drive optimizes the ICE operation in the high efficiency area and also reduces idling, supports power transients while accelerating, and use regenerative braking instead of mechanical braking during deceleration and downhill driving [4].

Traditionally, HEV are classified into two fundamental categories: series and parallel. The functional block diagrams of series and parallel HEVs are presented in Figure 1.5 and Figure 1.6, respectively. A key feature of the series hybrid is to couple the electric power from the ICE/generator and the battery to supply the electric power to propel the wheels, while the key feature of the parallel hybrid is to couple the mechanical power from the ICE and the electric motor to propel the wheels.

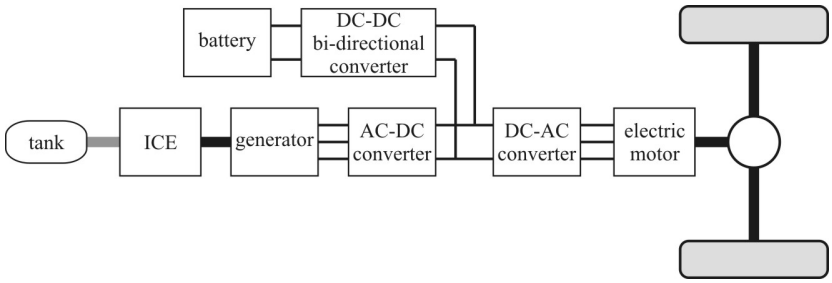

Figure 1.5. Series hybrid electric powertrain.

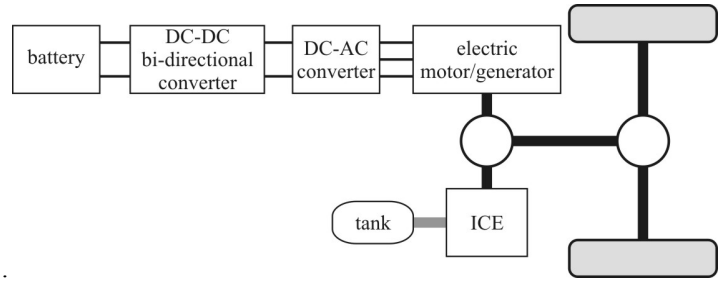

Figure 1.6. Parallel hybrid electric powertrain.

Other HEVs propulsion systems are available e.g. the series-parallel hybrid is a direct combination of both the series and parallel hybrids which allows for energy flow directly from the ICE to the battery.

Due to the variations in HEV configurations, different power control strategies are necessary to regulate the power flow to or from different components. These control strategies aim to satisfy a number of goals for the HEV. The four key goals are: maximum fuel economy, minimum emissions, minimum system costs, and good driving performance.

In general, the hybrid electric vehicle offers the following benefits as compared with the conventional engine: potentially less maintenance, better gas mileage, reduction in air pollution and subsequent greenhouse gas (CO_2) emissions and petroleum use, less noise and vibration, improved acceleration, and the ability to operate various appliances with the engine off.

The hybrid vehicle is an intermediate step towards complete vehicle electrification. If the ICE is removed from the HEV the vehicle becomes the battery electric vehicle shown in Figure 1.7. The battery provides energy for entire vehicle and can be charged either from the household socket or high power charger.

The fuel cell vehicle (FCV) can be considered as the ultimate solution allowing for independent long-range operation with zero emissions. As shown in Figure 1.8, the FCV structure is the same as for series HEV [4].

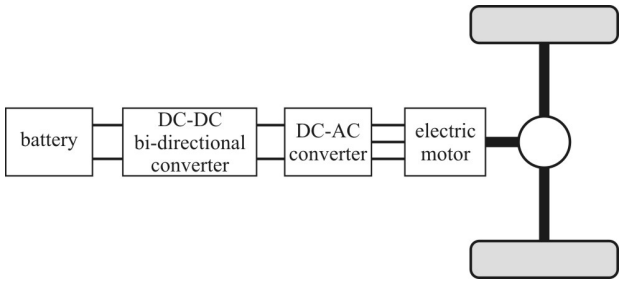

Figure 1.7. Battery electric powertrain.

The presented vehicle system configurations are the most common. However, many configurations are reported in literature and gathered in [39] and [40]. In general, the fuel cell can be connected to the system dc-bus directly or through the dedicated uni-directional dc-dc converter as the fuel cell is an irreversible source of electrical energy. Due to the poor time response it is necessary to support the fuel cell with a supercapacitor or battery pack from the impact of high energy instantaneous transients and braking energy recuperation. The battery pack or supercapacitor itself may be connected directly to the dc-bus or through the bi-directional dc-dc converter.

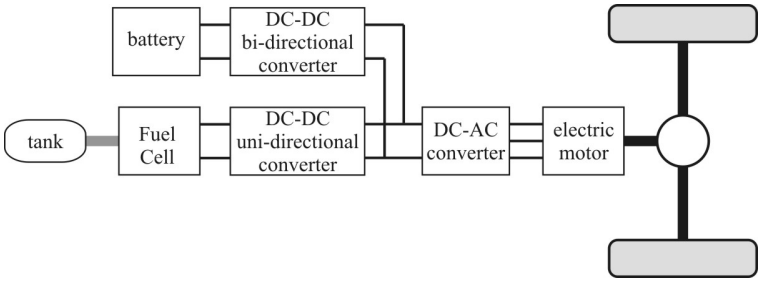

Figure 1.8. Fuel cell electric powertrain.

In transportation, hybrid vehicles offer significant advantages over the internal combustion engine alone as improved fuel efficiency directly translates into reduction of tailpipe emissions. The ICE supported by an electric motor can be optimized and downsized allowing for the most efficient fuel usage, while maintaining the same performance.

1.5. A DC-DC Interface For Electric Vehicle

As shown in the previous section the dc-dc converter couples the fuel cell or battery to the vehicle's inverter dc-bus. In general, the isolation between primary and secondary of the powertrain dc-dc converter is not necessary, but isolation is required for grid-connected chargers [7][11][27]. This divides available topologies into groups suitable for each application. Moreover, the fuel cell and battery have output characteristic voltages which are a function of many constraints. The terminal voltage variations as a function of the power and state of charge for the fuel cell and Li-ion battery are shown in Figure 1.9 *(a)* and *(b*), respectively.

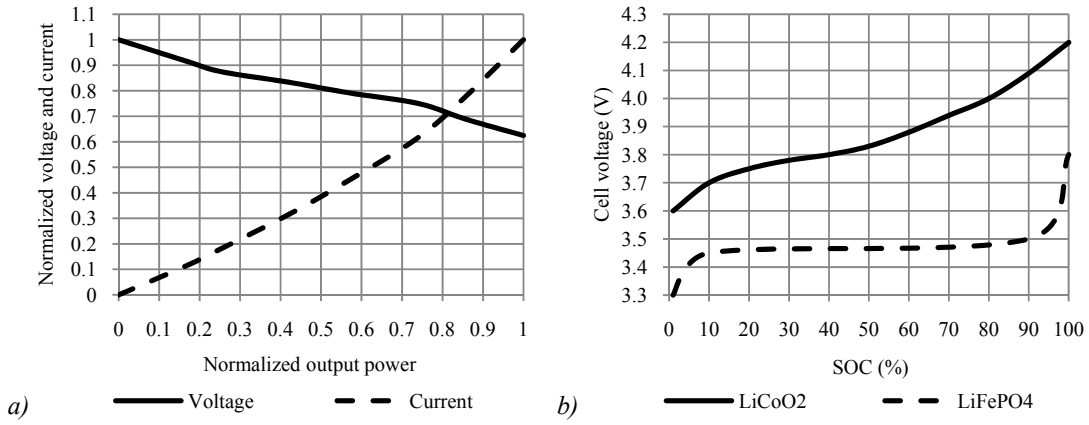

a) *b)*

Figure 1.9. Output characteristic of: *(a)* fuel cell voltage and current vs. normalized power; (*b)* and lithium based battery voltage vs. state of charge [45][46].

The fuel cell terminal voltage at full load can be reduced compared to the no-load voltage. The fuel pressure and fuel flow affects the terminal voltage as well, but this is usually kept under control. Thus, the fuel cell dc-dc converter has to deal with significant input voltage variation.

Since a single fuel cell produces approximately only 1 V, it has to be stacked into a module in order to provide a high terminal voltage; some vehicle prototypes use fuel cell stacks of 200-400 V. However, reliability issues can reduce the fuel cell stack voltage to the range of 100 V as explained in [46]. Therefore, the high boost ratio is another challenge for the dc-dc converter design and some solutions are already proposed [47].

The battery terminal voltage varies with the state of charge and the electrode material as shown in Figure 1.9 *(b)* for lithium-based batteries. The terminal voltage variability is lower than for the fuel cell and some batteries may have flat voltage characteristics. The terminal voltage depends as well on the discharge current rate and the battery temperature [48].

There are many battery chemistries available, but only a few are suitable for use in an electric or hybrid vehicle. Battery cells differ by their chemistry and electrode technology. Some

batteries have a high energy density but relatively low specific power, while others have a lower energy density but a very high power.

The battery chemistry sets the cell voltage which ranges between 4 V for Li-ion to 1.2 V for NiMH. Thus, similar to the fuel cell, the battery cells are stacked to form high voltage packs. The battery cell is fragile for deep discharging, over charging, over current, and high and low temperatures which may compromise its safety. Therefore, an individual cell management system is an inherent part of the battery pack.

1.5.1. DC-DC Converter

The dc-dc converter is an essential part of the vehicle powertrain for fuel cell vehicles and is often used in battery-electric and hybrid-electric vehicles. There is a great variety of dc-dc converter topologies suitable for the fuel cell or battery interface. The following sections outline the basic topologies for the vehicle charger and powertrain.

The hybrid or electric vehicle power train does not require galvanic isolation [4][7][8][11][13]. Typically, the battery or fuel cell voltage is significantly lower than the main dc-bus voltage and, assuming that the battery voltage is never higher than the dc-bus voltage, a simple bi-directional buck-boost converter can be employed as shown in Figure 1.10 *(a)* [7][27]. The simple half-bridge buck-boost topology allows for an energy conversion from the low voltage source to a high voltage in boost mode and from the high voltage to low in buck mode. If the battery voltage is similar to the main dc-bus, a bi-directional cascade converter may be employed shown in Figure 1.10 *(b)* [7][8][9]. The cascade converter allows for the smooth battery or supercapacitor operation with the dc-bus, where the storage unit voltage may be higher or lower than the dc bus according to the state of charge.

The single-phase buck-boost converter, as used in the Toyota hybrid system, shows relatively low part-load efficiency. The multi-phase interleaved buck-boost was developed with phase disabling in order to increase part-load efficiency [8][11]. The interleaved converter with discrete phase inductors is shown in Figure 1.10 *(c)*. The advantage of the interleaved converter is significant as input and output capacitance is reduced due to current ripple cancellation. Advanced magnetic design approaches may also further reduce the converter size. An interleaved buck-boost converter with inter-phase magnetic coupling is presented in Figure 1.11 *(a)* [13][14]. The magnetic coupling introduces a transformer and allows for a significant inductance reduction.

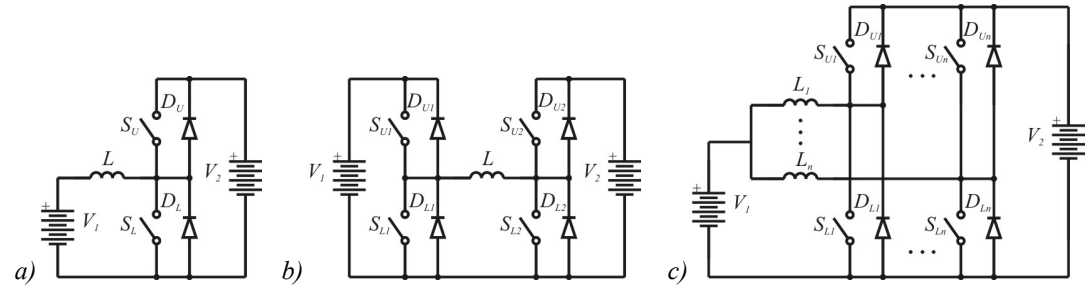

Figure 1.10. Non-isolated dc-dc converter: *(a)* buck-boost, *(b)* cascade, *(c)* interleaved buck-boost.

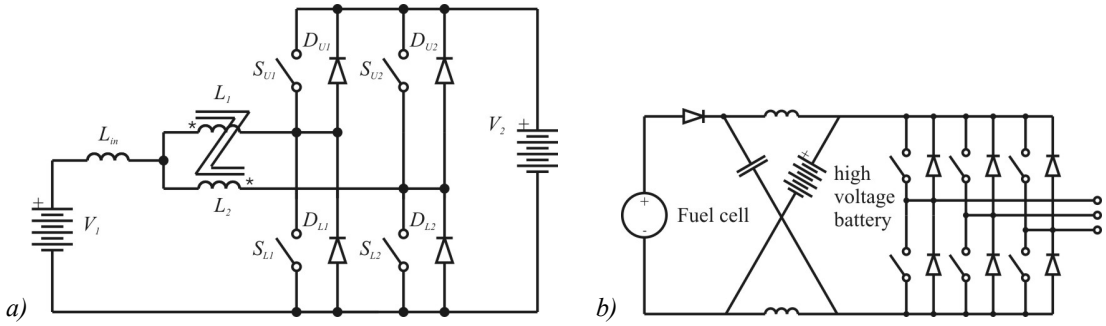

Figure 1.11. Non-isolated dc-dc converter: *(a)* interleaved buck-boost with inter-phase coupling, *(b)* Z-source inverter.

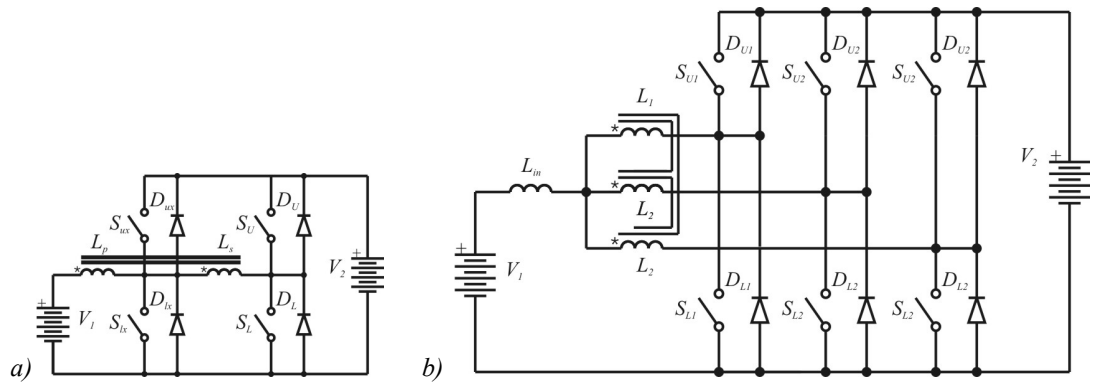

Figure 1.12. Non-isolated dc-dc converter: *(a)* soft-switched buck-boost, *(b)* interleaved buck-boost with diode soft switching.

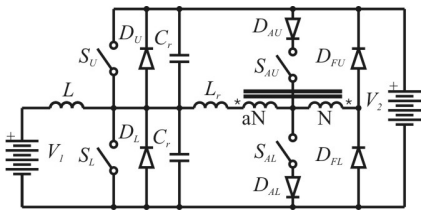

Figure 1.13. Non-isolated buck-boost with auxiliary soft-switching cell.

For FCVs, the fuel cell voltage to the inverter decreases with an increase in the power drawn from the fuel cell. Therefore, the obtainable output voltage of the traditional PWM inverter is low at high power resulting in an over-sized inverter and motor. The dc-dc boosted PWM inverter does not have this problem but the extra dc-dc stage increases the cost and complexity of the circuit, and reduces the overall system efficiency. The Z-source inverter provides single stage power conversion, higher efficiency and a reduced system component count. Figure 1.11 *(b)* presents the Z-source inverter [15].

The dc-dc converter efficiency may be increased by employing soft-switching techniques. While ac resonant-based converters can operate without significant topology change, a dc-dc converter requires a complex system for a soft-switching operation. There is great variety of the soft-switching dc-dc converters. Figure 1.12 *(a)* and *(b)* shows soft-switched converters with magnetic coupling. The converter shown in Figure 1.12 *(a)* uses an auto-transformer linked with the auxiliary half bridge in order to achieve zero-voltage transition and zero-current transition as explained in [16]. The multiphase converter presented in Figure 1.12 *(b)* uses inter-phase coupling in order to achieve soft-switching as explained in [17]. Note that magnetic coupling is different than for the interleaved converter shown in Figure 1.11 *(a)*. The diode's turn off process is softened by controlling the diode's current fall. A frequency adjustment is necessary in order to keep the system in the minimum recovery loss region. The dc-dc converter with an auxiliary cell with the voltage source is shown in Figure 1.13. The soft-switching auxiliary cell for a bi-directional converter is the main subject of Chapter 2; the main advantage of this quasi-resonant topology over the others is the minimized stress on the components.

The generalized analysis of soft-switching dc-dc converters is presented in [18]. The soft switching is obtained by increased cell complexity. In general, a soft-switching cell or snubber takes over the diode turn-off process by limiting the rate of change of current. The cell often provides for the zero voltage turn-on of the main transistor.

A natural commutation or zero-crossing conduction mode for 2-quadrant converters may be employed for the soft switching operation as explained in [20]. The switching frequency may be modulated in order to improve efficiency.

1.5.1.1. Hard Switching vs. Soft Switching

The basic non-isolated dc-dc converter is composed of semiconductor power switches, diode and transistor, and LC filtering network. Some other converters may use a transformer to provide galvanic isolation.

The transistor operation is penalized by the power loss due to turn-on and turn-off transients. The switching power loss during transient is equal to the product of current and voltage across the switch, as shown in Figure 1.14. The energy lost during a single switching period limits the maximum energy transferred through the switch and affects converter efficiency. The switching power losses sets the operating frequency area for the switch as the switching power losses becomes a significant contributor as frequency increases.

The silicon-based diode suffers significant power loss due to reverse recovery. The reverse-recovery power loss depends on several factors such as temperature, initial current and switching current rate of change. Due to reverse recovery the diodes power loss can be a significant contributor to the total semiconductor losses. Some low power loss alternatives exist, but are beyond the scope of this thesis due to high cost and availability for a high power converter.

The switching power loss phenomenon is well known and recognized as in [49]. A number of snubber circuits were developed throughout the years in order to reduce switching power losses. The snubber circuitry softens the voltage and current transients and allows for so called soft-switching. Typicall soft-switching waveforms are illustrated in Figure 1.15. As shown, at turn-on the current rise may be delayed by the inductive snubber or soft-switching cell, while turn-off is usually assisted by the capacitive snubber. The diode turn-off process is usually softened by the controlled rate of change of current descend. Reference [49] is a very extensive source of knowledge of snubbers.

In general, the soft-switching allows for semiconductors switching loss reduction at the expense of increased circuit complexity and some power loss in the snubber itself. The snubber circuit requires design compromises between: cost, complexity, reliability, power loss, and circuit performance.

Note that waveforms and associated energy loss shown in Figure 1.14 and Figure 1.15 are with the same scale.

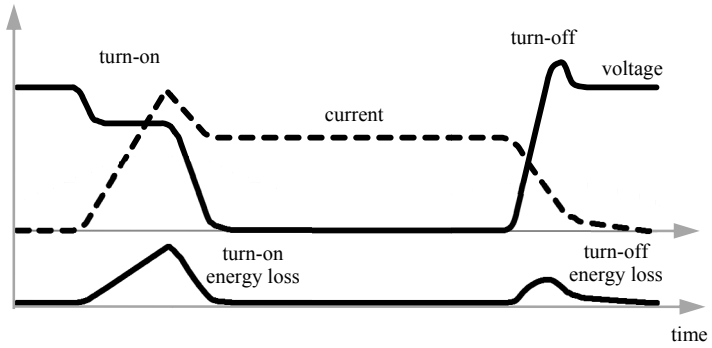

Figure 1.14. Hard-switched transistor operation.

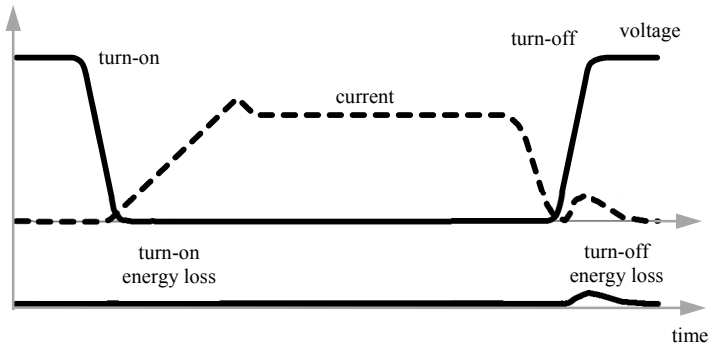

Figure 1.15. Soft-switched transistor operation.

1.6. DC-DC Converter Components

DC-DC converter optimization requires an in-depth analysis of the component selection in order to satisfy given assumptions and requirements. This section briefly outlines fundamental components of the dc-dc converter such as the power switch, magnetics and capacitor. The control unit is not in the scope of this work and is omitted.

1.6.1. Power Switch

The power switch selection and optimization is the first step of the converter design as the semiconductor power devices are the main cost driver. The ideal switch should have near zero power losses, low on-state resistance, attractive thermal coefficients, fast switching speed,

low energy stored in output capacitance and freedom from charge recombination losses.

The IGBT and MOSFET transistors and the PN diode are the main components for the automotive power converter design. The IGBT and PN diode are minority carrier (bipolar) devices while the MOSFET is a majority carrier (unipolar) device. Currently silicon-based power devices dominate; however, advanced materials such as silicon-carbide, SiC, and gallium-nitride, GaN, are under development. Only SiC Schottky diodes are already available in high volume, while SiC transistors are still at the prototype stage. Low voltage GaN devices are already available.

The Si-based devices are penalized by intrinsic silicon properties. The p-n junction charge is substantial and it is the main contributor to the switching power loss in bipolar devices. The Si-based bipolar diode suffers significant reverse-recovery loss. The IGBT is penalized by so-called tail current, which increases turn-off power loss. Both the IGBT and diode are unidirectional and often the IGBT is equipped with an anti-parallel diode.

The MOSFET transistor is a majority carrier device, which is controlled by voltage at the gate electrode. However, the MOSFET is penalized by the anti-parallel intrinsic body diode. This diode has very poor reverse recovery characteristic, and the MOSFET's application is limited to the topologies where the body diode does not have a significant effect on the circuit performance.

The Si-based devices are in continuous development. The structure optimization is a key challenge. The main improvements are achieved through conductivity modulation and electric-field reduction.

The IGBTs are improved by conductivity modulation and the state-of-art is the thin-wafer punch-through IGBT where the electric field and stored carrier during the on-state is optimized. The IGBT is an excellent power switch for high voltage circuits from 300V up to several kV. Unfortunately, the switching power loss limits the operating frequency of the IGBT to low to medium frequencies, although some lower powered 100 kHz devices are available [51][52].

The power MOSFETs revolutionary concept of E-field reduction is termed the super junction. The concept is also known commercially as RESURF or COOLMOS. The super junction concept is based on charge compensation across the p-n junction. For the same doping profile, the electric field across the super junction is much lower than in the conventional p-n junction. Therefore, a much higher breakdown voltage is achieved [50]. The super junction MOSFET can handle more power than the conductivity modulated IGBT, and does so at a much lower switching loss because of the absence of storage charges. Note that the MOSFET is typically penalized by a significantly higher output capacitance than the IGBT, which may result in parasitic ringing when combined with the low channel resistance.

The typical Si-based semiconductor devices application range is shown in Figure 1.16. The power MOSFETs are usually limited to 1.2 kV devices while available IGBTs are rated up to 6.5 kV [53].

The Si-based devices reach structural and material limits and further improvement requires either significant technological changes or new materials. Devices based on wide-band gap (WBG) materials SiC and GaN are under development and are now being commercialized.

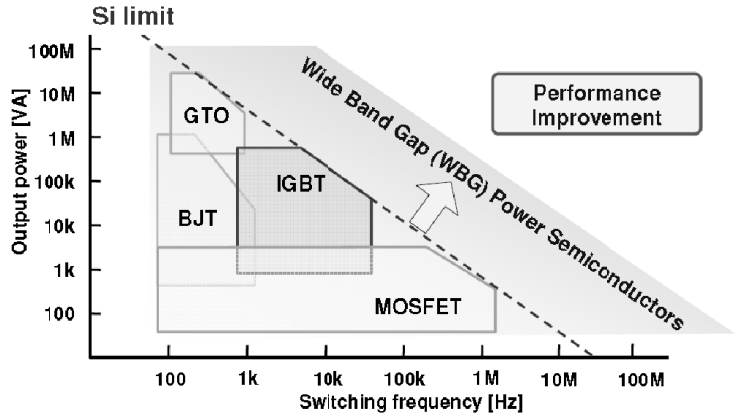

Figure 1.16. Application of various device types [50].

SiC and GaN and other wide-band-gap semiconductors offer significant advantages in high power applications as their critical electric field for avalanche breakdown is much higher than silicon. This allows for building thinner layers and lower conduction power losses. The intrinsic concentration is much lower for SiC and GaN than for Si. Therefore, WBG devices do not suffer from the stored charge effect and switching power loss is reduced. WBG semiconductors allow for high voltage Schottky diodes of excellent performance. Also, SiC and GaN allow for high temperature operation up to 250 °C, while Si is limited to 175 °C. Additionally, SiC has over two times higher thermal conductivity than Si and GaN which allows for more efficient heat removal [50].

Today, the largest applications in potential SiC revenue remain power factor correction, uninterruptible power supply and ac motor drives. In the future, EV/HEV and inverters for PV installations will take the lead exhibiting higher CAGR (>15%/year) [56]. “Cost issues slow-down SiC penetration and we only forecast approximately 4% of the overall Silicon-based power discrete market to be displaced by SiC in 2019” is noted in [56].

The entrance of SiC into the EV/HEV field has been postponed to 2014 as no switch has yet reached large volume production and car makers are still improving silicon IGBT technology. Many of the current or new entrant EV/HEV manufacturers are working on both GaN and SiC [56].

1.6.2. Magnetic Component

The magnetic component is a second-largest cost contributor of the converter. Magnetics for high power converters are usually custom designed. Major concerns are the size, weight and efficiency, as the inductor or transformer may be the single heaviest component in the entire converter. In-depth magnetic material and design analysis allows for an efficient and compact inductor as it is critical for overall dc-dc converter size, cost and power loss reduction.

A significant portion of this thesis is devoted to the magnetic design. Detailed magnetic material selection and state-of-art magnetic materials are compared and contrasted using a novel performance factor presented in Chapter 3. Inductor size analysis based on the purpose-developed inductor design algorithm is presented in Chapter 4. The experimental material comparison, algorithm validation and fundamental design issues are investigated in Chapter 5.

1.6.3. Capacitor

The capacitor is usually the last, but not least component of the design optimization. The capacitor size follows the converters input and output voltage ripple requirement [87].

There is a variety of capacitors available to the designer [60][61][62]. In general, every single capacitor is characterized by capacity, equivalent series resistance, maximum operating voltage and current ripple, and operating temperature range. The capacitance and resistance constitutes the capacitor dynamics and affect the transient response, which is critical for high frequency converters. It is very easy to link the capacitance with capacitor size. In general, capacitor selection is not an extremely challenging task and usually is limited to the type of the capacitor and its properties.

The topology selection and operating regime is a very important when it comes to the capacitor sizing. The capacitor size can be reduced if a low-current ripple is employed. High-frequency operation usually reduces the capacitance requirement, but the capacitor may be penalized by increased power loss.

In general, the capacitor sizing is closely linked with the magnetic component sizing, and the two components should be considered together for system optimization.

1.7. Thesis Structure

The thesis is organised into 6 chapters. The research motivation and background of the bi-directional dc-dc converters role in the electric vehicle powertrain has been presented in this introductory chapter. Also, a brief overview of batteries, fuel cells, and bi-directional dc-dc converters topologies have been presented.

The soft-switched quasi-resonant bi-directional high-frequency dc-dc converter is proposed and investigated in Chapter 2. Detailed mode-by-mode analysis of the soft-switching cell converter operation is presented and an averaged model developed. The theoretical considerations are validated by the experimental results. The hard- and soft-switched converters are compared and contrasted. The limitations and advantages of the soft-switched converter over the traditional hard-switched counterpart are explained. The soft-switching converter operation at frequencies above 100 kHz proves that soft-switching enables the new operating area for traditional off-the-shelf components. A short discussion on new semiconductor advances is provided.

Chapter 3 introduces novel performance factors for magnetic material comparison for convection- and conduction-cooled transformers and ac and dc inductors. The magnetic materials comparison from various vendors is presented.

A custom inductor design algorithm is developed in Chapter 4. A number of designs are compared and contrasted.

Chapter 5 presents an experimental investigation of high-flux magnetic materials for high-current dc inductors. The algorithm developed in Chapter 4 is validated with experimental results. The study investigates the effects of frequency, dc-bias, extreme duty cycle, air gap, and thermal configuration.

Finally, the summary, conclusions and suggestions for future work are collected in Chapter 6.

Chapter 2

A Soft-Switched DC-DC Converter

High-power and high-density bi-directional dc-dc converters are key component of the efficient energy management in industrial applications and in automotive battery power systems. The cost, efficiency and size of the converter are usually the main constraints for a system designer. Especially for high-volume industrial and automotive products cost is a critical factor. Semiconductor devices are the main cost contributor followed by the magnetic component. Thus, special attention is paid to the semiconductor size optimization including switching and conduction power loss reduction. Semiconductor power loss reduction can be achieved by technological improvements and by employing soft-switching techniques for switching power loss reduction. Soft-switching usually removes switching power loss from the switches at cost of the auxiliary circuit and thus, increases complexity.

In this chapter a novel variation of a bi-directional dc-dc converter with an auxiliary auto-transformer based soft-switching cell is presented. The converter's mode-by-mode operation is analysed and closed-form expressions are presented for the average current gain of the converter. The expressions are validated by simulation and experimental results. The circuit limitations are discussed.

Two well established buck-boost converters have been designed and constructed in order to compare their performance relative to the novel soft-switching cell which has been developed in this chapter. The first of these uses a high-ripple regime together with MOSFET's using a bipolar current mode of operation to achieve soft-switched commutation. The second is a conventional low-ripple hard-switched bi-directional dc-dc converter using IGBT devices together with co-packaged ultrafast diodes.

The experimental results show that the soft-switching converter allows for operation at elevated frequency with high efficiency and low current ripple. The free-wheeling diode power loss is reduced; thus, intrinsically the MOSFET's poor diode can be employed without penalty. The soft-switching cell allows for efficient operation beyond 100 kHz.

Part of the work presented in this chapter has been published at the EPE 2007 conference.

2.1. Introduction

The use of a bi-directional dc-dc converter as the power management interface between a high-voltage main bus and a low-voltage battery storage unit is becoming a standard solution in many industrial applications and in Hybrid Electric Vehicles (HEV's). In particular, the HEV requirement for high power levels with restricted weight and volume favours non-isolated topologies as the electrical isolation is not required [7]. As the interface between the battery pack and the main power bus, the converter design is constrained in number of ways. The voltage from a high-voltage battery pack varies typically from 150 V to 350 V, a significant change which depends upon the state of charge of the battery. The main power bus may be of the order of 650 V or more [10][11][29][30]. The converter is required to transfer power to, or from, the battery pack depending on the balance of power available from all power sources and the required output traction and auxiliary load powers.

Low and medium frequency, IGBT-based, hard-switched converters are widely used. Higher switching frequencies result in lower passive component size and are employed for a compact design [63]. However, at the higher operating frequencies, semiconductor switching losses become a dominant factor in the system power loss. To limit switching losses, snubbers, soft switching cells or a high current ripple regime can be employed. The use of a soft-switching cell eliminates turn-on losses in the main power devices at the expense of increased circuit complexity and some smaller losses in the soft switching cell itself.

The magnetic component can be reduced as frequency increases as will be shown in Chapter 4 and in [63]. However, the maximum allowable magnetic component current ripple must be reduced at elevated frequency due to power loss limitations. Thus, size reduction does not strictly follow the frequency increase. A high-frequency and high-ripple operation is usually penalized by eddy current effects and therefore high-frequency operation with a high current ripple may lead to multiphase design as shown in [11]. In general, a high power inductor tends to operate at rather low current ripple at high frequency e.g. about 15-30 % at 100 kHz for an amorphous based inductor as will be shown in Chapter 4.

In order to identify the most appropriate solution, this research proposes and investigates a novel variant of the non-isolated bi-directional half-bridge dc-dc converter, which is based on a previously-published autotransformer soft-switching cell [28][64]-[66]. The chosen circuit permits use of intrinsic body diode of MOSFET transistors. It is widely known that the body diode is a major constraint in bi-directional dc-dc MOSFET applications and limits somewhat the benefits of the MOSFET structure. The MOSFET is successfully used in uni-directional dc-dc converters e.g. buck and boost with a discrete fast-switching, soft-recovery free-wheeling diode. However, in the bi-directional converter, both of the diodes take a part in energy

processing. The intrinsic diode-recovery-loss phenomenon is a significant factor in the total power balance. The proposed topology uses intrinsic body diodes with a soft-switching cell which facilitates the body-diode's turn-off process, thus limiting the associated losses. Inevitably, however, this results in an additional loss in the soft-switching cell.

While the use of the soft-switching cell improves the overall efficiency of the bi-directional MOSFET-based converter, it can significantly reduce the average pole voltage as a function of operating duty-cycle. An accurate analysis of this phenomenon is quite involved. This chapter presents novel normalised expressions for the average pole voltage and the output current gain of the bi-directional cell. The full mode-by-mode analysis is provided. The results include the combined effects of controlled-diode turn off, resonant-pole-voltage turn-on and turn-off transitions, as well as the impact of output-current ripple. Consequently, closed-form expressions are derived for the duty cycles corresponding to discontinuous conduction operation in both directions. The accuracy of these equations, which are useful from a design perspective, is verified through corresponding PSpice simulations and confirmed by experimental results. The soft-switched cell converter component selection and limitations are outlined. As well as the detailed analysis, a performance comparison with a high-ripple MOSFET-based converter and a low-ripple IGBT-based converter, all operating at 100 kHz, is presented.

2.2. The Topology of Choice

The topologies investigated in this research are a conventional bi-directional dc-dc converter and novel variant of soft-switching converter with auxiliary switching cell shown in Figure 2.1 *(a)* and *(b)*, respectively. Energy can be transferred in both directions; in boost mode from V_1 to V_2, and in buck mode from V_2 to V_1.

The hard-switched converter comprises a standard half-bridge switching pole, while the auxiliary voltage based soft-switching cell [28],[64]-[66] is introduced in the soft switching converter. The soft-switching cell was previously proposed for uni-directional converter and this work introduces cell's modification for bi-directional operation. The cell comprises an autotransformer, two uni-directional auxiliary switches and two free-wheeling diodes. The parasitic capacitance and leakage inductance are utilized in the resonant circuit operation.

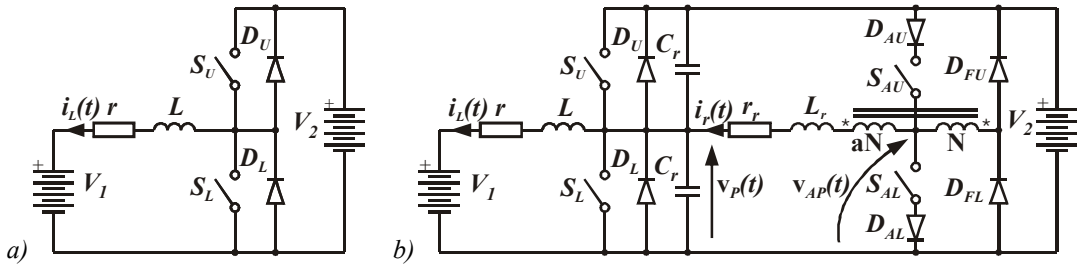

Figure 2.1. Bi-directional buck-boost converter: *(a)* conventional hard-switched, and *(b)* soft-switched.

2.3. Soft-Switching Converter Mode-by-Mode Analysis

The bi-directional dc-dc converter operates under fixed bus voltage conditions. The soft-switched cell is used in the low-ripple current converter. The theoretical analysis presented is an extension of previous work [28], [64] and [66]. The soft-switching cell application in the bi-directional dc-dc converters requires an auxiliary transformer. The transformer mid-point with the auxiliary switch network creates an auxiliary pole voltage, v_{AP}, as shown in Figure 2.1 *(b)*. The following normalisation parameters are defined:

$$V_{base} = V_2\,, \quad Z_{base} = \sqrt{\frac{L_r}{2\,C_r}}\,, \quad I_{base} = \frac{(1-a)V_{base}}{Z_{base}} \tag{2.1}$$

$$\omega_{base} = \omega_0 = \frac{1}{\sqrt{L_r\,2\,C_r}}\,, \quad V_{1n} = \frac{V_1}{V_{base}} \tag{2.2}$$

where L_r and C_r are the resonant inductance and capacitance used to achieve soft-switching of the pole. The converter is symmetrical in operation, with the autotransformer, of turns ratio a, being used to divert current from the main diodes D_U and D_L in a controlled manner during their respective turn-off intervals. It is this turns ratio which defines the boundary of SS operation as described previously [28][64]. Since it is a bi-directional converter it can operate in continuous or discontinuous-current buck or boost modes. The following notation is used: t_{onSU}, t_{onSAU}, t_{onSL}, t_{onSAL}, are on-time signals applied to the drivers of upper-main-transistor, upper-auxiliary-transistor, lower-main-transistor and lower-auxiliary-transistor respectively; L and r are the main filter inductance and ESR, Z_0 is the resonant impedance, ω_0 is the resonant radian frequency, L_m is the transformer magnetizing inductance, i_r is the resonant inductor current, i_{DL} is the lower-diode current, i_{DU} is the upper-diode current, i_{SU} is the lower-switch current, i_L is the main-inductor current, and v_p is the main-pole voltage.

The detailed converter steady-state analysis encompasses ten distinct modes over a single switching period. Figure 2.2 shows the detailed modes and Figure 2.3 presents the relevant waveforms. Buck operation at 500 kHz operating frequency is taken as an example. The waveforms were produced using a Pspice simulation of an idealised soft-switched converter with the following conditions: V_1 = 125 V, V_2 = 250 V, L = 50 μH, r = 0.5 Ω, L_r = 4 μH, C_r = 2 nF, L_m = 8.65 mH, a = 0.34, t_{onSU} = 1.3 μs. The main and auxiliary signals to the upper or lower transistors pair are applied to their drivers at the same time. Time t_{onSAU} is set arbitrary at 0.9 t_{onSU}. The main-switch driver employs a zero-voltage detection circuit across the switch which guarantees that the main switch goes into conduction only when the drain-source voltage is near zero [28][66].

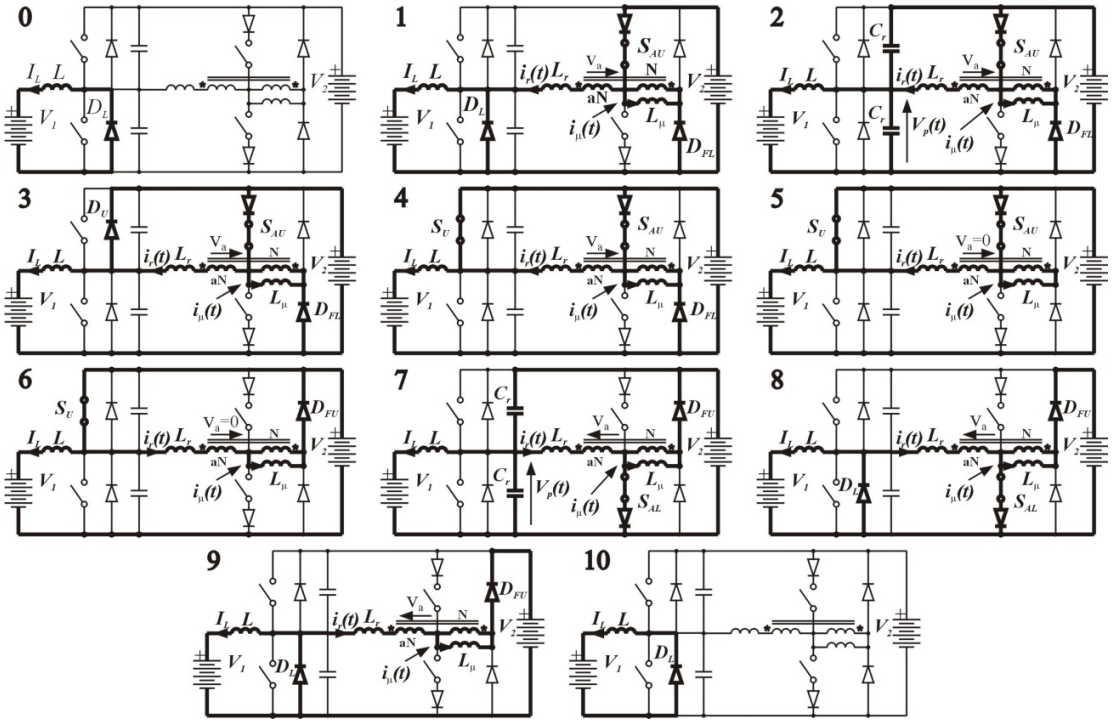

Figure 2.2. Detailed converter modes, buck mode.

Mode 0 ($t < 0$): In this mode, the load current is free-wheeling through the lower diode D_L. The main and auxiliary pole voltages are zero ($v_P = 0$, $v_{AP} = 0$).

Mode 1 ($0 \le t < t_1$): Both of the gate-drive signals for the upper switches are applied but the actual gate drive to S_U is inhibited by its local ZVS circuitry. The SS-cell starts to reduce the current in the main diode D_L with a constant di_r/dt ratio. A magnetizing current in the SS transformer starts to builds up. Since the upper auxiliary switch is on, the aux. pole voltage: v_{AP} equals V_2 and magnetizing current starts building up while the main pole voltage is zero. The resonant inductor current, lower diode current, Mode 1 time duration and magnetizing current are given by:

$$i_r(t) = \omega_0 I_{base}\, t \tag{2.3}$$

$$i_{DL}(t) = I_{L-\min} - i_r(t) \tag{2.4}$$

$$\Delta t_1 = \frac{I_{Ln-\min}}{\omega_0} \tag{2.5}$$

$$i_m(t) = \frac{V_2}{L_m} t \tag{2.6}$$

where $I_{Ln\text{-min}}$ is the normalised main inductor current, $I_{Ln\text{-min}} = I_{L\text{-min}}/I_{base}$.

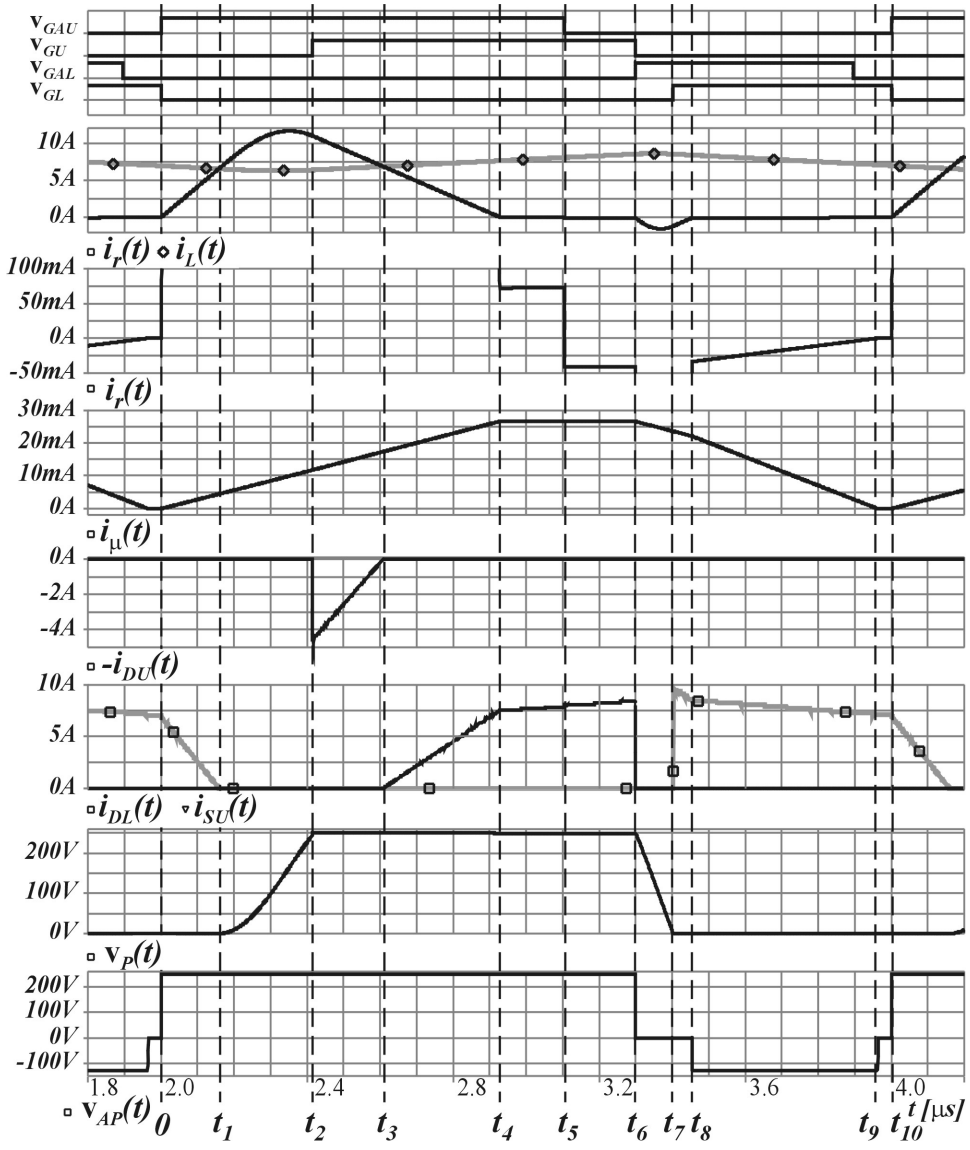

Figure 2.3. Operation waveforms, buck mode.

Mode 2 ($t_1 \le t < t_2$): When the cell resonant-inductor current, i_r, reaches the main inductor current, $I_{L\text{-min}}$, a resonant pole voltage transition begins. The main pole voltage resonates to V_2, where it is clamped by the upper diode D_U. The magnetizing current continues to increase as given by (2.6). The cell resonant current, main pole voltage and Mode 2 time duration are as follows:

$$i_r(t) = I_{L-\min} + I_{base} \sin \omega_0 t \tag{2.7}$$

$$v_P(t) = (1-a) V_2 (1 - \cos \omega_0 t) \tag{2.8}$$

$$\Delta t_2 = \frac{1}{\omega_0} \arccos\left(\frac{-a}{1-a}\right) \tag{2.9}$$

Mode 3 ($t_2 \le t < t_3$): As the pole voltage is clamped to V_2 the diode D_U conducts the cell current resonant component. This ensures ZVS for the main switch which now has on applied gate voltage, and again the magnetizing current continues to increase. The upper-diode current, resonant inductor current and Mode 3 time duration are calculated:

$$i_{DU}(t) = \frac{V_2}{Z_{base}}\sqrt{1-2a} - a\frac{V_2}{L_r}t \tag{2.10}$$

$$i_r(t) = I_{L-\min} + i_{DU}(t) \tag{2.11}$$

$$\Delta t_3 = \frac{\sqrt{1-2a}}{a\,\omega_0} \tag{2.12}$$

Mode 4 ($t_3 \le t < t_4$): In this mode, the upper main switch current and the autotransformer magnetizing current continue to increase while the resonant auxiliary current decreases. The resonant current, upper diode current and Mode 4 time duration are as follows:

$$i_r(t) = I_{L-\min} - a\frac{V_2}{L_r}t \tag{2.13}$$

$$i_{SU}(t) = a\frac{V_2}{L_r}t \tag{2.14}$$

$$\Delta t_4 = \frac{L_r}{a\,V_2} I_{L-\min} \tag{2.15}$$

Mode 5 ($t_4 \le t < t_5$): At $t = t_4$, the lower free-wheeling diode D_{FL} stops conducting, and the voltage across the transformer core reduces to 0. The magnetizing current is clamped at a constant level. The main pole voltage and the auxiliary pole voltage are both equal V_2. The magnetizing current, resonant current, upper switch current and Mode 5 time duration are given by:

$$I_{m5} = \frac{V_2}{L_m}\left(\Delta t_1 + \Delta t_2 + \Delta t_3 + \Delta t_4\right) \tag{2.16}$$

$$I_{r5} = \frac{I_{m5}}{a} \tag{2.17}$$

$$i_{SU}(t) = i_L(t) - I_{r5} \tag{2.18}$$

$$\Delta t_5 = t_{onSAU} - \left(\Delta t_1 + \Delta t_2 + \Delta t_3 + \Delta t_4\right) \tag{2.19}$$

Mode 6 ($t_5 \le t < t_6$): At time t_5, the auxiliary switch turns off. The transformer primary current, $i_r(t)$, reverses rapidly and a new equilibrium point is set with the resonant inductor current reversed as explained in Appendix A.1. Because the magnetising inductance is greater than the resonant inductance, $L_m >> L_r$, the magnetising current, i_m, does not change much during this mode and this change may be neglected. In this condition the magnetising current, resonant inductor current and Mode 6 time duration can be found as:

$$I_{m6} = (1-a)\frac{(1-a)L_m I_{m5} - L_r I_{r5}}{L_r + (1-a)^2 L_m} \tag{2.20}$$

$$I_{r6} = -\frac{I_{m6}}{1-a} \tag{2.21}$$

$$\Delta t_6 = t_{onSU} - t_{onSAU} \tag{2.22}$$

Mode 7 ($t_6 \le t < t_7$): The main switch turns off at t_6, at the same time as the lower auxiliary switch turns on, clamping the auxiliary pole voltage to the ground. The turn-off current is distributed between the auxiliary cell and the capacitive snubber. For small inductor currents, the main-pole-voltage fall time duration is decreased by the SS-cell operation in comparison to the HS snubber case. The maximum fall time occurs when the main inductor current, $I_{L\text{-max}}$, equals zero, and then is equal exactly to Δt_2. The impact of the cell on the pole voltage fall time becomes negligible for the higher current. This feature allows for soft switching at turn off over the full converter operating range. When the main switch turns off, the autotransformer demagnetizing process begins. The extended analysis of mode 7 is provided in Appendix A.2. Note that uni-directional variants of this converter [28][66] revert to a hard switching mode at low turn-off currents. The soft-switching cell assists the turn-off process by injecting the extra current into the pole, speeding up the resonant capacitor recharging in a similar manner as for the turn-on process. The magnetizing current, resonant current, main pole voltage and Mode 7 time duration are as follows:

$$i_m(t) = I_{m6} - \frac{V_2}{L_m}t \tag{2.23}$$

$$i_r(t) = -\left[\frac{i_m(t)}{1-a} + I_{base}\sin\omega_0 t - I_{L-\max}(1-\cos\omega_0 t)\right] \tag{2.24}$$

$$v_P(t) = V_2 - (1-a)V_2\left[(1-\cos\omega_0 t) + I_{Ln-\max}\sin\omega_0 t\right] \tag{2.25}$$

$$\Delta t_7 = \frac{1}{\omega_0}\arccos\left[\frac{-a + I_{Ln-\max}\sqrt{1-2a+(1-a)^2 I_{Ln-\max}^2}}{(1-a)\left(1+I_{Ln-\max}^2\right)}\right] \tag{2.26}$$

Mode 8 ($t_7 \le t < t_8$): At $t = t_7$, the pole voltage, v_P, falls to zero. The excess of the resonant current in the resonant inductor decays until it reaches the transformer magnetizing-current $i_r(t_8) = \frac{i_m(\Delta t_8)}{1-a}$. During this time, the transformer is demagnetising, as governed by (2.23). The auxiliary pole is clamped to zero volts through switch S_{AL}. The resonant-current value at t_7, at the actual resonant current, the lower-diode current and the Mode 8 time duration are given by:

$$i_{r7}(\Delta t_7) = -\left[\frac{L_m I_{m6} - V_2 \Delta t_7}{(1-a)L_m} + I_{base}\sin\omega_0\Delta t_7 - I_{L-\max}(1-\cos\omega_0\Delta t_7)\right] \tag{2.27}$$

$$i_r(t) = i_{r7}(\Delta t_7) + \frac{V_2}{(1-a)L_m}t + a\frac{V_2}{L_r}t \tag{2.28}$$

$$i_{DL}(t) = I_{L-\max} + i_r(t) \tag{2.29}$$

$$\Delta t_8 = \frac{I_{base}\sin\omega_0\Delta t_7 - I_{L-\max}(1-\cos\omega_0\Delta t_7)}{aV_2} \tag{2.30}$$

Mode 9 ($t_8 \le t < t_9$): At time $t = t_8$, the transformer mid-point potential is no longer clamped. The magnetising current, resonant-inductor current, auxiliary-pole voltage, Mode 9 time duration and lower-diode current are as follows:

$$i_m(t) = I_{m6} - \frac{V_2}{L_m}(\Delta t_7 + \Delta t_8) - \frac{V_2}{(1-a)L_m}t \tag{2.31}$$

$$i_r(t) = \frac{-i_m(t)}{1-a} \tag{2.32}$$

$$v_{AP} = -\frac{a}{1-a}V_2 \tag{2.33}$$

$$\Delta t_9 = \frac{(1-a)L_m}{V_2}\left[I_{m6} - \frac{V_2}{L_m}(\Delta t_7 + \Delta t_8)\right] \tag{2.34}$$

$$i_{DL}(t) = I_{L-\max} + \frac{i_m(t)}{1-a} \tag{2.35}$$

Mode 10 ($t_9 \le t < t_{10}$): In this final mode, the load current is free-wheeling through the lower diode D_L, $i_L(t) = i_{DL}(t)$. The transformer is demagnetised and thus completes the PWM switching cycle. The main and auxiliary pole voltages are zero, $v_P = 0$, $v_{AP} = 0$ and the Mode 10 time duration is

$$\Delta t_{10} = T - (t_{onSU} + \Delta t_7 + \Delta t_8 + \Delta t_9) \tag{2.36}$$

2.4. Soft-Switching Converter Operation

The hard-switched (HS) and soft-switched (SS) converters are assumed to operate under fixed bus voltage conditions and the converter average output current gain is investigated. In the case of the hard-switched topology, the pole voltage has an approximately square wave shape; while the soft-switching converter's pole-voltage is affected by both the turn-on and turn-off mechanisms as shown in Figure 2.4. Note that in a HS converter some volt-seconds are lost during the turn on process, but this loss is compensated during the turn-off. However, the SS converter displays significant volt-second loss during the turn-on process. This results in a SS converter current gain that can differ significantly from the HS case and has to be accounted for in the expression for the overall converter gain.

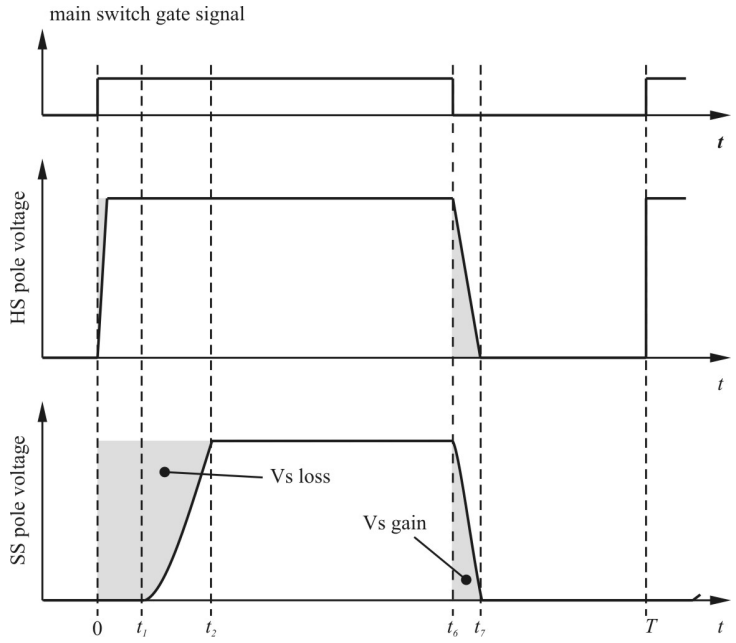

Figure 2.4. Volt-seconds loss due to soft-switching cell operation.

Taking the buck mode with positive output current as an example, which is shown in Figure 2.1b and the respective waveforms in Figure 2.3, it is assumed initially that the diode, D_L, of the lower switch, S_L, is conducting at time $t = 0$. Thus, Mode 1 commences when the auxiliary switch, S_{AU}, is turned on in order to turn-off the lower diode, D_L, under a controlled rate of change of current. The current in the resonant inductor, L_r, rises linearly and the mode ends when the resonant inductor current reaches the output inductor current, $i_L(t)$, and the main diode, D_L, turns off. It is assumed with reasonable accuracy that the normalized minimum output inductor current taking ripple into account occurs at this instant, $i_{Ln}(t_1) = I_{Ln\text{-}min}$. Mode 2 consists

of the second-order resonance, during which time the voltage at the pole rises to the input voltage, V_2. After the resonant swing time, Δt_2, the main upper switch, S_U, can be turned on under zero-voltage conditions. As described above, further modes then occur during which time the current in the auxiliary circuitry is reduced to zero. The final mode of interest, designated here as Mode 7, is the turn off of S_U which occurs at a reduced loss due to the action of the resonant capacitors, C_r. Importantly, in the converter control strategy which is implemented here, the lower auxiliary switch, S_{AL}, is turned on at this time, thus injecting an additional current contribution into the pole to assist in the soft-switching of S_U down to zero load current. It is assumed that this commutation occurs at the maximum output inductor current, $I_{Ln\text{-}max}$. The time taken for the turn-off transition in Mode 7 is given by (2.26).

In the hard-switched converter, the average normalised output current is given by:

$$I_{Ln-ideal} = d - V_{1n} \tag{2.37}$$

where $d = \frac{t_{on}}{T}$ is the duty cycle at the switching frequency $f = \frac{1}{T}$ of the converter and $I_{base-ideal} = \frac{V_2}{R}$ and R is the ESR of the output filter inductor.

However, in the bi-directional auxiliary pole converter, appreciable volt seconds can be lost in each cycle due to the action of the soft switching circuit and the prediction of the output current as a function of duty cycle using (2.37) can be very inaccurate. Specifically, it is clear from Figure 2.4 that compared to the full duty cycle, d, a quantity $\Delta t_1/T$ is lost in Mode 1, during which time the normalised output voltage is zero. During Mode 2, the contribution to the average output voltage is the average value of the pole voltage over the period Δt_2 instead of simply $\Delta t_2/T$. Finally, during Mode 7, additional volt-seconds over the time period given by Δt_7 is added to the pole voltage since the negative-going transition is not instantaneous. Hence, the average normalised pole voltage, $V_{Pn\text{-}effective}$, is given by

$$V_{Pn-effective} = \frac{1}{T}\left[\left(t_{onSU} - \Delta t_1 - \Delta t_2 \right) + \int_{\Delta t_2} v_{Pn}(t)\,dt + \int_{\Delta t_7} v_{Pn}(t)\,dt \right] \tag{2.38}$$

For a unidirectional version of the converter [28][66], and also at high output current levels in the bi-directional converter described here, the contribution of the auxiliary pole to the main-switch turn off is negligible and it can be assumed that the pole voltage commutates linearly under the influence of the maximum output current, $I_{L\text{-}max}$. In this case, a closed-form expression for the output-current gain and the duty cycle for discontinuous-current operation can be derived. In normalised form, (2.38) leads to the following generalised expression for the average output current in both buck and boost modes, where sgn = +1 for buck mode and

sgn = -1 for boost mode:

$$I_{Ln} = \frac{\left\{ d - \frac{\omega_n}{2\pi}\left[I_{Ln-\min} - \operatorname{sgn}\sqrt{1-2a} + a\arccos\left(\frac{-a}{1-a}\right)\right] + f\left(I_{Ln-\max}\right)\right\} - V_{1n}}{R_n} \qquad (2.39)$$

where the function $f(I_{Ln\text{-}max})$ depends on the approximation which is made to the turn-off transient. The parameter ω_n is the normalised radian frequency defined as $\omega_n = 2\pi f/\omega_0$ and R_n is the normalised ESR of the output filter inductor $R_n = (1-a)\frac{R}{Z_0}$. Note that this equation depends on both the maximum and minimum output currents, so for optimum accuracy over the full load range the output current ripple should be taken into account. The minimum and maximum output currents are given by

$$I_{Ln-\min} = \frac{I_{Ln} - \operatorname{sgn}(1-V_{1n})\frac{\pi d}{\omega_n L_n (1-a)}}{1 - \operatorname{sgn}\frac{1-V_{1n}}{L_n}} \quad \text{and} \quad I_{Ln-\max} = 2I_{Ln} - I_{Ln-\min} \qquad (2.40)$$

where L_n is the normalized inductance of the input filter inductor $L_n = \frac{L}{L_r}$.

If the incremental voltage due to the turn-off transient is assumed to be inversely proportional to $I_{Ln\text{-}max}$, then (2.40) can be reduced to a simple quadratic expression which can be solved in closed form for the average output current, I_{Ln}, and the maximum and minimum currents of the bi-directional converter as a function of the duty ratio, d. Also, solving these equations for the critical duty cycles corresponding to zero minimum current gives the operating boundaries for the soft-switching circuit. Inside these limits, the circuit operates with a bipolar output inductor current waveform. However, it is important to note that at lower current levels, the auxiliary pole plays a major role in the soft switched turn-off process and the turn-off time is no longer directly inverse proportional to $I_{Ln\text{-}max}$ as explained in Appendix A.2. In this case, numerical techniques can be used to fit a curve of the form $\left(a + b\, I_{Ln-\max}\right)^{-1}$ to the average normalised pole voltage increment due to the finite switch turn-off time. A closed-form expression can then be derived in a manner identical to that described above.

The results of this analysis and the corresponding PSpice simulation, for a typical 100 kHz converter, are illustrated in Figure 2.5. Both PSpice simulation and calculations are provided for following parameters: V_1 = 125 V, V_2 = 250 V, L = 50 μH, r = 0.5 Ω, L_r = 1.7 μH, C_r = 2 nF, L_m = 8.65 mH, a = 0.34, and the operating duty cycle was changed from 0.2 to 0.8. The PSpice simulation circuit is presented in Appendix A.3.

The simulation results are shown in Figure 2.5 as circles while soft-switched and hard-

switched calculations are given as continuous lines with corresponding labels. The graph shows three lines for each converter which corresponds to the maximum, average and minimum current. It is clear that the expressions which have been developed accurately predict the average, minimum and maximum output currents as well as the critical transitions to the discontinuous current mode of operation. The inclusion of the corresponding ideal average current gain clearly illustrates the importance of more accurately predicting the actual converter currents. The formulae have been validated experimentally for a range of input to output voltage ratios, as shown later.

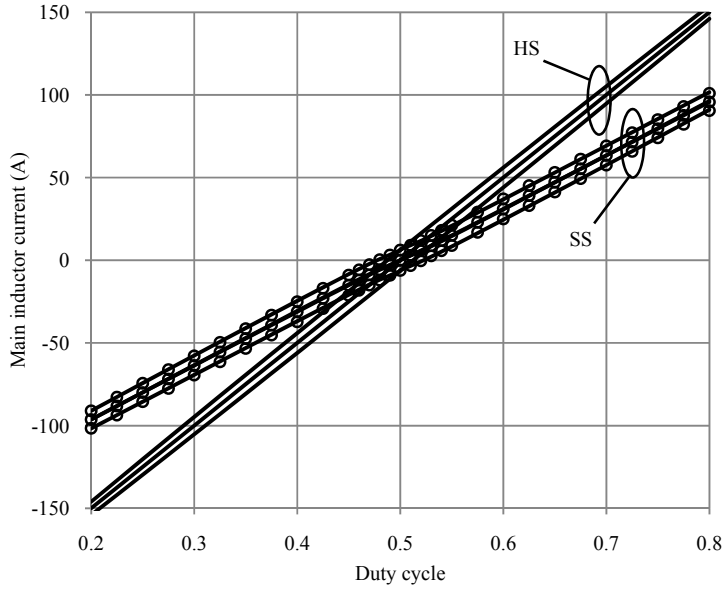

Figure 2.5. Idealised and predicted converter current gain characteristic for buck and boost modes. HS-hard-switched, SS-soft-switched, markers show simulation results. Three lines for each converter correspond to maximum, average and minimum main inductor current.

2.5. Limitations

The maximum power transfer capability of the idealized hard-switched converter is mainly limited by the circuit *ESR*, while the soft-switched converter is limited by the *ESR* and the main inductor current due to the volt-seconds lost during modes 1 and 2 as shown in Figure 2.4. Since the turn-on procedure given in Mode 1 is frequency invariant and solely depends on the commutation current rate, the converter power capability decreases as the frequency increases for a given L_r. The idealized converter power capability is limited by a finite *ESR* and turn-on delay due to cell current rise and pole voltage resonant swing while cell resistance and other second order effects are neglected. However, in practice the converter is penalized further by increased transformer turn ratio in order to satisfy soft switching and zero voltage conditions across the main switch as well as minimum time, during which the main diode is free-wheeling, necessary for the transformer demagnetization in Mode 7-9 as shown in Figure 2.3. The maximum power of an idealized and practical soft-switched converter as a function of switching frequency and cell current rise rate is shown in Figure 2.6 and Figure 2.7, respectively. The converter's power capability can be extended by increasing the cell current rise rate or by increasing the main inductor current ripple. Alternatively, a multi-phase topology may be employed to increase the power output.

Both graphs in Figure 2.6 and Figure 2.7 are produced for the following input data: switching frequency, f = 100 kHz, low-voltage, V_1 = 200 V, high-voltage, V_2 = 400 V, main inductor current ripple ratio $\Delta I/I_{DC}$ = 0.15, the circuit equivalent resistance, *ESR* = 40 mΩ, resonant capacitance, C_r = 30 nF, magnetizing inductance, L_m = 300 μH, transformer turn ratio a = 0.5 for ideal case and non-ideal turn ratio is evaluated individually for each case following the analysis provided in Section 2.6.

The resonant inductance L_r controls the cell current rise rate and according to following formula:

$$L_r = \frac{(1-a)V_2}{di/dt} \tag{2.41}$$

Since the current ripple is fixed the main converter inductance L varies with the maximum power capability as it is closely related to the inductor's average current.

The non-ideal converter analysis considers such parameters as switching cell *ESR*, voltage drop on the auxiliary components and main diode turn-off time. The resonant capacitance is a function of the main inductor current as it depends on size of the main transistor.

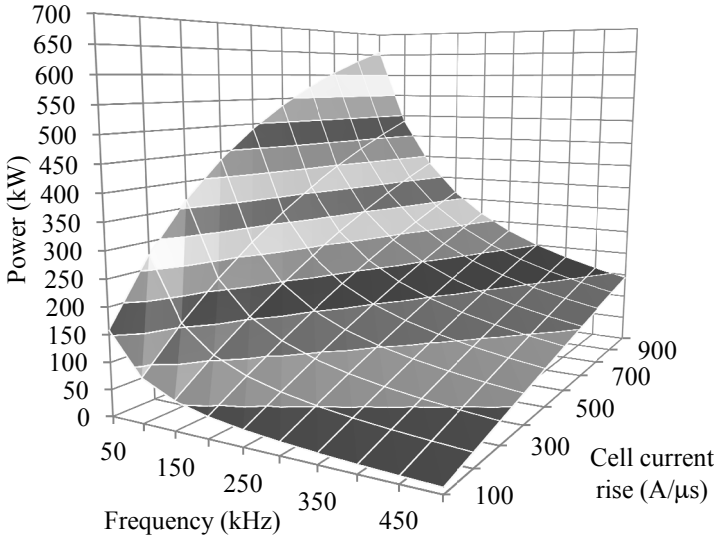

Figure 2.6. Maximum power capability of the ideal soft-switched converter.

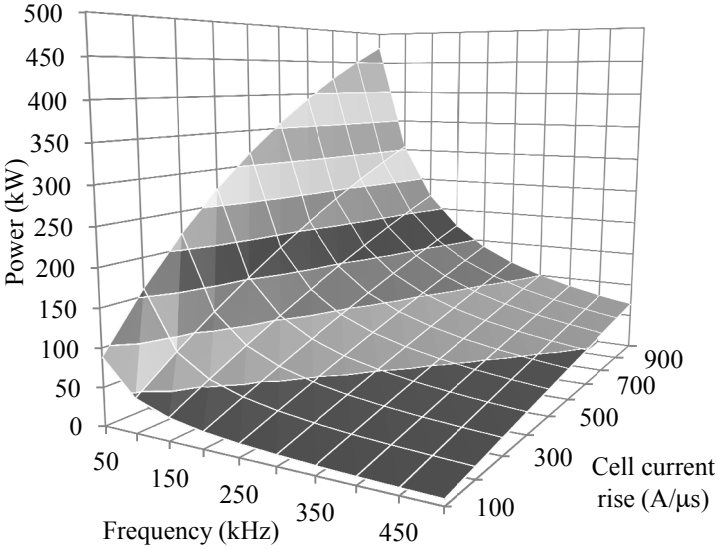

Figure 2.7. Maximum power capability of the non-ideal soft-switched converter.

2.6. Auxiliary Transformer Turns Ratio Considerations

In the analysed circuit an auxiliary voltage source is realised by a transformer and diode network. The transformers turns ratio has to be carefully selected in order to achieve the soft-switching operation and avoid unnecessary energy storage in the system. In this section transformer turns ratio is investigated and practical turns ratio selection formula is presented.

The transformer's voltage ratio defines the auxiliary and high dc bus voltage proportion for which soft switching is achieved. Auxiliary voltage source is induced on primary transformer winding and is defined as voltage ratio a_v:

$$a_V = \frac{V_a}{V_2} \tag{2.42}$$

The pole voltage for buck and boost mode is given by

$$v_{p-buck}(t) = (V_2 - V_a)(1 - \cos\omega_0 t) \tag{2.43}$$

$$v_{p-boost}(t) = V_a + (V_2 - V_a)\cos\omega_0 t \tag{2.44}$$

Consider buck mode operation. Since the pole voltage must swing through V_2 in order to achieve zero voltage switching (ZVS) and the maximum of $(1-\cos\omega_0 t)$ is 2, then boundary conditions for voltage ratio of auxiliary source and hi-voltage dc bus are the following

$$(1 - a_V)(1 - \cos\omega_0 t)V_2 \geq V_2 \tag{2.45}$$

Thus

$$a_V \leq \frac{1}{2} \tag{2.46}$$

The same result is obtained for a boost mode. This establishes ideal conditions for a resonant swing which satisfies ZVS. However, in a physical system many other factors affect the actual turns ratio and the ideal prediction on a_V has to be reduced by number of factors in order to take into account actual parasitic parameters. The following parasitics influence the transformer turns ratio:

- Soft-switching cell damping resistance
- Boundary conditions of resonant mode
- Cell auxiliary diodes and switch voltage drop
- Conduction time effect of main switch anti-parallel diode.

The following analysis in this chapter specifically investigates a boost mode operation, but buck mode operation is similar and corresponding equations can be readily derived.

2.6.1. Damping Resistance Effect

Damping resistance is an equivalent series resistance of the circuit as a result of intrinsic resistances of devices and wires. The resistance reduces the resonant voltage amplitude, which can result in excursions outside the soft switching plane. The equivalent cell resistance R_d is defined as:

$$R_d = R_{Lr} + R_T + R_{switch} \tag{2.47}$$

where R_{Lr} is resonant inductor *ESR*, R_T is the transformer winding resistance and R_{switch} is an auxiliary MOSFET resistance, otherwise the IGBT voltage drop is introduced into the diode effect. The auxiliary cell equivalent circuit in Mode 2 is shown in Figure 2.8.

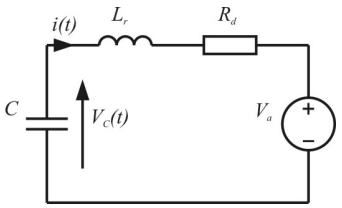

Figure 2.8. Mode 2 cell resonant equivalent circuit for boost operation.

The auxiliary cell is a 2nd order series resonant circuit, the pole voltage undergoes a resonant swing given by

$$v_c(t) + LC\frac{d^2 v_c(t)}{dt^2} + R_d C\frac{dv_c(t)}{dt} = V_a \tag{2.48}$$

It can be shown that the pole voltage is given by

$$V_c(t) = aV_2 + (1-a)V_2 e^{-\alpha t}\left(\frac{\alpha}{\omega}\sin\omega t + \cos\omega t\right) \tag{2.49}$$

The detailed solution of this equation is provided in Appendix A.4.

Because the equivalent resistance must inevitably be small the damping is relatively low; thus, the pole voltage would oscillate if not clamped by the switching circuit as can be seen in Figure 2.9. As can be seen, the resistance and turns ratio combination may result in a soft or hard switched mode of operation. Since zero voltage detection across the main switch is employed, the converter would not operate if the pole voltage resonant excursion is insufficient. The critical condition occurs when the pole voltage first resonant peak-to-peak oscillation is equal to the high voltage dc bus. In order to achieve the soft-switching, the pole oscillating peak-to-peak voltage must be greater than or equal to the high dc-bus voltage. Therefore the following condition must be satisfied:

$$V_c\left(\frac{\pi}{\omega}\right) \le 0 \tag{2.50}$$

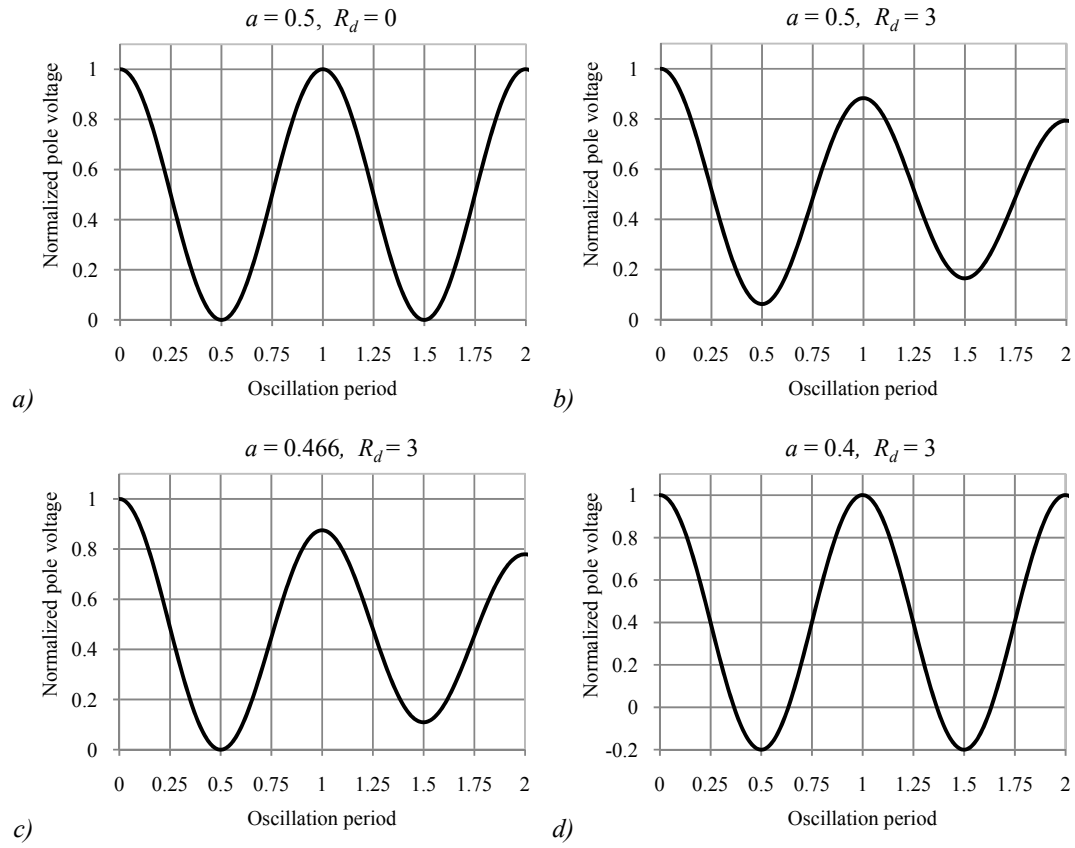

Figure 2.9. Pole voltage resonant swing for various auxiliary voltage ratio and cell *ESR*: *(a)* ideal case, *(b)* overdamped voltage swing, *(c)* critical condition, *(d)* low transformers turns ratio.

Hence, the damped cell voltage ratio is given by

$$a_\alpha \le \frac{1}{1+e^{\frac{\alpha}{\omega}\pi}} \tag{2.51}$$

Intuitively the auxiliary voltage in a cell with finite *ESR* is lower than the idealised prediction provided by (2.46). The damped de-rating factor as a component of general voltage ratio is defined as:

$$a_d = a_V - a_\alpha \tag{2.52}$$

The situation is analogous for buck mode operation.

2.6.2. Boundary Conditions Of Resonant Mode

The previous section considers damping resistance, but refers only to the region of the resonant swing. The resistive voltage drop caused by the current flow in Mode 1 is not taken into account. The resonant swing starts when the main freewheeling diode stop conducting and diode reverse voltage is increasing. At this time the resonant inductor is already conducting the main inductor current. Unavoidably, such current cause voltage drop across the auxiliary cell *ESR*, which directly affects the soft switching boundary as the voltage drop across the *ESR* adds to V_a. Thus, the transformer voltage ratio has to be further reduced.

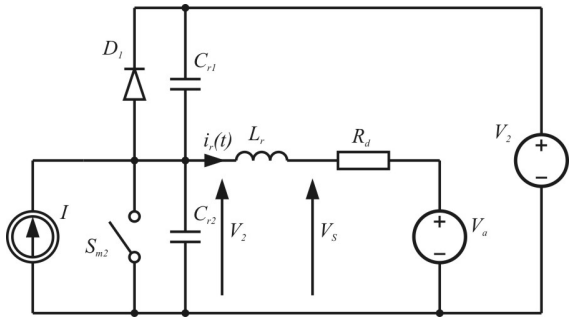

Figure 2.10. Equivalent circuit for boundary conditions between Mode 1 and Mode 2.

The circuit state at end of Mode 1 is shown in Figure 2.10. The voltage V_S is a resultant auxiliary voltage given by

$$V_S = i_r(t) R_d + V_a \tag{2.53}$$

Hence a new voltage ratio factor is defined that must satisfy inequality

$$\frac{V_S}{V_2} \le a_V \tag{2.54}$$

Thus the, new boundary can be find as follows

$$a_B \le a_V - \frac{R_d}{V_S} i_r(t) \tag{2.55}$$

The transformer turns ratio must be adjusted in order to facilitate the elevated current in the auxiliary cell. The boundary de-rating factor is provided for a maximum allowable inductor current and is given as

$$a_b \le \frac{R_d}{V_S} I_{MAX(\min)} \tag{2.56}$$

Note that at main switch turn-on, the main inductor current is at its minimum.

2.6.3. Auxiliary Diodes Voltage Drop

The auxiliary components voltage drop affects the soft-switching cell operation. Some components can be represented by *ESR* while the minority carrier semiconductors such as p-n diode and IGBT, are modelled by a parasitic on-state voltage source. If the auxiliary cell is based on MOSFET transistors it requires additional diodes in series with them. The $R_{DS(on)}$ adds to *ESR*, while the diode is represented as a voltage drop. If MOSFET is replaced by a discrete IGBT, then the extra diode is not required. The soft-switching cell during operation is shown in Figure 2.11. As can be seen, the diode D_4 forward voltage drop increases the resultant auxiliary voltage V_S while the diode D_5 forward voltage drop decrease. The effect of the diodes on the circuit can be found directly from KVL:

$$\begin{cases} V_S = V_a + V_{D4} \\ V_2 = V_x + V_{D4} - V_{D5} \end{cases} \tag{2.57}$$

Having defined

$$\frac{V_S}{V_2} = a_V \qquad \text{and} \qquad \frac{V_a}{V_x} = a \tag{2.58}$$

it can be seen that

$$a_R = \frac{a_V V_2 - V_{D4}}{V_2 - V_{D4} + V_{D5}} \tag{2.59}$$

Finally the auxiliary voltage factor is given by

$$a_r = a_V - a_R \tag{2.60}$$

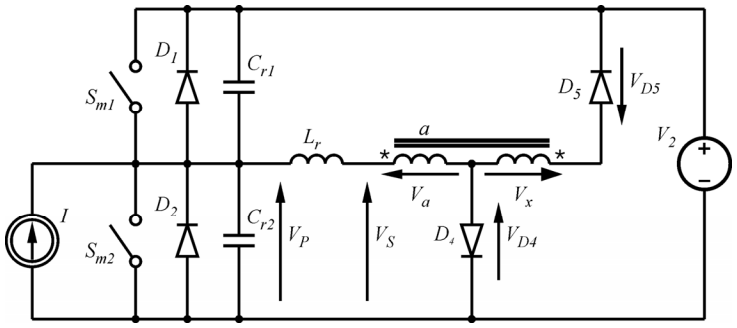

Figure 2.11. Equivalent circuit for diode voltage drop effect.

2.6.4. Main Switch Anti-Parallel Diode Conduction Time Effect

The turn-on time of the main switch is rather short but critical from the point of the anti-parallel diode, which should be conducting during the turn-on in order to ensure zero voltage and current turn-on. If diode stops conducting before the main switch completes the turn-on process it will cause additional power loss as the transistor will be in active mode.

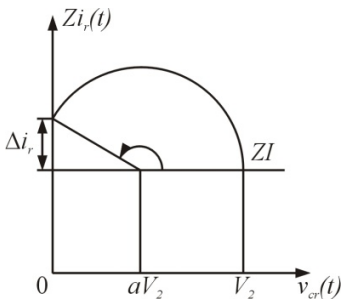

Figure 2.12. State-plane trajectory.

A graphical interpretation of the pole voltage changes is shown in Figure 2.12. For a given resonant inductor current at the end of resonant mode $i_r(0)$ and known circuit parameters it can be shown that

$$i_r(t) = i_r(0) - a\frac{V_2}{L_r}t \tag{2.61}$$

Time t has to be long enough to allow main transistor to fully switch-on and can be defined as:

$$t_{Di} = t_{d(on)} + t_r \tag{2.62}$$

where $t_{d(on)}$ is turn-on delay time and t_r is rise time, both provided and defined in the transistor datasheet. Hence

$$\Delta i_r = a\frac{V_2}{L_r}t_{Di} \tag{2.63}$$

and from Figure 2.12 can be written

$$\Delta i_r = \frac{1}{Z_0}\sqrt{(V_2 - aV_2)^2 - (aV_2)^2} \tag{2.64}$$

$$a\frac{V_2}{L_r}t_{Di} = \frac{1}{Z_0}\sqrt{(V_2 - aV_2)^2 - (aV_2)^2} \tag{2.65}$$

$$a^2\left(\frac{Z_0}{L_r}\right)^2 t_{Di}^2 + 2a - 1 = 0 \tag{2.66}$$

since resonant impedance and frequency are given as

$$Z_0 = \sqrt{\frac{L_r}{2C_r}} \quad \text{and} \quad \omega_0 = \frac{1}{\sqrt{L_r 2C_r}} \tag{2.67}$$

Eq. (2.66) can be written as follows

$$a^2\omega_0^2 t_{Di}^2 + 2a - 1 = 0 \tag{2.68}$$

and the solution is given by

$$a_{1,2} = \frac{-1 \pm \sqrt{1+\omega_0^2 t_{Di}^2}}{\omega_0^2 t_{Di}^2} \tag{2.69}$$

Finally, defining

$$a_T = \frac{-1 + \sqrt{1+\omega_0^2 t_{Di}^2}}{\omega_0^2 t_{Di}^2} \tag{2.70}$$

the main switch anti-parallel diode conduction factor can be written as

$$a_t = a_V - a_T \tag{2.71}$$

2.6.5. The Autotransformer Turns Ratio

The actual autotransformer turns ratio is defined as auxiliary voltage ratio including all of the developed factors:

$$n = \frac{n_{pri}}{n_{\text{sec}}} = a_V - a_d - a_b - a_r - a_t \tag{2.72}$$

Since there is zero voltage detection across the main switch the proper turns ratio selection may provide intrinsic over current protection as any condition outside the soft-switching plane would disable the main switch and naturally limit the system maximum power output as the circuit transitions to a hiccup mode of operation.

2.7. Converters Experimental Comparison

A prototype 1.25 kW, 125 V/250 V, 100 kHz, bi-directional dc-dc converter employing MOSFET's, (SS-MOSFET), has been designed and constructed based on the auxiliary soft-switching cell described in this chapter. This experimental converter is used to verify the topology and to validate the theoretical analysis derived above. Two other converters have also been built; a conventional high-ripple MOSFET-based converter (HR-MOSFET) and a hard-switched IGBT-based converter (HS-IGBT). The HS-IGBT and SS-MOSFET converters are low ripple current converters of 31 %, while the HS-MOSFET converter is a high ripple design with a current ripple of 220 %. The main MOSFETs are Infineon type CoolMOS SPW47N60. The main IGBTs are International Rectifier type IRGP50B60 Warp2, while the auxiliary MOSFETs are Infineon type CoolMOS SPP12N50C3. Both the auxiliary inductor and the autotransformer magnetic cores use Ferroxcube 3C85. The cell passive components are L_m = 3.43 mH, L_r = 4.7 μH, C_r = 2.2 nF. The autotransformer turns ratio is a = 0.33 and power rating 140 VA which is 11% of the converters power rating. Input and output capacitance is large enough so that the bus voltages are constant with negligible voltage ripple. Two main inductors were designed, one for low ripple operation and the other for high ripple operation. Both inductors are based on an EE65, 3F3 core from Ferroxcube. The low-ripple inductance is specified at 200 μH and the winding fabricated with a round wire of 1.5 mm diameter and 19 turns. The total air gap is 1.44 mm. The inductance of high-ripple inductor is 28 μH and is based on 7 turns winding fabricated from 25 strands of Litz wire of 0.3 mm diameter each. The total air gap is 2.38 mm. Both inductors are shown in Figure 2.13. One of the cores allows for easy inductance adjustment.

The experimental setup is shown in Figure 2.14. The main part of the converter is enclosed in a box with forced air cooling. The control signal is generated by DSP TMS320F2808 based board shown in Figure 2.15. The control board was developed for the project with the support of Daithi Power of the Power Electronics Research Laboratories at UCC and the detailed schematic diagram is shown in Appendix A.5.

The TMS320F2808-based board has a number of features and can be adopted for many projects. The board has 6 PWM outputs with drivers capable of delivering 9 A peak current. Each driver has dedicated zero voltage detection circuitry, which prevents the driver from turn-on unless the voltage across the transistor is close to zero. This feature can be overridden by a disabling control signal from the DSP and the system can operate solely in hard-switching mode. All drivers are isolated and can be implemented individually. The TMS320F2808 has a number of A/D inputs, which are utilized for 6 voltage inputs, 2 voltage differential inputs and

2 high sensitivity current inputs. The board comprises a number of digitally driven diodes and input keys as well as 4 I/0 pins. The system reads from 2 potentiometers. The board has an LCD interface, a JTAG programming interface and a RS-232 interface.

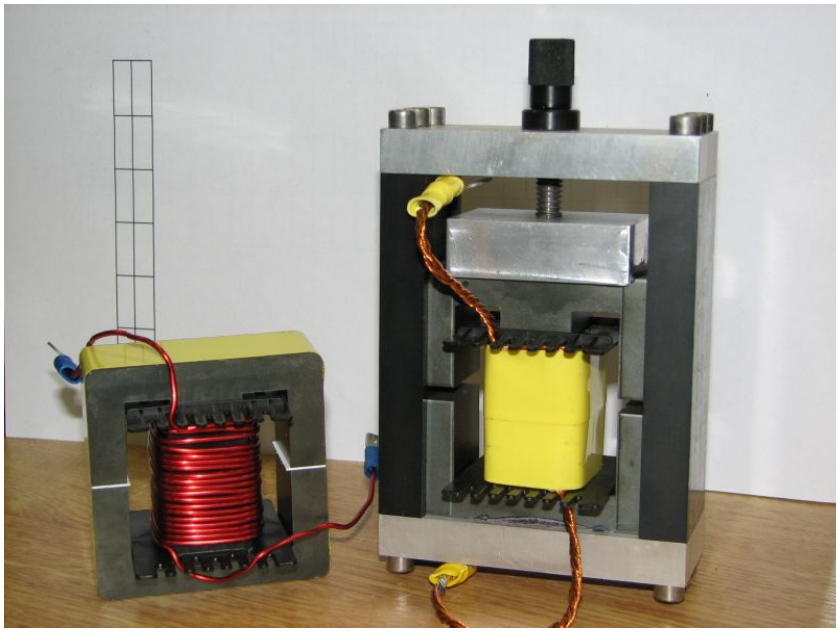

Figure 2.13. Experimental inductors 200 μH (left) and 28 μH (right).

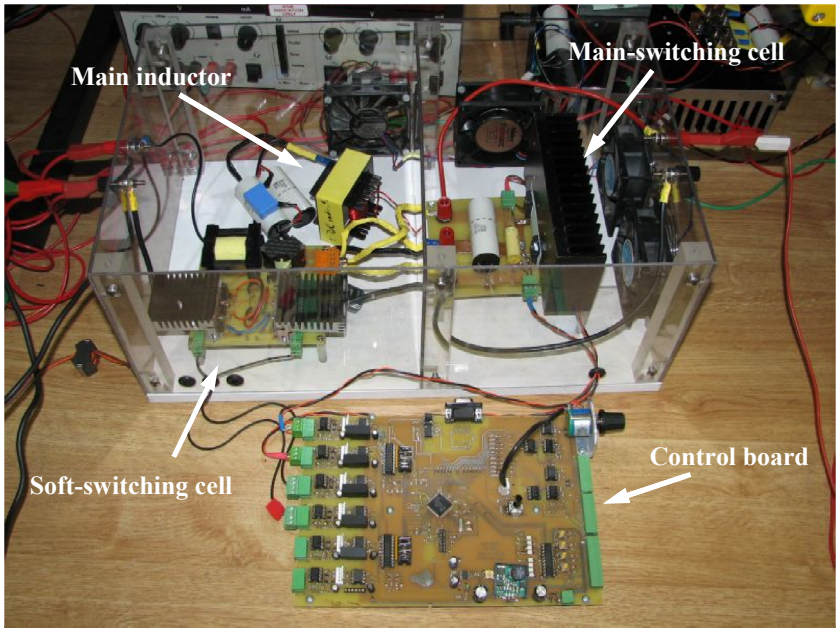

Figure 2.14. Soft-switched dc-dc converter.

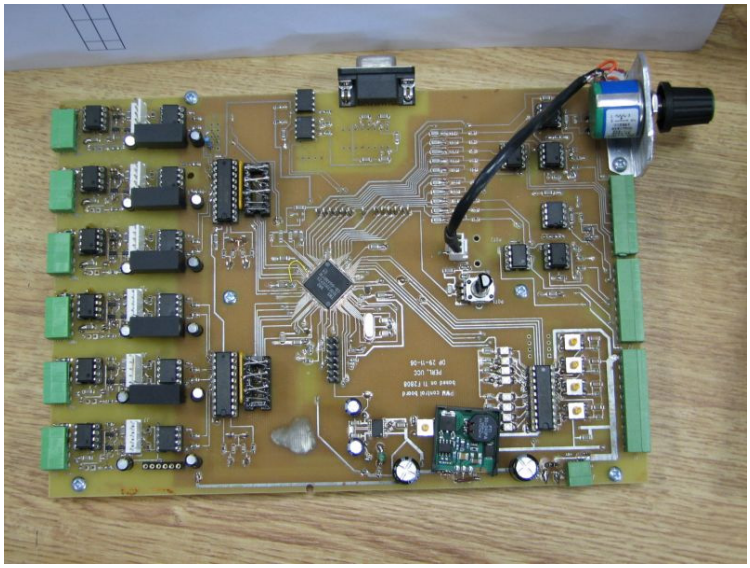

Figure 2.15. Control board based on TMS320F2808.

Figure 2.16 illustrates the experimentally measured and theoretically predicted average output current versus duty cycle characteristic of the soft-switched MOSFET-based converter in both buck and boost modes of operation. Note that, in this case, the *ESR* of the output inductor has been artificially increased to $r = 0.8\ \Omega$ by the addition of a discrete resistance in order to facilitate the taking of accurate results at a relatively low current and reasonable duty cycle range. The theoretical predictions for the corresponding converter parameters are superimposed on these experimental results. It is clear that the theoretical expressions derived in this chapter produce a very accurate prediction of the current-gain characteristics of the soft-switched converter in both buck and boost modes of operation.

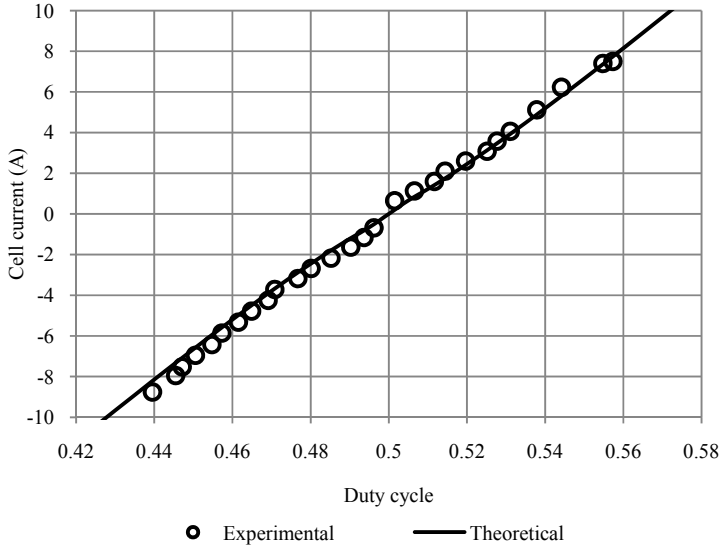

Figure 2.16. Experimental and theoretical inductor average current vs. duty cycle for SS converter.

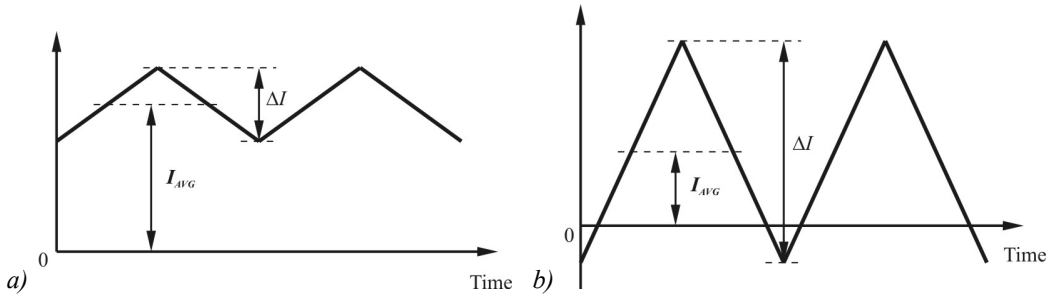

Figure 2.17. Low ripple *(a)* and high ripple *(b)* regime.

The efficiency comparison shows the soft-switching cell capability to reduce switching power loss. The efficiency of the three converters across the 0 to 1.25 kW load range is compared: high-ripple MOSFET-based, low ripple hard-switched IGBT-based and low ripple soft-switched MOSFET-based. The converter switching pole is arranged in a half-bridge and uses exactly the same PCB in all tests. The half-bridge configuration allows for two-quadrant bi-directional operation as a buck in one direction and boost in the other. The MOSFET's intrinsic anti-parallel diodes are employed as free-wheeling diodes, while the IGBT's uses co-pack ultrafast soft recovery diodes. The MOSFET's intrinsic diodes are generally penalized by the high turn-off power loss due to reverse recovery; thus, many efforts are directed towards its reduction.

All of the converters under investigation are based on a bi-directional half-bridge topology with uni-directional output current. However, as noted, the high-ripple converter employs a two-quadrant conduction mode which is critical in order to minimise the detrimental impact of the poor intrinsic MOSFET anti-parallel diode. The hard-switched IGBT-based converter is equipped with diodes of very good switching characteristic thus resulting in relatively low diode turn-off losses. This allows for a low current ripple converter as the IGBT suffers significant tail-current power loss at high ripple operation. Finally, the converter with soft switching cell is examined. The soft-switching cell allows for significant reduction of the diode turn-off power loss; thus, facilitating the use of MOSFET's operation in the bi-directional low ripple dc-dc converters. The basic concept of low and high current ripple operation is shown in Figure 2.17 *(a)* and *(b)*, respectively.

The high ripple current benefits in a significant diode turn-off power loss reduction due to the resonant nature of the voltage swing during the pole voltage commutation. However, high ripple magnetic components may suffer significant power loss due to winding eddy currents and core power loss. From the high power dc-inductor perspective, high frequency and low current ripple is recommended; thus, a hard-switched IGBT or a soft-switched MOSFET based converter is preferable.

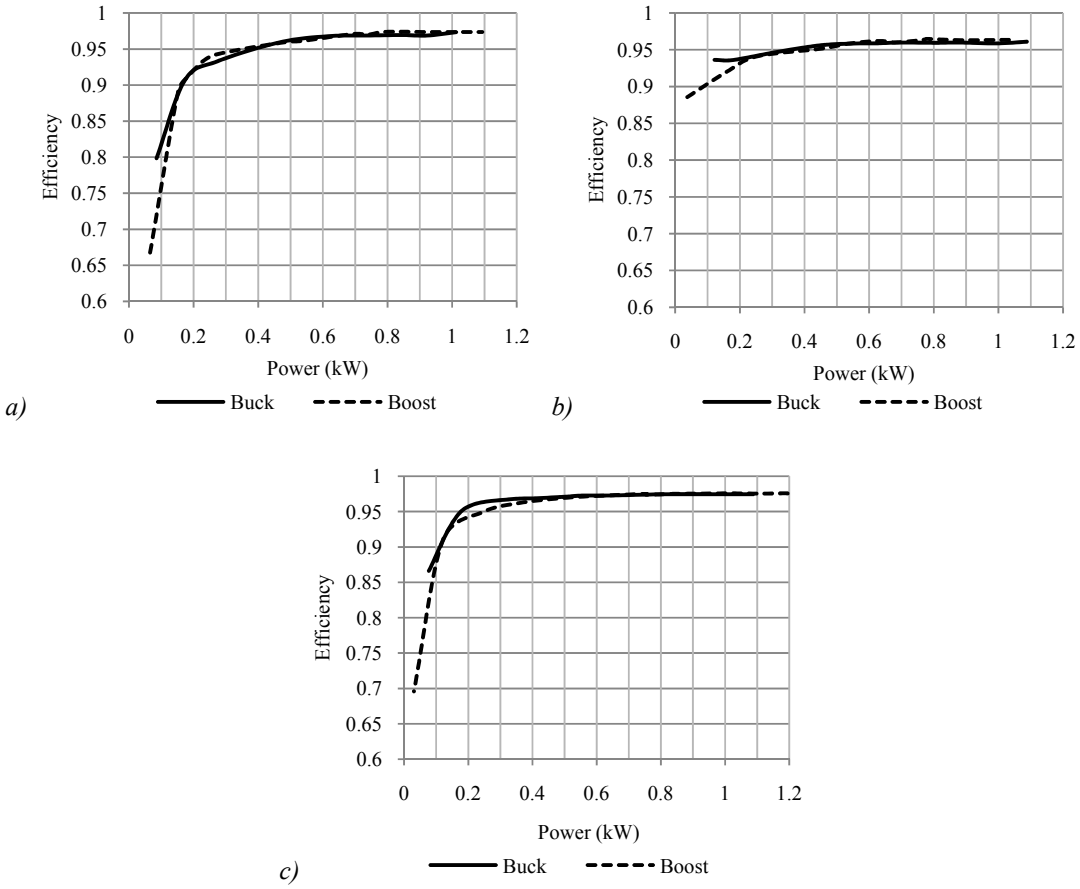

Figure 2.18. Efficiency vs. output power: *(a)* high current ripple (220 %) MOSFET based converter, *(b)* low current ripple (31%) hard-switched IGBT based converter, *(c)* current ripple (31 %) soft-switched MOSFET based converter.

The measured efficiency graphs for the three converters are shown in Figure 2.18 *(a)*, *(b)* and *(c)* for high-current ripple MOSFET-based converter, HS IGBT-based converter and SS MOSFET-based converter, respectively. The corresponding efficiency at maximum power is tabulated in Table 2.1. The measured efficiency of the converter as a function of the output load illustrates that efficiencies of the order of high 90's are achieved over a very wide load range for all converters.

The converters were tested with fixed input and output voltages and duty cycle was adjusted to vary the output power. Thus, the magnetic component operates with the same current ripple over the converter power range as the duty cycle change is marginal. This results in a constant ac power loss in the inductor and only the dc component changes.

All of the converters demonstrate similar efficiencies for both buck and boost mode. The high-ripple converter peak efficiency of 97.4 % is achieved at maximum power of 1.1 kW. The efficiency deteriorates at low loads as the high ripple magnetic component significantly contributes to the generated power loss and yields 90 % at 125 W (10 % of rated power). The low ripple magnetic component allows for a significant efficiency improvement at low load. The soft-switched MOSFET-based converter is 97.6 % efficient at rated power and its efficiency drops to 93 % at 10 % load. The hard-switched IGBT-based converter demonstrates the lowest full load efficiency of 96.5 %, but it displays 92.5 % efficiency at 10 % load.

Detailed power loss breakdown is tabulated in Table 2.2. Note that switching power loss is shown only for main transistors and it includes turn-on, turn-off, and diode reverse recovery loss. Transistor's gate signals are complimentary therefore MOSFET based converters allows for channel conduction during freewheeling mode. High ripple converter is penalized by significant ac component therefore high power converter design may be a challenging task when comes to the magnetic design. Soft-switching converter shows that switching power loss of the main switch is almost eliminated by the soft-switching cell. The main switch power loss is associated only with turn-off as turn-on is under ZVC. The hard-switched IGBT converter shows significant switching power loss, but this may be reduced if SiC diodes are employed. Nevertheless, lower efficiency of the IGBT converter is offset by its simplicity and low component count in respect to more efficient converter with soft-switching cell.

The results clearly show that soft-switching cell effectively reduces the switching power loss of the converter by reducing the free-wheeling diode current fall rate and ensures the main switch zero voltage conditions at turn-on.

Table 2.1. Converters comparison

Parameter	high-ripple	soft-switched	hard-switched
Transistors	MOSFET	MOSFET	IGBT
Rated power	1.25 kW		
V_1	125 V		
V_2	250 V		
L	28 μH	200 μH	
f	100 kHz		
ΔI	22 A	3.1 A	
I_{AVG}	10.0 A		
Peak Eff.100 % load	97.40 %	97.60 %	96.50 %
Peak Eff.10 % load	90 %	93 %	92.50 %

Table 2.2. Power loss breakdown at power of 1.25 kW

Device	high-ripple	soft-switched	hard-switched
Transistors	MOSFET	MOSFET	IGBT
Main transistor cond.	10.5 W	7 W	7.5 W
Main transistor sw.	~0	2 W	25 W
Main diode cond.	10.5 W	9 W	7 W
Main inductor	8 W	3.3 W	3.3 W
Aux. transistor	-	2 W	-
Aux. diodes	-	3 W	-
Resonant inductor	-	1 W	-
Cell transformer	-	2 W	-
Total calculated power loss	29 W	29.3 W	42.8 W
Experimental power loss	32.5 W	30 W	43.75 W

Further tests were performed on both the hard- and soft-switched converters in order to show efficiency change due to different switching regimes, frequency and type of transistors employed as shown in Table 2.3. The tests were carried out at 1.2 kW and 125/250 V low to high voltage ratio. The inductors are the same as described above.

The soft-switched converter with MOSFET transistors for both the main and auxiliary switches records the highest efficiency at 100 kHz and displays high efficiencies of 95.5 % and 92.4 % as the switching frequency increases to 200 kHz and 300 kHz, respectively. If the main switches are replaced with IGBT's the efficiency drops to 97 %, 95 % and 93.1 % for 100, 200 and 300 kHz, respectively. The replacement of the auxiliary switch with an IGBT, while main switch is a MOSFET, results in an efficiency of 97.3 % at 100 kHz. Finally, an all IGBT-based converter was examined and was 96.5 % efficient, the lowest among the soft-switched tests. The main reason in efficiency drop at higher frequency is due to switching cell itself which is the same for all frequencies. Note that the results depend on the actual device ratings. The replacement devices were selected on the basis of similar blocking voltage together with the corresponding on-state voltages at the rated currents and the same packaging format.

The low-ripple hard-switched IGBT-based converter efficiency is comparable to the soft-switching cell converters at 100 kHz; however, the efficiency decreases dramatically as frequency increases and is measured of 91.5 % and 80 % for 200 and 300 kHz, respectively. The switching power loss becomes dominant at high frequencies and dramatically impacts on efficiency. The high-ripple MOSFET-based converter is very efficient due to 2-quadrant operation with the resultant free-wheeling diode loss is minimized. Finally, the test was performed on a conventional HSMOSFET at low-ripple and the results showed an unacceptably low efficiency of 88 %, due to the poor intrinsic body diode.

Table 2.3. Converters efficiency comparison

Converter switches		100 kHz	200 kHz	300 kHz
Main	Aux			
Soft-switched low ripple				
MOSFET	MOSFET	97.6 %	95.5 %	94.2 %
IGBT	MOSFET	97.0 %	95.0 %	93.1 %
MOSFET	IGBT	97.3 %	-	-
IGBT	IGBT	96.5 %	-	-
Hard-switched				
IGBT low ripple		96.5 %	91.5 %	80 %
MOSFET high ripple		97.4 %	-	-
MOSFET low ripple		88.0 %	-	-

The soft-switched MOSFET-based converter efficiency is high and satisfies expectations. This is due to the fact that the main switch turn-on is implemented under zero voltage conditions. In addition, the main-switch turn-off is soft-switched using a small capacitive snubber which is resonantly discharged. The auxiliary transistor turn-on is implemented at zero current with the inductive snubber. The main-diode turn-off is softened by the action of the resonant inductance. The turn-off of the auxiliary diodes is also softened by the resonant inductance. However, the main inductor, the resonant inductor, and the transformer give rise to additional copper and core losses. In general, the original switching power loss is shifted to the low power loss auxiliary cell components.

Tests performed on the IGBT transistors under the soft-switching regime did not demonstrate any significant improvements over the soft-switched pole.

Figure 2.19, Figure 2.20 and Figure 2.21 illustrates the waveforms for the output inductor current, the resonant inductor current and the pole voltage for buck mode, boost mode and zero current crossing mode, respectively for the soft-switched converter. The waveforms show the converter operation for the following cell passive components: L_m = 3.43 mH, C_r = 2.2 nF and main inductor L = 200 μH and transformer turns ratio a = 0.33. The 125 V/250 V low to high voltage ratio and 100 kHz switching frequency are used for the results illustrated.

The operating waveforms show good agreement with the presented theory. The magnetizing current effect is marginal thus not visible as the magnetizing inductance is very high. The resonant inductance is the sum of the additional resonant inductor and the auxiliary transformers leakage inductance. As can be seen the pole voltage is free of inductive voltage spikes, although the transistor gate resistance is as low as possible in order to improve switching time in the zero voltage region. The visible noise was eliminated later with prototype improvements.

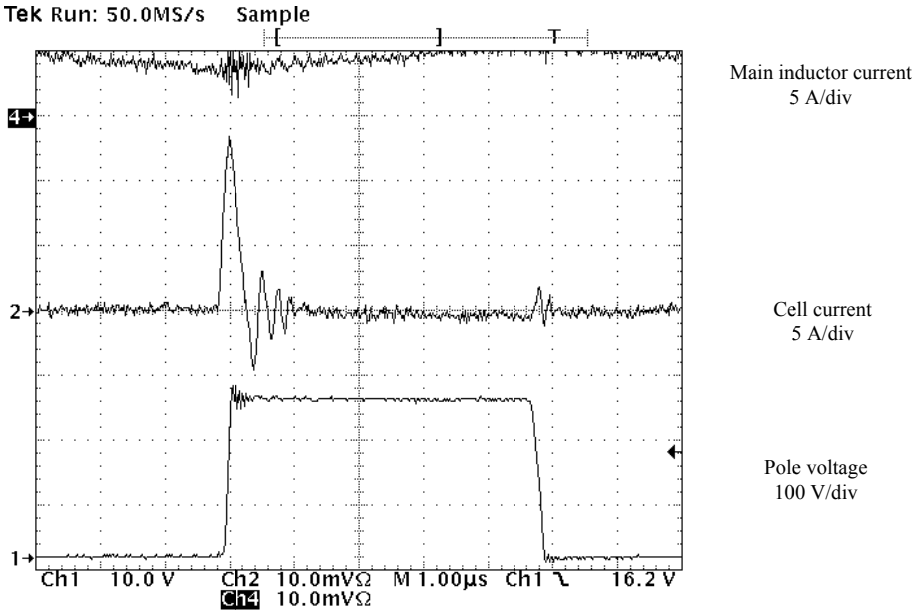

Figure 2.19. Buck mode experimental waveform.

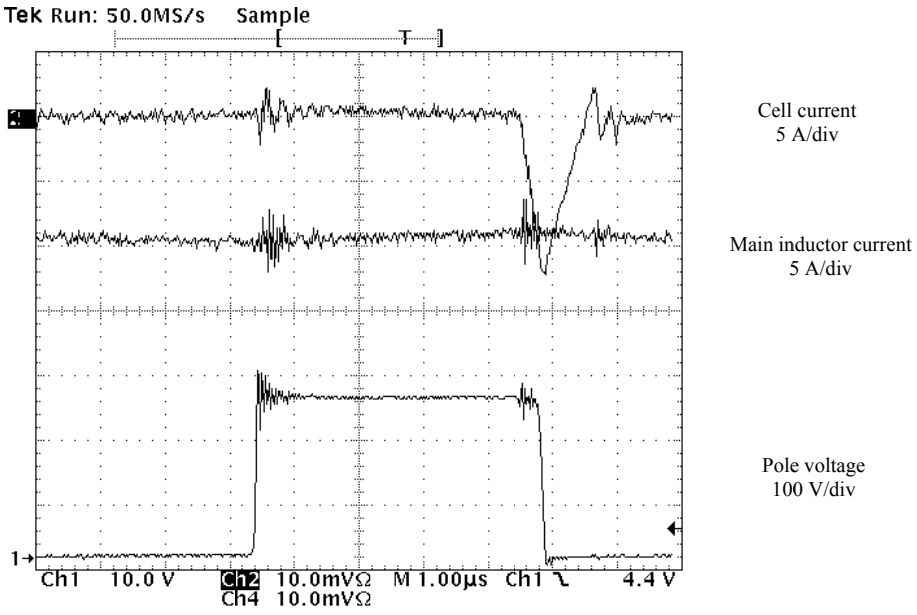

Figure 2.20. Boost mode experimental waveform.

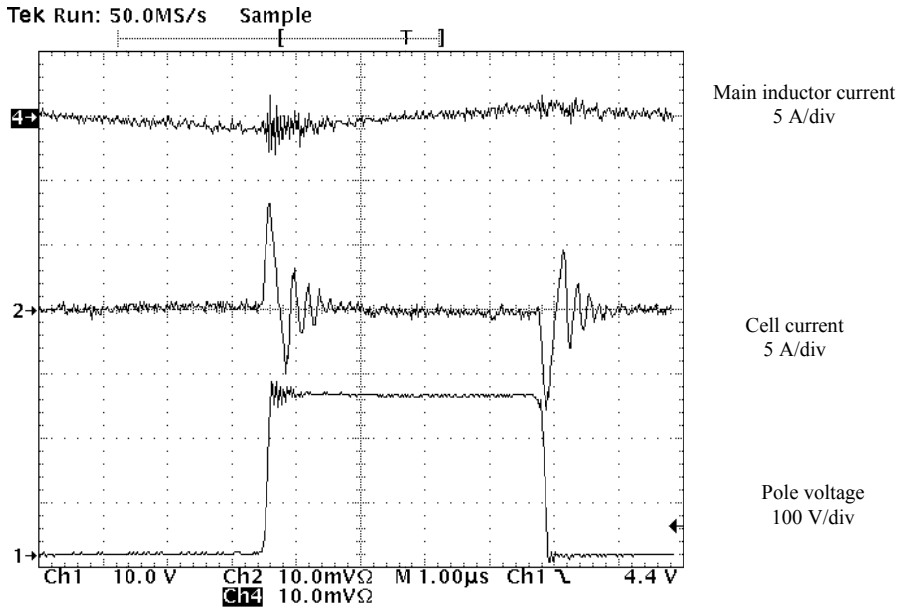

Figure 2.21. Zero current crossing mode experimental waveform.

The converter cell operation was examined in detail. The cell connections with the main switching pole were reinforced with a transient absorber beads and additional filter capacitance was added to the high-voltage dc-bus. This improves the system operation and results in very clean waveforms. However, the additional filtering components reduce the efficiency to 97.2 %. In order to develop magnetizing current effect the transformer magnetizing inductance was reduced to L_m = 300 µH while transformer turns ratio remains at a = 0.33. The resonant capacitance, C_r, uses the transistors output capacitance which for MOSFET equals 2.2 nF. The resonant inductor L_r was set to 12 µH in order to develop a distinctive resonant cell current.

The waveforms shown in Figure 2.22 and Figure 2.23 were captured during the converter operation in a boost mode at 1 kW load and V_1 = 100 V, V_2 = 200 V. The average pole voltage loss due to soft switching cell operation at 50 kHz and 100 kHz is shown. It is clear that the pole voltage fall is delayed until resonant cell current equals the main inductor current. The switching frequency does not affect switching cell operation and cell current is the same for both frequencies. The magnetizing current effect is clearly visible.

The analytical solution is compared with experimental results and are shown in Figure 2.24. The comparison is shown for a 100 kHz converters operation, as shown in Figure 2.23. The developed model is with a good agreement with the experimental waveform. Some inaccuracy is introduced by circuit parasitics and requires further investigation.

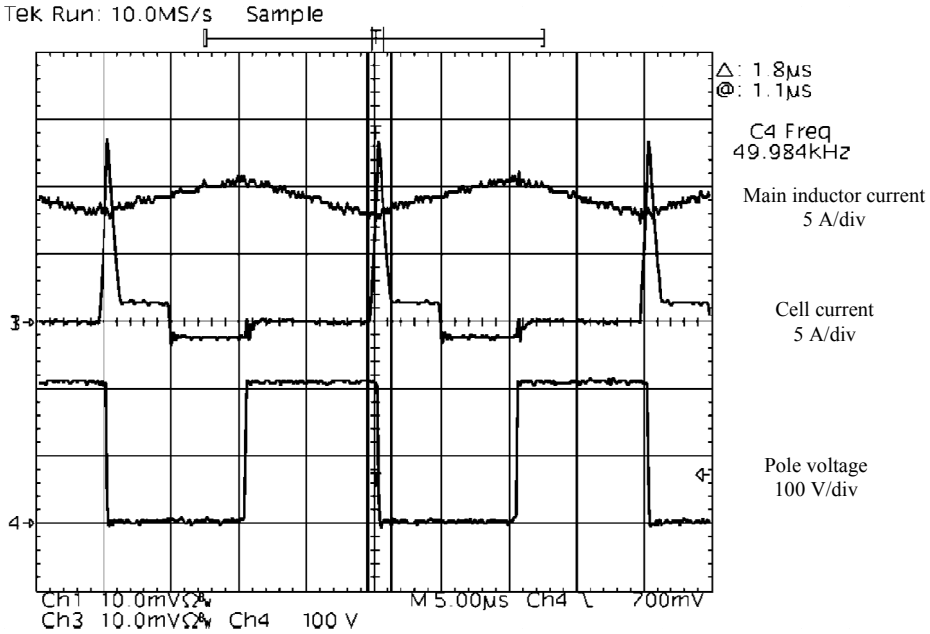

Figure 2.22. Converters pole voltage loss due to soft switching cell at 50 kHz.

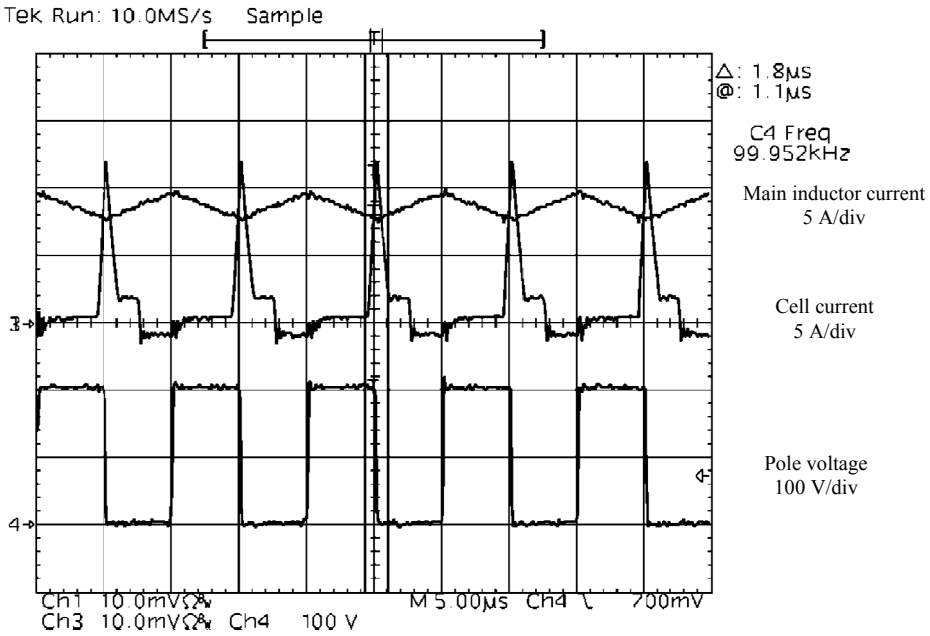

Figure 2.23. Converters pole voltage loss due to soft switching cell at 100 kHz.

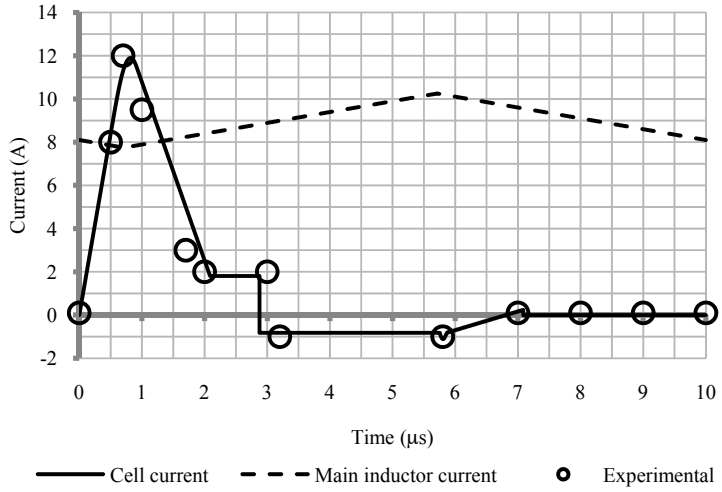

Figure 2.24. Experimental validation of the theoretical model at 100 kHz.

2.8. Conclusions on the Soft-Switched and Hard-Switched Converter

Variation of the autotransformer-based auxiliary-pole bi-directional dc-dc converter has been presented and analysed. Novel expressions have been derived for the current gain characteristics of the converter in the buck and boost modes of operation and these have been validated both by simulation and by experimental results. It is shown that the auxiliary pole assists in achieving soft-switching over the full load range. Efficiencies of the order of 97 % have been measured over a wide load range in the practical converter.

The experimental converter efficiency drops as frequency increases as soft-switching cell was optimized for 100 kHz only and therefore the cell exhibits increased power loss as frequency is increased. The cell requires optimization for a high frequency operation.

The high efficiency of the soft-switched converter is achieved at the expense of the circuit complexity and the maximum power limitation due to soft-switching cell operation. On the other hand the topology which has been presented is extremely robust and operates to a large extent in a self-protected mode in which the well known shoot-through fault phenomenon cannot occur. It is also interested to note that the auxiliary circuit does not contain a direct shoot-through path consisting of two active devices connected directly across the bus. For 100 kHz converter the auxiliary autotransformer is rated for approx. 11 % of the total power processed with some variation allowed for cells current rise rate and minor effect of the magnetizing inductance. In general auxiliary autotransformer rating is strongly related with the operating frequency and its power rating is proportional to the frequency as the constant commutation transient is assumed as provided by Mode 1 to 4.

The soft-switched IGBT-based converter shows good efficiency over the frequency range

and thus confirms feasibility of using IGBT's at a higher frequencies. At 100 kHz, the soft-switching cell has similar power loss to the eliminated power loss from the hard-switched converter. Thus, efficiency is similar. This sets the area of the soft-switching cell application to the MOSFET-based low-current-ripple bi-directional converters in the frequency range from 20 kHz up and IGBT-based converters from 100 kHz above. The clear benefit of the soft-switching cell at higher frequencies is shown and compared to the hard-switched IGBT based converter. Intuitively, the hard-switched IGBT converter efficiency drops with an increase it frequency due to switching power loss. The MOSFET transistors in a hard-switched low current ripple regime did not display satisfactory efficiency.

Part of the material presented in this chapter was published at the EPE 2007 conference, but further development was put on hold as new power switching devices appear. The original work with a soft-switching cell started in autumn 2005 and continued through 2006 till spring 2007. Around this time, intensive research was ongoing into the new semiconductor materials for power switching devices. Silicon Carbide, SiC, devices were at the embryonic stage since a SiC Schottky diode was released in 2001 by Infineon. The SiC diode was pioneered by Cree and Infineon initially with relatively low progress. In 2006 great expectations were placed on SiC MOSFETs, which at the time were seen potentially to revolutionize the semiconductors market. However, manufacturing issues have significantly limited the progress of these devices. Other transistors structures such as bipolar devices based on SiC were also proposed, notably by Swedish company TranSic [59]. Furthermore, a SiC JFET from SemiSouth was another step towards SiC switches, having been launched in 2008 [57]. In addition, the development in recent years of GaN devices has been quite significant and it is seen as a material which may yet revolutionize power-electronics in voltage ranges up to 1 kV.

Nevertheless, notwithstanding the intensive research in this area, SiC and GaN semiconductors market gain has been rather small and it will take a significant time before wide band gap semiconductors will dominate. In the mean time, Si-based switching devices are continuously being improved, but it is a fact that GaN and SiC have significantly better high frequency switching properties compared to silicon.

Which technology will ultimately become the industry standard for high frequency switching cells is still in question but it is certain that new materials other than Si will have a major impact on power converter topologies. Accordingly, having presented a novel bi-directional auto-transformer based switching cell and proven its theory of operation, it was felt that the next most pressing challenge in the development of a useful and viable high-power dc/dc converter is the design and optimisation of the main magnetic component, which is now the topic of the subsequent chapters of this thesis.

Chapter 3

Magnetic Material Comparison

This chapter presents various magnetic material comparisons and introduces new magnetic material comparison charts. The presented performance factors are applicable for dc inductors or ac inductor or transformer material selection. Material B_{sat} in addition to conduction cooling are considered. The new factors are supported by the dc inductor Area Product analysis presented in Chapter 4, which is based on an inductor design algorithm for both gapped and gapless magnetic materials. Some of the practical issues related to the inductor design algorithm and performance factors are explained later in Chapter 5.

3.1. Introduction

High-power-density magnetic devices are increasingly required in industrial, automotive and aerospace applications. A compact and efficient magnetic design is critical to ensure that the overall weight and volume of hard-switched dc-dc converters is reduced [69]. As discussed in [7], several design options have an effect on the size of the inductor, e.g. frequency, number of stages and continuous vs. discontinuous conduction. An optimal choice of core dimensional ratios can also significantly reduce the size of the inductor [70], and further size reduction can be achieved by using improved cooling methods [71]. There is a wide variety of ferromagnetic materials available to the magnetic designer [72]-[80].

The optimum choice of the magnetic material is difficult and rarely straightforward to a designer. The operating dc current, current ripple, air gap length, number of air gaps, operating frequency, duty cycle, ambient and heat sink temperature and thermal path all have strong influence on the inductor size in addition to cost and manufacturability.

As shown in Chapter 4 with an area product analysis and in [81]-[84], the ideal material for the minimum size design, is with a small or distributed air gap together with high saturation flux and generally low power loss.

This chapter presents the usual magnetic material comparisons and introduces new magnetic material performance factors. The presented charts are applicable for the dc inductor and transformer or ac inductor material selection. Natural convection and conduction cooling are considered.

3.2. Magnetic Materials

The general specifications for the magnetic materials of interest in the medium-to-high frequency range are presented in Table 3.1 [72]-[80]. The table features a sample of laminated cores; two iron-based amorphous metal cores of type 2605SA1 and 2605S3A from Metglas, two 6.5% silicon steel cores of type 10JNHF600 and prototype from JFE, and nanocrystalline of type Vitroperm 500F from Vacuumschmelze. Also included are samples of ferrite, 3C93 from Ferroxcube, and powdered iron, type -26 from Micrometals. A range of pressed powdered cores of various permeabilities is provided by vendors such as Magnetics Inc., Chang Sung Corp., Arnold Magnetics and Ferroxcube.

There are four general types of powder core available. Molypermalloy, MPP, is commonly used by all manufacturers and is an alloy of iron, nickel and molybdenum. The High Flux core is a second material which shares the same name for all manufacturers and is an iron-nickel alloy. A third type is an alloy of iron, aluminium and silicon and it appears as KoolMu from Magnetics Inc., Sendust from CSC and Ferroxcube or MSS from Arnold Magnetics. The last group is formed by iron-silicon alloy which appears as XFlux from Magnetics Inc., Mega flux from CSC or Fe-Si from Arnold Magnetics. There is unique material from Arnold Magnetics named Crystal-X, whose composition is not revealed. In general, the core material magnetic properties depend on the basic material used and the manufacturing processes [72]-[80][10][85][86].

The various materials are produced using different manufacturing processes. The iron-based amorphous metal and nanocrystalline materials are tape wound while the silicon steel is stamped and stacked. Ferrite is manufactured as a ceramic. The powdered-iron core is an iron dust bonded in epoxy. There are many different mixes of the powdered-iron cores which have different permeabilities and power losses depending on the iron content. Pressed powder cores form a significant group and have considerably lower power losses than the powdered-iron cores. The power loss of the pressed powder core is related to the material's particle size and can be adjusted by the manufacturing process. The finer the grain the lower is the power loss, but the higher is the price. The core's permeability depends on many factors, including the alloy content, particle type and size, bonding material, applied pressure and heat treatment, etc.

Silicon steel has the highest saturation flux (1.88 T), followed by XFlux (1.6 T) and Mega Flux (1.6 T), amorphous metal (1.41-1.56 T), Fe-Si6% (1.5 T), Crystal-X (1.5 T), High Flux (1.5 T), powdered iron (1.38 T), nanocrystalline (1.2 T), KoolMu (1.05T), MPP (0.75 T), and ferrite (0.35 T). The nominal core loss for each material at 20 kHz and 0.1 T is shown in Table 3.1. The highest losses are in the powdered iron and the lowest losses are in the ferrite and nanocrystalline.

Table 3.1. Magnetic Materials Properties

Magnetic Material Type	Manufacturer	Material	Composition	Saturation flux density (T)	Rel. Permeability (100C @20kHz)	Curie temp. (ºC)	Continuous operating temperature (ºC)	Thermal conductivity (W/(m K))	Density (g/cm^3)	Core Loss @0.1T, 20kHz (kW/m^3) 60µ for powder cores	Core Loss @0.1T, 100kHz (kW/m^3) 60µ for powder cores
AM	Metglas	2605SA1	Fe-B-Si	1.56	600	395	150*	10***	7.18	70	1380
AM	Metglas	2605S3A	Fe-B-Cr-Si	1.41	35000	358	150*	10***	7.29	17	200
SS	JFE	10JNHF600	Fe-Si 6.5%	1.88	600	700	150*	18.6***	7.53	150	1750
SS	JFE	Prototype	Fe-Si 6.5%	1.88	600	700	150*	18.6***	7.4	120	1400
NC	VAC	VP500F	Fe-Cu-Nb-Si-B	1.2	50000	600	120*	TBD	7.3	5	73
Ferrite	Ferroxcube	3C93	Mn-Zn	0.35	1800	240	140	3.5-5	4.8	5	49
PI	Micrometals	Mix -26	Fe	1.38	75	-	<75**	4.2	7	630	4760
PC	Magnetics	MPP	Fe-Ni-Mo	0.75	4-550	460	200	8	8.2	45	370
PC	Magnetics	High Flux	Fe-Ni	1.5	4-160	500	200	8	7.7	116	1300
PC	Magnetics	KoolMu	Fe-Al-Si	1.05	66-125	500	200	8	6.8	83	900
PC	Magnetics	Xflux	Fe-Si	1.6	26-60	700	200	8	7.5	200	1800
PC	CSC	MPP	Fe-Ni-Mo	0.7	26-200	450	200	TBD	TBD	65	500
PC	CSC	High Flux	Fe-Ni	1.5	26-160	500	200	TBD	TBD	100	700
PC	CSC	Sendust	Fe-Al-Si	1	26-125	500	200	TBD	TBD	76	700
PC	CSC	Mega Flux	Fe-Si	1.6	26-90	725	200	TBD	6.8	186	1600
PC	Arnold	MPP	Fe-Ni-Mo	0.75	14-350	TBD	TBD	TBD	TBD	70	600
PC	Arnold	High-Flux	Fe-Ni	1.5	14-160	TBD	TBD	TBD	TBD	130	1000
PC	Arnold	MSS	Fe-Al-Si	1	14-147	TBD	TBD	TBD	TBD	90	800
PC	Arnold	Fe-Si 6%	Fe-Si	1.5	14-147	500	200	TBD	TBD	240	1650
PC	Arnold	Crystal-X	TBD	1.5	14-600	TBD	TBD	TBD	TBD	100	650
PC	Ferroxcube	MPP	Fe-Ni-Mo	0.75	14-300	460	200	TBD	8.7	TBD	TBD
PC	Ferroxcube	High-Flux	Fe-Ni	1.5	14-160	500	200	TBD	8.2	TBD	TBD
PC	Ferroxcube	Sendust	Fe-Al-Si	1.05	26-125	500	200	TBD	7	83	900

* limited by the lamination adhesive, ** limited by thermal aging, *** along laminations - preliminary data
AM – amorphous metal, SS – silicon steel, NC – nanocrystalline, PI – powder iron, PC – powdered core
TBD – to be determined

Since inductors winding carries electric current, the core is subjected to magnetic flux, which may cause saturation; thus, a high permeability magnetic core requires gapping in order to decrease the magnetic flux density. The air gap role in the magnetic circuit is explained in [87][88]. A low permeability powder cores usually do not require gapping, however, the low permeability material may be penalized by additional stray field fringing around the core.

The core maximum operating temperature is limited theoretically by the Curie temperature and practically by the lamination and coating thermal capability limits. The amorphous metal and silicon steel cores are limited by the lamination adhesive thermal capability and are typically specified at 150 °C. The nanocrystalline material is specified at 120 °C as elevated temperature may trigger thermal ageing due to material re-crystallization although the crystallization temperature exceeds 500 °C when manufactured [75][86].

The powder iron is limited by the bonding epoxy used. This epoxy is usually organic based and can undergo thermal aging at elevated temperature, making the powdered iron core temperature sensitive, thus limiting its reliability and lifetime [77]. Some powdered iron cores can operate without thermal ageing up to 200 °C.

The pressed-powder cores' maximum temperature is limited by the coating thermal capability and is specified at a max temperature of 200 °C. Finally, the ferrite material is generally designed to operate at the unique material temperature at which specific power loss reaches its minimum for a given flux density. These temperatures are typically in the 80 - 150 °C for ferrites. For 3C93 the minimum specific power loss occurs at about 140 °C, [76].

The core cooling is enhanced by the thermal conductivity of the material. The powder cores have the highest maximum operating temperatures. However, their thermal conductivity at 8 $W \cdot m^{-1} \cdot K^{-1}$ is lower than amorphous metal at 10 $W \cdot m^{-1} \cdot K^{-1}$ and silicon steel 18 $W \cdot m^{-1} \cdot K^{-1}$, but higher than ferrite 3-5 $W \cdot m^{-1} \cdot K^{-1}$. Amorphous metal, silicon steel and nanocrystalline have anisotropic thermal conductivities, which are significantly higher along the laminations than across the laminations. This thermal path anisotropy must be considered when optimizing the cooling path. Ferrite and powdered iron have the lowest thermal conductivities.

In general, the performance of magnetic materials degrades at higher operating temperatures, e.g. the saturation flux density is lower at elevated temperatures, while the power loss is higher. Ferrite material is usually optimized for minimum power loss at a given temperature.

The material density becomes important for applications where a low mass is required, such as aerospace or some moving parts of low inertia. The iron-based materials density is usually close to the iron 7.87 g/cm^3. Ferrites are low mass materials of about two thirds of the iron based material.

The nominal core losses for each material at 20 kHz and 100 kHz for flux density amplitude 0.1 T are shown in Table 3.1. The materials' power loss properties are not easy to characterize as generated loss is a function of operating frequency and flux density amplitude. Due to this fact some materials may perform better at lower frequency, while other materials outperform at higher frequency. The power losses generated in magnetic materials for 20 kHz and 100 kHz operation are shown in Figure 3.1 and Figure 3.2, respectively. The graphs in Figure 3.1 and Figure 3.2 are based on manufacturers datasheets and show only the representative materials sample.

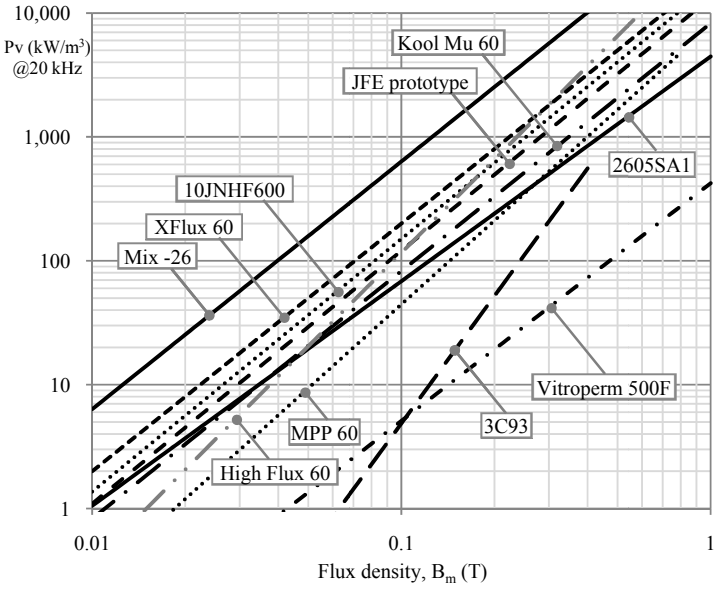

Figure 3.1. Volumetric power loss density vs. flux density amplitude at 20 kHz.

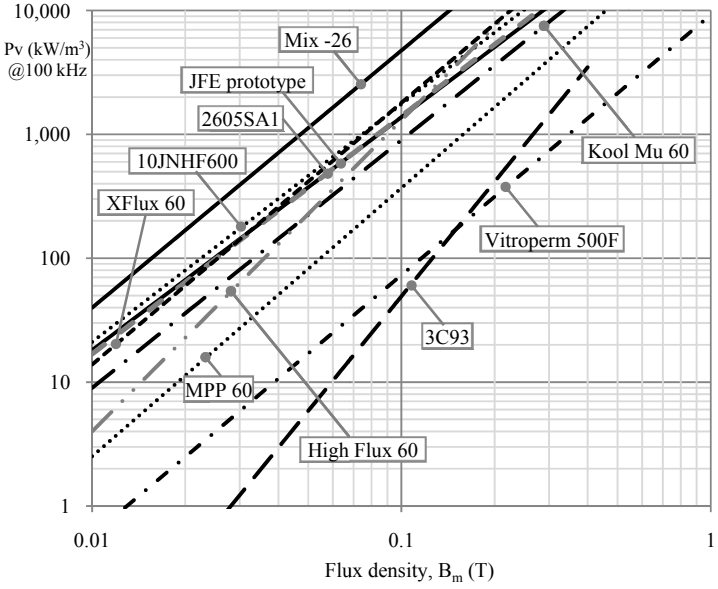

Figure 3.2. Volumetric power loss density vs. flux density amplitude at 100 kHz.

Let's first focus on the results presented in Table 3.1 for 20 kHz and 0.1 T. The highest core loss is observed in the powdered iron core at 630 W/m^3. The power loss in iron-silicon alloys, such as XFlux at 200 W/m^3, is significantly lower than powdered iron and is still higher than laminated silicon-steel, 10JNHF600 with 150 W/m^3 and JFE prototype core with 120 W/m^3, while Crystal-X and High Flux have lower power losses of 100 W/m^3 and 115 W/m^3, respectively. MPP shows the lowest power loss among the powder materials with core losses between 45 and 70 W/m^3. The amorphous materials have lower power loss with 2605SA1 at 70 W/m^3 and the chromium-added material 2605S3A at 17 W/m^3. As expected, nanocrystalline and ferrite 3C93 come in lowest at about 5 W/m^3. This relation may change if different flux density amplitude is selected, as shown in Figure 3.1. The most visible is the ferrite and nanocrystalline materials crossing, where ferrite displays the lowest power loss for flux density amplitude below 0.1 T, while in the range above nanocrystalline has lower power loss than ferrite.

Similarly as for 20 kHz, in Table 3.1 power losses at 100 kHz and 0.1 T are presented. The order of the materials has changed. Again, the highest power loss is observed in powdered iron core at 4760 W/m^3. The power loss generated in silicon steel 10JNHF600 is similar to the XFlux powder core at 1750 W/m^3 and about 1700 W/m^3, respectively. The amorphous metal 2605SA1 displays similar power loss as a prototype silicon steel core at 1380 W/m^3 and 1400 W/m^3, respectively. High Flux and KoolMu has slightly lower power loss between 700 W/m^3 and 1300 W/m^3 and between 700 W/m^3 and 900 W/m^3, respectively. Crystal-X is just about at the lower range of High Flux and KoolMu with 650 W/m^3. Again, MPP has the lowest power loss among powder cores between 370 W/m^3 and 600 W/m^3. The amorphous metal 2605S3A has lower power loss at 200 W/m^3. The nanocrystalline material displays higher power loss than ferrite with 73 W/m^3 and 49 W/m^3, respectively. Power loss curves at 100 kHz are shown in Figure 3.2.

As can be seen from Figure 3.1 and Figure 3.2, the power generated in the material changes with the flux density amplitude and operating frequency. At a given frequency some materials may perform better at lower flux density amplitude while other materials are better at higher flux density amplitude. The power loss generated in the various materials is varying with the frequency. While at 20 kHz the power loss generated in silicon steel 10JNHF600 is 2.14 times greater than in amorphous metal 2605SA1, the power loss ratio for the same materials at 100 kHz is 1.27. It is interesting that the JFE prototype material displays similar power loss to 2605SA1 at 100 kHz, but nearly twice at 20 kHz.

At high frequency the power losses generated in powder materials are in the range of the traditional gapped materials such as silicon steel 10JNHF600.

A plot of volumetric power density vs. frequency is presented in Figure 3.3 for amorphous metal 2605SA1, silicon steel 10JNHF600 and powder material Mega Flux 60. Power loss generated in the material varies with the flux density magnitude. The plot in Figure 3.3 shows that powder material performs better or similar to silicon steel at flux density amplitude up to 0.1 T. At high frequency and low flux density amplitude, the powder materials display similar power loss to the amorphous metal. The higher powder core power losses are overcome by the low cost and gapless design.

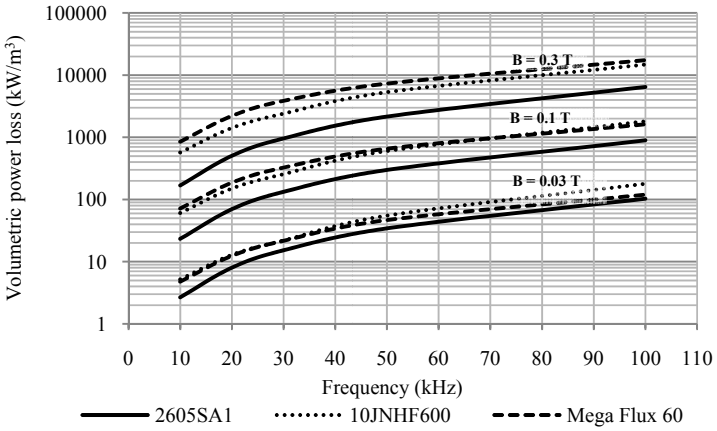

Figure 3.3. Volumetric power density vs. frequency and flux density amplitude.

Although powder core eliminates need of the air gap, it is possible to build powder core based inductor with an air gap. A plot of volumetric power loss vs. permeability is presented in Figure 3.4 for KoolMu, MPP, High Flux, and Mega Flux powder materials. The powder core permeability depends on the material composition. Thus, the nominal power loss in pressed powder materials is closely related to its permeability. The low permeability materials are penalized by higher power loss, which stabilizes at higher permeabilities with exceptions of the High Flux material, whose power loss is the lowest for a relative permeability of 55 and then increases again.

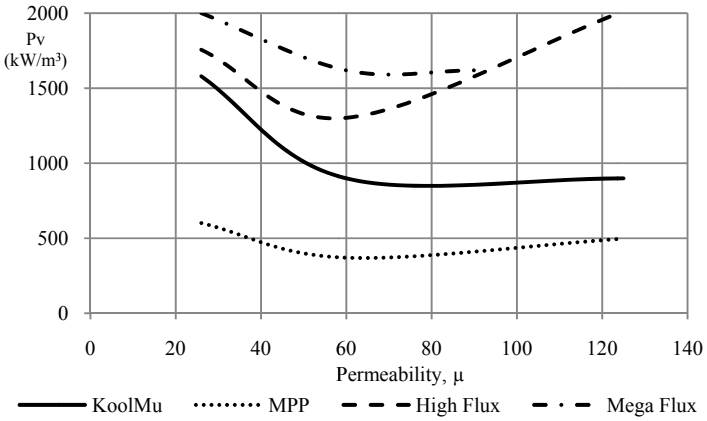

Figure 3.4. Pressed powder material power loss vs. permeability at 100 kHz and 0.1 T.

Additional information for selected materials is provided in Table 3.2 as full data is not available for all magnetic materials at this time.

The specific heat capacity indicates how much energy is needed to increase 1 kg materials sample temperature by 1 Kelvin. The specific heat capacity is useful in material thermal dynamic evaluation; however, it is not concerned in this dissertation.

The electrical resistivity is additional information which may be useful when the eddy-current-power-loss-component calculation in the core is required. The Steinmetz equation provides bulk solution for power loss generated in the core without the need of the eddy current and hysteresis loss separate evaluation. It is interesting that the power loss in nanocrystalline material is mostly generated by eddy currents [85].

The lamination thickness is an indication of how thick is the ribbon used in the core. The amorphous core and nanocrystalline cores use very thin ribbons of about 20 μm. The core fill factor is an important number which provides the effective core cross-section area as inter-lamination spaces are virtually occupied by air. Thus, the same core cross-section area at the same permeability material may result in different flux density amplitude if core fill factor is different.

Magnetostriction and the resulting audible noise can be a determining factor in inductor design if the switching frequency is in the audible range (20 Hz – 20 kHz). While magnetostriction values are cited in Table 3.2 magnetostriction is not investigated in this analysis.

Table 3.2. Magnetic Materials Properties

Magnetic Material Type	Manufacturer	Material	Specific Heat Capacity [J/(K kg)]	Electrical Resistivity [μΩ m]	Lamination Thickness [μm]	Core Fill Factor	Magnetostriction [ppm]
AM	Metglas	2605SA1	540*	1.37	23	>0.79	27
AM	Metglas	2605S3A	~540*	1.38	20	>0.75	20
SS	JFE	10JNHF600	536*	0.82	100	0.9	0.1*
SS	JFE	Prototype	536*	0.82	80	0.9	0.1*
NC	VAC	VP500F	~500*	1.15	23	0.7	0.5
Ferrite	Ferroxcube	3C93	~750*	5x106	bulk	1	0.6

* preliminary data

Cost is often a driving factor in the magnetic material selection. The basic material cost is a critical factor as are advanced processing. However, raw material cost can be in continuous change and the processing technology is progressing. Thus, economic issues are not considered in this chapter.

A serious concern for the dc inductor designer is material's dc-bias capability, which represents the materials stability at elevated dc-magnetization. The magnetic material subjected to the excessive magnetic flux will saturate. Moreover, the material saturation is accompanied by a permeability drop, which is usually not desired for a dc filter inductor. The air gap increases the inductor dc-bias capability and energy storage at the expense of decreased inductance. Figure 3.5 shows typical hysteresis loops and corresponding dc-bias characteristics with air gap for amorphous metal [73]. The inductor dc-bias property depends on the core cross-section area, magnetic path length and applied magnetizing force.

A typical dc-bias characteristic of various powder cores is shown in Figure 3.6. The powder core by default has an intrinsic distributed air gap, although it may be gapped for greater linearity and energy storage. The powder core dc-bias capability depends on the materials composition. The best dc-bias capability belongs to the XFlux material.

The gapped materials usually have a sharp dc-bias characteristic, which fall sharply when the material saturation is reached as shown in Figure 3.5. The gapless powder cores have a soft dc-bias characteristic, whose permeability decreases gently as the magnetizing force increases as shown in Figure 3.6. It is critical that inductance roll-off is allowed for powder based cores, which may affect design size. The allowed inductance roll-off typically do not exceeds 30 % drop from its initial value at no dc-bias.

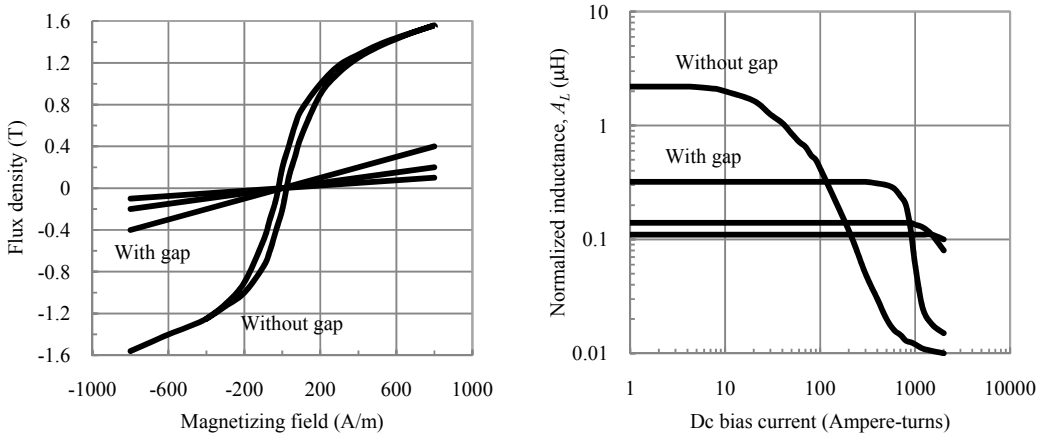

Figure 3.5. Typical hysteresis loops and its corresponding dc bias characteristics with air gap [73].

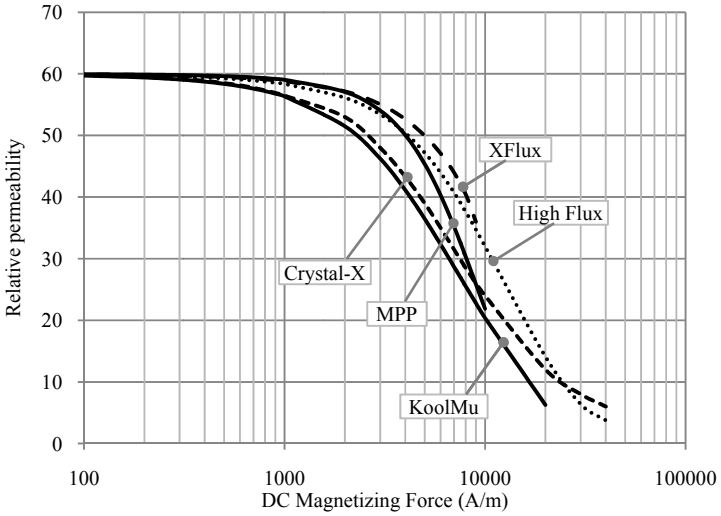

Figure 3.6. Magnetization characteristic of μ60 powder cores.

The variety of available magnetic materials complicates selection and it is a difficult process even for an experienced designer. The magnetic design depends on the material selection; the core shape, the cooling method and the winding. The following sections present a powerful magnetic material selection method which improves the magnetic design process.

3.3. Comparison of the Magnetic Materials

The optimum choice of the magnetic material for an inductor design is not straightforward. The material selection starts with the inductor design constraints such as maximum power, efficiency, input and output voltage, inductance and operating frequency. On the other hand, the system cooling capability, size and cost requirements may determine the preferred option. The component can be cooled by natural convection or by forced air. However, the most efficient heat removal is achieved by using a cold plate or submerging the device in high dielectric oil.

Power loss curves are a common comparison method used by manufacturers. The volumetric power loss density against the flux density for the various materials at 20 kHz and 100 kHz are shown in Figure 3.1 and Figure 3.2, respectively. Individualized core selection charts [76]-[80] are available, which are exclusively prepared for the specified cores range.

Silicon steel manufacturer JFE [74] uses a simple approach for the material comparison, as shown in Figure 3.7 and Figure 3.8 for 20 kHz and 100 kHz, respectively. The JFE comparison chart shows the saturation flux density vs. power loss at a given frequency and flux density amplitude. In general, an ultimate material is aiming towards high maximum flux density and low power loss.

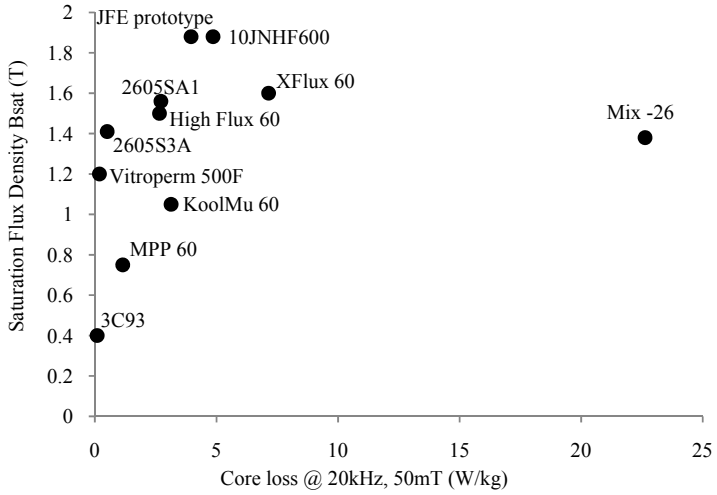

Figure 3.7. JFE proposed material comparison at 20 kHz.

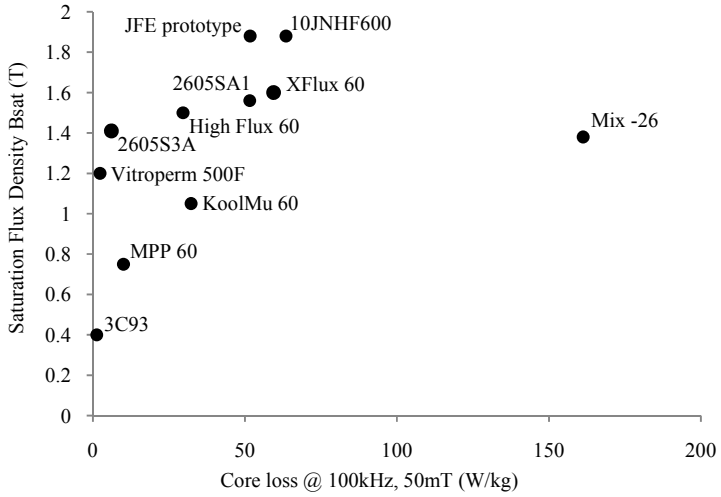

Figure 3.8. JFE proposed material comparison at 100 kHz.

The performance factor is a very commonly used comparison method [76][78]. In this thesis, the performance factor of a transformer or ac inductor is designated PF_{ac}. The PF_{ac} is developed for a fixed component's VA and current density. It can easily be shown that the physical size of a transformer or ac inductor is inversely related to PF_{ac}, which is shown as the product of frequency and maximum ac flux density B_{ac}:

$$PF_{ac} = f \cdot B_{ac} \tag{3.1}$$

where B_{ac} is limited either by saturation or the allowable specific power loss, as defined by the Steinmetz equation [87]-[89], given by

$$B_{ac} = \sqrt[n]{\frac{P_V}{k f^m}} \tag{3.2}$$

where k, m, and n are the Steinmetz equation parameters as shown in Appendix B.1.

A similar derivation of a dc inductor for energy storage does not feature the frequency component and so the performance factor of a dc inductor, PF_{dc}, is simply related to the allowable dc bias flux density, B_{dc}.

$$PF_{dc} = B_{dc} \tag{3.3}$$

A performance factor for an inductor with dc and ac components, PF_{ac+dc}, is not as simply derived due to the dissimilar nature of the dc and ac performance factors. However, the square root of product of the performance factors intuitively provides a quantitative insight into the relative sizing of PF_{ac+dc}. Thus, PF_{ac+dc} is given by

$$PF_{ac+dc} = \sqrt{f \cdot B_{ac} \cdot B_{dc}} \tag{3.4}$$

where B_{dc} is the difference between the maximum flux density B_{max} and the peak ac flux density, B_{ac}.

$$B_{dc} = B_{\max} - B_{ac} \tag{3.5}$$

It is further distinguished that the performance factors for free-air convection cooling is subscripted (conv), and conduction cooling using a cold plate is subscripted (cond). Thus, $PF_{ac(conv)}$, $PF_{ac+dc(conv)}$, $PF_{ac(cond)}$ and $PF_{ac+dc(cond)}$ are the performance factors for ac and ac+dc inductors for conduction and convection cooling, respectively.

A conduction-cooled performance factor considers magnetic material thermal conductivity and is developed for use in high-power-density designs utilizing liquid-cooled cold plate.

Heat transfer by conduction involves transfer of energy within a material without any motion of the material as a whole. The law of Heat Conduction, also known as Fourier's law, states that the time rate of heat transfer through a surface is proportional to the negative gradient of the temperature and thermal conductivity [88][90] [91]:

$$\frac{dQ}{dt\,A} = -\lambda \nabla T \tag{3.6}$$

Where $dQ/dt{\cdot}A^{-1}$ is the heat through the surface in $W{\cdot}m^{-2}$, λ is the material's thermal conductivity in $W{\cdot}m^{-1}{\cdot}K^{-1}$ and ∇T is the temperature gradient in $K{\cdot}m^{-1}$.

For many simple applications, Fourier's law is used in its one-dimensional form as shown in Figure 3.9 *(a)*. The temperature rise in a heat conducting material is integrated over the sample length h, and equals:

$$\Delta T = \frac{P_y\, h}{\lambda\, A} \tag{3.7}$$

where P_y is total power flowing through the material in y direction.

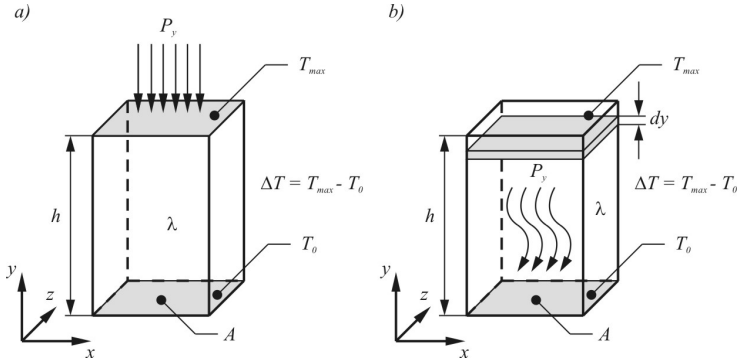

Figure 3.9. 1-D heat conduction from the *(a)* external source and *(b)* internally generated.

The situation differs for a material in whose power loss is generated internally as shown in Figure 3.9 *(b)* rather than applied externally as shown in Figure 3.9 *(a)*. The volumetric power loss P_V is assumed to be constant and the elemental power loss *dp* generated in the material is proportional to the specimen size. Since the 1-D model is considered, the absolute power generated in the material increases with its length *h*; thus, the total power as a function of the sample length can be found from the basic integration:

$$\int dp = P_V \, A \int dy \quad \Rightarrow \quad P_{tot} = P_V \, A \, y \tag{3.8}$$

Thus, substituting eq. (3.8) into transformed eq. (3.7) yields

$$\int dT = \frac{P_V \, A}{\lambda \, A} \int_h y \, dy \tag{3.9}$$

Since material volume *V* is a product of *A* and *h*, the temperature increase of the sample with internal power loss source is as follows

$$\Delta T = \frac{P_V \, V \, h}{2 \lambda \, A} \tag{3.10}$$

The conduction-cooled performance factor assumes a constant temperature rise ΔT of a cube made of the investigated material and placed on the cold plate as shown in Figure 3.10. The cube edge dimension has a height, *h*, and material thermal conductivity, λ. The power loss per unit volume as a function of the temperature rise is given by:

$$P_V \left(\Delta T \right) = \frac{2 \Delta T \, \lambda}{h^2} \tag{3.11}$$

Thus for conduction cooling, the allowable B_{ac} is determined by

$$B_{ac} = \sqrt[n]{\frac{2 \Delta T \, \lambda}{k \, h^2 \, f^m}} \tag{3.12}$$

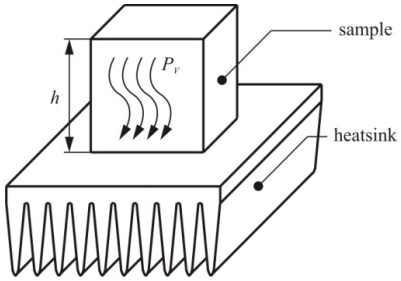

Figure 3.10. Conduction cooled sample.

Sample performance factor charts are plotted in Figure 3.11 to Figure 3.13 and Figure 3.14 to Figure 3.16 for gapped and gapless materials, respectively. The convection-cooled charts plot the performance factors for specific volumetric power loss densities of 30 mW/cm^3, 100 mW/cm^3, and 300 mW/cm^3 in Figure 3.11 and Figure 3.14, Figure 3.12 and Figure 3.15, Figure 3.13 and Figure 3.16, respectively. The conduction-cooled charts show the performance factor for sample lengths of 10 mm, 30 mm, and 100 mm in Figure 3.17 and Figure 3.20, Figure 3.18 and Figure 3.21, Figure 3.19 and Figure 3.22 for gapped and gapless materials, respectively. Each figure plots the curves for *(a)* the ac inductor, or transformer, and *(b)* the ac+dc inductor. These charts are plotted for two relatively-low-loss materials, nanocrystalline 500F and ferrite 3C93, and three relatively-lossy materials, amorphous metal 2605SA1, silicon steel 10JNHF600 and powder core XFlux 60.

These curves provide a useful insight into material selection for magnetic components. In the case of the convection-cooled ac inductor or transformer with a low volumetric power loss density of 30 mW/cm^3, as shown in Figure 3.11 *(a)*, ferrite can be competitive with nanocrystalline, while both of these materials significantly outperform the high-flux, but lossier, materials plotted.

When the inductor is required to provide energy storage in the case of the ac+dc inductor, the low saturation flux density of ferrite makes it very uncompetitive with respect to all the high flux materials, as shown in Figure 3.11 *(b)*. At this low level of power loss, all the materials tend to be power-loss limited and may be far from saturation. Thus, the high flux materials can operate significantly up the magnetization curve and outperform the low-saturation-flux-density ferrite.

Increasing the volumetric power loss density to a reasonably high value of 300 mW/cm^3 results in a more dramatic change. The lossier materials tend to be outperformed by ferrite and nanocrystalline as shown in Figure 3.13 *(a)* for ac inductors and transformers. However, the high-flux, lossier materials can be competitive with nanocrystalline at low-frequencies due to their higher saturation flux densities as shown in Figure 3.13 *(b)* for the ac+dc inductor.

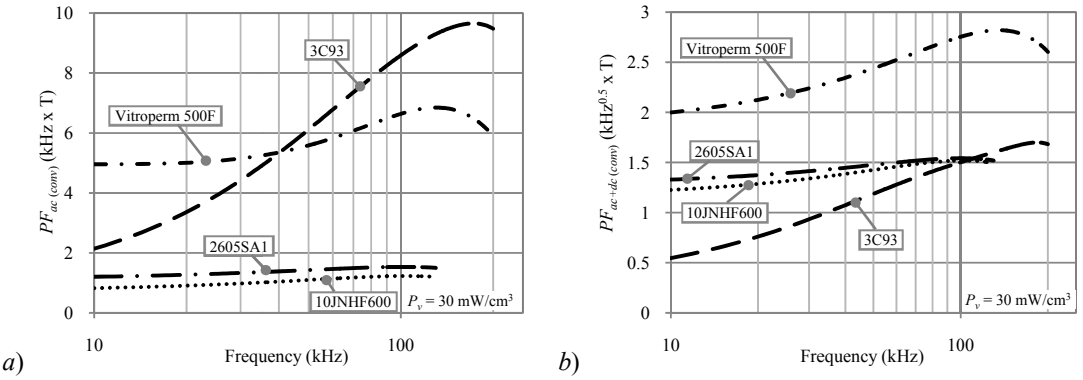

Figure 3.11. Gapped materials convection-cooled *PF* vs. freq. at P_V = 30 mW/cm^3 for *(a)* an ac inductor or transformer, and *(b)* an ac+dc inductor.

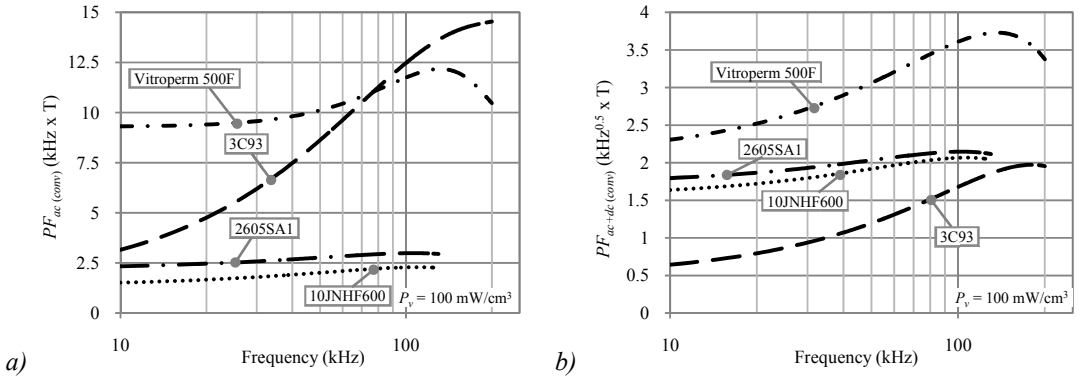

Figure 3.12. Gapped materials convection-cooled *PF* vs. freq. at P_V = 100 mW/cm^3 for *(a)* an ac inductor or transformer, and *(b)* an ac+dc inductor.

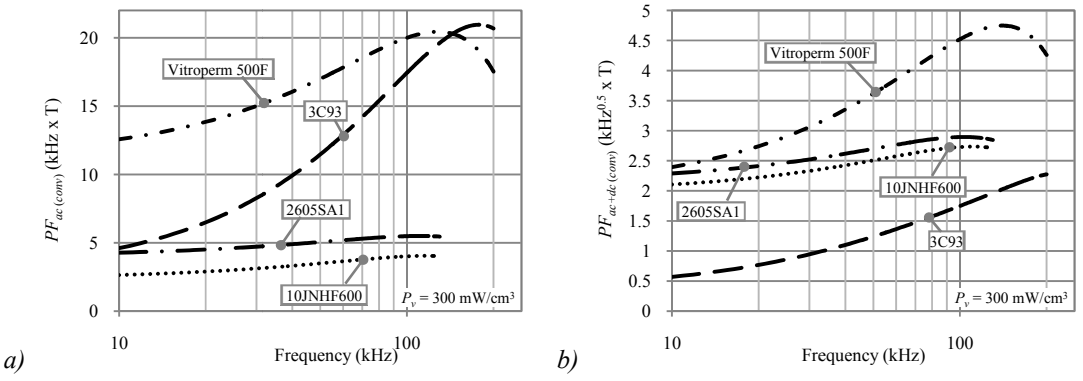

Figure 3.13. Gapped materials convection-cooled *PF* vs. freq. at P_V = 300 mW/cm^3 for *(a)* an ac inductor or transformer, and *(b)* an ac+dc inductor.

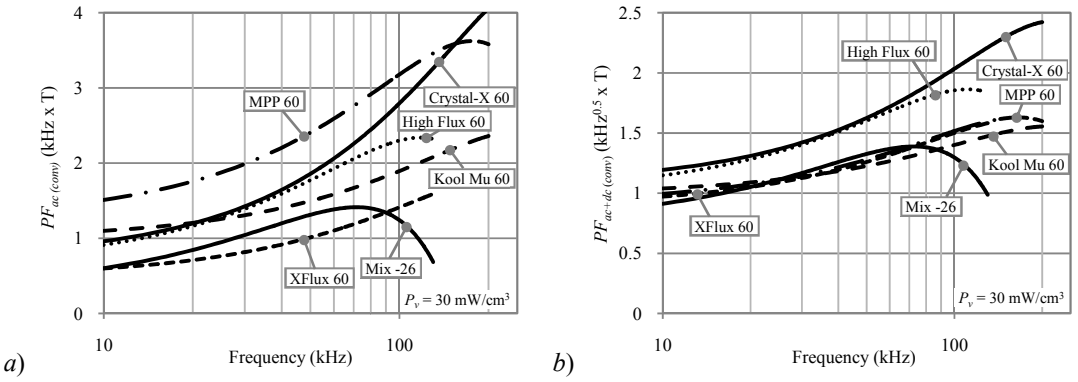

Figure 3.14. Gapless materials convection-cooled *PF* vs. freq. at P_V = 30 mW/cm^3 for *(a)* an ac inductor or transformer, and *(b)* an ac+dc inductor.

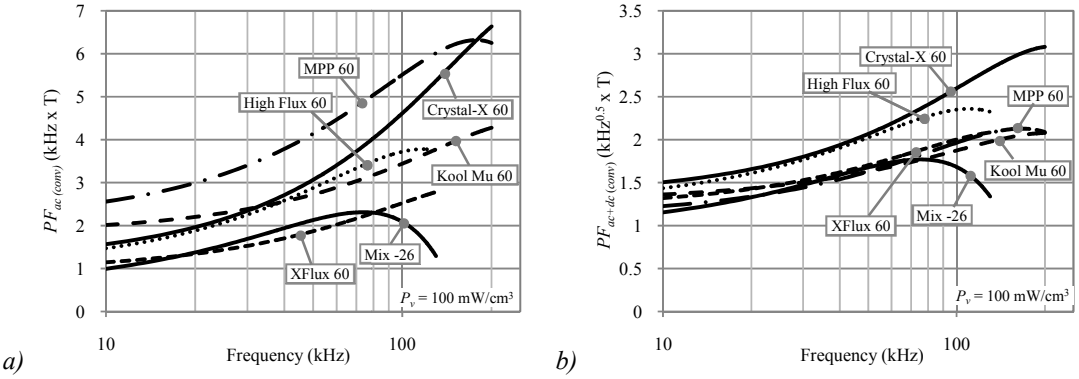

Figure 3.15. Gapless materials convection-cooled *PF* vs. freq. at P_V = 100 mW/cm^3 for *(a)* an ac inductor or transformer, and *(b)* an ac+dc inductor.

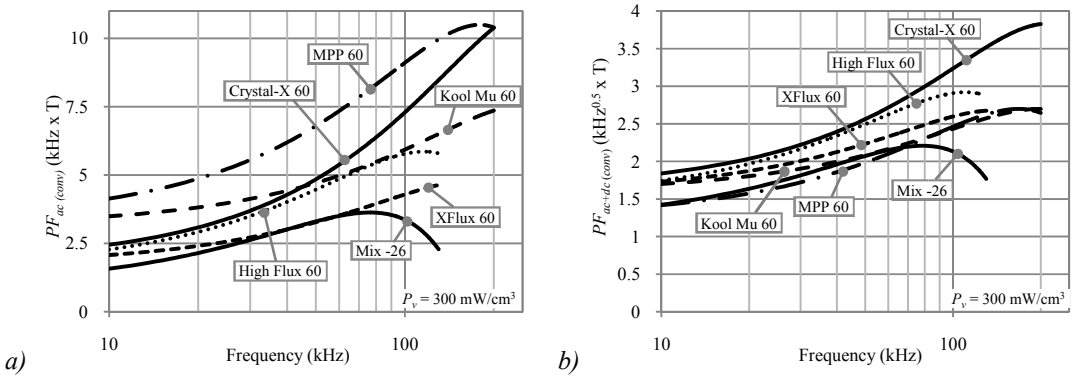

Figure 3.16. Gapless materials convection-cooled *PF* vs. freq. at P_V = 300 mW/cm^3 for *(a)* an ac inductor or transformer, and *(b)* an ac+dc inductor.

The conduction-cooled performance factor accounts for the capability of a material to remove heat from a hotspot, to maximize power handling and minimize component size, albeit at the possible expense of lower component efficiency. Figure 3.17 to Figure 3.19 and Figure 3.20 to Figure 3.22 plot the material characteristics for different material heights. If the material height and consequent thermal path is low, then the good thermal conductors tend to outperform

due to their increased thermal conductivity and despite their higher losses. This is clearly the case for the h = 10 mm and h = 30 mm curves plotted in Figure 3.17 and Figure 3.18, respectively. However, as the material thickness is increased, the ability of the material to remove substantial heat becomes limited for the lossier materials, and the low-loss nanocrystalline outperforms the lossier materials, as shown in Figure 3.19 for h = 100 mm.

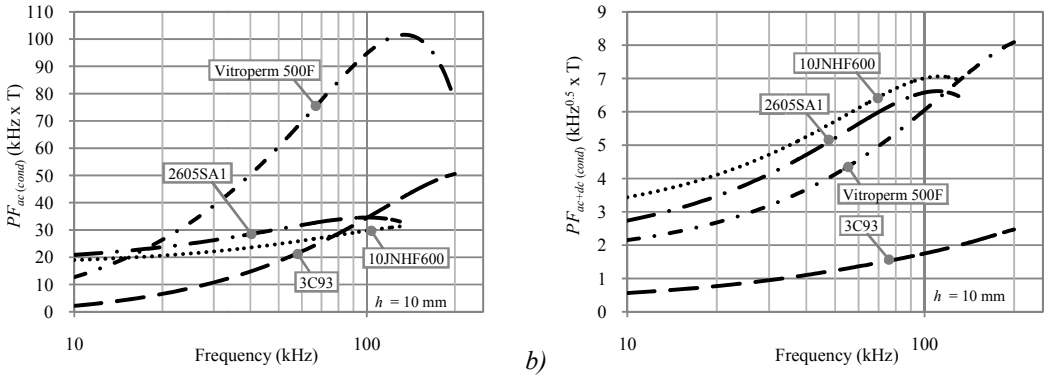

Figure 3.17. Gapped materials conduction-cooled *PF* vs. freq. with length h = 10 mm and max. temp. rise ΔT = 40 K for *(a)* an ac inductor or transformer, and *(b)* an ac+dc inductor.

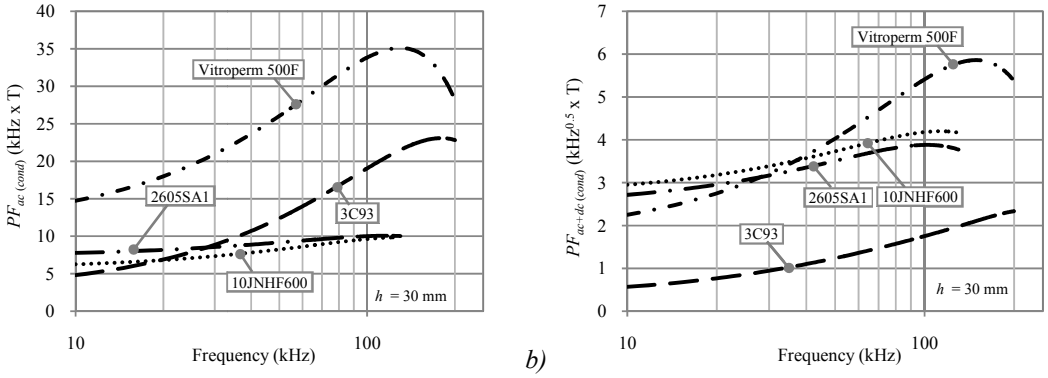

Figure 3.18. Gapped materials conduction-cooled *PF* vs. freq. with length h = 30 mm and max. temp. rise ΔT = 40 K for *(a)* an ac inductor or transformer, and *(b)* an ac+dc inductor.

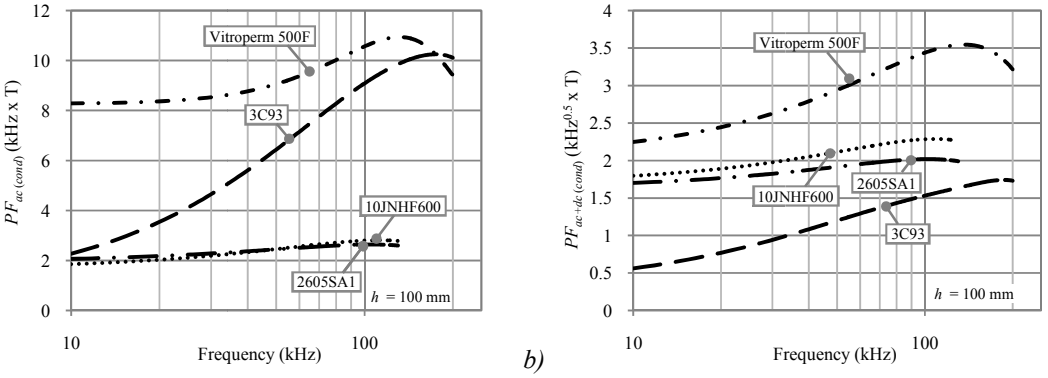

Figure 3.19. Gapped materials conduction-cooled *PF* vs. freq. with length h = 100 mm and max. temp. rise ΔT = 40 K for *(a)* an ac inductor or transformer, and *(b)* an ac+dc inductor.

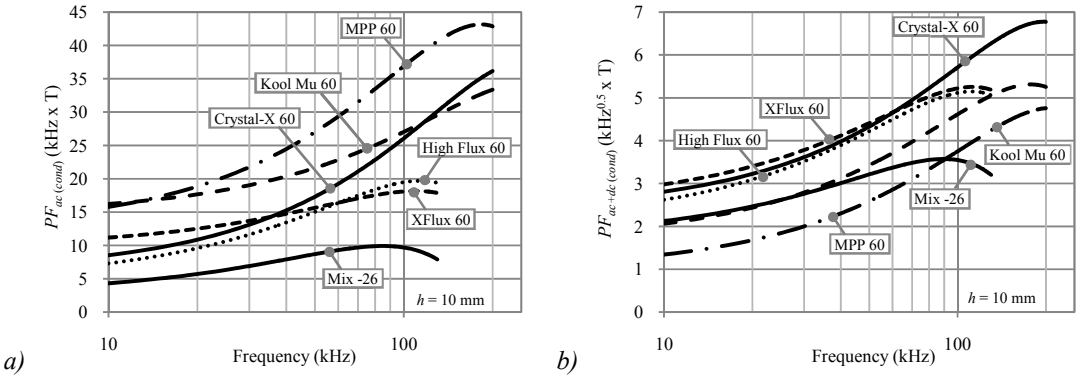

a) *b)*

Figure 3.20. Gapless materials conduction-cooled *PF* vs. freq. with length h = 10 mm and max. temp. rise ΔT = 40 K for *(a)* an ac inductor or transformer, and *(b)* an ac+dc inductor.

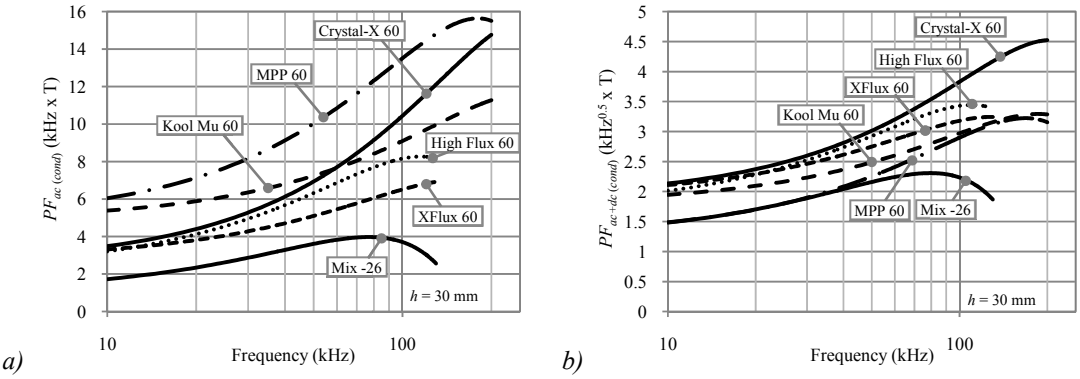

a) *b)*

Figure 3.21. Gapless materials conduction-cooled *PF* vs. freq. with length h = 30 mm and max. temp. rise ΔT = 40 K for *(a)* an ac inductor or transformer, and *(b)* an ac+dc inductor.

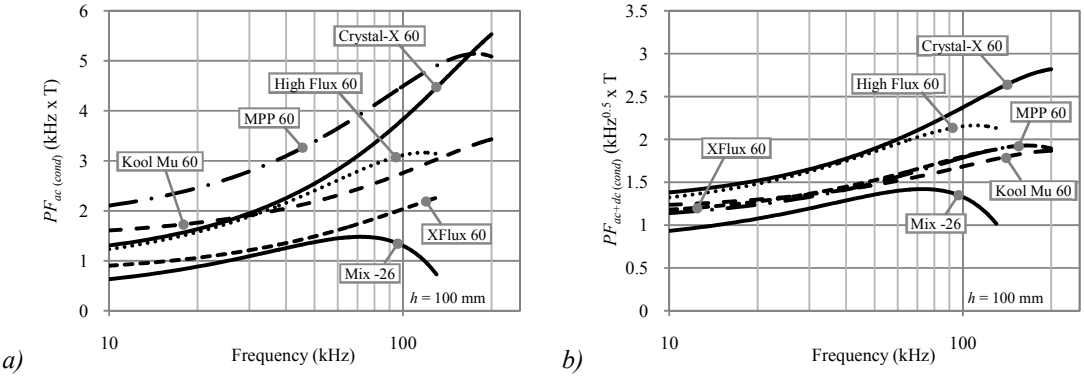

a) *b)*

Figure 3.22. Gapless materials conduction-cooled *PF* vs. freq. with length h = 100 mm and max. temp. rise ΔT = 40 K for *(a)* an ac inductor or transformer, and *(b)* an ac+dc inductor.

As discussed above, the performance factor can be shown to relate to the area product of a magnetic component for a given power handling or energy storage, or both. The greater is the performance factor, the smaller is the area product. It logically follows that it may be more intuitive, when much of the design discussion is about area product, to create a new parameter, known as the inverted performance factor, which directly correlates area product and the performance factor. Thus, the inverted performance factor (*IPF*) is simply

$$IPF = PF^{-1} \tag{3.13}$$

As before, it is appropriate to distinguish between the performance factors for ac and dc magnetic components, and for free-air convection cooling, subscripted (conv), and conduction cooling using a cold plate, subscripted (cond). Thus, $IPF_{ac(conv)}$, $IPF_{ac+dc(conv)}$, $IPF_{ac(cond)}$ and $IPF_{ac+dc(cond)}$ are the inverted performance factors for ac and ac+dc inductors for conduction and convection cooling, respectively.

The *IPF*s are plotted in Figure 3.23 to Figure 3.28 for the gapped and gapless materials for convection and conduction cooling.

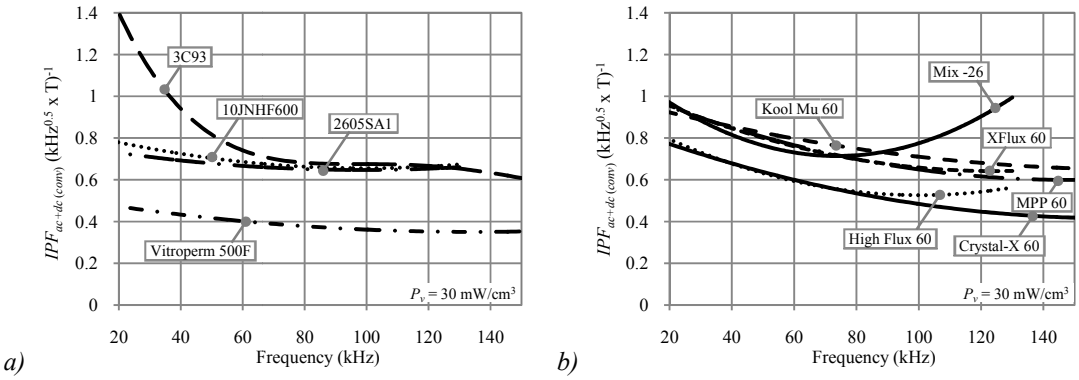

Figure 3.23. Convection-cooled inverted $PF_{ac+dc\,(conv)}$ vs. freq. at P_V = 30 mW/cm^3 for *(a)* gapped materials, and *(b)* gapless materials.

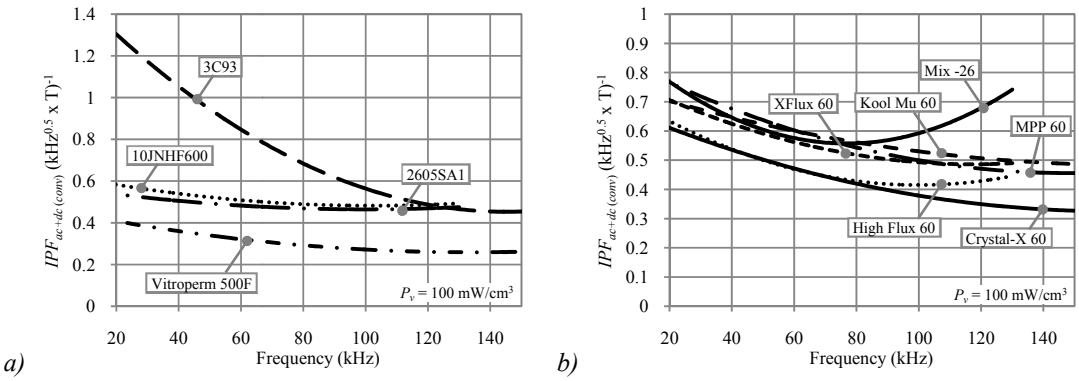

Figure 3.24. Convection-cooled inverted $PF_{ac+dc(conv)}$ vs. freq. at P_V = 100 mW/cm^3 for *(a)* gapped materials, and *(b)* gapless materials.

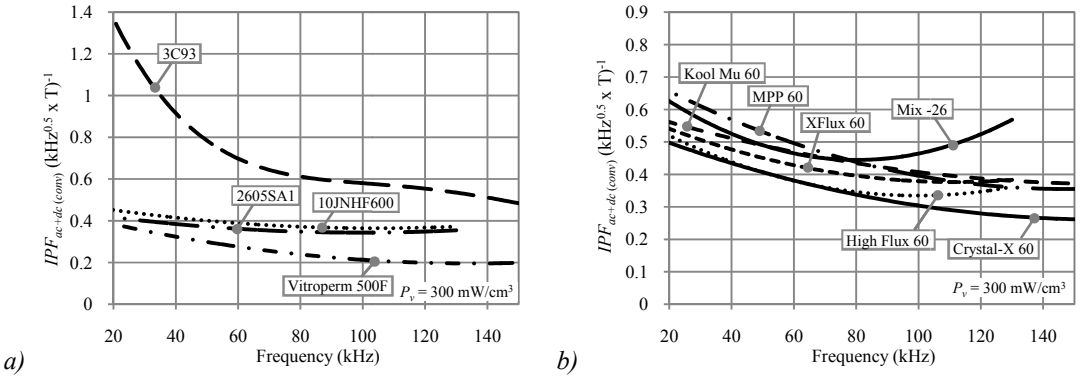

Figure 3.25. Convection-cooled inverted $PF_{ac+dc\ (conv)}$ vs. freq. at P_V = 300 mW/cm^3 for *(a)* gapped materials, and *(b)* gapless materials.

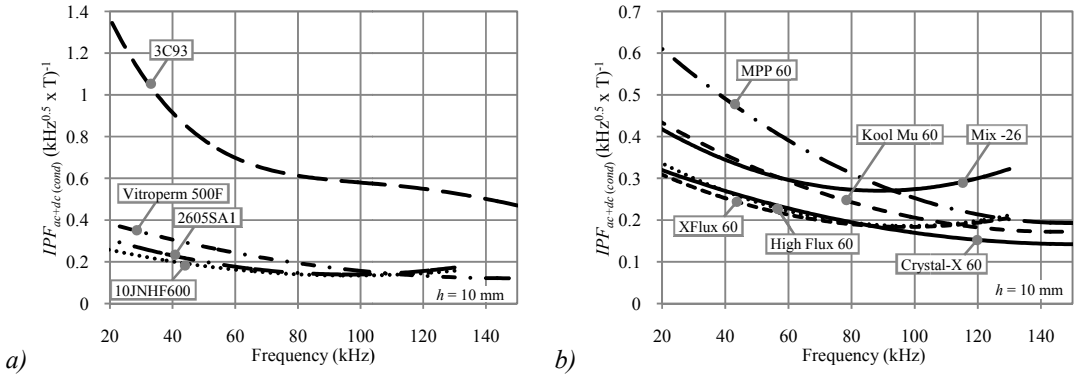

Figure 3.26. Conduction-cooled inverted $PF_{ac+dc\ (cond)}$ vs. freq. with length h = 10 mm and max. temp. rise ΔT = 40 K for *(a)* gapped materials, and *(b)* gapless materials.

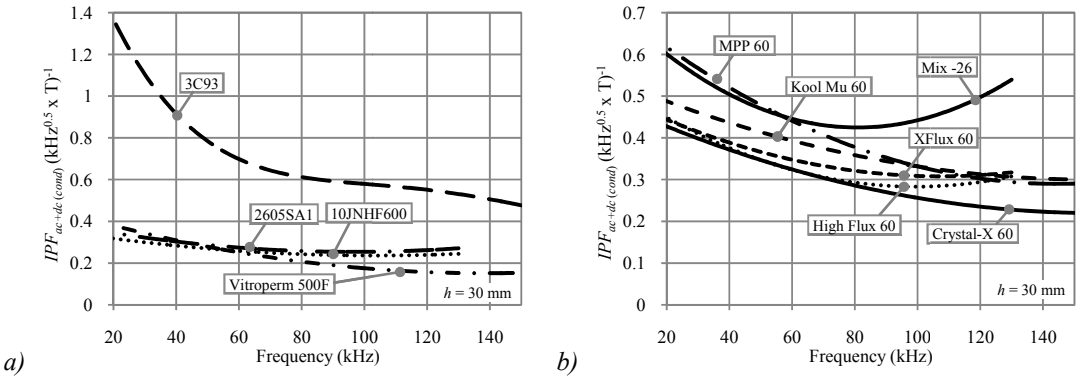

Figure 3.27. Conduction-cooled inverted $PF_{ac+dc\ (cond)}$ vs. freq. with length h = 30 mm and max. temp. rise ΔT = 40 K for *(a)* gapped materials, and *(b)* gapless materials.

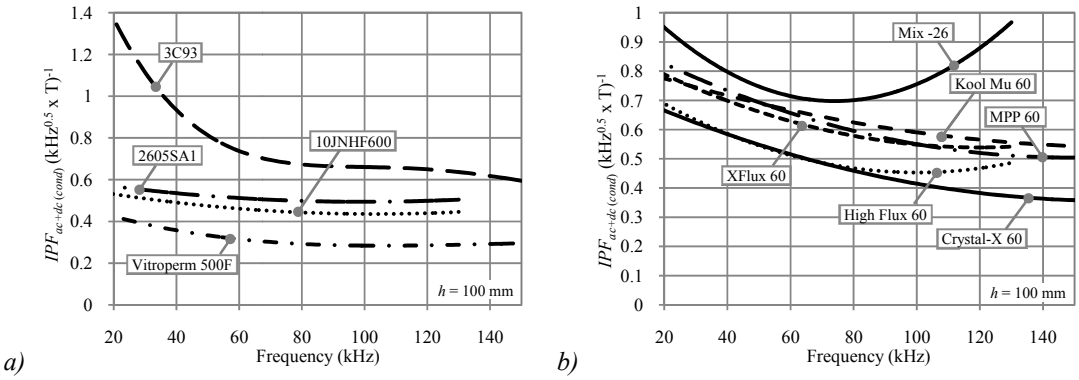

a) *b)*

Figure 3.28. Conduction-cooled inverted $PF_{ac+dc\ (cond)}$ vs. freq. with length h = 100 mm and max. temp. rise ΔT = 40 K for *(a)* gapped materials, and *(b)* gapless materials.

3.4. Conclusions on Performance Factor Materials Selection

The performance factor analysis is a simple and intuitive approach for magnetic materials comparison. The approach has previously been developed for sizing ac magnetics for a given allowable specific power loss. The approach has been extended in this chapter to factor in the effects of dc magnetization and thermal conductivity. Thus, performance factors can now be used to aid in the selection of the optimum material for a dc inductor with ac ripple for convection or conduction cooling.

The analytical background of the performance factor with relevant graphs was presented in Section 3.3. The graphs are shown for gapped and gapless materials separately. The convection-cooled graphs are presented for a three specific volumetric power's 30, 100 and 300 mW/cm^3, while the conduction-cooled graphs assume 40 K temperature rise for three sample lengths of 10, 30 and 100 mm. The selected power loss densities and sample lengths are representative approximations for the parameters of high-power magnetic components.

In general, the optimum materials change with specific power loss. There is a significant difference between the air-cooled and conduction-cooled graphs as conduction-cooling allows for a very efficient heat removal and size reduction.

The conduction-cooled dc inductor performance factor chart highlights the capability of the material to remove heat together with saturation capability. The most suited materials for a high-power-density inductor are those with high thermal conductivity and high saturation flux density. The material optimum selection is strongly related to the thermal path length.

Technically, the nanocrystalline material has the best overall characteristics in all cases, but presently is significantly more expensive than the other materials. The cost of the nanocrystalline material increases further due to the manufacturing process required to cut the material. The best solution for an air-cooled ac inductor or transformer is the ferrite material as it compromises low power loss and low overall cost.

Chapter 4

Inductor Size – Area Product Analysis

In this chapter various magnetic materials are analysed and investigated for use in a CC-core inductor. The investigated materials are selected from the Table 3.1 and are as follows: amorphous metal 2605SA1, silicon steel 10JNHF600, nanocrystalline Vitroperm 500F and ferrite 3C93.

A novel approach to the inductor-design algorithm is presented and used in order to compare the various magnetic materials over a range of frequencies, ripple ratios, two cooling methods and efficiency. The algorithm is developed for foil-wound inductors with CC cores in the low (20 kHz) to high (150 kHz) frequency range.

As expected, inductor size varies with a current ripple for a given frequency. The minimum size is achieved for the design which meets temperature rise and flux density limitation at the same time. As operating frequency increases, the current-ripple ratio for minimum size decreases. In general, the inductor size decreases as the frequency increases in the considered frequency range. The conduction-cooled design allows for very efficient cooling and significant size reduction can achieved with respect to the air-cooled design. However, an efficiency restriction can disturb this relation and cause inductor size to increase.

4.1. Inductor Design Flowchart

The inductor design is a complicated process. Most of the inductor design flow charts involve the selection of a core size in an iterative design procedure [81][87][88][89][91][93]. In this section, an algorithm is developed to solve for the optimum inductor design. Various electrical and magnetic parameters and constraints are input into the algorithm and the minimum-sized inductor is determined based on the inputs.

Two different flow charts are used to compare the magnetic materials. The first algorithm is dedicated for gapped materials with an air gap where operation is restricted to the linear part of the B-H characteristic, as shown in Figure 4.1 *(a)*. This algorithm is used for the high permeability materials such as amorphous metal, silicon steel, nanocrystalline and ferrite. The second algorithm, shown in Figure 4.1 *(b)*, is created to deal with powder materials for a gapless design and is based on the materials dc-bias curve, where up to 30% permeability roll-off is allowed.

In general, the solution is obtained by seeking a minimum area product, where the core's basic dimensions are the variables. The result is the core area product AP which is proportional to the inductor volume and mass. The algorithm relies on Excel's built in minimum seeker function; however, it can be implemented in any mathematical package. Both flowcharts allow for relatively simple use of the material parameters straight from the datasheet.

Both algorithms have a similar modular structure as shown in Figure 4.1. The modular structure improves the algorithm clarity as well as enabling easy modification of the design. Each section can be modified or swopped easily to match the design requirements. This enables fast initial designs for the various magnetic materials, core shapes and winding arrangements as well as the cooling options. The algorithm structure is based on a set of linear equations but also factors in the gapless core dc-bias characteristic. The presented algorithms calculates a filter inductor for a boost converter based on CC core set with a foil winding split between the core legs and an air gap placed in the core leg centre.

Each algorithm consists of nine main modules (A) – (I) and the minimum seeker loop with defined constraints in (J). If conditions (J) are satisfied the minimum area product is calculated and the gapless algorithm ends. The gapped algorithm continues calculation in the next loop (K) – (M) where additional turns are added to the design to seek a further optimization by moving core loss to the copper. The area product is calculated with a new number of turns and is compared with the previous iteration. If (L) is satisfied then the algorithm finishes its calculation with the final area product.

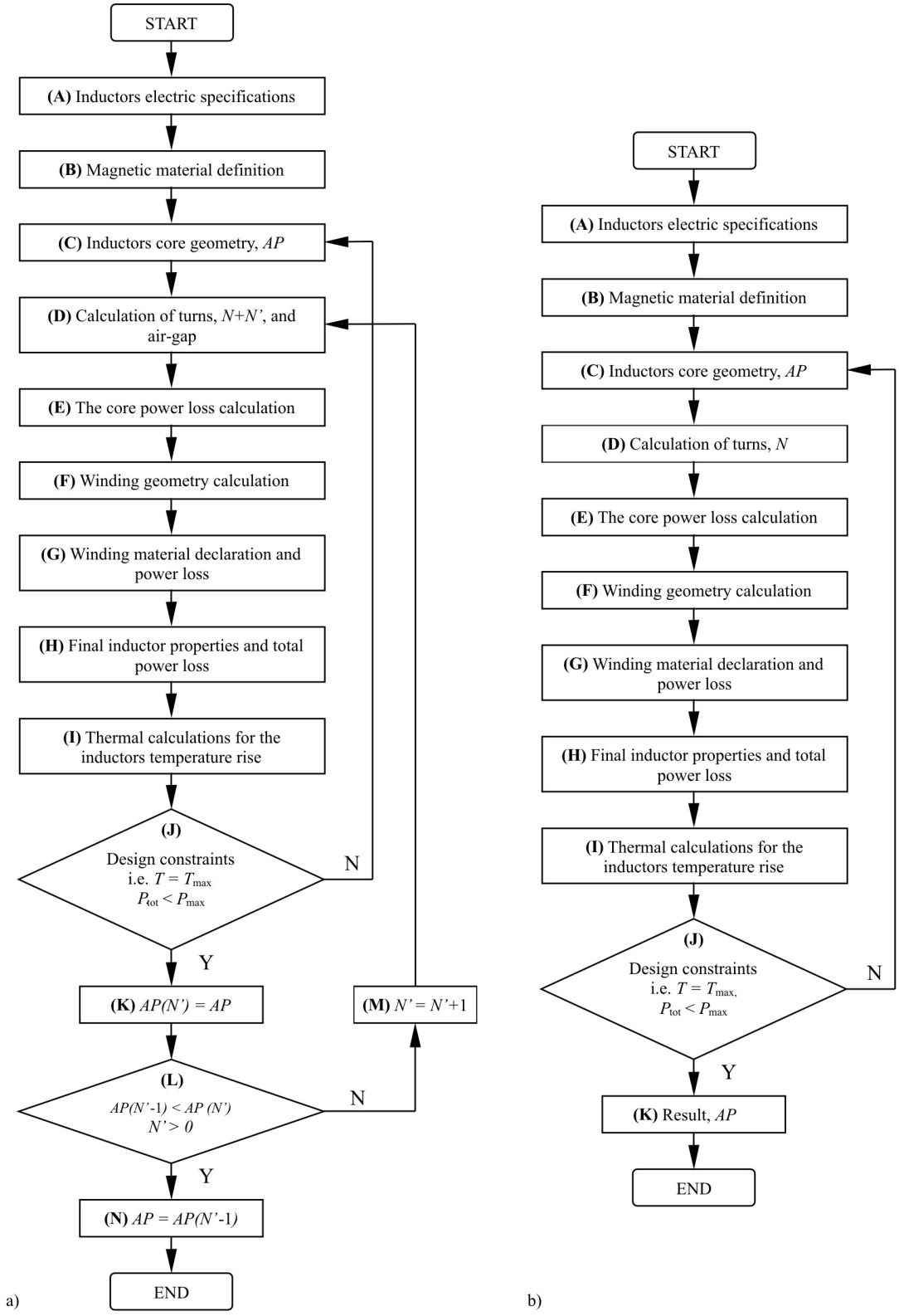

Figure 4.1. Design algorithm for *(a)* gapped and *(b)* gapless inductor.

The algorithm calculates such factors as: air gap fringing factor, rounded and even turns number, core power loss, winding clearance and creepage, distance between winding and air gap, winding skin and proximity effect.

Firstly, the gapped inductor algorithm is presented in Section 4.1.1 and then the differences in the gapless inductor algorithm are highlighted Section 4.1.2.

4.1.1. Gapped Inductor Design Flowchart

In (A) the inductor electric specifications are specified: input voltage, V_{in}, output voltage, V_{out}, maximum output power capability, P_{out}, converter efficiency, η, inductor efficiency, η_i, current-ripple ratio, r, and operating frequency, f. The electric specifications are generated for the design: dc input current, I_{in}, peak-to-peak inductor current, ΔI_{pp}, duty ratio, D, inductor inductance, L, inductor peak current, I_{max}, allowable inductor power loss, ΔP_i.

$$I_{in} = \frac{P_{out}}{\eta \cdot V_{in}}, \quad \Delta I_{pp} = I_{in} \cdot r, \quad D = 1 - \frac{V_{in}}{V_{out}}, \quad L = \frac{V_{in} D}{f \cdot \Delta I_{pp}} \tag{4.1}$$

$$I_{\max} = I_{in} + \frac{1}{2}\Delta I_{pp}, \quad \Delta P_i = P_{out}\frac{1-\eta_i}{\eta} \tag{4.2}$$

The magnetic material is defined in (B): relative permeability, μ_r, saturation flux density, B_{sat}, core fill factor, k_{cf}, core mass density, ρ_{cm}, the core power loss, P_c, is parameterised by Steimetz equation parameters: k, m, n shown in Appendix B.1. The saturation flux is de-rated by factor k_d in order to operate in the linear region of the materials B-H curve.

Block (C) introduces the core dimension variables: core width, a, window width, b, window length, c, and core thickness, d as shown in Figure 4.2. Initial core dimensions must be set in the algorithm. The core dimension allows for further calculations as the core window ratio, r_w, core profile ratio, r_c, and the core shape ratio, r_s, as well as the core cross-sectional area, A_c, effective cross-sectional area, A_{ceff}, window area, A_w, and the area product, AP. The core mean magnetic path length, l_c, effective cross-section area, A_{ceff}, core volume, V_c, and mass, m_c, is calculated.

$$r_w = \frac{c}{b}, \quad r_c = \frac{d}{a}, \quad r_s = \frac{2a+c}{2a+b}, \quad A_c = a \cdot d, \quad A_w = b \cdot c \tag{4.3}$$

$$AP = A_c A_w, \quad l_c = 2(b+c) + \pi \cdot a, \quad A_{ceff} = k_{cf} \cdot A_c \tag{4.4}$$

$$V_c = l_c \cdot A_c, \quad m_c = \rho_{mc} \cdot V_c \tag{4.5}$$

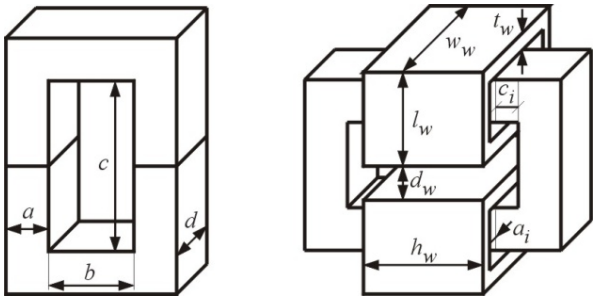

Figure 4.2. Core and winding dimensions.

The number of turns and air-gap is calculated in (D): The initial peak-to-peak flux swing, ΔB_{ppi}, is used to estimate the initial turns, N_i. The absolute turns number equals the sum of the rounded-up initial turns number and the additional turns, N', from the design iteration loop. Initially, N' equals zero. Then the total air-gap, l_g, is calculated. The air-gap calculation involves iteration in order to adjust the fringing field factor [88][89], F_g, which initially equals 1. The air gap length iteration loop is shown in Figure 4.3 where ε_{max} is a calculation error usually set to 0.005. Finally, the adjusted ac-flux magnitude, B_{ac}, and the peak flux, B_{peak}, are obtained

$$\Delta B_{ppi} = \frac{\Delta I_{pp}}{I_{\max}} B_{\max}, \quad N_i = \frac{V_{in} D}{\Delta B_{ppi} A_{ceff} f}, \quad N = ceiling\left[N_i + N'\right] \tag{4.6}$$

$$l_g = \frac{\mu_0 \cdot A_{ceff} \cdot N^2}{L} F_g - \frac{l_c}{\mu_c}, \quad F_g = 1 + \frac{l_g(j)}{\sqrt{A_{ceff}}} \ln\left(\frac{2 \cdot c}{l_g(j)}\right) \tag{4.7}$$

$$B_{ac} = \frac{V_{in} D}{2 N A_{ceff} f}, \quad B_{peak} = \frac{I_{\max}}{I_{pp}} 2 B_{ac} \tag{4.8}$$

The core power loss is calculated in (E). The hysteresis and eddy-current core specific power loss, P_{csp}, comes from the Steimetz equation shown in Appendix B.1, while the gap power loss can be evaluated from the McLyman equation [89], Where k_i is a core constant (i.e. 0.388 for CC core) and l_i is the lamination width. The feasibility of the McLyman equation is the subject of a separate investigation presented in Section 5.5.1, which shows that power loss in the core due to air gap fringing flux are marginal in a dc inductor built with modern advanced magnetic materials. Thus, the gap loss equation is optional and is neglected in the area product analysis.

$$P_{csp} = k \cdot f^m \cdot B_{ac}^n, \quad P_g = k_i \cdot l_i \cdot l_g \cdot f \cdot B_{ac}^2 \tag{4.9}$$

$$P_c = P_{csp} V_c + P_g \tag{4.10}$$

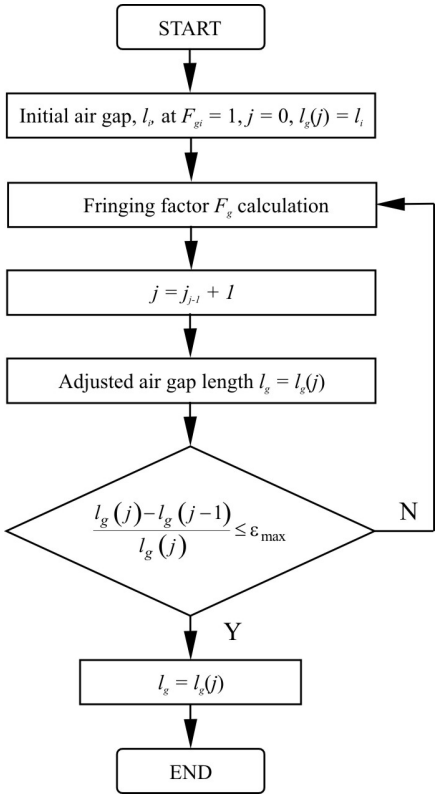

Figure 4.3. Air gap iteration loop.

Winding arrangements and geometry are defined in (F). The inputs are defined as follows: the air-gap factor, k_g, which sets the distance between the winding and the core leg, a_i, typically $k_g = 2$; the distance between the core and winding tips, c_i; the distance between the two adjacent windings on the CC core, d_w; the area for the winding, A_{wa}; the interlayer insulation thickness, t_i, and the total insulation thickness, t_{itot}; the conductor fill factor, k_{con}; the conductor total cross-sectional area, $A_{contot;}$ the single turn conductor cross-section area, A_{con}; the foil thickness, t_{con}, and the foil total length, l_{con}; the conductor volume, V_w, and winding dimensions; winding thickness, t_w, winding outer width, w_w, winding outer thickness, l_w, winding inner width, w_{iw}, winding inner thickness, l_{iw}, winding height, h_w, as shown in Figure 4.2.

$$a_i = 0.5 \cdot k_g \cdot l_g \,, \quad A_{wa} = \left(b - 2a_i - d_w\right)\left(c + 0.5l_g - 2c_i\right) \tag{4.11}$$

$$t_{itot} = N \cdot t_i \,, \quad k_{con} = 1 - \frac{t_{itot}}{b - 2a_i - d_w} \,, \quad A_{contot} = k_{con} A_{wa} \tag{4.12}$$

$$A_{con} = \frac{A_{contot}}{N} \,, \quad t_{con} = \frac{A_{con}}{c + 0.5l_g - 2h_i} \tag{4.13}$$

$$l_{con} = 2\left\{\left(a + d + 4a_i + 2t_{con}\right)N + 4\left(t_{con} + t_i\right)\left[1 + 0.5\left(N - 2\right)\right]\left(N - 1\right)\right\} \tag{4.14}$$

$$V_w = l_{con} A_{con}\,, \quad t_w = 0.5\left(b - 2a_i - d_w\right) \tag{4.15}$$

$$w_w = 2t_w + 2a_i + a\,, \quad l_w = 2t_w + 2a_i + d \tag{4.16}$$

$$w_{iw} = 2a_i + a\,, \quad l_{iw} = 2a_i + d\,, \quad h_w = c + 0.5l_g - 2c_i \tag{4.17}$$

Block (G) provides information about the conductor type and power loss in the winding. Typically the conductor of choice is copper; however, aluminium might be preferred in some applications [94]. The material input sets the material conductivity, σ_x, at the operating temperature, T_x, and the mass density, ρ_w, the conductor permeability, μ_w, and the conductivity at 20°C, σ_{20}, and the temperature coefficient, k_t. Once the winding conductivity, σ_x, is known the winding resistance, R_{dc}, can be found. However, the current in the inductor contains an ac component. Therefore, the total power loss in the winding is calculated by decomposition of the triangular current waveform into the harmonics, I_{dc}, $I_{h=1}...I_{h=\infty}$ [95]. The penetration depth, δ_h, for each harmonic is calculated followed by the stretch factor, η_h, and the porosity factor, ξ_h. Using the Dowell equations the proximity factor for each harmonic, F_h, is calculated [87][88] [96]. Finally, the effective proximity factor, F_{eff}, is obtained and the effective resistance, R_{eff}, is calculated. The winding power loss, P_w, can now be found.

$$m_w = \rho_{mw} \cdot V_w\,, \quad \sigma_{\max} = \frac{\sigma_{20}}{1 + k_t\left(T_{\max} - 20\right)} \tag{4.18}$$

$$R_{dc\max} = \frac{l_{con}}{\sigma_{\max} A_{con}}\,, \quad I_h(h) = \Delta I_{pp} \frac{\sqrt{2\left[1 - \cos\left(2\pi h D\right)\right]}}{\pi^2 h^2 D\left(1 - D\right)} \tag{4.19}$$

$$I_{rms} = \sqrt{I_{dc}^2 + 0.5\sum_{h=1}^{\infty} I_h(h)}\,, \quad \delta_h(h) = \frac{1}{\sqrt{\pi \sigma_{\max} \mu_0 \mu_w h f}} \tag{4.20}$$

$$\eta_h = \frac{c + 0.5l_g - 2c_i}{c + 0.5l_g}\,, \quad \xi_h(h) = \frac{t_{con}}{\delta(h)}\sqrt{\eta_h} \tag{4.21}$$

$$M = \xi_h(h)\frac{\sinh\left(2\xi_h(h)\right) + \sin\left(2\xi_h(h)\right)}{\cosh\left(2\xi_h(h)\right) - \cos\left(2\xi_h(h)\right)} \tag{4.22}$$

$$D = 2\xi_h(h)\frac{\sinh\left(\xi_h(h)\right) - \sin\left(\xi_h(h)\right)}{\cosh\left(\xi_h(h)\right) + \cos\left(\xi_h(h)\right)} \tag{4.23}$$

$$F_h(h) = M + \frac{(0.5N)^2 - 1}{3} D\,, \qquad F_{eff} = \frac{I_{dc}^2 + 0.5\sum_{h=1}^{\infty} I_h^2(h) F_h(h)}{I_{rms}} \tag{4.24}$$

$$R_{eff\,\max} = F_{eff}\, R_{dc\,\max}\,, \qquad P_w = R_{eff\,\max} I_{rms}^2 \tag{4.25}$$

The final inductor properties are gathered in block (H). The inductor is characterized by its outer dimensions, width, w_i, length, l_i, height, h_i, and the inductor volume, V_i, and total mass, m_i. Finally, the inductors total power loss, P_i, is calculated.

$$w_i = 2a + b + 2t_w + 2a_i\,, \qquad l_i = 2a + c + 0.5l_g\,, \quad h_i = w_w \tag{4.26}$$

$$V_i = w_i\, l_i\, h_i\,, \qquad m_i = m_c + m_w\,, \quad P_i = P_c + P_w \tag{4.27}$$

The last module, (I), estimates the component temperature rise. The algorithm can generate convection- or conduction-cooled designs. The natural convection cooling assumes that the heat removed from the object is 50 % by radiation and 50 % by convection. The convective surface, SA, is calculated for the total of all surfaces exposed for heat exchange, P_i. The temperature rise, ΔT, can be approximated empirically as follows [72][88]:

$$SA = 2\left(2a + c + 0.5l_g\right)\left(2a + 3b + d\right) + 4\left(a + b\right)\left(b + d\right) \tag{4.28}$$

$$\Delta T = \left(\frac{P_i}{SA}\right)^{0.909} \tag{4.29}$$

where the 0.909 exponent is an empirical number related to the surface emissivity and may vary between 0.833 for amorphous material [72] and 0.909 for ferrite [88].

The cold-plate cooling relies on conductive heat transfer as shown in Figure 4.4 *(a)*. The heat path for the core and winding are assumed to be separate. The 2D heat transfer problem can be simplified by reduction to a 1D model. For simplicity, the core is assumed to be placed on the cold-plate such that the cold-plate makes contact with both sides of the core as shown in Figure 4.4 *(b)*. The heat generated in the core, P_c, is removed along the core, l_c, with heat transfer surface, A_{hc}, and thermal conductivity, λ_c. The power loss generated in the core due to fringing flux, P_g, may be included if applicable and added as heat flowing through the core from the air-gap to the cold-plate. The core temperature rise is given as follows:

$$\Delta T = \frac{P_c \cdot l_c}{2 \cdot \lambda_c \cdot A_{hc}} + \frac{P_g \cdot l_c}{\lambda_c \cdot A_{hc}} \tag{4.30}$$

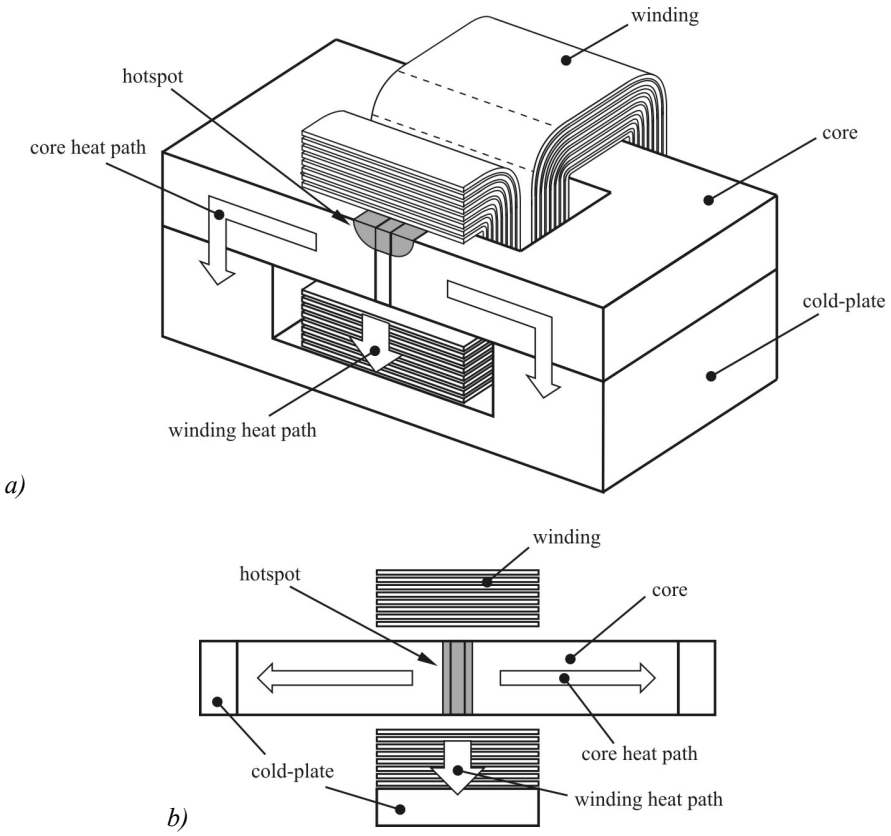

Figure 4.4. Inductor section mounted on the cold-plate: *(a)* heat flow and *(b)* simplified 1D cooling model.

The winding is modelled as an equivalent straight bar with a length equal to the average heat path, l_{eqCu}, from the winding hotspot to the cold-plate as shown in Figure 4.5. The copper has a thermal conductivity, λ_{Cu}. The total power loss generated in the copper, P_{Cu}, is transferred through the insulation layer, with thermal conductivity, $\lambda_{i,}$ between the winding and the cold-plate resulting in the following temperature rise:

$$\Delta T_{Cu} = \frac{P_{Cu} \cdot l_{eqCu}}{2 \cdot \lambda_{Cu} \cdot A_{Cu}} + \frac{P_{Cu} \cdot l_i}{\lambda_i \cdot A_{Cu}} \tag{4.31}$$

Block (J) closes the first design loop in order to achieve the design constraints. The iteration area product is stored in (K) indexed with the second loop iteration number. The second loop, (L), iterates the turns by adding the extra turns to the design in order to decrease the flux swing. Once the absolute minimum is achieved, the algorithm ends.

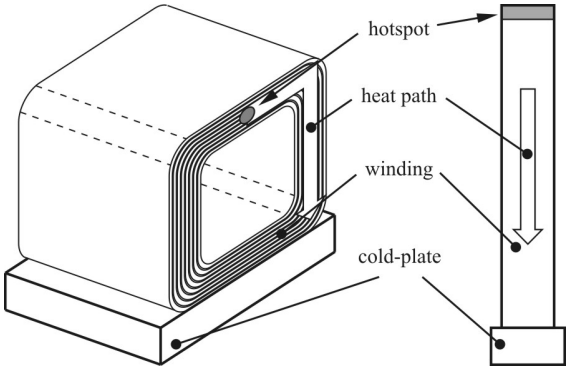

Figure 4.5. Winding cooling patch and its 1D equivalent model.

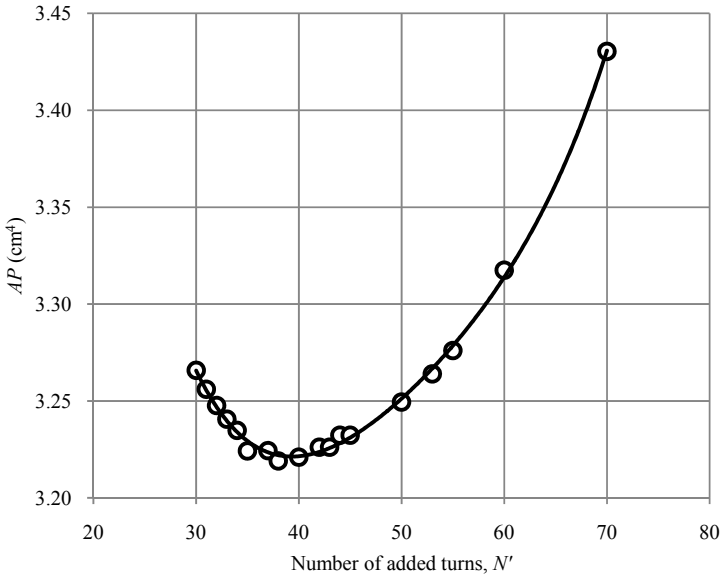

Figure 4.6. Local area product minima (1 kW 10JNHF600 design at 50 kHz).

The local minima may occur in power-limited designs as shown in Figure 4.6 for a 1 kW silicon-steel 10JNHF600 design. The following constraints are applied: natural convection-cooled with a maximum temperature rise of 80 K, core window ratio $0.5 \le r_w \le 3$, core profile ratio $0.5 \le r_c \le 2$, maximum air gap $l_g \le 3\,\mathrm{mm}$. The boost converter has a 200/400 V boost ratio at 1 kW power and 50 kHz switching frequency. The required inductance is 1 mH. Foil winding is applied with 0.1 mm interlayer insulation and 2.4 mm is assumed between the coils. The foil is assumed to be a single sided insulator, thus creepage distance is 4 mm for each side.

4.1.2. Gapless Inductor Design Flowchart

The gapless algorithm shares most of the modules with the gapped algorithm. The electric circuit inputs in block (A) are the same. The material characteristics (B) include the magnetizing B-H curve and the dc-bias μ-H curve is defined as follows:

$$B(H) = \frac{H}{a_B H^2 + b_B H + c_B} \tag{4.32}$$

$$\mu_r(H) = \sqrt{\frac{\mu_{ir}^2 + a_\mu \mu_{ir}^3 H + b_\mu \mu_{ir}^4 H^2}{1 + c_\mu \mu_{ir} H + d_\mu \mu_{ir}^2 H^2}} \tag{4.33}$$

The inductors geometry (C) is defined in the same way in both algorithms. The block (D) in the gapless algorithm is very different from the gapped algorithm. In the gapped algorithm the air-gap length is adjusted to the number of turns at μ = constant, while the gapless algorithm is adjusting the number of turns to the dc-bias curve. The turns calculation is an iterative process as the core's permeability, $\mu_r(H)$, depends on the magnetizing force related to the number of turns, N, the operating current, I_{in}, and the magnetic flux mean path length, l_c. The core flux bias, B_0, is calculated from the B-H curve. The peak-to-peak flux density, ΔB_{pp}, and its magnitude, B_{ac}, are found and the minimum and maximum flux density, B_{min} and B_{max}, are calculated respectively. The respective magnetizing force swing is found from the B-H curve.

$$N = \sqrt{\frac{L l_c}{A_{ceff} \mu_0 \mu_r}}, \quad H = \frac{I_{in} N}{l_c}, \quad \Delta B_{pp} = \frac{V_{in} D}{N A_{ceff} f} \tag{4.34}$$

$$B_{ac} = 0.5 \Delta B_{pp}, \quad B_{\min} = B_0 - B_{ac}, \quad B_{\max} = B_0 + B_{ac} \tag{4.35}$$

$$H_{\min/\max} = \frac{-b_B - B_{\min/\max}^{-1} - \sqrt{\left(b_B - B_{\min/\max}^{-1}\right)^2 - 4 a_B c_B}}{2 a_B} \tag{4.36}$$

The core power loss due to the air-gap does not apply in (E). Winding geometry (F) and power loss (G) are calculated as in the gapped algorithm. The inductor properties (H) are developed similarly to the gapped algorithm; however, without the air-gap and core gap loss. The thermal calculations in (I) are carried out in the same way as in the gapped algorithm. Block (J) closes the design loop in order to achieve the design constraints. Finally, in (K) the result is displayed and the algorithm ends.

Note that the gapless algorithm involves a lower number of the optimization steps than the gapped algorithm due to the absence of the air gap.

4.2. Area-Product Analysis

The area-product algorithm is a powerful tool for fast prototyping and design comparison analysis. It allows for solution of a wide range of the design aspects. In this section, an inductor size variation is investigated as a function of frequency, current ripple and efficiency for two cooling methods.

In general, the inductor design can be saturation or power loss limited, where the power loss limit is due to temperature rise or efficiency. The most optimum use of the material is achieved when all three constraints are meeting their limits, resulting in the smallest design.

Firstly, the efficiency-limited inductor minimum size is investigated as a function of the current ripple and frequency for convection- and conduction-cooled designs. Secondly, the variation of inductor size with efficiency is investigated. Finally, the performance factor curves generated in Chapter 3 are compared with the area-product analysis.

The procedures developed in the previous section are used to analyse inductors for 1 and 10 kW boost converters. The following materials presented in Table 3.1 are investigated: 2605SA1, 10JNHF600, Vitroperm 500F, 3C93. Graphs for powder materials MPP 60, High Flux 60, KoolMu 60 and Xflux 60 are provided in Appendix C.

All designs presented and compared in this chapter share the same input data. Operating frequency is increased from 20 to 150 kHz in the following steps: 20, 50, 100 and 150 kHz. The following are the electrical specifications for the boost converter: input voltage, V_{in} = 200 V, output voltage, V_{out} = 400 V. The ambient or cold-plate temperature is set at 70 °C. The maximum temperature rise allowed for each material is dependent on the continuous operating temperature of the material, as shown in Table 3.1. For example, the maximum operating temperature of amorphous material is 150 °C and so the maximum temperature rise is 80 °C. A CC core is assumed. The core profile ratio, r_c, is allowed to change in the range between 0.5 and 2. The core window ratio, r_w, is allowed to vary between 0.5 and 2. The air gap is limited to 3 mm per leg and 25 % saturation flux de-rating factor is applied for all gapped materials. The permeability of the powder materials is allowed to decrease down to 50 % of its initial value, but typically it settles at an effective permeability roll-off of about 30 %. The winding interlayer insulation is assumed to be 0.1 mm and the distance between the core and winding tips is set to 4 mm, while the distance between windings is 2.4 mm.

The area product is a popular figure of merit [72][81][83][87][89]. Despite being very indicative, the area product is not an exhaustive comparison tool. Since the area product algorithm has a 4-dimensional freedom in the CC core geometry there may be different area product results for the mass and volume optimized designs. The area product does not necessary results in component minimum mass or volume; however, it is closely related to them.

4.2.1. Current-Ripple Analysis

The area product vs. current ripple analysis for gapped amorphous metal 2605SA1 is presented in Figure 4.7 and Figure 4.8 for 1 kW and 10 kW inductor designs, respectively. The curves are for gapped materials 10JNHF600, Vitroperm 500F, and 3C93; and for gapless materials: MPP 60, High Flux 60, KoolMu 60 and Xflux 60 are presented in Appendix C.1 and C.2 for 1 kW and 10 kW, respectively.

The 1 kW area-product curves are presented in Figure 4.7 *(a)* and *(b)* for natural convection-cooling and conduction-cooling, respectively, for gapped amorphous metal 2605SA1 based inductor design. There is a minimum inductor area product for a particular frequency. The product minima occur at lower current ripple with increased frequency. This is because the power loss generated in the material grows rapidly as the frequency increases, but the inductance and the number of turns are reduced. The area-product minimum is the balancing point between the saturation flux density limited design and inductor total power loss limited design. The efficiency constraint limits the total allowable power loss of the component, and thus limits the inductor minimization potential.

Since the design is efficiency limited the 1 kW conduction-cooled inductor size is similar to natural-convection cooled as shown in Figure 4.7 *(a)* and *(b)*. The power loss generated in the efficiency limited inductor is small enough that the convection-cooled design allows for an efficient heat removal without exceeding the maximum temperature. This may be especially applicable for an inductor based on less efficient magnetic material, whose size is predominantly power loss limited due to efficiency rather than temperature rise or saturation flux density.

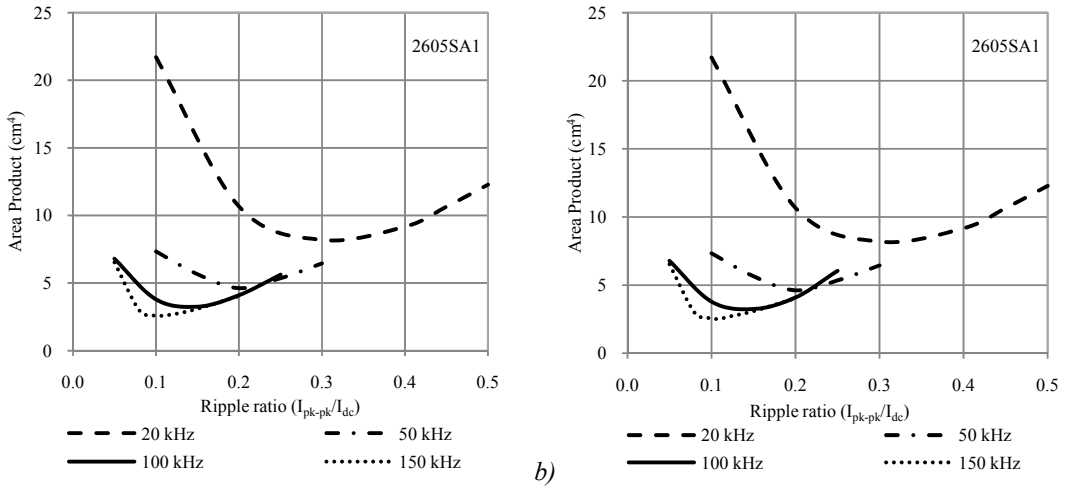

Figure 4.7. *AP* vs. current ripple with frequency as a parameter (1 kW) for gapped amorphous metal design: *(a)* natural convection cooling, *(b)* cold-plate conduction cooling.

The various magnetic materials area product vs. current-ripple curves for a 1 kW inductor design are shown in Appendix C.1 and C.2. Most of the 1 kW designs are power loss limited due to the efficiency restriction, and so the area products for convection-cooled and conduction-cooled inductors are similar, but not the same. The nanocrystalline and ferrite materials are different as they are temperature- rise limited for the convection-cooled design and efficiency limited while conduction-cooled.

The 2605SA1 10 kW inductor area product vs. current-ripple curves for convection-cooling and conduction-cooling are shown in Figure 4.8 *(a)* and *(b)*, respectively. The dc-current is ten-times higher than for 1 kW inductor and this is reflected in the inductor size. Note, that the relative current-ripple ratio results in a significantly higher peak-to-peak current in 10 kW design than in 1 kW, but the flux density amplitude and dc bias are similar for both designs.

The 10 kW inductor produces significant power loss and the convection-cooled design is temperature-rise limited while the conduction-cooling allows the design to be efficiency limited; allowing the size to be significantly reduced.

In general, the design tends to be saturation limited for low ripple ratios, and then reach the minimum size where the size becomes power-loss limited due to maximum temperature rise or efficiency restriction.

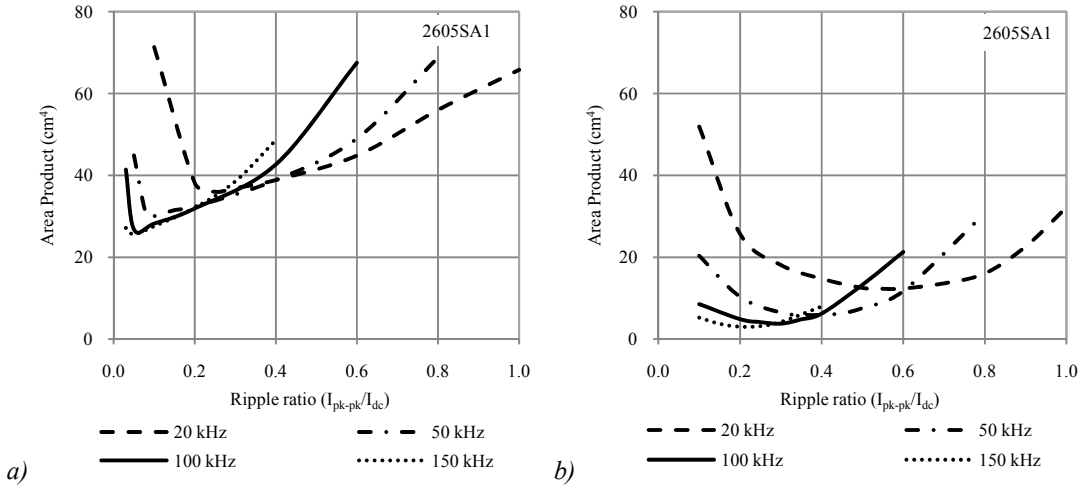

Figure 4.8. *AP* vs. current ripple with frequency as a parameter (10 kW) for gapped amorphous metal design: *(a)* natural convection cooling, *(b)* cold-plate conduction cooling.

Note that the convection-cooling and conduction-cooling approaches are very different. The convection-cooled component tends to achieve the best cooling surface, while the conduction-cooled design is optimized for the shortest cooling path. Due to this fact, the component area product may vary significantly for the same design constraints.

4.2.2. Efficiency and Inductor Size

In this section, the variation of the inductor size with the frequency, current ripple and efficiency is investigated. The analysis is carried for the 10 kW gapped amorphous metal 2605SA1 based inductor at 20 kHz and the circuit constraints are the same as in the previous section. Firstly, the variation of inductor size with current ripple is plotted vs. efficiency for a conduction-cooled amorphous metal inductor is presented. Secondly, The inductor size is analysed for a 99 % efficiency limitation and for minimum size without an efficiency limitation.

As shown in Section 4.2.1 the inductor size is related to the current ripple for given frequency. Intuitively, the inductor size is likely to increase for improved efficiency. Plots of inductor size vs. efficiency for 20 %, 60 %, and 100 % current ripple are shown in Figure 4.9 *(a)* and *(b)* and *(c),* respectively. These corresponds to the saturation limited, size optimized and power loss limited designs as can be traced in Figure 4.8 *(b).* The size increases together with efficiency and the most dramatic size increase is accounted for a power-loss limited inductor, as is the case for the 100 % current ripple.

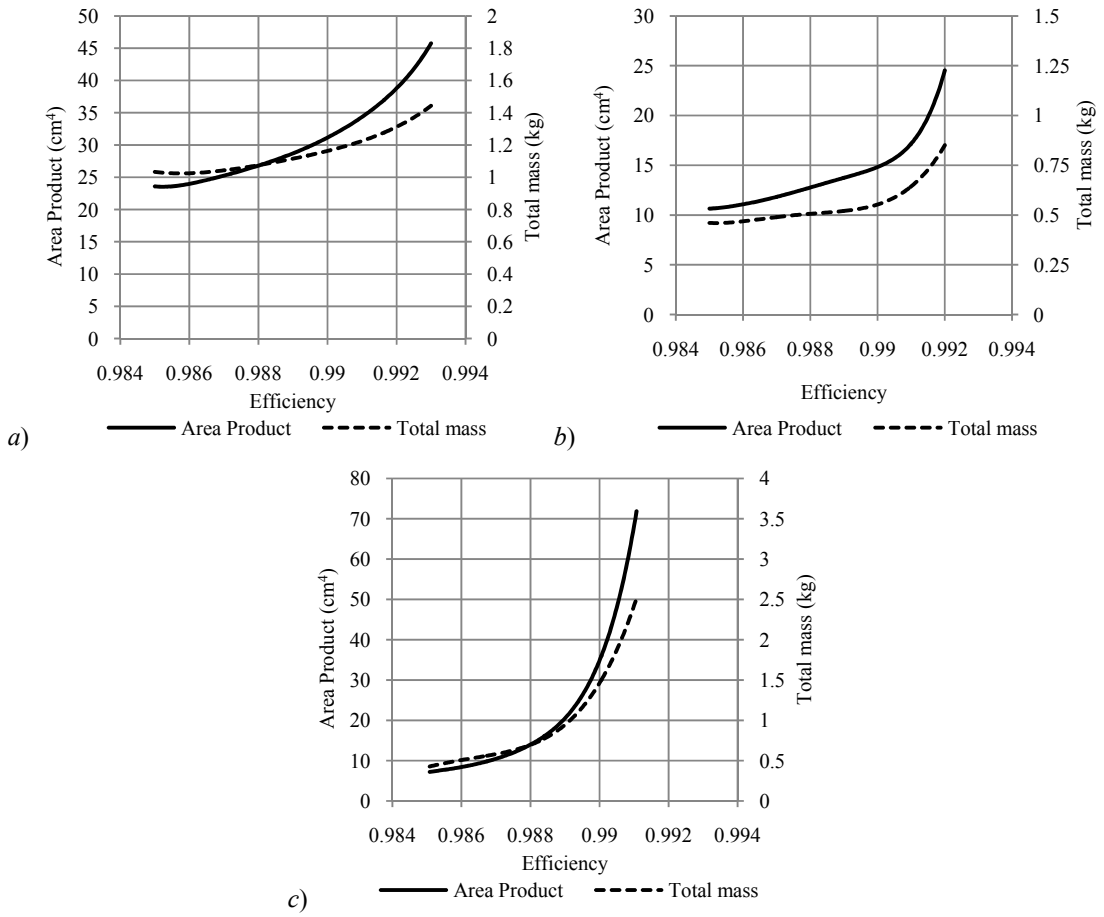

Figure 4.9. Area Product vs. inductor efficiency for *(a)* 20 % and *(b)* 60 % and *(c)* 100 % current ripple. Gapped, amorphous metal (2605SA1) based inductor.

Next, a 100 μH inductor is used for size comparison for a 99 % efficiency limit and for minimum size without an efficiency limit. The analysis is carried for the 10 kW inductor across frequency range from 20 kHz to 150 kHz.

Since inductance is constant, the current ripple decreases as frequency increases with current-ripple ratios of 1 at 20 kHz, 0.4 at 50 kHz, 0.2 at 100 kHz and 0.13 at 150 kHz. The low current ripple at the high frequency is beneficial for the design as the windings skin and proximity effects may become a serious power loss contributor.

The convection- and conduction-cooled inductor area product with and the without efficiency restriction is presented in Figure 4.10 and Figure 4.11, respectively, and also in Table C.5 in Appendix C.4. Additional figures for gapless materials are shown in the Appendix C.4.

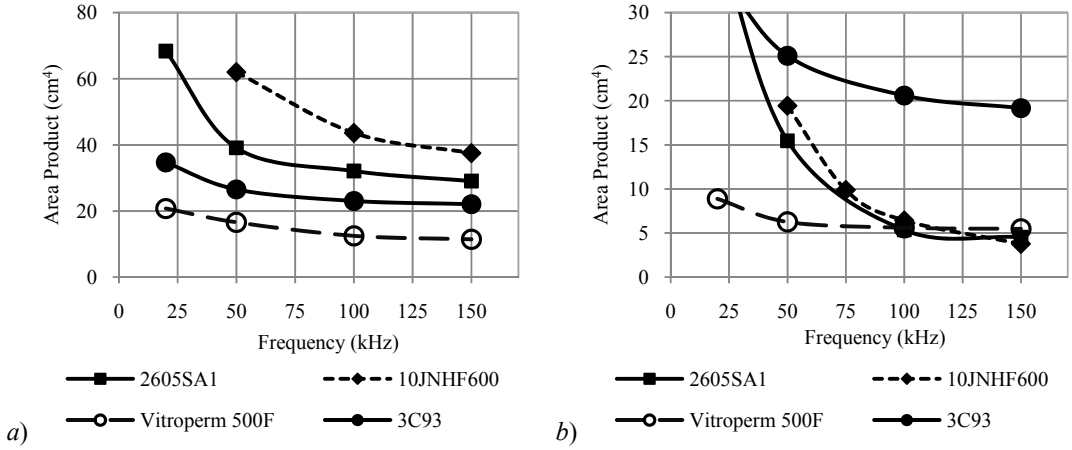

Figure 4.10. *AP* vs. frequency for a 100 μH gapped inductor (10 kW, 99% efficient): *(a)* convection-cooling and *(b)* conduction-cooling.

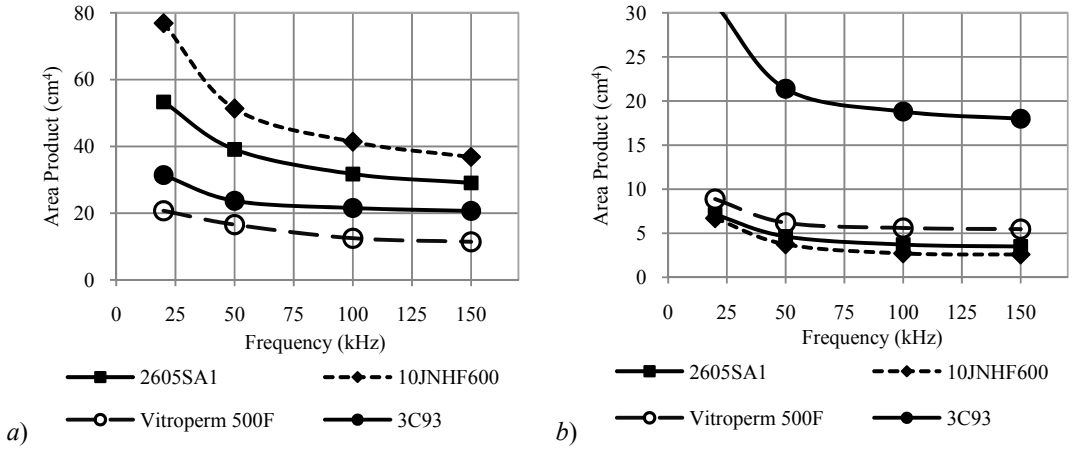

Figure 4.11. *AP* vs. frequency for a 100 μH gapped inductor (10 kW, no efficiency restriction): *(a)* convection-cooling and *(b)* conduction-cooling.

The analysis shows that the high power-loss materials, such as silicon steel, are very large with an efficiency limit for convection cooling, while the low power-loss materials allow for minimum size. Nanocrystalline material is the smallest for a convection-cooled inductor while ferrite appears to be a close second, at a fraction of the cost. The high thermally conductive materials have a more optimised heat transfer path for conduction cooling and so the high-saturation lossy materials can be significantly reduced in size with conduction cooling.

4.2.3. Area Product Curves

In this section, area-product curves are generated to contrast and compare the materials and to show the optimum material for a particular design.

Area product vs. current ripple curves presented in Section 4.2.1 are rearranged and shown in Figure 4.12 and Figure 4.13 for convection- and conduction-cooled 10 kW inductor designs with 99% efficiency, respectively. The principal materials of interest are shown.

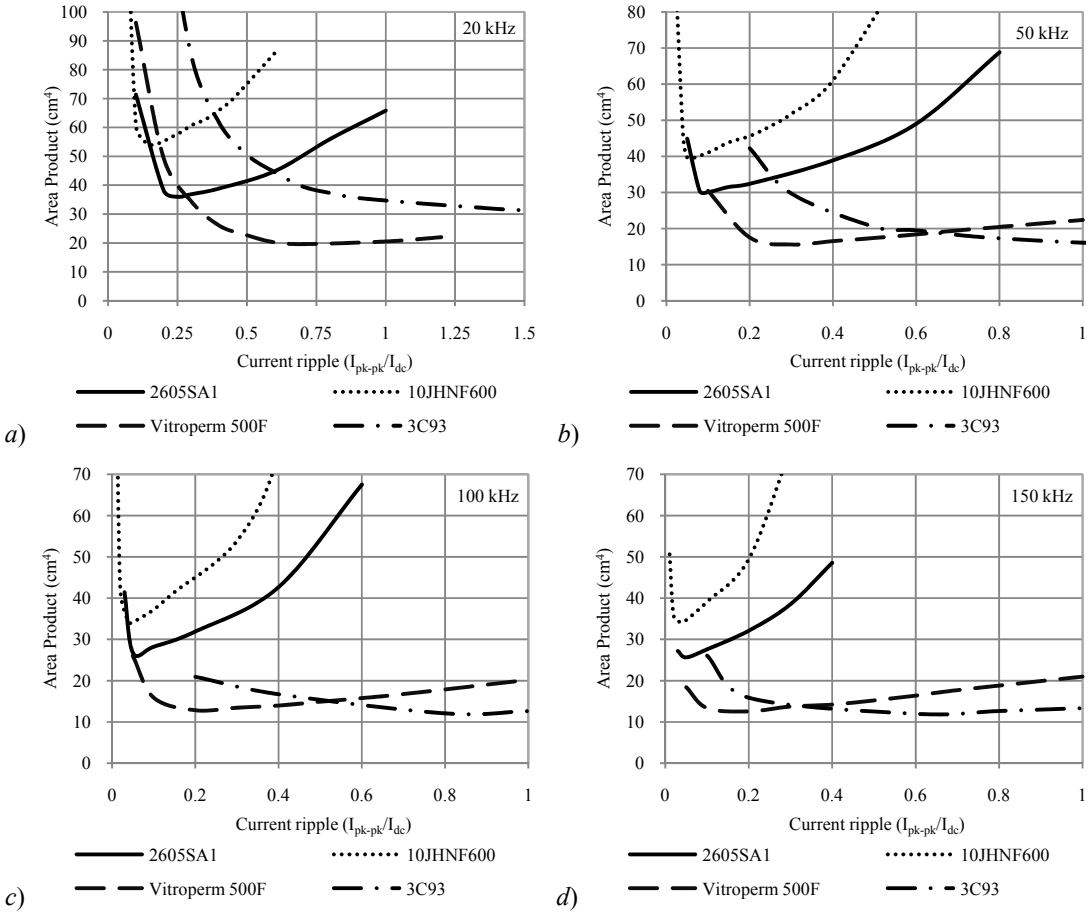

Figure 4.12. Convection-cooled Area Product vs. current ripple for frequency parameter (10 kW, 99% eff.): *(a)* 20 kHz and *(b)* 50 kHz and *(c)* 100 kHz and *(d)* 150 kHz.

Generally, for the convection-cooled designs, amorphous metal is very competitive with nanocrystalline for low ripple ratios while ferrite tends to be very competitive at high ripple ratios. These results tend to correlate with the performance factors for ac and ac+dc materials in Chapter 3.

The curves for the conduction-cooled devices tend to show the high-B_{sat} lossy materials being competitive with nanocrystalline for low frequency and low-to-medium frequency due to their high thermal conductivity. Ferrite is generally uncompetitive except at higher ripple and higher frequencies. These results are also as generally predicted by the performance factors in Chapter 3.

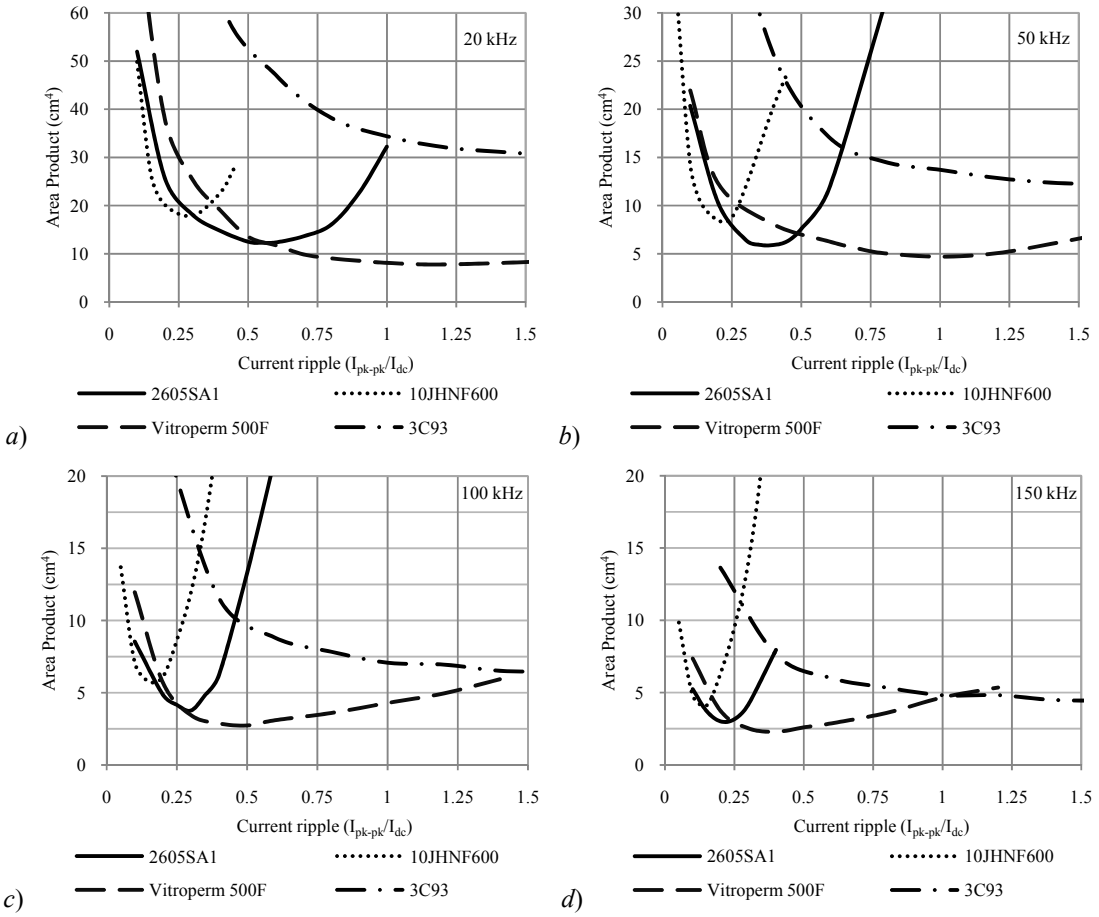

Figure 4.13. Conduction-cooled Area Product vs. current ripple for frequency parameter (10 kW, 99% eff.): *a*) 20 kHz and *b*) 50 kHz and *c*) 100 kHz and *d*) 150 kHz.

While the area-product curves generally relate to the performance factor curves, the performance factor curves are inherently limited with respect to the area product curves. The performance factors do not factor in core geometry and current ripple and the possibly significant difference in operating conditions between the materials for a particular design. The core loss densities and peak flux densities are shown in Figure 4.14 *(a)* and (*b*) for the 20 kHz,

conduction-cooled curves shown in Figure 4.13 *(a)*. As can be seen, these are widely varying and such information cannot easily be factored into the performance curves.

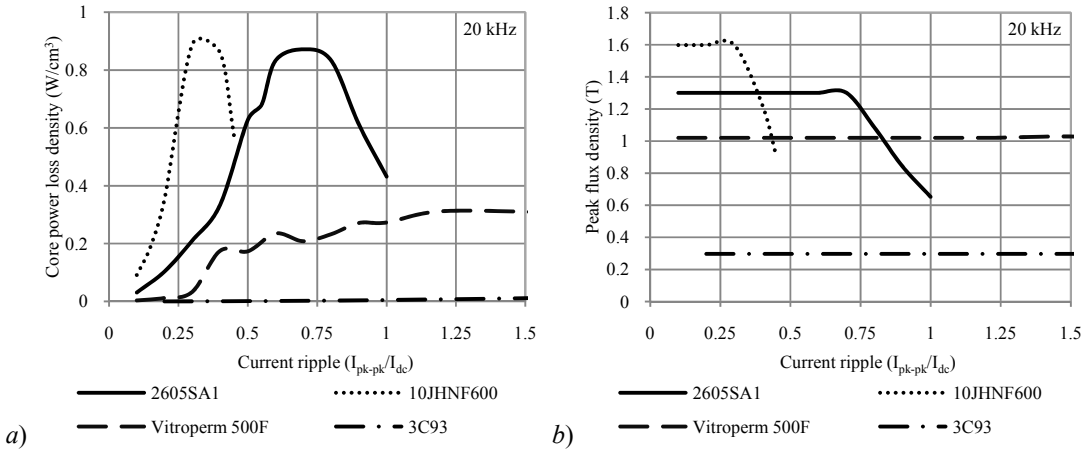

Figure 4.14. Conduction-cooled 10 kW, 99% efficient inductor design at 20 kHz: *(a)* core power loss density vs. current ripple *(b)* and peak flux density vs. current ripple.

4.3. Summary

In this chapter a novel approach to the widely-known problem of an inductor design is presented. The inductor design is considered as a multivariable function in the purpose developed algorithm for convection- and conduction-cooled setup. The modular structure allows for rapid prototyping of any inductor with a given constraints set.

The analysis indicates that the right choice of the magnetic material results in the most optimum design size. The design constraints of operating frequency, current ripple, dc-bias, cooling method, maximum temperature rise, and efficiency impact the design size and material selection. In general, the inductor size decreases as frequency increases in the considered frequency range. The optimum current ripple decreases as frequency increase for a minimum area product analysis. This means that the component size decreases with frequency and the current ripple decreases as well. Thus, the converter input and output capacitance requirement will drop and as a result further converter size reduction may occur. Since the minimum size at a given frequency is unique property of the material with respect to the current ripple the most suitable material can be selected for the anticipated current ripple ratio.

Chapter 5

Experimental Comparison of High-Flux Magnetic Materials

The high-flux magnetic material is a critical component of a high-power dc-inductor. In this chapter, well-established high-flux magnetic materials such as Fe-based amorphous metal and 6.5% silicon steel are compared and contrasted with Fe-based powder core and a JFE silicon-steel prototype core.

The practical effects of frequency, dc-bias and duty cycle on core power loss, air-gap fringing on the core and winding losses, and the core conduction cooling are experimentally investigated for the Fe-amorphous metal, 6.5% silicon steel and powder core.

For the various materials, variation of core loss with frequency is approximately as predicted by the specifications and the algorithm developed in Chapter 4. The multi-cut core displays elevated power loss due to manufacturing.

All materials can experience increased core losses with dc bias and appropriate de-rating should be used when operating high on the magnetization curve. The investigation suggests de-rating at about 75 % of the nominal saturation flux density at 25 °C. Similarly, asymmetric duty cycles result in increased core losses. The modified Steinmetz equations are useful predictors of these increased losses.

It has been suggested in the literature [89][98] that increased core loss can occur due to air gap fringing. Testing in this study suggests that these effects can be insignificant for these cores with thin laminations and high resistivity. Distributing the air gap is shown to result in reduced copper losses, but added cuts can result in material degradation for amorphous metal.

Finally, it is demonstrated that lamination direction is key to the optimum thermal cooling path for the laminated gapped cores.

5.1. Experimental Setup

The inductors were tested in a boost converter. Two converter variants were used. A hard-switched 2.5 kW converter is used from low (15 kHz) to medium (30 kHz) frequency range and is shown in Figure 5.1. A soft-switched 1.25 kW converter, developed in Chapter 2, is used to test in the medium (50 kHz) to high (150 kHz) frequency range. Comprehensive experimental data are provided in Appendix D.

Figure 5.2 shows the various magnetic cores. The single-cut amorphous metal inductor is composed of two C-core halves. The silicon steel (both 10JNHF600 and JFE prototype) and the powder core inductors use block cores. The amorphous metal and silicon-steel cores are cut by the manufacturers to the desired shape. The powder core is build of the off-shelf blocks.

The core characteristic dimensions are shown in Figure 5.3 and presented in Table 5.1. The multi-cut amorphous metal core and silicon steel 10JNHF600 core '*I*' have the same dimensions and the core cross-sectional area is about 30 % larger than the single-cut amorphous core and the silicon steel 10JNHF600 '*II*' and JFE prototype. The Mega Flux core is composed of 4 blocks and its core cross-sectional area is about 20 % larger than the single-cut amorphous metal core.

The inductor hotspot temperatures are measured for the core and winding with J-type thermocouples. The Teflon barier was used to isolate core and winding thermal paths. The core temperature was measured in the middle of leg under the winding. The winding temperature was measured on the winding in the core window between the windings.

The converter was placed in the thermally isolated chamber in order to reduce influence from the ambient. The chamber is in form of metal box with walls cushioned with styrofoam.

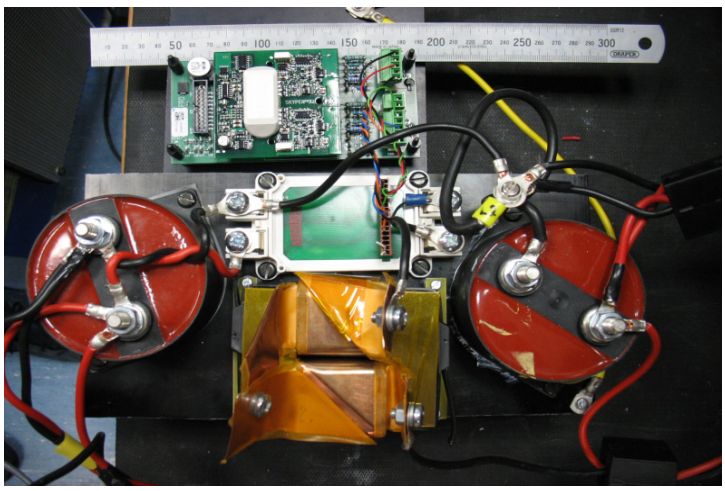

Figure 5.1. Hard switched dc-dc converter setup.

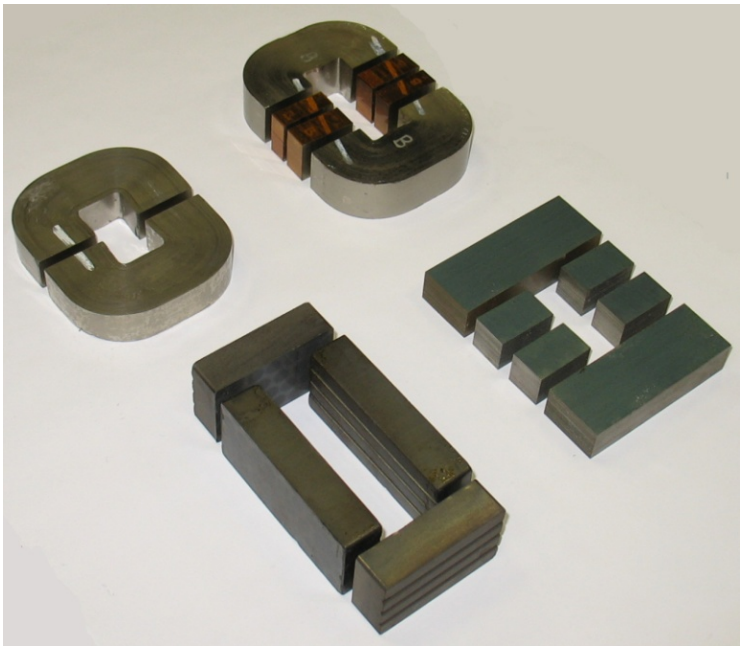

Figure 5.2. Single-cut Fe-based amorphous (left), multi-cut Fe-based amorphous (top), 6.5% Si-steel (right) and Fe-based powder core (bottom).

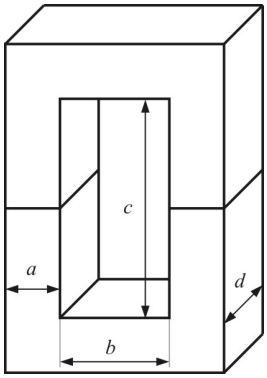

Figure 5.3. Drawing of core dimensions.

Table 5.1. List of experimental cores

Dimensions		2605SA1	2605SA1	10JNHF600		JFE Core	Mega Flux 60
		single cut	multi cut	I	II		
a	mm	25	25	25	25	25	15
b	mm	18	20	20	18	18	20
c	mm	28	37	37	28	28	70
d	mm	15	20	20	15	15	30
mass	g	459	698	732	482	482	756
volume	cm^3	64	97	97	64	64	111

5.2. Frequency Effect Analysis

The following sections show the effect of frequency on the inductor power loss. The results presented are in good agreement with the calculations based on the algorithm presented in Chapter 4. The power losses of the constant-inductance inductor for four high flux materials are compared for a range of flux densities and frequencies.

Since hard- and soft-switched boost converters are employed the results are divided into two sections: low (15 kHz) to medium (30 kHz) frequency range; and medium (50 kHz) to high (150 kHz) frequency range.

The various inductors shown in Table 5.2 were built and tested in order to validate the material losses. The inductors were tested under similar conditions with similar flux density amplitude and dc bias in the experimental hard-switched boost converter set up. Although of different sizes, the inductors were examined with a constant inductance and varied frequency. Natural convection cooling was used and each test was run until the inductor reached a steady state temperature.

Table 5.2. Investigated inductors details

Item	Inductor 1	Inductor 2	Inductor 3	Inductor 4	Inductor 5	Inductor 6
Experimental test	Low to medium frequency	Low to medium frequency	Low to medium frequency	Medium to high frequency	Medium to high frequency	Medium to high frequency
Material	2605SA1	10JNHF600	Mega Flux 60	2605SA1	10JNHF600	JFE Prototype
Core type	single cut CC	block core	block core	single cut CC	block core	block core
Window area (mm^2)	504	720	1400	504	504	504
Effective cross section area (mm^2)	311	460	450	311	460	450
Mean magnetic path length (mm)	170	212	227	170	170	170
Winding	Copper foil 0.6 x 22 mm	Copper foil 0.3 x 32 mm	Litz wire 4x5x5x0.3mm	Copper foil 0.6 x 22 mm	Copper foil 0.6 x 22 mm	Copper foil 0.6 x 22 mm
No of turns	16	22	28	16	16	16
Air gap per leg	2 mm	1 mm	0	1 mm	1 mm	1 mm
Inductance (μH)	55	125	125	90	70	66
Input/output voltage	65 V/130 V	125 V/250 V	125 V/250 V	125 V/250 V	125 V/250 V	125 V/250 V
Inductor avg. current (A)	20	20	20	10	10	10

5.2.1. Low to Medium Frequency

Three magnetic materials are compared in the low-to-medium frequency experiment: amorphous metal 2605SA1, silicon steel 10JNHF600 and powder core Mega Flux 60 summarized in Table 5.2 as Inductor 1, Inductor 2, and Inductor 3, respectively. The inductor cores are of different geometry due to availability and their details are provided in Table 5.1. In this test, the inductors are examined with a constant inductance and varied frequency from 15 kHz to 30 kHz in steps of 5 kHz.

Figure 5.4 and Table 5.3 shows the theoretical and experimental core temperature rises above ambient for the iron-based amorphous metal, silicon-steel and powder core inductors. As expected, the measured and theoretical temperature rises of the cores decrease with increasing frequency. The theoretical predictions are generated by the algorithm developed in Chapter 4. Since the same inductor is used across the frequency range (15-30 kHz), the flux density amplitude decreases as frequency increases, and the peak ac flux density and resulting core power loss decrease with frequency.

The experimental results are in good agreement with the theoretical predictions, which over estimates the temperature rise by up to 15 %. The amorphous metal and silicon steel inductors are operating with the same flux density amplitude while the Mega Flux 60 inductor operates with about 80 % of the flux density amplitude of the other two inductors. The detailed experimental results are presented in Appendix D, Table D.1.

As predicted, the silicon steel core temperature rise is twice that of amorphous metal for the same excitation. The powdered core has comparable temperatures to the silicon steel but is running at lower flux than the silicon steel. As predicted, the silicon steel core has a temperature rises twice that of amorphous metal for the same excitation. The powdered core has comparable temperatures to the silicon steel but is running at lower flux than the silicon steel. As noted earlier, as the frequency increases, decreasing the flux level, the powder core loss reduces significantly.

During the experimental testing, a multi-cut amorphous metal core showed excessive power loss. This anomaly is consistent for this core and it is a side effect of the cutting process as the core laminations become shorted at the cutting surfaces. The anticipated and measured temperature rise is shown in Figure 5.5 and in Table 5.4. The power loss generated in the core is provided in Table 5.4. The multi-cut core power loss is twice that expected. This issue is known and documented in [100], where it is pointed out that manufacturing may degrade the amorphous material core loss by 68 %. The complementary experimental data are presented in Appendix D, Table D.2.

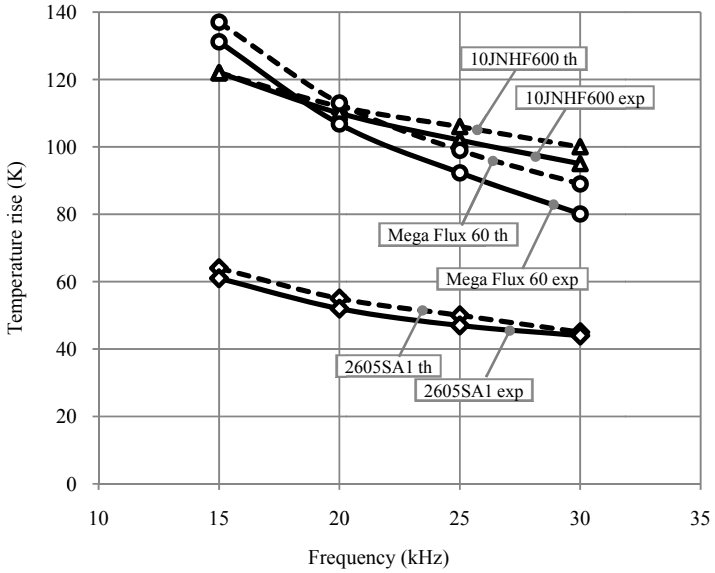

Figure 5.4. Inductor temperature rise vs. low to medium frequency range for constant inductance.

Table 5.3. Losses and temperature rise for constant inductance in low to medium frequency range

Material	f (kHz)	P_{core} (W)	P_{Cu} (W)	P_{tot} (W)	ΔT_{th} (K)	ΔT_{exp} (K)
2605SA1	15	12.1	10.2	22.3	64	61
2605SA1	20	10.7	8	18.7	55	52
2605SA1	25	10	6.7	16.7	50	47
2605SA1	30	10.3	5.3	15.6	45	44
10JNHF600	15	42	8.1	50.1	122	122
10JNHF600	20	40	7.2	47.2	112	110
10JNHF600	25	39	6.5	45.5	106	102
10JNHF600	30	38	5.7	43.7	100	95
Mega Flux 60	15	40	16	56	137	131
Mega Flux 60	20	31	11.5	42.5	113	107
Mega Flux 60	25	25.5	10	35.5	99	92
Mega Flux 60	30	22	8.5	30.5	89	80

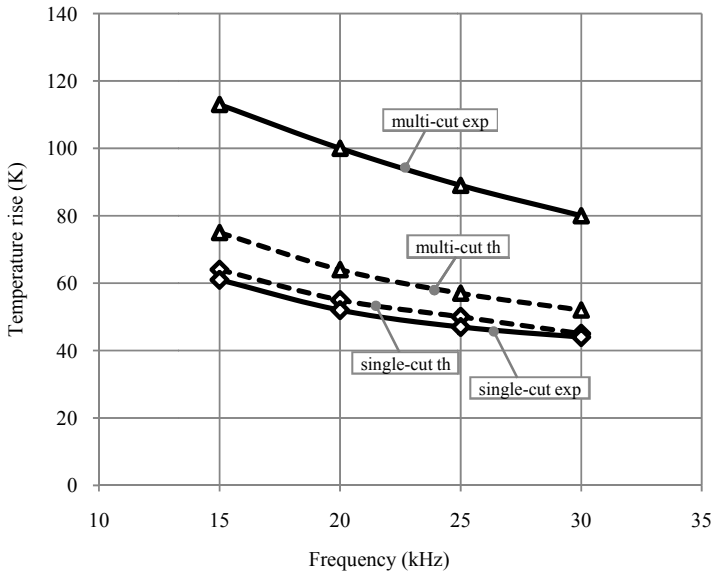

Figure 5.5. Multi-cut amorphous metal-based inductor temperature rise anomalies in low to medium frequency range for constant inductance.

Table 5.4. Losses and temperature rise for constant inductance in low to medium frequency range for single- and multi-cut amorphous metal-based inductors

Material	f (kHz)	$P_{core\ th}$ (W)	$P_{core\ exp}$ (W)	P_{Cu} (W)	ΔT_{th} (K)	ΔT_{exp} (K)
2605SA1 single-cut	15	13.4	12.1	10.2	64	61
2605SA1 single-cut	20	11.9	10.7	8	55	52
2605SA1 single-cut	25	11.2	10	6.7	50	47
2605SA1 single-cut	30	10.6	10.3	5.3	45	44
2605SA1 multi-cut	15	22.8	42.4	11.7	75	113
2605SA1 multi-cut	20	19.5	37.8	9.5	64	100
2605SA1 multi-cut	25	17.3	33.5	8.2	57	89
2605SA1 multi-cut	30	16.2	30.0	6.8	52	80

5.2.2. Medium to High Frequency

Three almost identical inductors were built to compare the JFE prototype silicon steel core with single-cut 2605SA1 amorphous metal and 10JNHF600 silicon steel core 'II' specified in Table 5.1 and in Table 5.2 as Inductor 4 to 6, respectively. The inductors are tested in the soft-switched half-bridge boost converter introduced in Chapter 2. The temperature rise, in the natural convection cooled system, is observed for three frequency points: 50 kHz, 100 kHz and 150 kHz. The experimental results are shown in Figure 5.6 and Table 5.5 and corresponding complete experimental data points are shown in Appendix D, Table D.3.

As expected, the estimated and experimental temperature rise of the core decrease with increasing frequency. The silicon steel 10JNHF600 shows 55 to 79 % higher power loss than the single-cut amorphous metal while the JFE prototype core losses are 24 to 43 % higher than single cut amorphous metal. The JFE prototype is built of thinner laminations than 10JNHF600 which result in a lower eddy current loss in the material. In general, the experimental results show a consistent power loss relation between the magnetic materials across the low to high frequency range.

The multi-cut core, shown in Figure 5.7, displays a similar discrepancy with the theoretical predictions as for the lower frequency range as shown in Figure 5.4. The multi-cut core uses 22 turns winding with 0.3 mm foil of 32 mm width. The single-cut amorphous metal inductor is built with 16 turns winding. The corresponding data points and power loss breakdown for Figure 5.7 are shown in Table 5.6.

It is remarkable that the multi-cut core temperature rise discrepancy decreases as the frequency increases. The reduced flux density amplitude results in lower eddy currents in the shorted core cutting surfaces. The multi-cut core power loss is 20 to 60 % higher than theoretical predictions.

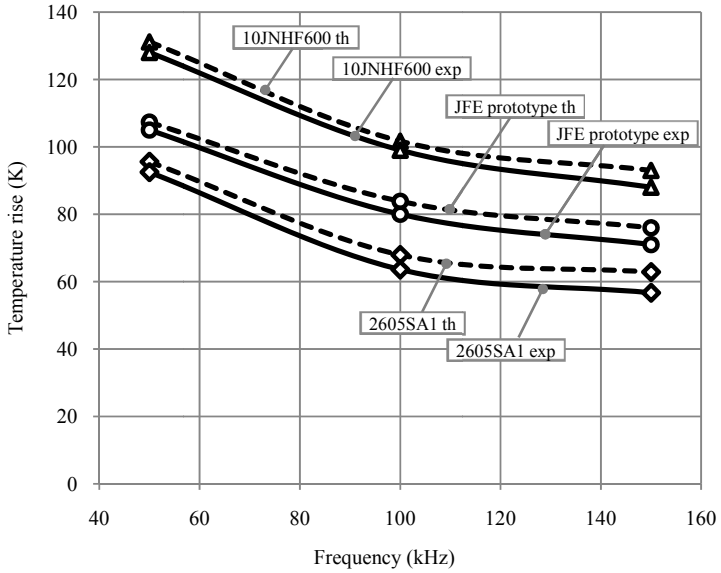

Figure 5.6. Inductor temperature rise vs. medium to high frequency range for constant inductance.

Table 5.5. Losses and temperature rise for constant inductance in medium to high frequency range

Material	f (kHz)	P_{core} (W)	P_{Cu} (W)	P_{tot} (W)	ΔT_{th} (K)	ΔT_{exp} (K)
2605SA1	50	28.7	0.59	29.3	96	93
2605SA1	100	24.9	0.36	25.2	68	64
2605SA1	150	22.8	0.33	23.2	63	57
10JNHF600	50	51.5	0.73	52.2	131	128
10JNHF600	100	39.0	0.46	39.5	102	99
10JNHF600	150	35.4	0.41	35.8	93	88
JFE prototype	50	41.2	0.77	42.0	107	105
JFE prototype	100	31.2	0.41	31.6	84	80
JFE prototype	150	28.3	0.35	28.7	76	71

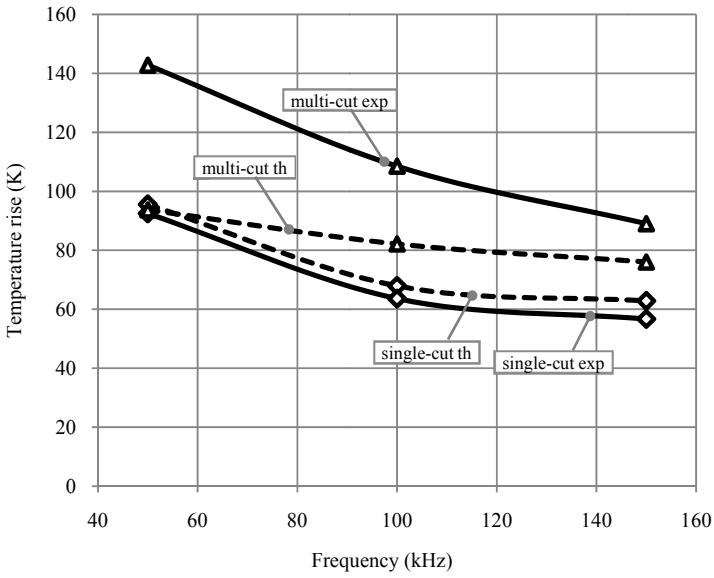

Figure 5.7. Multi-cut amorphous metal-based inductor temperature rise anomalies in medium to high frequency range for constant inductance.

Table 5.6. Losses and temperature rise for constant inductance in medium to high frequency range for single- and multi-cut amorphous metal-based inductors

Material	f (kHz)	$P_{core\ th}$ (W)	$P_{core\ exp}$ (W)	P_{Cu} (W)	ΔT_{th} (K)	ΔT_{exp} (K)
2605SA1 single-cut	50	28.7	35.3	0.79	96	93
2605SA1 single-cut	100	24.9	23.4	0.63	68	64
2605SA1 single-cut	150	22.8	20.6	0.60	63	57
2605SA1 multi-cut	50	43.7	69.4	0.59	94	143
2605SA1 multi-cut	100	37.8	51.4	0.36	82	109
2605SA1 multi-cut	150	34.7	41.3	0.33	76	89

5.3. DC-Bias Effect on the Core Power Loss

The magnetic material permeability varies with magnetic field and it is a function of frequency, dc bias and flux density amplitude and temperature. The permeability change of the materials presented is negligible in the frequency range of interest [72]-[80]. The magnetic material permeability generally decreases with the applied dc-magnetizing force [72][76][80][100]. Note that the dc effect exists in all of the magnetic materials and usually is controlled by the dominant air-gap reluctance. The power loss generated in the core at constant flux density magnitude is not constant and depends on the dc magnetizing force applied to the core, as discussed in [99] and [101] for ferrites.

Three inductors were built and tested in order to investigate the power loss generated in the amorphous metal and two silicon steel cores as function of the dc bias. The inductors, based on amorphous metal 2605SA1 and silicon steel 10JNHF600 II core and JFE prototype core, presented in Table 5.1, are built without an air gap and are examined at 100 kHz operating frequency in a 1.25 kW soft-switched boost converter. The high frequency provides a low current ripple resulting in a low winding ac power loss. This allows the core power loss to be the dominant source of power loss and temperature rise. The amorphous metal based inductor winding power loss is about 10 % of the total component power loss and is small in comparison to the core losses. The silicon steel based inductor winding power loss is about 25 % of the total component power loss and its effect is noticeable.

The magnetic cores are almost identical, but the amorphous metal inductor has a 30-turn winding while the silicon steel inductor has a 50-turn winding. This is due to materials' dc bias characteristics as the silicon steel core with a 30-turn winding would not enter into deep saturation. Thus, the amorphous metal core operates at 35 mT and the silicon steel core at operates at 20 mT across the wide range of the dc magnetizing force. Natural convection cooling is used and the system is run until the inductor reaches a steady state temperature.

Figure 5.8 shows the inductor temperature rise above the ambient and the theoretical B-H curve for the amorphous metal 2605SA1 inductor. Figure 5.9 shows the associated inductance measurement and the theoretical B-H. The related data points and power loss are presented in Table 5.7 and in Appendix D, Table D.5.

As the dc magnetizing force increases, the inductor operates at elevated flux density. The measured temperature rise is nearly constant and close to the calculated temperature rise in the first region of the curve and then increases significantly as the dc bias increases beyond the knee point of about 0.6 kA/m and 1.2 T. The theoretical model clearly underestimates the core power loss at elevated dc-bias.

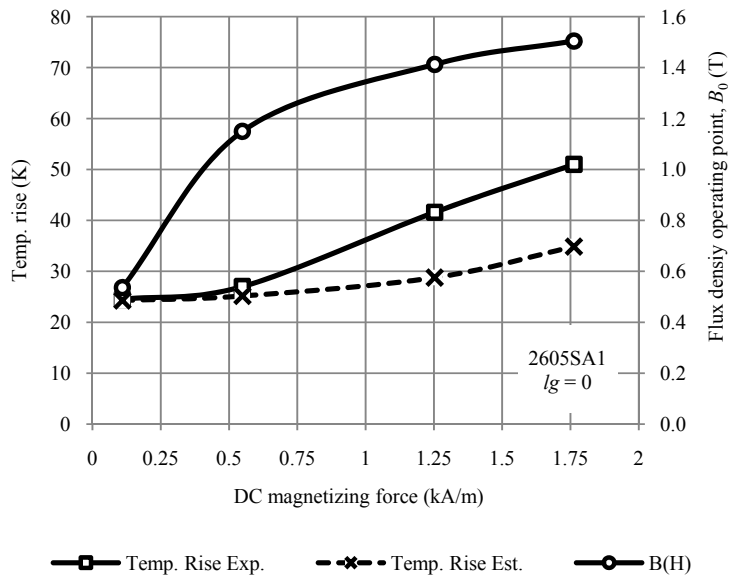

Figure 5.8. Amorphous metal based-inductor power loss and flux density vs. magnetizing dc-bias.

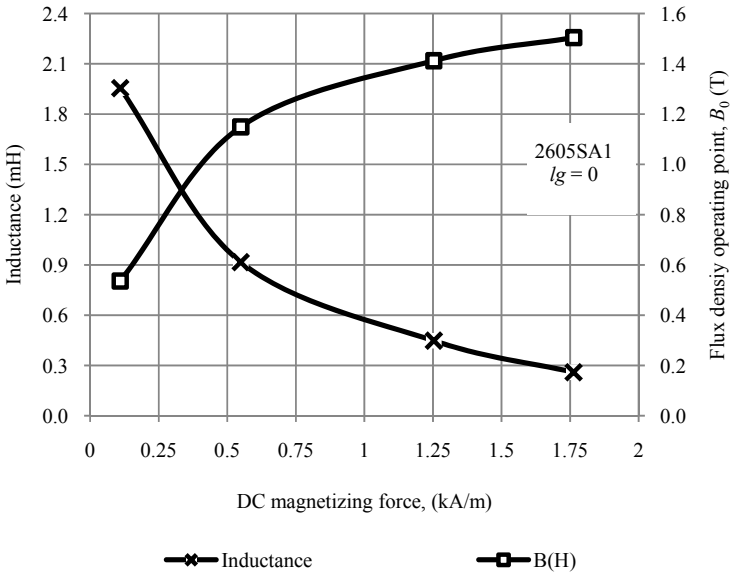

Figure 5.9. Amorphous metal based-inductor inductance and flux density vs. magnetizing dc-bias.

The core power loss starts to increase at a B-H curve knee point, which corresponds to about a 50% drop of the inductance as shown in Figure 5.9. This effect may be critical for the high-current inductor where the magnetizing force applied to the core may be relatively large and inductance roll-off is allowed. The power loss increase due to dc bias should be considered for the minimum size inductor design as it may be one of the limiting factors in the inductor minimization.

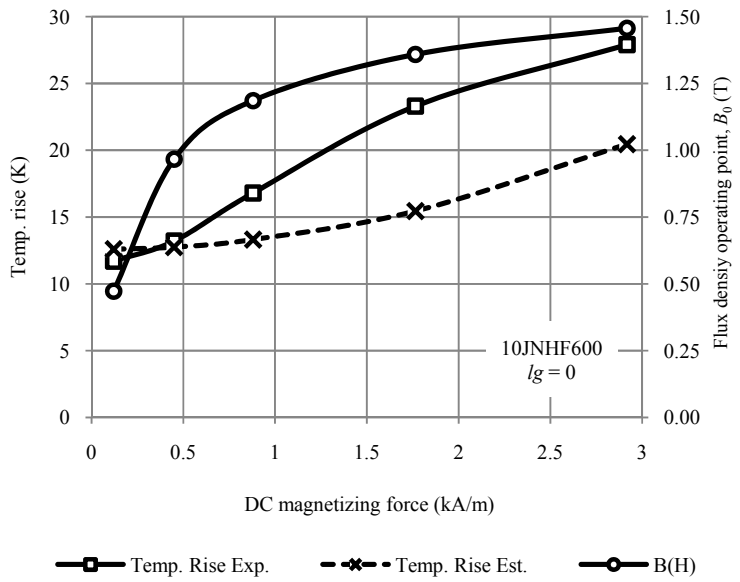

Figure 5.10. Silicon-steel 10JNHF600 based-inductor power loss and flux density vs. magnetizing dc-bias.

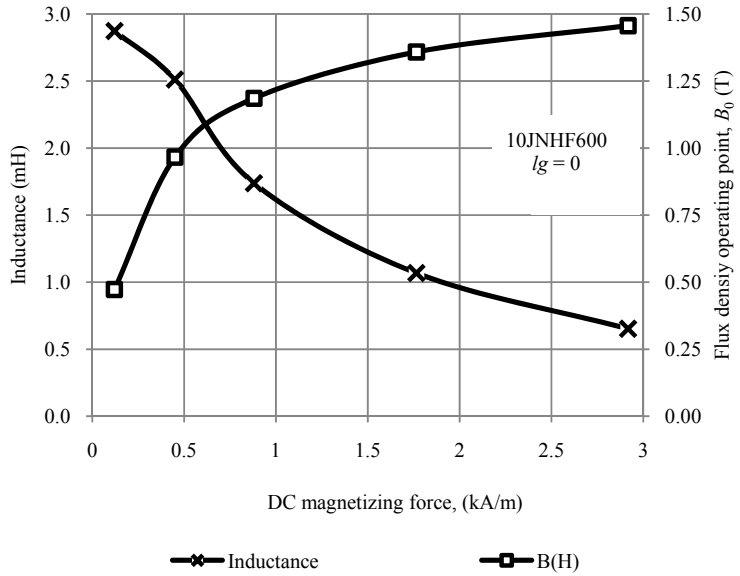

Figure 5.11. Silicon-steel 10JNHF600 based-inductor inductance and flux density vs. magnetizing dc-bias.

Similar behaviour is observed in Figure 5.10 and Figure 5.11 for the 10JNHF600 core and in Figure 5.12 and Figure 5.13 for the JFE prototype core. Due to the dc bias characteristics both silicon steel cores use 50-turn windings, which result in a lower flux density amplitude and higher winding power loss than for the amorphous metal inductor as shown in Table 5.7. Thus, the core power loss is not as well refined as for amorphous metal. However, Figure 5.10 and Figure 5.12 show the general trend of the core power loss increasing at elevated dc bias. Note that silicon steel has softer dc bias characteristics than amorphous metal because the B-H curve is not as sharp as for amorphous metal.

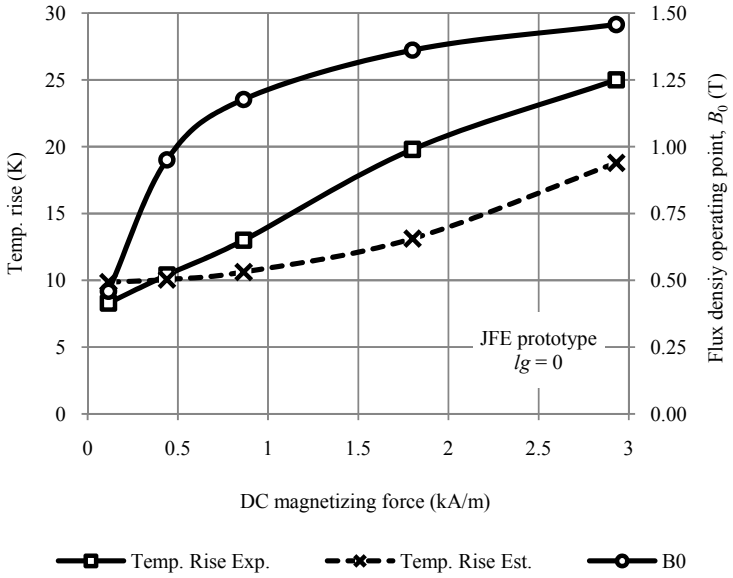

Figure 5.12. JFE prototype based-inductor power loss and flux density vs. magnetizing dc-bias.

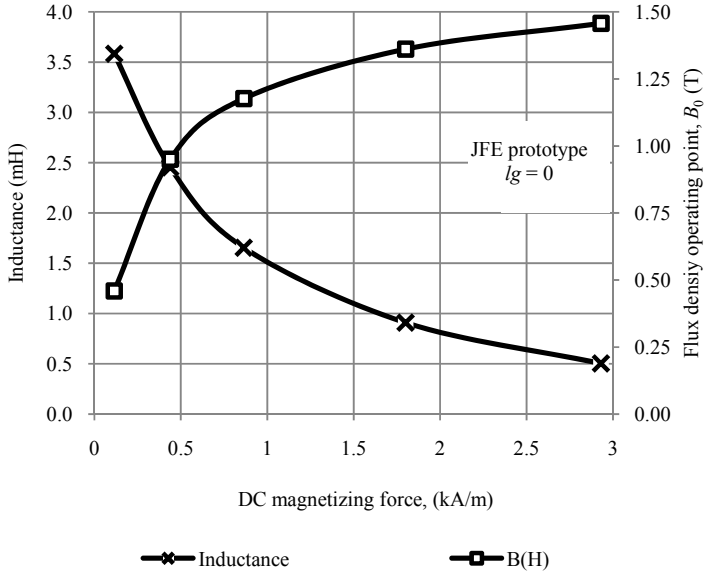

Figure 5.13. JFE prototype based-inductor inductance and flux density vs. magnetizing dc-bias.

It is critical for the inductor to keep its desired inductance over the required operating range. As is shown in Figure 5.8, Figure 5.10 and Figure 5.12 operation at elevated dc bias results in increased power loss. The other effect of dc bias is an inductance drop shown in Figure 5.9, Figure 5.11 and Figure 5.13. The air gap increases the core dc bias capability at the expense of lower inductance. The gapless core is usually not designed with a discrete air gap. Some low-permeability material (usually known as a gapless materials) based inductor designs do have a discrete air gap for the usual reasons of linearizing the inductance characteristic and

higher energy storage for a given flux density. Additionally, because the higher-permeability powder cores display lower specific core losses than lower-permeability powder cores, it may be more efficient to use a high-permeability core with an air gap. The gapless material's B-H curve is not as steep as for amorphous metal and silicon steel materials. The magnetization curves for amorphous metal, silicon steel and powder core are shown in Figure 5.14.

As can be seen from Figure 5.8, the maximum dc bias for 2605SA1 that is not causing elevated power loss is 1.2 T, and is a reasonable de-rating at about 75 % from the nominal saturation flux density of 1.56 T at 25 °C. The silicon steel 10JNHF600 and JFE prototype has a softer magnetization curve as shown in Figure 5.10 and Figure 5.12, respectively; but also experiences core loss increase with dc bias. A 75 % de-rating for silicon steel suggests a design maximum of 1.41 T vs. the nominal saturation level of 1.88 T. The powder core design uses the μ-H material characteristic; thus, some inductance roll-off is allowed. A maximum 30 % powder core-based inductor inductance roll-off is recommended by manufacturers [76][78][79].

Table 5.7. Inductance, Power losses and temperature rise for dc-bias analysis

Material	I_{in} (A)	H (kA/m)	B_0 (T)	L (mH)	P_{core} (W)	P_{Cudc} (W)	P_{Cuac} (W)	P_{tot} (W)	P_{totexp} (W)	ΔT_{th} (K)	ΔT_{exp} (K)
2605SA1	0.62	0.115	0.54	1.955	8.05	0.0057	0.05253	8.11	8.18	24.3	24.5
	3.11	0.546	1.15	0.92	8.05	0.1200	0.2598	8.43	9.10	25.2	27
	7.10	1.249	1.41	0.45	8.05	0.6274	1.09131	9.77	14.65	28.8	41.6
	9.99	1.759	1.50	0.25	8.05	1.2520	2.7578	12.06	18.52	34.9	51.5
10JNHF600	0.41	0.120	0.47	2.87	3.90	0.0038	0.0268	3.93	2.62	12.6	8.7
	1.53	0.455	0.97	2.51	3.90	0.0555	0.0319	3.99	3.12	12.8	10.2
	2.99	0.886	1.19	1.74	3.90	0.2098	0.0718	4.18	4.35	13.3	13.8
	6.00	1.771	1.36	1.07	3.90	0.8379	0.1864	4.92	6.65	15.4	20.3
	9.92	2.908	1.46	0.65	3.90	2.2518	0.5539	6.71	8.33	20.5	24.9
JFE prototype	0.39	0.115	0.46	3.58	2.99	0.0035	0.0179	3.01	1.52	9.9	5.3
	1.49	0.436	0.95	2.45	2.99	0.0505	0.0374	3.07	2.19	10.1	7.4
	2.94	0.859	1.18	1.66	2.99	0.1966	0.0800	3.26	3.05	10.6	10
	6.12	1.795	1.36	0.91	2.99	0.8580	0.2714	4.12	5.40	13.1	16.8
	9.96	2.920	1.46	0.50	2.99	2.2704	0.8518	6.11	7.27	18.8	22

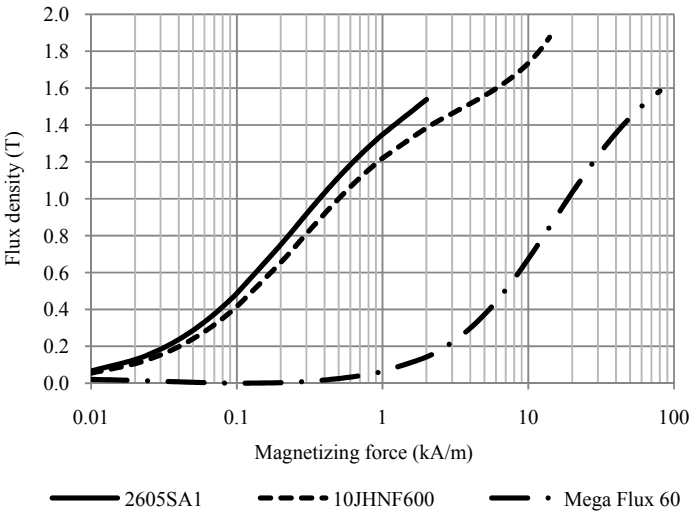

Figure 5.14. Magnetization curves.

5.4. Duty Cycle Effect on the Core Power Loss

The duty cycle directly influences the volt-seconds applied to the inductor and results in magnetic flux change. The rate of change is proportional to the applied voltage. However, the same volt-seconds applied in different conditions may result in a different flux change rate; as the exact shape of the B-H characteristic is dependent on the excitation, and is difficult to predict for arbitrary waveforms. Publications based on ferrite [88][97][101][102] show elevated power loss in the ferrite when subjected to asymmetrical flux change patterns. Such conditions are common for boost and buck converter operation on low or high duty cycles. Similar results have been demonstrated in [103] for nanocrystalline material along with the development of an empirical core loss calculation method using a waveform-coefficient Steinmetz equation (WcSE).

There is little published on duty-cycle effects on the high-flux lossy materials under investigation in this section. In order to examine this effect two laminated cores and one powder core inductors were built and tested. The core's geometry specification is shown in Table 5.1. Again, the single-cut amorphous metal and silicon steel 10JNHF600 'II' laminated core inductors are very similar. The 16 turn winding is distributed evenly, 8 turns on each core leg. The copper foil is 22 mm width and 0.6 mm thick. The amorphous metal and silicon steel materials have different fill factors with effective cross-sectional areas of 311 mm^2 and 337 mm^2, respectively. Both laminated inductors have two 1 mm air gaps, one in each leg centre. The third inductor is based on the Mega Flux 60 powder core without an air gap. The core

effective cross-sectional area is 450 mm^2. The 28 turn winding is made of Litz wire with 100 strands of 0.3 mm diameter and distributed evenly on the core legs.

All cores are examined in a boost converter which operates at frequency of 10 kHz. The flux density amplitude in the core is kept constant across the duty cycle range from 0.2 to 0.5 and is 0.15 T for all inductors. The convection-cooled inductors were placed in thermal chamber and run until steady state was reached.

The experimental temperature rise is compared with calculations, which uses the inductor design flowchart presented in Chapter 4. The Steinmetz equation, *SE*, and its modified version, *MSE*, together with waveform-coefficient Steinmetz equation, *WcSE*, are used for calculation. The basic empirical Steinmetz equation predicts a specific power loss generated in the core and provides a high accuracy for a sinusoidal flux waveforms and good accuracy for a symmetrical triangular waveforms and it is given as follows:

$$P_{csp} = k \cdot f^m \cdot B_{ac}^n \tag{5.1}$$

where k, m, n are the Steinmetz equation factors, f is the switching frequency and B_{ac} is the ac flux density amplitude. However, when exposed to extreme duty cycles the standard equation underestimates the generated power loss. The improved formula of the Steinmetz equation which extends it over non-sinusoidal waveforms is presented in [97] as follows:

$$P_{MSE} = \left(k \cdot f_{eq}^{m-1} \cdot B_{ac}^n \right) f \tag{5.2}$$

where the equivalent sinusoidal frequency, f_{eq}, can be calculated from the averaged remagnetization rate and normalized by constant $2/(\Delta B\, \pi^2)$ as follows:

$$f_{eq} = \frac{2}{\Delta B^2\, \pi^2} \int_0^T \left(\frac{dB}{dt} \right)^2 dt \tag{5.3}$$

where ΔB is complete magnetization change from minimum to maximum and T is the equivalent period. The modified Steinmetz equation has proven its accuracy for ceramic ferrites as shown in [88][97]. The derivation of the *MSE* equation is presented in Appendix D, Section D.3.1.

The waveform-coefficient Steinmetz equation provides an intuitive approach to the non-sinusoidal waveforms by correlating them to the standard Steinmetz equation. As shown in [103], the original Steinmetz equation is completed by introduction of the flux waveform coefficient, *FWC*, which for square-wave voltages equals $\pi/4$.

$$P_{WcSE} = FWC\, k\, f^m\, B_{ac}^n \tag{5.4}$$

The experimental and predicted temperature rises using the standard Steinmetz equation and the modified Steinmetz equation MSE and the waveform-coefficient Steinmetz equation WcSE are presented for amorphous metal, silicon steel and powder core in Figure 5.15, Figure 5.16 and Figure 5.17, respectively. The corresponding data points are shown in Table 5.8 while experimental data is provided in Table D.6. It is clear that in all cases the material core loss and temperature increase for the reduced duty cycles and that this increase is reasonably predicted by both improved versions of the Steinmetz equation. Note that the prediction for the powder material shows some deviation which may indicate a different power loss mechanisms than in the laminated cores. The discussion related to the limitation of the WcSE is provided in [103].

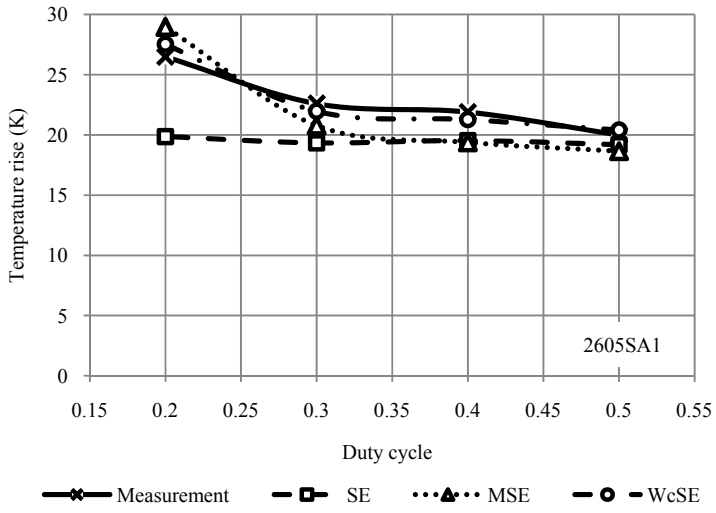

Figure 5.15. Comparison between measurement and calculated temperature rise as a function of duty cycle for amorphous metal.

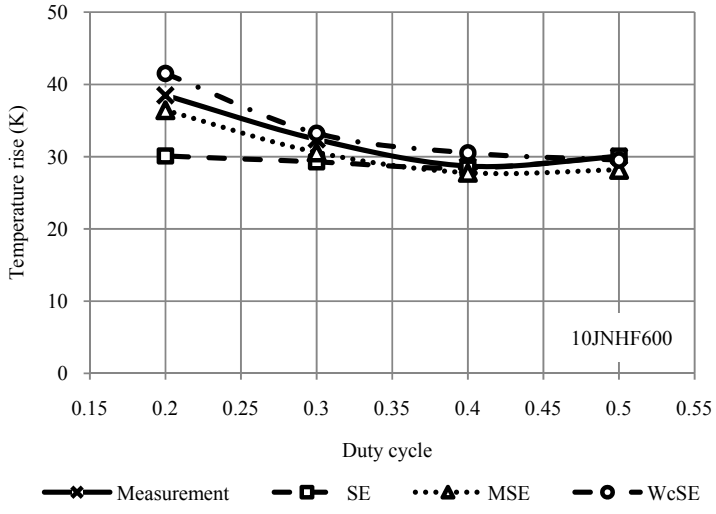

Figure 5.16. Comparison between measurement and calculated temperature rise as a function of duty cycle for silicon steel.

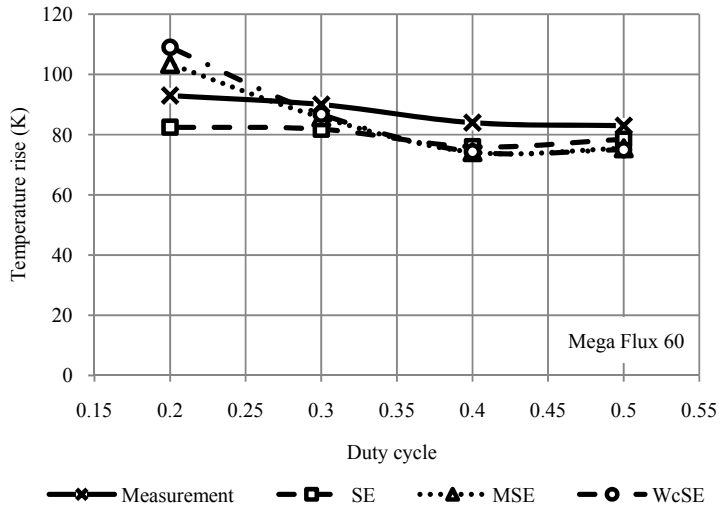

Figure 5.17. Comparison between measurement and calculated temperature rise as a function of duty cycle for powder material.

Table 5.8. Power loss generated in the inductor and temperature rise for duty cycle effect analysis

Material	D -	P_{SE} (W)	P_{MSE} (W)	P_{WcSE} (W)	P_{cudc} (W)	P_{cuac} (W)	P_{totSE} (W)	P_{totMSE} (W)	$P_{totWcSE}$ (W)	P_{totexp} (W)	ΔT_{thSE} (K)	ΔT_{thMSE} (K)	ΔT_{thWcSE} (K)	ΔT_{exp} (K)
2605SA1	0.20	4.30	9.37	6.85	1.06	3.49	8.85	13.92	11.4	8.98	19.9	29.0	27.5	26.5
	0.30	4.26	5.03	4.06	1.06	3.25	8.57	9.35	8.37	7.53	19.3	20.8	22	22.6
	0.40	4.47	4.39	3.81	1.07	3.14	8.67	8.60	8.01	7.28	19.5	19.4	21.3	21.9
	0.50	4.37	4.09	3.44	1.06	3.06	8.49	8.21	7.56	6.59	19.2	18.7	20.4	20.0
10JNHF600	0.20	9.57	13.72	13.47	1.12	3.89	14.58	18.73	18.48	13.58	30.1	36.4	41.5	38.5
	0.30	9.40	10.49	8.89	1.12	3.58	14.11	15.19	13.59	11.23	29.3	30.6	33.2	32.4
	0.40	9.14	8.98	7.57	1.12	3.35	13.60	13.45	12.	9.83	28.4	27.8	30.5	28.7
	0.50	9.90	9.29	6.82	1.12	3.54	14.56	13.94	11.48	10.32	30.1	28.2	29.5	30.0
Mega Flux 60	0.20	21.51	33.80	34.11	7.70	9.53	38.73	51.03	51.3	45.38	82.5	103.5	109	93
	0.30	21.35	24.38	22.27	7.70	9.43	38.48	41.50	39.4	43.78	81.8	85.7	86.8	90
	0.40	19.53	19.02	16.47	7.70	8.68	35.91	35.40	32.5	40.58	76.0	74.2	74.3	84
	0.50	20.80	19.21	16.33	7.70	9.16	37.66	36.07	33.2	40.05	78.5	75.5	75	83

5.5. Air Gap Effect

The air gap and associated fringing flux has a significant effect on the power losses generated in the inductor. The air gap is a necessary feature of the inductor based on the high permeability magnetic materials as it allows for operation under elevated dc-bias. In this section the air gap effects on the core and winding power loss are investigated. The windings shielding effect is also demonstrated.

5.5.1. Air Gap Effect on the Core

In this section the power loss in the core due to the air gap fringing flux is investigated. It is reported in the literature, [89], [98] and [100], that laminated materials can have significant additional eddy-current core loss due to the air gap fringing flux. These core losses due to the size of the air gap are caused by magnetic flux fringing around the gap re-entering the core in a direction of high loss. As the air gap increases, some of the fringing flux strikes the core perpendicular to the laminations and sets up eddy currents causing additional loss. The gap power loss was introduced in [98] and provided in [89] by following equation:

$$P_g = k_i \cdot l_i \cdot l_g \cdot f \cdot B_{ac}^2 \tag{5.5}$$

where k_i is the core constant (e.g. 0.388 for CC core), l_i is the lamination width in mm, l_g is the total air gap length in mm, f is the frequency in kHz, and B_{ac} is the flux density amplitude in T.

The inductor design software available from Metglas [72] uses equation (5.5) to estimate gap power loss. The gap power losses are also reported in [100]. However, in this study it is shown that the core air gap loss equation (5.5) provided by [89], [98] leads to significant overestimation of this phenomenon.

Further publications [104] and [105] show that power loss generated by the eddy current in the air gap vicinity can cause a substantial power loss increase. However, the area affected by the fringing flux is rather small; therefore, the gap loss may induce a local hotspot, but the absolute air gap heating is a rather small contributor to the overall core losses. The results shown in [104] suggest that the eddy current amplitude generated at higher frequency is larger, but it does not penetrate the material as deep as for lower frequency current. In general, the air gap fringing flux should not generate substantial power loss in a large laminated core as it is suggested in [89] and [98].

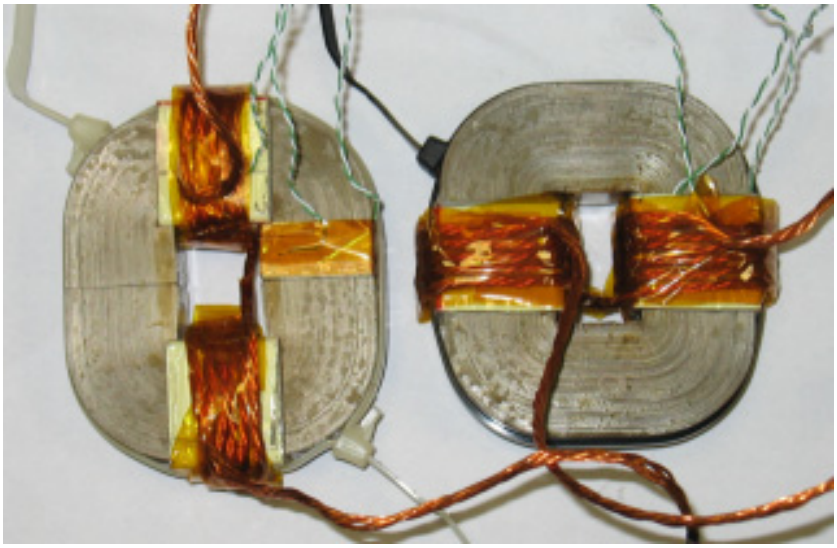

Figure 5.18. Air gap experimental inductors. Winding is far away from the air gap (left), winding is shielding air gap (right).

An experimental investigation was undertaken to determine the core associated power loss due to air gap fringing flux. Two inductors were built based on the same 2605SA1 AM core as shown in Figure 5.18.

The window area, core cross-sectional area and mean magnetic path length are 504 mm^2, 375 mm^2, and 170 mm, respectively. The core dimensions are specified in Table 5.1. The inductors have 10-turn windings, 5 turns on each leg made of Litz wire of 0.3 mm diameter and 5x5 strands. The Litz wire minimizes the winding power loss due to eddy currents [87]-[89]. One inductor has a winding placed far away from the air gap while the other inductor's winding is placed around the air gap. The inductors are examined in the dc-dc boost converter at a constant operating frequency of 50 kHz and constant flux density amplitude of 150 mT. The air gap was varied from 0 to 2 mm with 0.5 mm steps. Natural convection cooling was used and the inductors run until steady state was reached. The thermocouples were attached to the core and winding as shown in Figure 5.18. The core temperature was measured in the leg centre and on the side in the air gap vinicinity while winding hotspot was measured between turns.

The winding placed around the air gap is shaping the air gap fringing flux and so the air gap cross-sectional area is limited by the winding. The fringing flux is not able to close its path outside the winding and it is said that the air gap is shielded. The inductances of the shielded and unshielded inductors are plotted in Figure 5.19.

The shielded winding has significantly lower inductance of about 30 % lower than the unshielded inductor as shown in Figure 5.19. Shielding is a very important feature, which helps to minimize magnetic field generated outside the inductor.

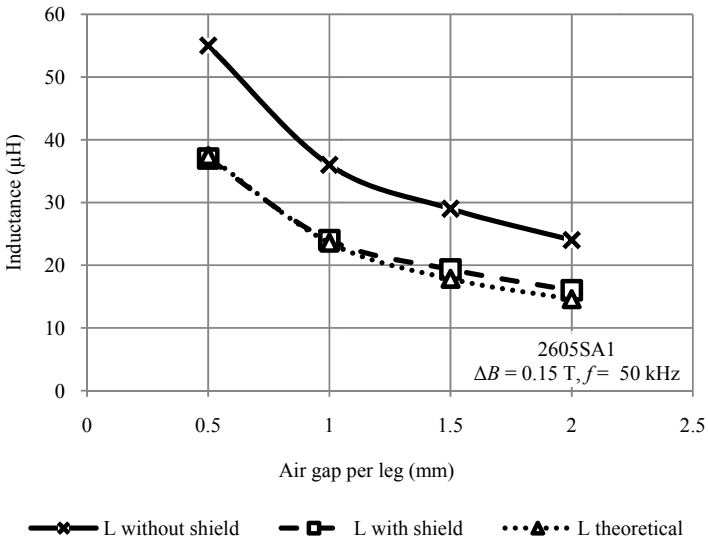

Figure 5.19. Inductance change due to the winding position.

The dc flux fringes through the winding and increases the bias. Some high frequency inductors may experience significant difference between dc and ac inductance due to the ac shielding effect.

The experimental and theoretical inductor temperature rises for the shielded and unshielded inductors are shown in Figure 5.20 and Figure 5.21 and Table 5.9, respectively. The experimental data is provided in Table D.7. The temperature rise is largely determined by core losses as the winding losses are minimal. The unshielded experimental inductor shows a good correlation with the theoretical predictions which do not use the air gap fringing core power loss formula (5.5). If the air gap fringing core power loss formula is used, then the core power loss and temperature are significantly overestimated. The same applies for the shielded inductor. The shielded inductor has a lower inductance and a higher current ripple with higher ac copper loss. These results show clearly that the formula (5.5) presented in [89] and [98] overestimates the air gap power loss in the amorphous metal core.

The advanced magnetic materials such as amorphous metal and 6.5% silicon steel are intended for use at higher frequencies; thus, the material's resistivity is increased and thin laminations are used. The high-frequency fringing flux induces eddy currents on the outer surface of the core and transverse fringing flux does not penetrate the core.

The authors have continued to investigate this topic using finite element analysis. These as yet unpublished results suggest that while the air gap fringing core loss is real, the loss tends to be insignificant for these types of inductors with very thin laminations and high resistivity. Similar results are reported in [103], which observes that air gap fringing core loss is only a minor factor for nanocrystalline material.

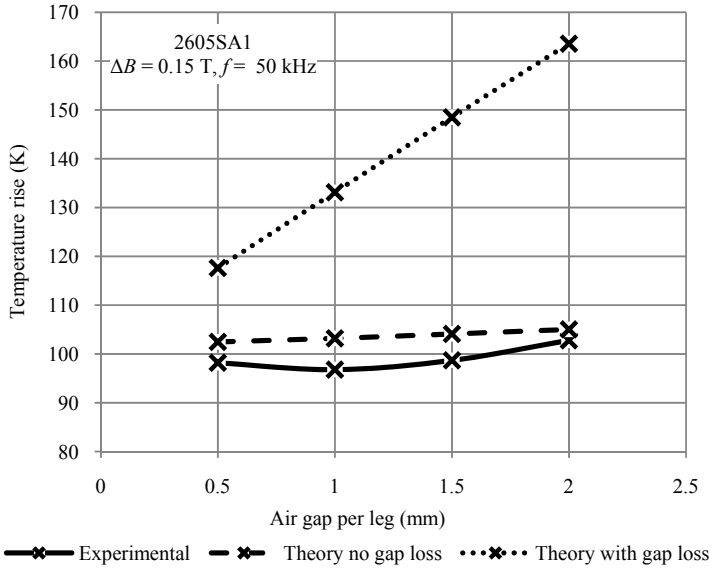

Figure 5.20. Core temperature rise vs. shielded gap length for constant frequency 50 kHz.

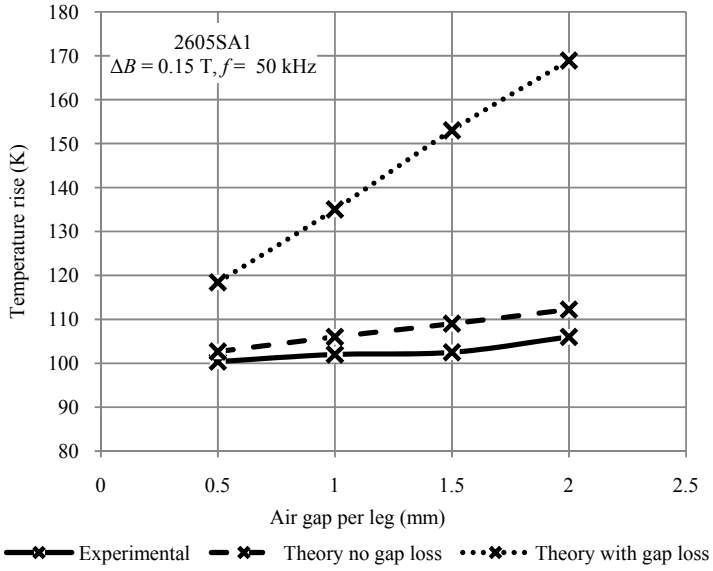

Figure 5.21. Core temperature rise vs. unshielded gap length for constant frequency 50 kHz.

Table 5.9. Power loss, temperature rise and inductance change in a relation to winding placement and air gap length

Material	l_g (mm)	P_{core} (W)	P_{Cu} (W)	P_{gap} (W)	L_{th} (μH)	L_{exp} (μH)	$\Delta T_{th\text{-}no\ gap\ loss}$ (K)	$\Delta T_{th\text{-}gap\ loss}$ (K)	ΔT_{exp} (K)
2605SA1 Shielded	0.5	38.34	1.07	6.49	37.4	37.0	102.7	118.4	100.4
	1.0	38.34	2.43	12.99	23.6	24.0	106.0	135.0	102.0
	1.5	38.34	3.94	19.48	17.8	19.3	109.0	153.0	102.5
	2.0	38.34	5.50	25.98	14.6	16.0	112.2	168.9	106.0
2605SA1 Unshielded	0.5	38.34	0.45	6.49	37.4	55.0	102.5	117.6	98.2
	1.0	38.34	1.02	12.99	23.6	36.0	103.2	133.1	96.8
	1.5	38.34	1.65	19.48	17.8	29.0	104.1	148.5	98.7
	2.0	38.34	2.30	25.98	14.6	24.0	105.0	163.6	102.8

5.5.2. Air Gap Effect on the Winding

A method of reducing air gap fringing copper loss is to distribute the air gap into several smaller air gaps. In this section, the effect of the multiple gaps on the winding is investigated for amorphous metal and silicon steel. The investigation uses QuckField a 2D finite element solver for electromagnetic, heat transfer and stress analysis [107].

Figure 5.22 shows a finite-element simulation for a single-gapped inductor core. By distributing a single gap into several smaller gaps the fringing flux is significantly reduced as seen in Figure 5.23. If the low permeability powder core is used an additional power loss in the winding is generated by the stray flux, which fringes outside the core as shown in Figure 5.24. The corresponding FEA model details are presented in Table 5.10.

Figure 5.25 shows finite element simulation results for the foil copper windings power loss as a function of the distance from the core for three air gap arrangements: single 3 mm air gap, 2 gaps of 1.5 mm and 3 gaps of 1 mm, and the gapless powder core, respectively. The corresponding data points are shown in Table 5.11. As expected, the losses in the copper are decreased by distributing the air gap and with the distance increase from the core.

The winding around the single air gap gives a power loss of 56.9 W where placed close to the core, but the power loss reduces as distance from the core increases and yields 35.7 W, 23 W, 16.2 W and 12.1 W for distances of 1 mm, 2 mm, 3 mm, 4 mm, respectively. A similar power loss reduction with the distance from the core is observed for the other air gap arrangements. However, the winding placed around the gapless core does not record the power loss increase when close to the core.

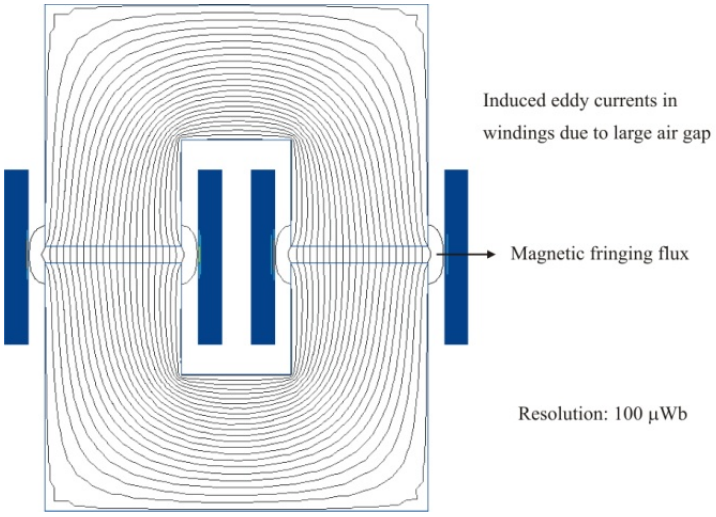

Figure 5.22. FEA of a single 3 mm inductor air gap per leg.

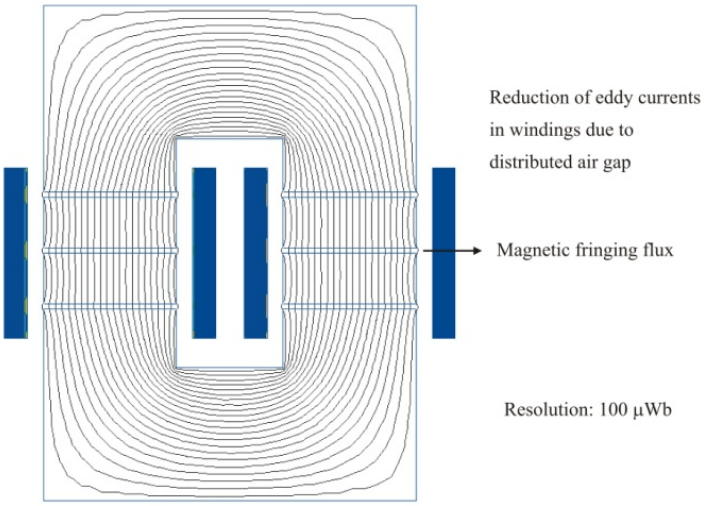

Figure 5.23. FEA of distributed inductor air gap per leg (3 x 1mm).

Table 5.10. FEA analysis model parameters

a (mm)	b (mm)	c (mm)	d (mm)	N	I_{pk} (A)	f (kHz)	μ_{gapped}	$\mu_{gapless}$
25	20	38	20	22 (2 x 11)	18.6	30	1000	31

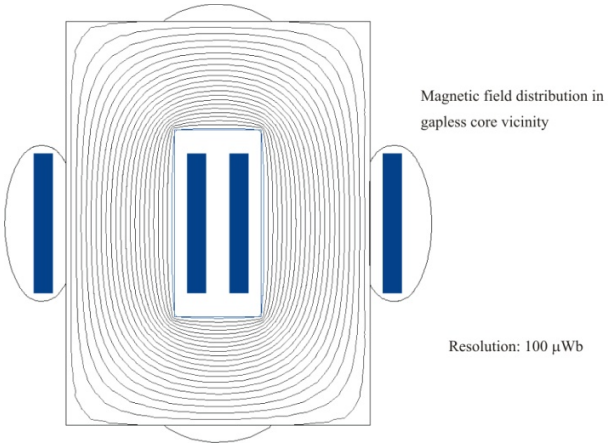

Figure 5.24. FEA of gapless core inductor.

The distributed air gap reduces the winding loss significantly, e.g. at 3 mm distance from the core the single gapped core records 16 W while two and three air gaps records 7 W and 4 W, respectively. The copper loss at distance 3 mm from the core is approx. 5 W with a gapless core.

The gapless core produces the lowest winding power loss if placed close to the core, while gapped designs suffer a significant power loss due to fringing flux. The distributed air gap helps to reduce the ac winding power loss and the power loss for 3 air gaps at the distance 2 mm from the core is similar to the gapless core. Note that in a practical high power design a 2 mm distance from the core is very common due to insulation requirements and manufacturing assembly.

The air gap arrangement and the distance between winding and the core have an effect on the inductance as shown in Figure 5.26 and Table 5.11. The winding placed further away from the air gap does not provide significant fringing flux shaping and the equivalent air gap area increases; thus, reluctance decreases. If the winding is close to the core, the air gap area is reduced and inductance drops. On the other hand the distributed air gap results in many small air gaps; therefore, the fringing flux range area is decreased by the structure, which results in a higher equivalent reluctance than for a single air gap. The winding distance increase from the multi gaped core causes the inductance to rise as area for the fringing flux extends. However, the inductance increase is lower than for a single gapped core. The gapless core inductance rise due to the distance rise between core and winding is marginal.

As expected, the winding placed further from the core results in the inductance increase by 5 % to 8 % for distributed gap and single gap, respectively.

The air gap distribution results in a lower inductance as shown in Figure 5.26. Some graph inconsistency results from the FEA solver resolution, which was a compromise between accuracy and time required for evaluation. However, it is clear that multi gapping results in an inductance reduction by approximately 5 %.

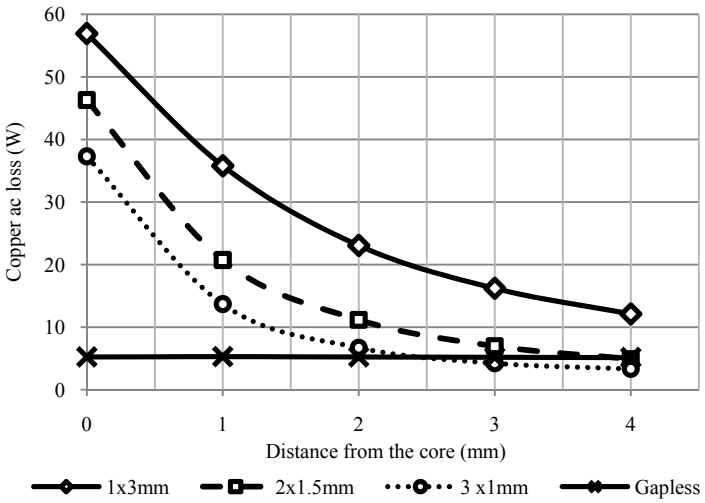

Figure 5.25. FEA foil winding ac power loss of distributed inductor air gap as function of the distance between the winding and the core.

Table 5.11. FEA ac power loss in foil winding and inductance for various air gaps and distances between winding and core

f = 30 kHz I_{pk} = 18.6 A	l_g (mm)	Distance from the core (mm)	P_{ac} (W)	L (μH)
high permeability core with gaps	1 x 3mm	0	56.91	114.4
	2 x 1.5mm		46.29	114.3
	3 x 1mm		37.30	114.0
	1 x 3mm	1	35.79	118.8
	2 x 1.5mm		20.73	116.8
	3 x 1mm		13.70	115.4
	1 x 3mm	2	23.06	121.0
	2 x 1.5mm		11.18	117.9
	3 x 1mm		6.72	116.9
	1 x 3mm	3	16.21	121.8
	2 x 1.5mm		6.98	120.0
	3 x 1mm		4.25	117.9
	1 x 3mm	4	12.12	123.6
	2 x 1.5mm		4.91	120.4
	3 x 1mm		3.34	120.7
Low permeability core without gapping	-	0	5.25	120.8
	-	1	5.30	120.8
	-	2	5.26	121.0
	-	3	5.20	121.2
	-	4	5.15	121.3

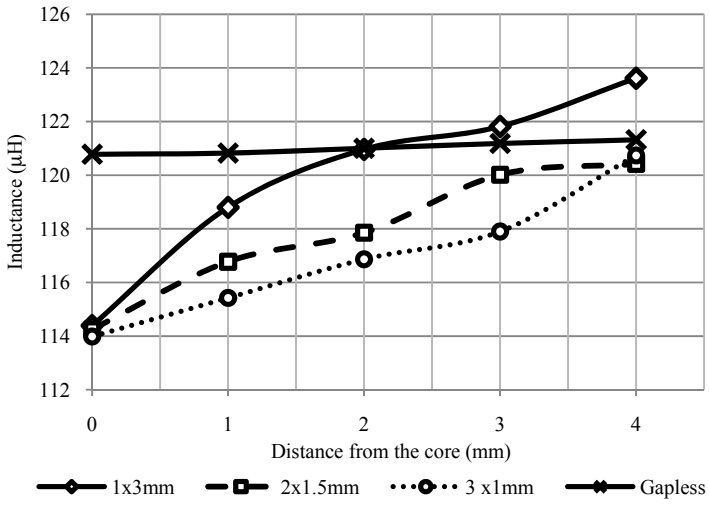

Figure 5.26. FEA inductance as a function of air gap and distance between the winding and the core.

An experimental test was carried out to investigate the fringing flux effects of the distributed gap. Three cores sets were tested: three-cuts-per-leg amorphous metal and silicon steel and single-cut-per-leg amorphous metal.

The total gap length per leg is 2.625 mm and the frequency is kept constant at 30 kHz. The effects of splitting this single gap into two and three smaller gaps are separately tested. For the first test, a single gap of 2.625 mm is located in the centre of the leg for the iron-based amorphous and the silicon steel cores. For the second test featuring only the multi-cut cores, there are two gaps in each leg with lengths of 1.625 mm and 1 mm respectively. The gaps are located at an equal distance from the core end sections for both materials. For the third test, again featuring only the multi-cut cores, there are three gaps in each leg with lengths of 1 mm, 1 mm, and 0.625 mm respectively. The gaps are located equally along the core leg for the iron-based amorphous core, but the silicon steel core, because of its manufacturing process, has a 0.625 mm gap at one end of the core leg. This affects the experimental results as is discussed below.

Figure 5.27 and Table 5.12 show the experimental temperatures of the cores and the copper windings decrease with the number of gaps for the three different core sets. The corresponding experimental data is shown in Appendix D, Table D.8. As expected, the core and copper temperatures drop significantly, e.g. 18 °C for the multi-cut amorphous metal copper windings. The core for the multi-cut silicon steel only drops 7 °C because the gap located at the end of the core leg generates less winding power loss. The single-cut amorphous metal is obviously only tested for a single gap. An interesting anomaly in this testing is that the multi-cut amorphous metal core is significantly hotter than the single-cut amorphous metal core for the

single gap test point. Generally, amorphous metal has significantly lower core loss than silicon steel. The single-cut standard amorphous metal core is operating at approx. half the temperature rise of the multi-cut amorphous metal core as shown in Section 5.2.

The multi-cut amorphous metal inductor tested in these experiments used a custom core with machined segments for use with the gaps. The cutting process appeared to cause shorts between the laminations and significantly increased the core heating and temperature rise as this multi-cut amorphous metal core is operating significantly hotter than predicted. In general, silicon steel allows easier generation of segments and multiple cuts than amorphous metal due to the manufacturing process. A similar increase in core power loss and performance degradation was observed in [103] for nanocrystalline cut cores compared to the raw material.

References [88][106] provide quantitative loss predictions for air gap fringing copper losses in the foil winding.

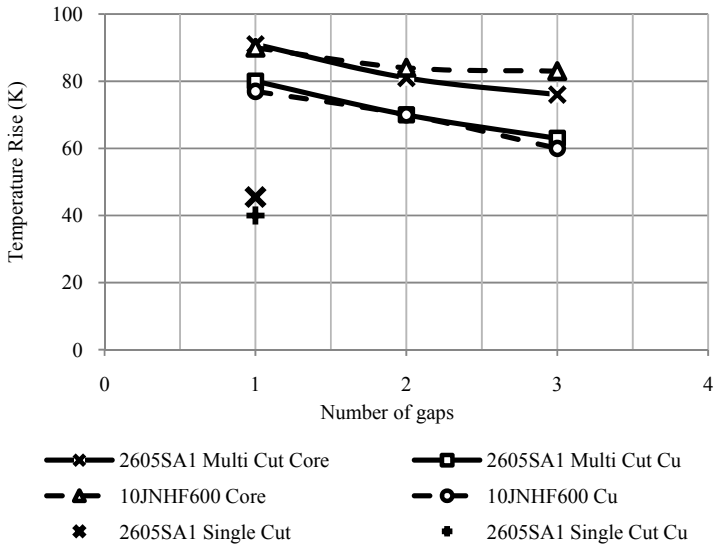

Figure 5.27. Reduced core and winding temperature due to distributed air gaps.

Table 5.12. Temperature rise reduction due to multi gap core

Material	f (kHz)	l_g (mm)	ΔT_{core} (K)	$\Delta T_{winding}$ (K)
2605SA1	30	single cut 1 x 3 mm	43	40
2605SA1	30	1 x 3 mm	91	80
2605SA1	30	1 x 1.625 mm, 1 x 1 mm	81	70
2605SA1	30	2 x 1 mm, 1 x 0.625 mm	76	62
10JNHF600	30	1 x 3mm	90	78
10JNHF600	30	1 x 1.625 mm, 1 x 1 mm	84	70
10JNHF600	30	2 x 1 mm, 1 x 0.625 mm	83	60

5.6. Thermal Configuration

In this section the inductor core temperature rise variation with thermal conductivity and lamination direction is investigated. The temperature rise, ΔT, of a material is proportional to the power loss, P, and thermal path, h, and is inversely proportional to the thermal conductivity, λ, and surface area, A [71].

$$\Delta T = \frac{P\,h}{\lambda\,A} \tag{5.6}$$

The lamination direction has a significant impact on the thermal conductivity and subsequent heating of the inductor core.

Figure 5.28 shows the core segments for silicon steel, amorphous metal and the powder core. The silicon steel material is developed using a stamping process. The thermal conductivity of the material is 18.6 $W{\cdot}m^{-1}{\cdot}K^{-1}$ along the lamination [74] as shown in Figure 5.28. However, the thermal conductivity against the lamination is much less (approx. 1 $W{\cdot}m^{-1}{\cdot}K^{-1}$). The iron-based amorphous metal is developed using a winding process. The thermal conductivity of this material is 10 $W{\cdot}m^{-1}{\cdot}K^{-1}$ along the lamination and only 0.5 $W{\cdot}m^{-1}{\cdot}K^{-1}$ against the lamination [72]. The powder material is bulk and has the same thermal conductivity in both directions. The manufacturer does not provide thermal conductivity for Mega Flux 60. However, similar cores from Magnetics Inc. are specified at 8 $W{\cdot}m^{-1}{\cdot}K^{-1}$.

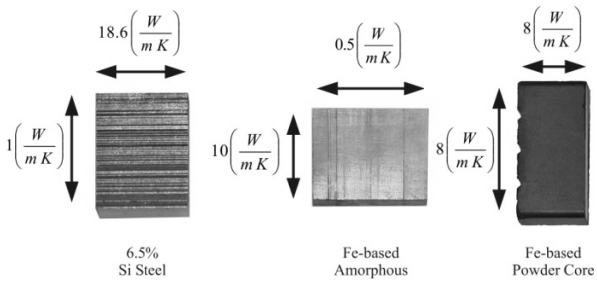

Figure 5.28. Magnetic core segments.

The lamination direction is a critical parameter regarding the inductor mounting as it affects both thermal conductivity and the length of the thermal path. The iron-based amorphous metal must be mounted horizontally to ensure the thermal conductivity along the lamination is used. Horizontal mounting also reduces the length of thermal path for regular inductor cores. The silicon steel material should be mounted vertically to ensure thermal conduction along the lamination direction unless another cooling path is provided for the core. The vertically mounting method increases the length of thermal path for most inductor cores.

For the experimental thermal comparisons an aluminium thermal bracket is designed as shown in Figure 5.29. The thermal bracket ensures that the surface area, A, and thermal path, h, in (5.6) are equal for both materials. The other two parameters of (5.6) are dependent on the core material. The inductor cores are mounted horizontally.

The copper winding is isolated from the inductor core using a Teflon bobbin. The thermal conductivity of Teflon (0.02 $W \cdot m^{-1} \cdot K^{-1}$) ensures that the heat distribution to the core from the copper is low. The aluminium bracket has a thermal conductivity of 206 $W \cdot m^{-1} \cdot K^{-1}$ [88], and extracts the heat out of the inductor core both along and against the lamination direction.

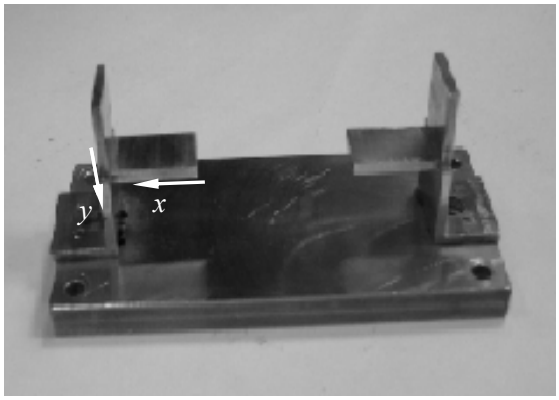

Figure 5.29. Aluminium thermal jig.

The test is carried at 30 kHz and inductors from Section 5.2.1 are used. . Three thermal conditions are tested. Firstly, heat is extracted from the cores optimally in the *x*-*y* directions. The silicon steel has the lowest temperature rise due to its higher thermal conductivity. The powder material has the highest temperature rise although lowest power loss. This is influenced by a lower thermal conductivity and a longer core. The experimental results are shown in Figure 5.30 and Table 5.13.

In the second test, heat is extracted along the *x* direction only as a Teflon barrier is used to block heat flow in the *y* direction. There is only a relatively small increase in temperature for the silicon steel core as the heat is still been extracted along the lamination. However, there is a larger increase in temperature for the iron-based amorphous core because the heat flow is against the lamination using the poorer thermal conductivity. The powder core temperature increases slightly as the heat exchange area decreases.

In the final test, heat is pulled out in the *y* direction only and a Teflon barrier is used to block heat flow in the *x* direction. This test is almost optimum for the amorphous metal but is against the lamination for silicon steel resulting in a significant temperature increase due to the poorer thermal conductivity. The powder core temperature rise is similar to *x* direction.

There is a small reduction in area, A, in (5.6), available for heat transfer when the Teflon barriers are introduced, introducing a minor experimental error.

In general, the experimental results correlate well with the specified thermal conductivities for the various materials and highlight the critical factor of lamination direction.

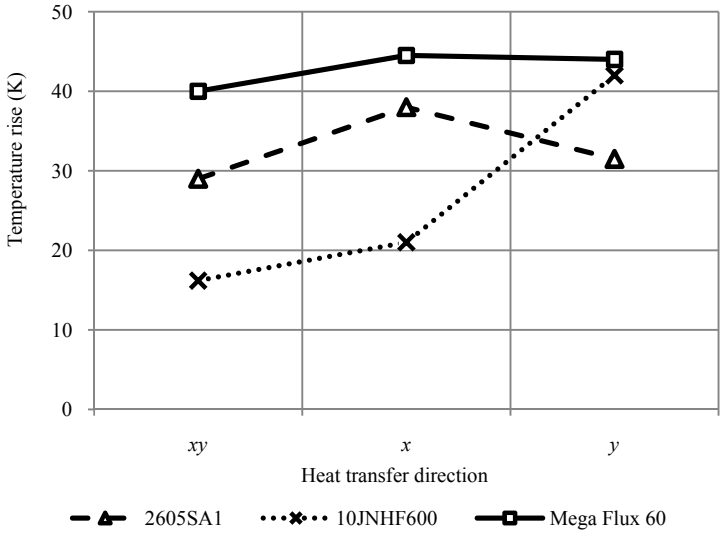

Figure 5.30. Heat flow considerations.

Table 5.13. Conduction cooled inductor cores temperature rise

Material	2605SA1			10JNHF600			Mega Flux 60		
Direction	*x*	*y*	*xy*	*x*	*y*	*xy*	*x*	*y*	*xy*
ΔT_{core} (K)	38	32	29	21	42	16	45	44	40

5.7. Summary

The practical effects of frequency, dc-bias and duty cycle on core power loss, air-gap fringing on the core and winding losses, and the core conduction cooling are experimentally investigated for the Fe-amorphous metal, 6.5% silicon steel and powder core.

The variation of the core loss with frequency for the various materials is approximately as predicted by the specifications and algorithm developed in Chapter 4. The multi-cut core displays elevated power loss due to manufacturing.

As it is shown, all materials can experience increased core losses with dc bias and appropriate de-rating should be used when operating high on the magnetization curve. The investigation suggests de-rating at about 75 % of the nominal saturation flux density at 25 °C. Similarly, asymmetric duty cycles result in increased core losses. The modified Steinmetz equations are a useful predictor of these increased losses.

It has been suggested in the literature [89][98] that increased core loss can occur due to air gap fringing. Testing is this study suggests that these effects can be insignificant for these cores with thin laminations and high resistivity. The distributed air gap and sufficient distance between winding and the core are efficient ways for winding ac power loss minimization. Added cuts to the core can result in core degradation for amorphous metal.

Finally, it is demonstrated than lamination direction is key to optimum thermal cooling path for the laminated gapped cores.

Chapter 6
Conclusions and Future Work

6.1. Thesis Summary

The thesis has focused on the development of a bi-directional dc-dc converter with soft-switching cell in the first part, and magnetic material comparison and analysis for the high-current inductor design in the second part. A custom inductor design flowchart is developed and practical design aspects are investigated.

Chapter 1 sets the thesis background. The research motivation and application area is identified and design constraints are outlined. The dc-dc converters topologies are presented and briefly contrasted. The state-of-art in power semiconductors is presented and general information about magnetic component and capacitors is provided. The extended magnetic materials comparison is presented in Chapter 3.

In Chapter 2 a novel bi-directional soft-switched dc-dc converter is presented and analysed. Novel expressions have been derived for the current gain characteristics of the converter in the buck and boost modes of operation and these have been validated both by simulation and by experimental results. It is shown that the auxiliary pole assists in achieving soft-switching over the full load range. As expected, the soft-switching boosts efficiency to more than 97 % over a wide load range in the practical converter. This is achieved at the expense of increased circuit complexity. On the other hand the topology which has been presented is extremely robust and operates to a large extent in a self-protected mode in which the well known shoot-through fault phenomenon cannot occur. It is also interesting to note that the auxiliary circuit does not contain a direct shoot-through path consisting of two active devices connected directly across the bus.

An investigation of performance factors for magnetic components is presented in Chapter 3 and novel performance factors are introduced. The well-established and intuitive performance factor approach has been extended to factor in the effects of saturation flux density

and thermal conductivity. Thus, the performance factors can now be used to aid in the selection of the optimum material for a dc inductor with ac ripple for convection or conduction cooling.

In general, the optimum materials change with specific power loss. There is a significant difference between the air-cooled and conduction-cooled performance factor as conduction-cooling can enable a very efficient heat removal and size reduction.

The conduction-cooled inductor performance factor chart highlights the capability of the material to remove heat together with saturation capability. The most suitable materials for a high-power-density inductor are those with high thermal conductivity and high saturation flux density. The optimum selection is strongly related to the thermal path length.

In general, the traditional laminated materials such as amorphous metal and silicon-steel are most suitable for a dc inductor with lower-frequency ac component while powder materials display advantages at higher frequencies. The ferrite material is best suited for ac designs and is severely penalized for dc applications due to low B_{sat}.

Technically, the nanocrystalline material has the best overall characteristics in almost all cases, but presently is significantly more expensive than the other materials. The cost and power loss of the nanocrystalline material increases further due to the manufacturing process required to cut the material. The best solution for an air-cooled ac inductor or transformer may be the ferrite material as it combines low power loss and low overall cost.

Although powerful, the performance factors are not the ultimate comparison methods as they do not consider the core geometry, winding arrangement, or efficiency. Nevertheless, the performance factor aids the material selection process by narrowing down the number of options. However, the final selection should be underpinned by the dedicated design comparison.

In Chapter 4 a novel approach to the inductor design algorithm is presented and used in order to compare the various magnetic materials over a range of frequencies, ripple ratios, two cooling methods and efficiency. The inductor design is considered as a multivariable function; therefore, the solution can be easily adjusted towards the design requirement. The modular structure of the design procedure allows for rapid design of any inductor with given constraints set.

As shown by the analysis the inductor size varies with current ripple for a given frequency. The minimum size is achieved for the design which meets temperature rise and flux density limitation at the same time. As the operating frequency increases, the current-ripple ratio for minimum size decreases. In general, the inductor size decreases as the frequency increases in the considered frequency range. The conduction-cooled design allows for very efficient cooling and significant size reduction can be achieved with respect to the air-cooled design. However, an

efficiency constraint can disturb this relation and cause inductor size to increase.

The analysis indicates that the right choice of the magnetic material results in the most optimum design size. The design constraints are operating frequency, current ripple, dc-bias, cooling method, maximum temperature rise, and efficiency.

In general inductor size decreases as frequency increases in the considered frequency range. The optimum current ripple decreases as frequency increases for a minimum area product analysis. This means that the component size decreases with frequency and the current ripple decreases as well. Since the minimum size at a given frequency is an unique property of the material with respect to the current ripple the most suitable material can be selected for the anticipated current ripple ratio.

In Chapter 5 the practical effects of frequency, dc-bias and duty cycle on core power loss, air-gap fringing on the core and winding losses, and core conduction cooling are experimentally investigated for the Fe-amorphous metal, 6.5% silicon steel and powder core.

The variation of the core loss of the various materials with frequency range is close to predictions by the specifications and algorithm developed in Chapter 4. The multi cut core displays elevated power loss due to manufacturing process.

All materials can experience increased core losses with dc bias and appropriate de-rating should be used when operating high on the magnetization curve. The investigation suggests de-rating at about 75 % of the nominal saturation flux density at 25 °C. Similarly, an asymmetric duty cycles result in increased core losses. The modified Steinmetz equation is a useful predictor of these increased losses.

It has been suggested in the literature [89][98] that increased core loss can occur due to air gap fringing. Testing is this study suggests that these effects can be insignificant for these cores with thin laminations and high resistivity. Distributing the air gap is shown to result in reduced copper losses, but added cuts can result in material degradation for amorphous metal

Finally, it is demonstrated than lamination direction is key to an optimum cooling path for the laminated gapped cores.

6.2. Future Work

Future work on the project may be divided into a number of areas all of which represent work outside the scope of the present thesis.

- **Interleaved converter with integrated magnetic**

  The hard-switched magnetic coupled dc-dc converter is increasingly pursued in recent years mainly by automakers as a main powertrain converter. The work on the magnetically-coupled dc-dc converter is continued in UCC and has already resulted in an APEC conference publication [68].

  In order to extend the power range, the soft-switching converter investigated in Chapter 2 may be configured into an interleaved topology with a coupled transformer and input inductor in order to reduce the size.

- **Wide band gap semiconductors**

  New wide band gap materials are characterised by low switching power loss and allow for a high switching frequency. The analysis conducted here in Chapters 3, 4, and 5 can be reproduced to determine the optimum materials at high frequencies.

- **Powder materials with an air gap**

  The design flowcharts are used for gapped materials with fixed permeability and for gapless materials with permeability as a function of dc-bias. Further development would be a design of a flowchart for powder inductor with an air gap as high permeability powder core displays lower power loss.

- **Optimum winding structures**

  The flowchart and analysis presented in Chapter 4 is based on the foil winding. Further work should be addressed to determine optimum winding structures for low to high frequency designs. This should include such effects as the core window fill factor, fringing flux effect on the winding power loss, proximity and skin effect, and thermal path.

- **Conduction cooling 2-D model**

  The flowchart presented in Chapter 4 uses a simplified 1-D cooling model. Future work should be addressed to increase model accuracy and development of the 2-D analytical model.

- **Improved performance factors**

  The various performance factors presented in Chapter 3 should be reviewed and investigated to possibly generate a more optimum version.

Bibliography

[1] "Global Warming," www.nytimes.com, 16th Aug 2010.

[2] "World Crude Oil Producers," www.mapsofworld.com, 16th Aug 2010.

[3] Matthew R. Simmons Chairman of Simmons & Company International, "What kangaroo court created our oil and gas markets?," Australian American Chamber of Commerce Houston, January 29, 2009.

[4] C.C. Chan and Y.S. Wong, "Electric vehicles charge forward" *IEEE power & energy magazine*, November/December 2004.

[5] Toyota Prius 2nd Generation Manual, Model 2004.

[6] J. Voelcker, "How green is my plug-in?," *spectrum.ieee.org*, March 2009.

[7] R.M. Schupbach, J.C. Balda, "35 kW ultracapacitor unit for power management of hybrid electric vehicles: bi-directional dc-dc converter design," *IEEE Power Electronics Specialists Conference*, 2004, pp. 2157-2163.

[8] F. Caricchi, F. Crescimbini, F. Giulii Capponi, L. Solero, "Study of bi-directional buck-boost converter topologies for application in electrical vehicle motor drives," *IEEE Applied Power Electronics Conference*, 1998, pp. 287-293.

[9] S. Waffler, J.W. Kolar, "A novel low-loss modulation strategy for high-power bi-directional buck+boost converters," 7*th International Conference on Power Electronics*, October 22-26, 2007/EXCO, Dageu, Korea, pp. 889-894.

[10] N. Nozawa, T. Maekawa, S. Nozawa, K. Asakura, "Development of power control unit for compact-class vehicle," *SAE International Journal of Passenger Cars-Electronic and Electrical Systems*, October 2009, vol. 2, no. 1, pp. 376-382.

[11] B. Eckardt, M. Marz, "A 100kW automotive powertrain dc/dc converter with 25kW/dm^3 by using SiC," *4th International Conference on Integrated Power Systems*, Naples, Italy, 2006.

[12] O. Garcia, P. Zumel, A. de Castro, J.A. Cobos, "Automotive dc-dc bidirectional converter made with many interleaved buck stages," *IEEE Transactions on Power Electronics*, Vol. 21, No. 3, May 2006, pp. 578-586.

[13] G. Caledron-Lopez, A.J. Forsyth, D.R. Nuttall, "Design and performance evaluation of a

10-kW interleaved boost converter for a fuel cell electric vehicle," *Power Electronics and Motion Control Conference,* IPEMC 2006, pp.1-5.

[14] G. Caledron-Lopez, A.J. Forsyth, "High-power dual-interleaved ZVS boost converter with interphase transformer for electric vehicles," *IEEE Applied Power Electronics Conference*, 2009, pp. 1078-1083.

[15] M. Olszewski, "Z-source inverter for fuel cell vehicles," U.S Department of Energy, 2005.

[16] D. Ho Lee, F.C. Lee, "Novel zero-voltage-transition and zero-current-transition pulse-width-modulation converters," *Power Electronics Specialists Conference*, 1997, Vol. 1, pp. 233-239.

[17] Wei Wen Yim-Shu Lee, Martin Hoi Lam Chow, David Ki-Wai Cheng, "Interleaved boost converter with zero diode reverse-recovery loss," *IEEE Transactions on Aerospace and Electronic Systems*, Vol. 40, No. 4, pp. 1271-1285.

[18] J. Abu-Qahouq, I. Batarseh, "Generalized analysis of soft-switching dc-dc converters," *IEEE International Symposium on Circuits and Systems*, Vol. 3, pp. 507-510.

[19] F.T. Wakabayashi, M.J. Bonato, C.A. Canesin, "A new family of zero-current-switching PWM converter," *PESC*, 1999, Vol. 1, pp. 451-456.

[20] S.G. Yoon, J.M. Lee, J.H. Park, I.K. Lee, B.H. Cho, "A frequency controlled bi-directional synchronous rectifier converter for HEV using super-capacitor," *PESC*, 2004, Vol. 1, pp. 135-140.

[21] A. Averberg, A. Mertens, "Characteristics of the single active bridge converter with voltage doubler," *IEEE EPE-PEMC*, 2008, pp. 213-220.

[22] J. Zhang, F. Zhang, X. Xie, D. Jiao, Z. Qian, "A novel ZVS dc-dc converter for high power applications," *IEEE Transactions on Power Electronics*, Vol. 19, No. 2, March 2004, pp. 420-429.

[23] J. Jacobs, A. Averberg, R. De Doncker, "A novel three-phase dc-dc converter for high-power applications," *PESC*, 2004, Vol. 3, pp. 1861-1867.

[24] K. Rigbers, P. Lurkens, M. Wendt, S. Schroder, U. Boke, R. De Doncker, "High-efficient soft-switching converter for three-phase grid connections of renewable energy systems," *International Conference on Power Electronics and Drives Systems*, 2005, Vol. 1, pp. 246-250.

[25] S.J. Jang, T.W. Lee, W.C. Lee, C.Y. Won, "Bi-directional dc-dc converter for fuel cell generation system," *PESC*, 2004, Vol. 6, pp. 4722-4728.

[26] H. Li, F.Z. Peng, J. Lawler, "A study of modeling and simulation for soft-switched bi-directional dc-dc converters," *IEEE Computer in Power Electronics, the 7th Workshop on*, 2000, pp. 68-73.

[27] R. De Doncker, *Power electronics for electric and hybrid vehicles; integration of power electronics in automotive applications; soft-switching dc-dc converters for supercapacitors and fuel cells*, EPE 2007 Tutorial Book.

[28] Martins, D.C.; de Seixas, F.J.M.; Brilhante, J.A.; Barbi, I., "A family of dc-to-dc PWM converters using a new ZVS commutation cell," *Power Electronics Specialists Conference*, 1993, pp. 524-530.

[29] S. Matsumoto, "Advancement of hybrid vehicle technology," *EPE-PEMC*, 2005.

[30] www.chevy-volt.net, Aug 2010.

[31] Holli Riebeek, "Global warming," www.earthobservatory.nasa.gov, 3rd June 2010.

[32] C. Harris, R. Mann, "Historical Worldwide Climate and Weather," www.longrangeweather.com, Aug 2010.

[33] M. King Hubbert, "Nuclear energy and the fossil fuels," Drilling and Production Practice, 1956.

[34] Hubbert peak theory, www.wikipedia.org, Aug 2010.

[35] Oil price history and analysis, www.wtrg.com, Aug 2010.

[36] History of Illinois basin posted crude oil prices, www.ioga.com, Aug 2010.

[37] Consumer Price Index inflation calculator, www.bls.gov, Aug 2010.

[38] Historical Crude Oil Prices, www.inflationdata.com, Aug 2010.

[39] J. Van Mierlo, "Propulsion systems for hybrid and fuel cell electric vehicles," EPE Tutorials, 2007.

[40] I. Cervantes, F.J. Perez-Pinal, J. Leyva-Ramos, A. Mendoza-Torres, "Hybrid control technique applied in a fc-sc electric vehicle platform," *IEEE VPPC*, 2010, pp. - .

[41] A. Thanheiser, D. Buecherl, H.G. Herzog, "Influence of different electrified vehicle concepts and driving cycles on the energetic efficiency of passenger cars,' *IEEE VPPC*, 2010, pp. -.

[42] P.T. Krein, 'Design and engineering of electric and hybrid automobiles," Department of Electrical and Computer Engineering University of Illinois at Urbana-Champaign, USA, 2006.

[43] UNECE Vehicle Regulations, "R 101 – Emissions of carbon dioxide and fuel consumption", Revision 2, 2005.

[44] M. Zolot, "Dual-source energy storage – control and performance advantages in advanced vehicles," *EVS-20*, 2003, pp. -.

[45] D.U. Sauer, *Propulsion systems for hybrid and fuel cell electric vehicles*, EPE 2007 Tutorial Book.

[46] D. Hissel, M.C. Pera, *Fuel cell systems for transportation applications*, VPPC 2010

Tutorials.

[47] M. Kabalo, B. Blunier, D. Bouquain, A. Miraoui, "State-of-the-art of dc-dc converters for fuel cell vehicles," *IEEE VPPC*, 2010, pp. -.

[48] J.G. Hayes, M. Rylko, M.G. Egan, "Technology review for electric vehicle charging," Technical Report for Irish Electricity Supply Board, January 2010.

[49] R. Severns, *Snubber circuits for power electronics*, Rudolf Severns 2008.

[50] J. Shen, "Advances and trends in power semiconductors," Tyndall presentation in Cork, March 2010.

[51] www.irf.com, Aug 2010.

[52] www.infineon.com, Aug 2010.

[53] www.abb.com, Aug 2010.

[54] Silicon carbide comes good in 2H09, www.imsresearch.com, 28th April 2010.

[55] SiC & GaN Power – Quarterly Market Watch, www.imsresearch.com, April 2010.

[56] Silicon-Carbide (SiC) transistors - future markets for SiC electronics, www.electronics.ca, 29th Sep 2009

[57] www.semisouth.com, Aug 2010.

[58] www.cree.com, Aug 2010.

[59] www.transic.com, Aug 2010.

[60] www.epcos.com, Aug 2010.

[61] www.kemet.com, Aug 2010.

[62] www.avx.com, Aug 2010.

[63] L. Lorenz, G. Deboy, I. Zverev, "Matched pair of CoolMOS transistor with SiC-Shottky diode – advantages in application," *IEEE Transactions on Industry Applications*, Vol. 40, No. 5, September/October 2004, pp. 1265-1272.

[64] Russi, J.; Martins, M.L.; Grundling, H.A.; Pinheiro, H.; Pinheiro, J.R.; Hey, H.L., "A design criterion to ZVT DC-DC PWM converters with constant auxiliary voltage source," *IEEE Transactions on Industrial Electronics*, 2003, pp. 527 – 532.

[65] Barbi, I., Martins, D.C., "A true PWM zero-voltage switching pole with very low additional RMS current stress," *Power Electronics Specialists Conference*, 1991, pp. 261-267.

[66] de Seixas, F.J.M., Martins, D.C., "The ZVS-PWM commutation cell applied to the dc-ac converter," *IEEE Transactions on Power Electronics*, 1997, pp. 726-733.

[67] J. Walczak, M. Pasko, *Elementy dynamiki liniowych obwodow elektrycznych*, Wydawnictwo Politechniki Slaskiej, Gliwice 2001.

[68] K.J. Hartnett, M.S. Rylko, J.G. Hayes, M.G. Egan, "A comparison of classical two phase

(2L) and transformer — coupled (XL) interleaved boost converters for fuel cell applications," *IEEE Applied Power Electronics Conference*, 2010, pp. 787-793.

[69] Brian J. Masserant, E. William Beans, Thomas A. Stuart, "A study of volume versus frequency for soft switching IGBT converters," IEEE *Transactions on Aerospace and Electronic Systems*, Vol. 31, No. 1, January 1995, pp. 280-287.

[70] Robert A. Jensen, Charles R. Sullivan, "Optimal core dimensional ratios for minimizing winding loss in high frequency gapped-inductor windings," *IEEE Applied Power Electronics Conference*, 2003, pp. 1164-1169.

[71] M. Gerber, J.A. Ferreira, I.W. Hofsajer and N. Seliger, "A very high density, heatsink mounted inductor for automotive applications," *IEEE Industry Applications Conference*, 2002, pp. 948-954.

[72] www.metglas.com, Aug 2010.

[73] www.amtmagnetics.com, April 2008

[74] www.jfe-steel.co.jp, Aug 2010.

[75] www.vacuumschmelze.de, Aug 2010.

[76] www.ferroxcube.com, Aug 2010.

[77] www.micrometals.com, Aug 2010.

[78] www.mag-inc.com, Aug 2010.

[79] www.changsung.com, Aug 2010.

[80] www.arnoldmagnetics.com, Aug 2010.

[81] B.J. Lyons, J.G. Hayes, M.G. Egan, "Magnetic material comparisons for high-current inductors in low-medium frequency dc-dc converters," *IEEE Applied Power Electronics Conference*, 2007, pp. 71-77.

[82] B.J. Lyons, J.G. Hayes, M.G. Egan, "Experimental Investigation of Iron-based Amorphous Metal and 6.5% Silicon Steel for high-current inductors in low-medium frequency dc-dc Converters," *IEEE Industrial Applications Conference*, 2007, pp. 1781-1786.

[83] M.S. Rylko, B.J. Lyons, K.J. Hartnett, J.G. Hayes, M.G. Egan, "Magnetic material comparisons for high-current gapped and gapless foil wound inductors in high frequency dc-dc converters," *EPE-PEMC*, 2008, pp. 1249-1256.

[84] M.S. Rylko, K.J. Hartnett, J.G. Hayes, M.G. Egan, "Magnetic material selection for high power high frequency inductors in dc-dc converters," *IEEE Applied Power Electronics Conference*, 2009, pp. 2043-2049.

[85] J. Petzold, "Advantages of soft magnetic nanocrystalline materials for modern electronic applications," *Journal of Magnetism and Magnetic Materials*, 2002, pp. 84 - 89.

[86] H. Gavrila, V. Ionita, "Crystalline and amorphous soft magnetic materials and their applications – status of art and challenges," *Journal of Optoelectronics and Advanced Materials*, June 2002, pp. 173-192.

[87] Robert W. Erickson, *Fundamentals of Power Electronics*, Kluwer Academic Publishers, 2000.

[88] Alex Van den Bossche, Vencislav Cekov Valchev, *Inductors and Transformers for Power Electronics*, CRC Press, 2005.

[89] Colonel Wm. T. McLyman, *Transformer and Inductor Design Handbook*, 2nd ed., Marcel Dekker, Inc., 1988.

[90] www.hyperphysics.phy-astr.gsu.edu, Aug 2010.

[91] Michael J. Moran, Howard N. Shapiro, *Fundamentals of Engineering Thermodynamics*, VCH Wiley, 1988.

[92] B.J. Lyons, J.G. Hayes, M.G. Egan, "Design algorithm for high-current gapped foil-wound inductors in low-to-medium frequency dc-dc converters," *IEEE Power Electronics Specialists Conference, 2007*, pp. 1760-1766.

[93] Sanjaya Maniktala, *Switching Power Supply Design & Optimization*, McGraw-Hill, 2004.

[94] Charles R. Sullivan, "Aluminium windings and other strategies for high frequency magnetics design in an era of high copper and energy costs," *IEEE Applied Power Electronics Conference*, 2007, pp. 78-84.

[95] Z. Cichowska, M. Pasko, *Wyklady z Elektrotechniki Teoretycznej*, 2nd ed., Wydawnictwo Politechniki Slaskiej, Gliwice 1998.

[96] Xi Nan, Charles R. Sullivan, "An improved calculation of proximity-effect loss in high-frequency windings of round conductors," *IEEE Power Electronics Specialist Conference*, 2003, pp. 853-860.

[97] J. Reinert, A.Brockmeyer, R.W.A.A. De Doncker, "Calculation of losses in ferro- and ferromagnetic materials based on the modified Steinmetz equation," *IEEE Transactions on Industry Applications*, Vol. 37, No. 4, July/August 2001, pp. 1055-1061.

[98] Reuben Lee, *Electronic Transformers and Circuits*, 2nd ed., John Wiley & Sons, Inc., 1955.

[99] C.A. Baguley, B. Carsten, U.K. Madawala, "The effect of dc bias conditions on ferrite core losses," *IEEE Transactions on Magnetics*, Vol. 44, No. 2, February 2008, pp. 246-252.

[100] M. Namikawa, H. Ninomiya, T. Yamaji, "High silicon steel sheets realizing excellent high frequency reactor performance," *JFE Technical Report*, 2005.

[101] A. Van den Bossche, V.C. Valchev, "Modeling ferrite core losses in power electronics,"

International Review of Electrical Engineering (I.R.E.E.), Vol. xx, n. x.

[102] K. Venkatachalam, C.R. Sullivan, T. Abdallah, H. Tacca, "Accurate prediction of ferrite core loss with nonsinusoidal waveforms using only Steinmetz," *IEEE Workshop on Computers in Power Electronics*, June 2002, pp. .

[103] Wei Shen; Fei Wang; D. Boroyevich; C. W. Tipton , "Loss Characterization and Calculation of Nanocrystalline Cores for High-Frequency Magnetics Applications," *IEEE Transactions on Power Electronics*, vol.23, no.1, pp.475-484, Jan. 2008.

[104] S. Nogawa, M. Kuwata, D. Miyagi, T. Hayashi, H. Tounai, T. Nakau, N. Takahashi, "Study of eddy-current loss reduction by slit in reactor core," *IEEE Transactions on Magnetics*, Vol. 41, No. 5, May 2005, pp. 2024-2027.

[105] S. Nogawa, M. Kuwata, T. Nakau, D. Miyagi, N. Takahashi, "Study of modelling method of lamination reactor core," *IEEE Transactions on Magnetics*, Vol. 42, No. 4, April 2006, pp. 1455-1458.

[106] Jiankun Hu and C. R. Sullivan, "AC resistance of planar power inductors and the quasi-distributed gap technique," *IEEE Transactions on Power Electronics*, vol. 16 , pp. 558-567, 2001.

[107] www.quickfield.com, December 2010.

Appendix A

Soft-Switched DC-DC Converter

A.1. Transformer Current Transient Between Modes 5 and 6

A current in the transformers primary winding change its direction as the auxiliary switch is turned off at the end of mode 5. The primary winding is in series with the resonant inductance L_r . The converters operation during mode 5 is shown in Figure A.1. The cell resonant current is closing through the upper auxiliary switch and resonant inductor and main switch. The switching cell equivalent circuit in mode 5 is shown in Figure A.2. Since the equivalent series resistance is neglected the same voltage is applied across the resonant circuit and the resonant and magnetizing currents are constant. At time when switch S_{AU} opens the circuit equilibrium shown in Figure A.2 is disturbed. The circuit transient is shown in Figure A.3. The current in the circuit changes in time and is transferred through transformers coupling. The resonant and magnetizing inductance energy is changing in pursue for a new equilibrium. Laplace transformation is employed and initial conditions for resonant current $i_r(0)$ and magnetizing current $i_m(0)$ are given in mode 5. The voltage V_X induced across the switch and magnetizing current after transient is pursued.

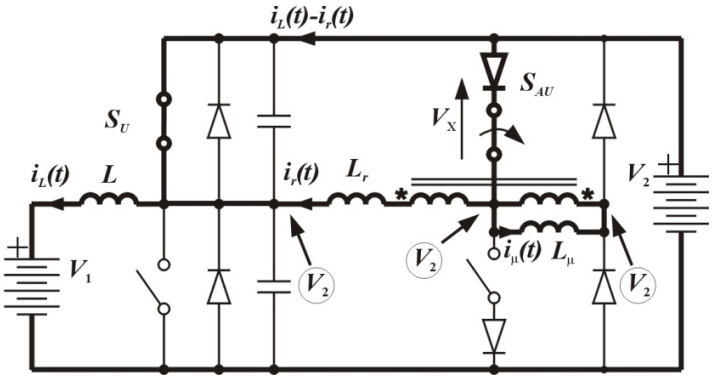

Figure A.1. Mode 5 circuit operation.

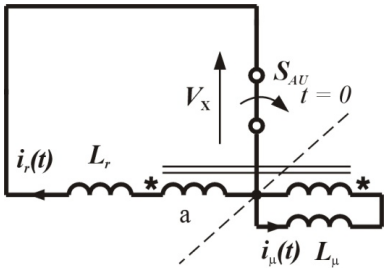

Figure A.2. Mode 5 resonant cell current.

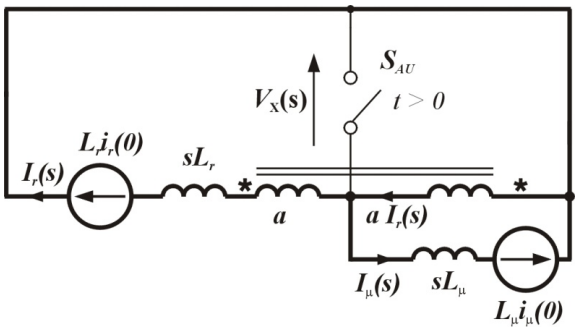

Figure A.3. Switch open transient.

From the Figure A.3 can be written:

$$\begin{cases} V_X(s) = L_m i_m(0) - sL_m I_m(s) \\ V_X(s) = L_r i_r(0) - sL_r I_r(s) + aV_X(s) \\ I_r(s) + I_m(s) = a\,I_r(s) \\ i_m(0) = a\,i_r(0) \end{cases} \tag{A.1}$$

and results in following solution:

$$\begin{cases} V_X(s) = \dfrac{(2a-1)}{a} \dfrac{L_m L_r i_m(0)}{L_r - L_m(1-a)^2} \\ I_m(s) = \dfrac{(1-a)}{s} \dfrac{(1-a)L_m i_m(0) - L_r i_r(0)}{L_r + (1-a)^2 L_m} \end{cases} \tag{A.2}$$

Finally in time domain:

$$\begin{cases} V_X(t) = L^{-1}\{V_X(s)\} = \delta(t) \\ I_m(t) = L^{-1}\{I_m(s)\} = (1-a)\dfrac{(1-a)L_m i_m(0) - L_r i_r(0)}{L_r + (1-a)^2 L_m} \end{cases} \tag{A.3}$$

As expected, the voltage is represented by Dirac function or a voltage spike. The magnetizing current change depends on the resonant and magnetizing inductance ratio. The current change is related to the energy stored in the inductor given by (A.4).

$$E = \frac{1}{2} L I^2 \tag{A.4}$$

If the energy stored in magnetizing inductance is greater than in resonant inductor, which is the usual case, the current in the resonant inductor change its flow direction rapidly accompanied by the voltage spike. In real circuit, part of transition energy is dissipated in cells ESR and transistor itself. This has its effect in the auxiliary switch power loss and may affect reliability if left unattended. In order to limit sudden voltage increase the transistor switching process is slowed, which is common practice. It is safe and convenient solution as auxiliary cell switching current is rather low. The magnetizing and resonant current are constant after transient as circuits resistance is neglected.

The transformer current in the mode 6 reaches its new equilibrium as shown in Figure A.4. The current change is given by:

$$i_r(t) = \frac{i_m(t)}{1-a} \tag{A.5}$$

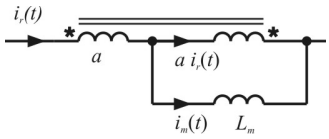

Figure A.4. Cell current distribution in mode 6.

A.2. Main Switch Turn-off Assisted by Soft-Switching Cell

The soft switched dc-dc converter main transistor turn-off may be assisted by soft-switching cell; otherwise the turn-off is in a hard switching mode softened by the output capacitive snubber. The classical capacitance assisted turn-off is presented in number of publications as [49][87][93] and turn-off time t_{off} is a function of the output capacitance C_{out}, transistor current I_{off} and off voltage V_{off}.

$$t_{off} = \frac{C_{out} V_{off}}{I_{off}} \tag{A.6}$$

Since the turn off transient time depends on the transistor current it will take a significant time to recharge capacitor at low current, while the turn-off time will reduce at high current.

The soft-switching cell allows for controlled capacitance recharge. The turn-off time is dependent on the transistor current; however, a low current switching time is reduced by the soft-switching cell.

The soft-switching cell assisted turn-off process involves resonant transient in a similar fashion as turn-on, but with a different initial conditions. The resonant capacitance is already charged and turn-off process is aimed to discharge the capacitance. The buck and boost mode equivalent circuits for initial conditions are shown in Figure A.5 and Figure A.7, while the transient Laplace equivalent circuits are shown in Figure A.6 and Figure A.8, respectively.

The presented equivalent circuit shows capacitors with non-zero initial conditions. The transformer with accompanying circuitry was simplified to a voltage source. Input filter inductor and voltage source V_1 is substituted by a current source $I_1(s)$. Equivalent circuit resistances R_1 and R_2 are considered. The transformer magnetizing current is neglected.

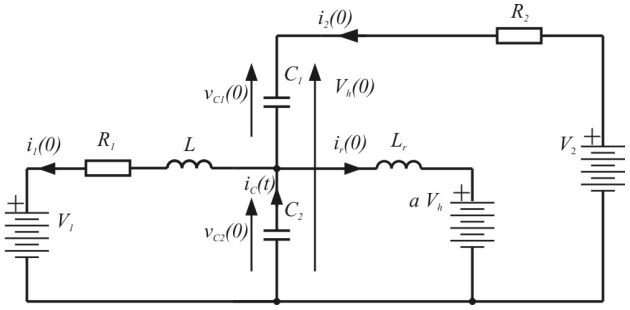

Figure A.5. Buck mode main transistor turn-off initial conditions.

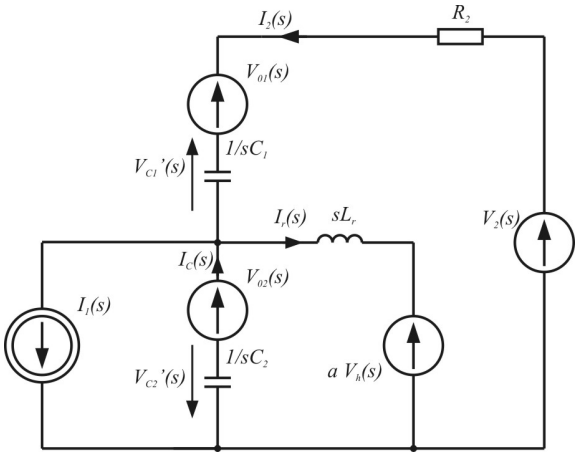

Figure A.6. Buck mode transient circuit for the main transistor turn-off.

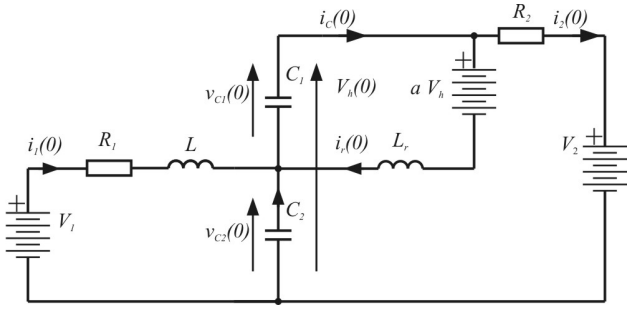

Figure A.7. Boost mode main transistor turn-off initial conditions.

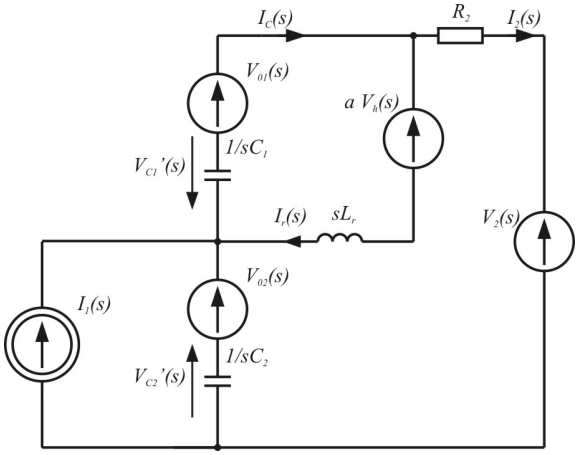

Figure A.8. Boost mode transient circuit for the main transistor turn-off.

The transient solution for buck and boost is similar. Following calculations are provided for a boost mode.

Circuit is assumed to be symmetrical $C_1 = C_2$. The initial conditions for a boost mode are following: $V_{01}(s) = V_h(s)$, $V_{02}(s) = 0$, where $V_h(s) = V_{h2}(s) + R_2 I_2(s)$. From KVL it can be written:

$$sL_r I_r(s) + aV_h(s) - V_{01}(s) + \frac{1}{sC_1} I_c(s) = 0 \tag{A.7}$$

since

$$I_c(s) = 0.5\left[I_1(s) + I_r(s)\right] \tag{A.8}$$

and

$$I_2(s) = 0.5\left[I_1(s) - I_r(s)\right] \tag{A.9}$$

After transformations the resonant current is found as

$$I_r(s) = \frac{\frac{1}{L_r}\left[V_{01}(s) - aV_2(s) - 0.5aR_2 I_1(s)\right]}{s^2 - a\frac{R_2}{2L_r}s + \frac{1}{2L_r C_r}} - \frac{\frac{1}{2L_r C_1} I_1(s)}{s\left(s^2 - a\frac{R_2}{2L_r}s + \frac{1}{2L_r C_r}\right)} \tag{A.10}$$

And can be written as:

$$I_r(s) = \frac{N_1}{D} - \frac{N_2}{sD} \tag{A.11}$$

The characteristic equation has following complex solution

$$s^2 - a\frac{R_2}{2L_r}s + \frac{1}{2L_rC_r} = 0 \tag{A.12}$$

$$\Delta = \left(\frac{aR_2}{2L_r}\right)^2 - \frac{2}{L_rC_r}s^2 < 0 \tag{A.13}$$

$$s_1, s_2 = \frac{aR_2}{4L_r} \pm \sqrt{\left(\frac{aR_2}{4L_r}\right)^2 - \frac{1}{2L_rC_r}} = \alpha \pm j\omega_0 \tag{A.14}$$

Where

$$\omega_0 = \sqrt{\alpha^2 - \omega_n{}^2}\,, \qquad \omega_n = \sqrt{\frac{1}{2L_rC_r}} \tag{A.15}$$

The back transformation:

$$\begin{aligned} i_r(t) &= L^{-1}\{I_r(s)\} = \\ &= \left[\underset{s=s_1}{res}\frac{N_1e^{s_1t}(s-s_1)}{(s-s_1)(s-s_2)} + \underset{s=s_2}{res}\frac{N_1e^{s_2t}(s-s_2)}{(s-s_1)(s-s_2)}\right] \\ &-\left[\underset{s=s_1}{res}\frac{N_2e^{s_1t}(s-s_1)}{s(s-s_1)(s-s_2)} + \underset{s=s_2}{res}\frac{N_2e^{s_2t}(s-s_2)}{s(s-s_1)(s-s_2)} + \underset{s=0}{res}\frac{N_2e^{0t}s}{s(s-s_1)(s-s_2)}\right] \end{aligned} \tag{A.16}$$

Finally

$$i_r(t) = \frac{N_1e^{s_1t}}{s_1-s_2} + \frac{N_1e^{s_2t}}{s_2-s_1} - \left[\frac{N_2e^{s_1t}}{s_1(s_1-s_2)} + \frac{N_2e^{s_2t}}{s_2(s_2-s_1)} + \frac{N_2}{s_1s_2}\right] \tag{A.17}$$

Neglecting resistance the resonant current equals:

$$i_r(t) = \frac{(1-a)V_2}{Z_0}\sin\omega_0t + I_1(\cos\omega_0t - 1) \tag{A.18}$$

The associated capacitor voltage is given by

$$V_{C1}(s) = V_{01}(s) - V'_{C1}(s) \tag{A.19}$$

$$V'_{C1}(s) = \frac{1}{sC_1}I_C(s) \tag{A.20}$$

Substituting (A.8) and (A.10) the capacitor voltage is

$$V'_{C1}(s) = \frac{I_1}{2s^2C_1} + \frac{\frac{1}{2L_rC_1}[V_{01} - aV_2 - 0.5aR_2I_1]}{s(s-s_1)(s-s_2)} - \frac{\frac{1}{4L_rC_1^2}I_1}{s^2(s-s_1)(s-s_2)} \tag{A.21}$$

The back transformation has three components:

$$V'_{C1}(s) = L^{-1}\left\{\frac{I_1}{2s^2C_1}\right\} + L^{-1}\left\{\frac{\frac{1}{2L_rC_1}\left[V_{01} - aV_2 - 0.5aR_2I_1\right]}{s(s-s_1)(s-s_2)}\right\} - L^{-1}\left\{\frac{\frac{1}{4L_rC_1^2}I_1}{s^2(s-s_1)(s-s_2)}\right\} \tag{A.22}$$

Because components of characteristic equations contain multiple poles a differential residuum theorem is employed [67]:

$$\underset{s=s_k}{res}\left[F(s)e^{st}\right] = \frac{1}{(\alpha_k - 1)!}\lim_{s\to s_k}\left\{\frac{d^{\alpha_k - 1}}{ds^{\alpha_k - 1}}\left[F(s)(s-s_k)^{\alpha_k}e^{st}\right]\right\} \tag{A.23}$$

where

α_k –pole s_k multiplicity of function $F(s)$

Hence first component of (A.22) is as follows

$$L^{-1}\left\{\frac{I_1}{2s^2C_1}\right\} = \underset{s=0}{res}\left[\frac{1}{s^2}\frac{I_1}{2C_1}e^{st}\right] = 1\cdot\lim_{s\to 0}\left(\frac{d}{dt}\frac{1}{\cancel{s^2}}\frac{I_1}{2C_1}e^{st}\cancel{s^2}\right) = \lim_{s\to 0}\left(\frac{I_1}{2C_1}te^{st}\right) = \frac{I_1}{2C_1}t \tag{A.24}$$

The second component of (A.22) is found in a similar way to the resonant current in (A.16)

$$L^{-1}\left\{\frac{\frac{1}{2L_rC_1}\left[V_{01} - aV_2 - 0.5aR_2I_1\right]}{s(s-s_1)(s-s_2)}\right\} = \frac{N_1e^{s_1t}}{s_1(s_1-s_2)} + \frac{N_1e^{s_2t}}{s_2(s_2-s_1)} + \frac{N_1}{s_1s_2} \tag{A.25}$$

Where N_1 is the nominator of a left hand side.

The last component of (A.22) employs differential residuum theorem and theorems of derivative of product of two functions and derivative of quotient of two functions shown in (A.26) and (A.27), respectively.

$$\left[g(x)\cdot h(x)\right]' = g'(x)\cdot h(x) + g(x)\cdot h'(x) \tag{A.26}$$

$$\left[\frac{g(x)}{h(x)}\right]' = \frac{g'(x)\cdot h(x) - g(x)\cdot h'(x)}{\left[h(x)\right]^2} \tag{A.27}$$

Hence the following solution

$$L^{-1}\left\{\frac{\frac{1}{4L_rC_1^2}I_1}{s^2(s-s_1)(s-s_2)}\right\} = \frac{N_2t}{s_1s_2} + \frac{N_2}{s_1s_2^2} + \frac{N_2}{s_1^2s_2} + \frac{N_2e^{s_1t}}{s_1^2(s_1-s_2)} + \frac{N_2e^{s_2t}}{s_2^2(s_2-s_1)} \tag{A.28}$$

where N_2 is the nominator of left hand side.

Finally the capacitor voltage change is given as follows:

$$V'_{C1}(t) = \frac{I_1}{2C_1}t + \frac{N_1 e^{s_1 t}}{s_1(s_1 - s_2)} + \frac{N_1 e^{s_2 t}}{s_2(s_2 - s_1)} + \frac{N_1}{s_1 s_2} - \left[\frac{N_2 t}{s_1 s_2} + \frac{N_2}{s_1 s_2^2} + \frac{N_2}{s_1^2 s_2} + \frac{N_2 e^{s_1 t}}{s_1^2(s_1 - s_2)} + \frac{N_2 e^{s_2 t}}{s_2^2(s_2 - s_1)}\right] \tag{A.29}$$

where

$$N_1 = \frac{1}{2L_r C_1}\left[V_{01} - aV_2 - 0.5aR_2 I_1\right] \tag{A.30}$$

$$N_2 = \frac{1}{4L_r C_1^2} I_1 \tag{A.31}$$

$$s_1, s_2 = \frac{aR_2}{4L_r} \pm \sqrt{\left(\frac{aR_2}{4L_r}\right)^2 - \frac{1}{2L_r C_1}} \tag{A.32}$$

The capacitor voltages are given as follows:

$$V_{C1}(t) = V_{01} - V'_{C1}(t) \tag{A.33}$$

$$V_{C2}(t) = V_h - V_{C1}(t) \tag{A.34}$$

Neglecting the resistance and assuming the circuit symmetry ($C_1 = C_2 = C_r$ and $V_{01} = V_{02} = V_2$) the capacitor voltage change given by (A.29) can be reduced to:

$$V'_{C1}(t) = \frac{I_1}{2C_r}t - (1-a)V_2(\cosh s_1 t - 1) - \frac{I_1}{4L_r C_r^2}\left(\frac{\sinh s_1 t}{s_1^3} - \frac{t}{s_1^2}\right) \tag{A.35}$$

Since

$$s_1, s_2 = \pm\sqrt{-\frac{1}{2L_r C_1}} = \pm j\omega_0 \tag{A.36}$$

$$s_1^* = s_2, \qquad s_1 s_1^* = \omega_0 \tag{A.37}$$

and

$$\cosh j\omega t = \cos\omega t, \qquad \sinh j\omega t = j\sin\omega t \tag{A.38}$$

Finally the following capacitor voltage can be found

$$V_{C1}(t) = (1-a)V_2(1 - \cos\omega_0 t) + Z_0 I_1 \sin\omega_0 t \tag{A.39}$$

Thus the buck and boost mode pole voltage change during the main transistor turn off can be found. Since the boost pole voltage change from 0 to V_2 a rise time can be found from the equality:

$$V_2 = (1-a)V_2(1 - \cos\omega_0 t) + Z_0 I_1 \sin\omega_0 t \tag{A.40}$$

Finally the time duration is given

$$t = \frac{1}{\omega_0}\arccos\frac{-a(1-a)V_2^2 + Z_0 I_1\sqrt{V_2^2(1-2a)+Z_0^2 I_1^2}}{(1-a)^2 V_2^2 + Z_0^2 I_1^2} \tag{A.41}$$

Note that for a very small current the solution limit is the turn on resonant swing time:

$$\lim_{I_1\to 0}\left\{\frac{1}{\omega_0}\arccos\frac{-a(1-a)V_2^2 + Z_0 I_1\sqrt{V_2^2(1-2a)+Z_0^2 I_1^2}}{(1-a)^2 V_2^2 + Z_0^2 I_1^2}\right\} = \frac{1}{\omega_0}\arccos\left(\frac{-a}{1-a}\right) \tag{A.42}$$

When compared to capacitive snubber, the soft-switching cell reduces turn-off time at low current as shown in Figure A.9. The turn-off time difference vanishing as current increase. This soft-switching cell property allows for a soft switching in the entire region of converters operation.

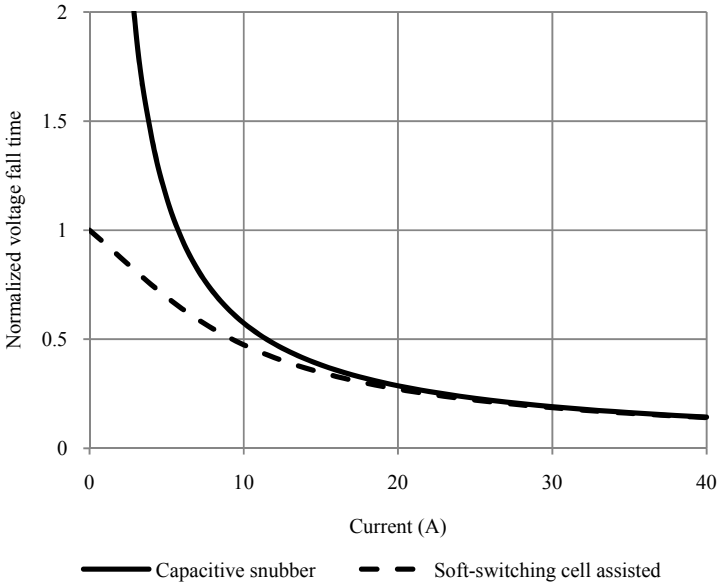

Figure A.9. The capacitor voltage fall time as a function of the inductor current.

A.3. PSpice Simulation Schematic of the Soft-Switching Converter

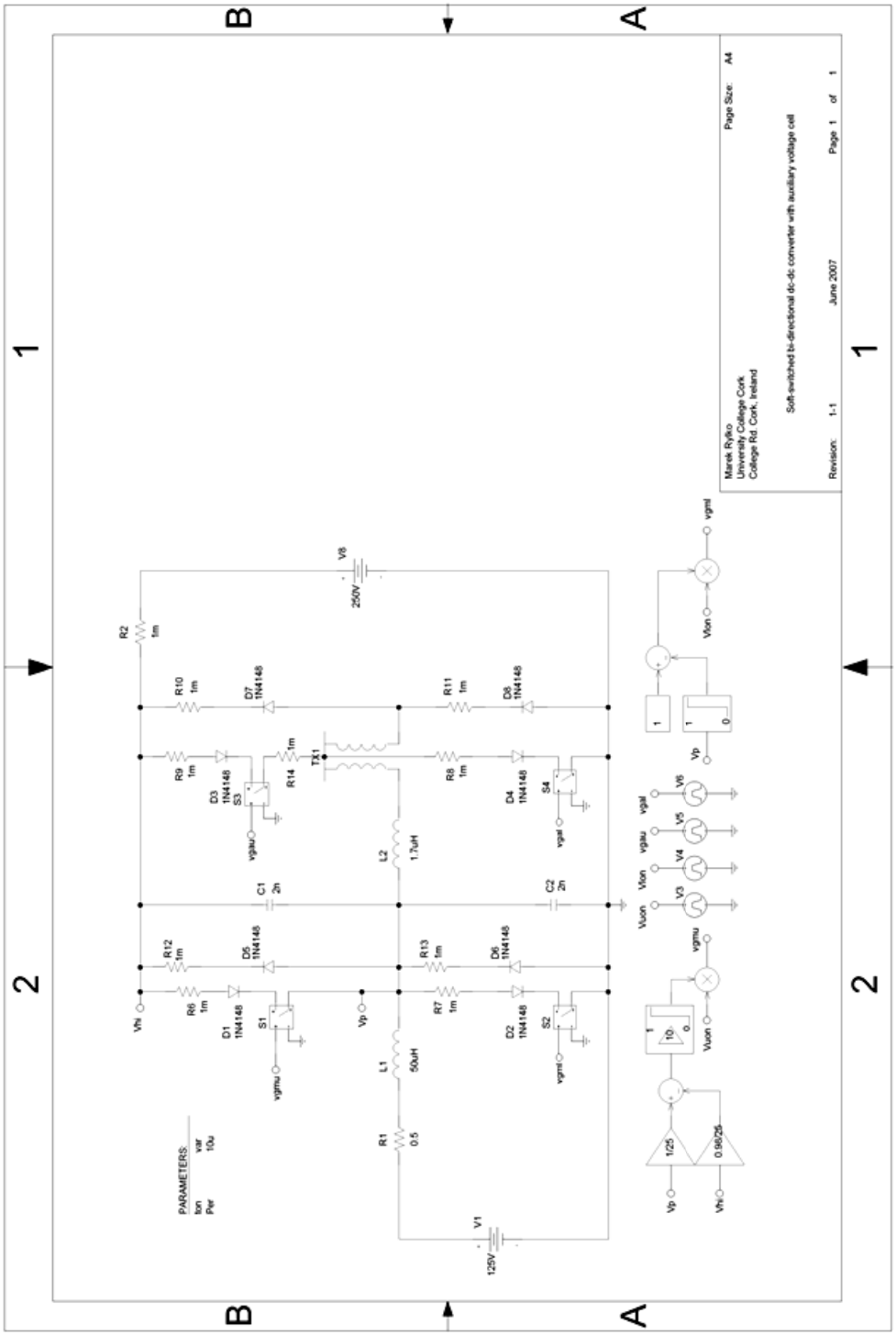

A.4. Resonant Cell ESR Effect on Transformers Voltage Ratio

This section provides detailed solution of the 2nd order resonance with a low damping factor. The soft switching cell equivalent circuit in Mode 2 is shown in Figure A.10.

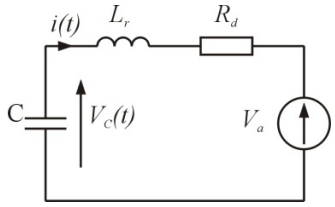

Figure A.10. Resonant mode equivalent circuit.

The solution is a total of steady-state and transient analysis:

$$V_c(t) = v_{st}(t) + v_{tr}(t) \tag{A.43}$$

The steady-state solution is following

$$v_c(t) = V_a \quad \text{and} \quad i(t) = 0 \tag{A.44}$$

The transient analysis require to solve 2nd order differential equation. From KVL we can write:

$$v_c(t) + L_r \frac{di(t)}{dt} + R_d i(t) = V_a \tag{A.45}$$

knowing that

$$i(t) = C \frac{dv_c(t)}{dt} \tag{A.46}$$

And substituting into (A.45) we get

$$v_c(t) + L_r C \frac{d^2 v_c(t)}{dt^2} + R_d C \frac{dv_c(t)}{dt} = V_a \tag{A.47}$$

The characteristic equation

$$L_r C \frac{d^2 v_c(t)}{dt^2} + R_d C \frac{dv_c(t)}{dt} + v_c(t) = 0 \tag{A.48}$$

Introducing differential operator p it can be written as

$$L_r C p^2 + R_d C p + 1 = 0 \tag{A.49}$$

and result in following solution

$$p_{1,2} = -\frac{R_d}{2L_r} \pm \sqrt{\left(\frac{R_d}{2L_r}\right)^2 - \frac{1}{L_r C}} = -\alpha \pm \sqrt{\alpha^2 - \omega_0^2} \tag{A.50}$$

where α is a damping factor and ω_0 is a pulsation of L_rC oscillation.

For $\alpha < \omega_0$ and $\Delta < 0$ the solution has two conjugated poles and the circuit is oscillating:

$$p_1 = -\alpha + j\omega, \qquad p_2 = -\alpha - j\omega = p_1^*, \qquad \omega = \sqrt{\left|\omega_0^2 - \alpha^2\right|} \tag{A.51}$$

The transient voltage

$$v_c(t) = A_1 e^{p_1 t} + A_2 e^{p_2 t} \tag{A.52}$$

Substituting (A.44) and (A.52) into (A.43)

$$V_c(t) = V_a + A_1 e^{p_1 t} + A_2 e^{p_2 t} \tag{A.53}$$

And solving

$$\begin{cases} V_c(0) = V_a + A_1 + A_2 \\ \left.\dfrac{dV_c(t)}{dt}\right|_{t=0} = 0 = A_1 p_1 + A_2 p_2 \end{cases} \tag{A.54}$$

$$\begin{cases} V_2 = a V_2 + A_1 + A_2 \\ 0 = A_1 p_1 + A_2 p_2 \end{cases} \tag{A.55}$$

$$\begin{cases} A_1 = (1-a) V_2 \dfrac{-p_2}{p_1 - p_2} \\ A_2 = (1-a) V_2 \dfrac{p_1}{p_1 - p_2} \end{cases} \tag{A.56}$$

Finally

$$V_c(t) = a V_2 + (1-a) V_2 \left[\frac{\alpha + j\omega}{2j\omega} e^{(-\alpha + j\omega)t} + \frac{-\alpha - j\omega}{2j\omega} e^{(-\alpha - j\omega)t} \right] \tag{A.57}$$

Having kown

$$\sin \omega t = \frac{e^{j\omega t} - e^{-j\omega t}}{2j} \quad \text{and} \quad \cos \omega t = \frac{e^{j\omega t} + e^{-j\omega t}}{2} \tag{A.58}$$

The (A.57) can be written as

$$V_c(t) = a V_2 + (1-a) V_2 e^{-\alpha t} \left(\frac{\alpha}{\omega} \sin \omega t + \cos \omega t \right) \tag{A.59}$$

A.5. TMS320F2808 Based Board Schematics

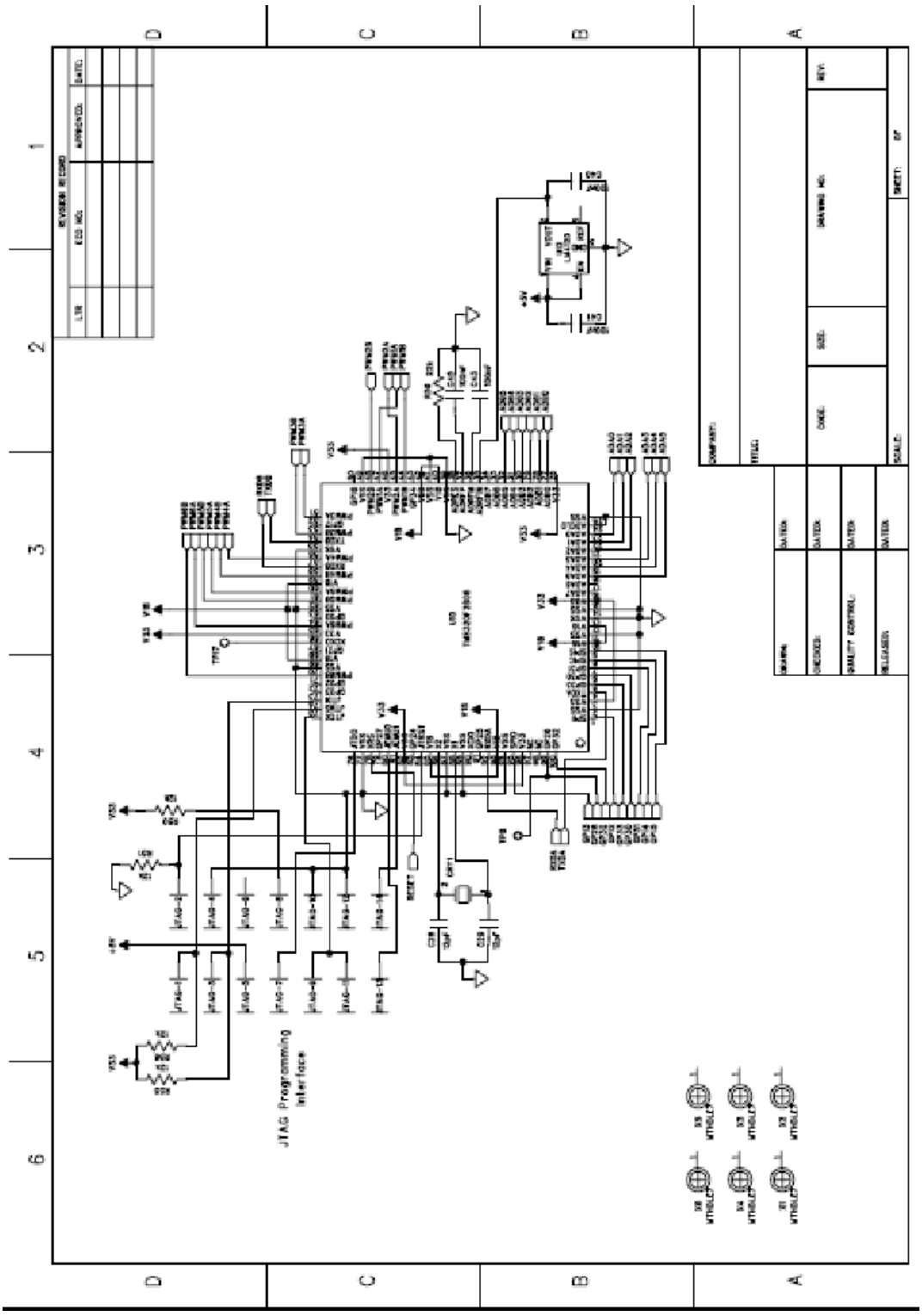

Figure A.11. Main TMS320F2808 connection schematic.

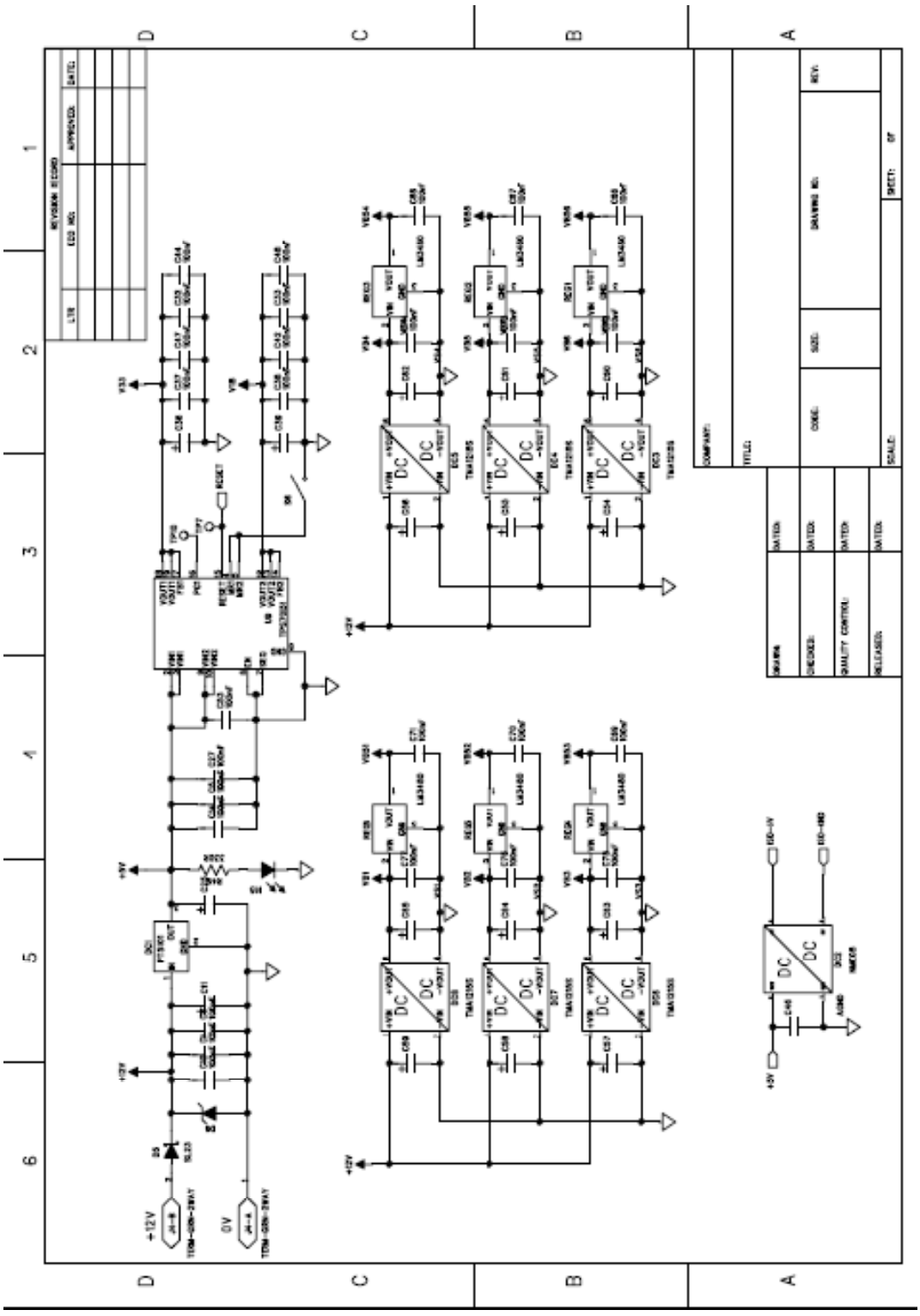

Figure A.12. Power supply and decoupling capacitors.

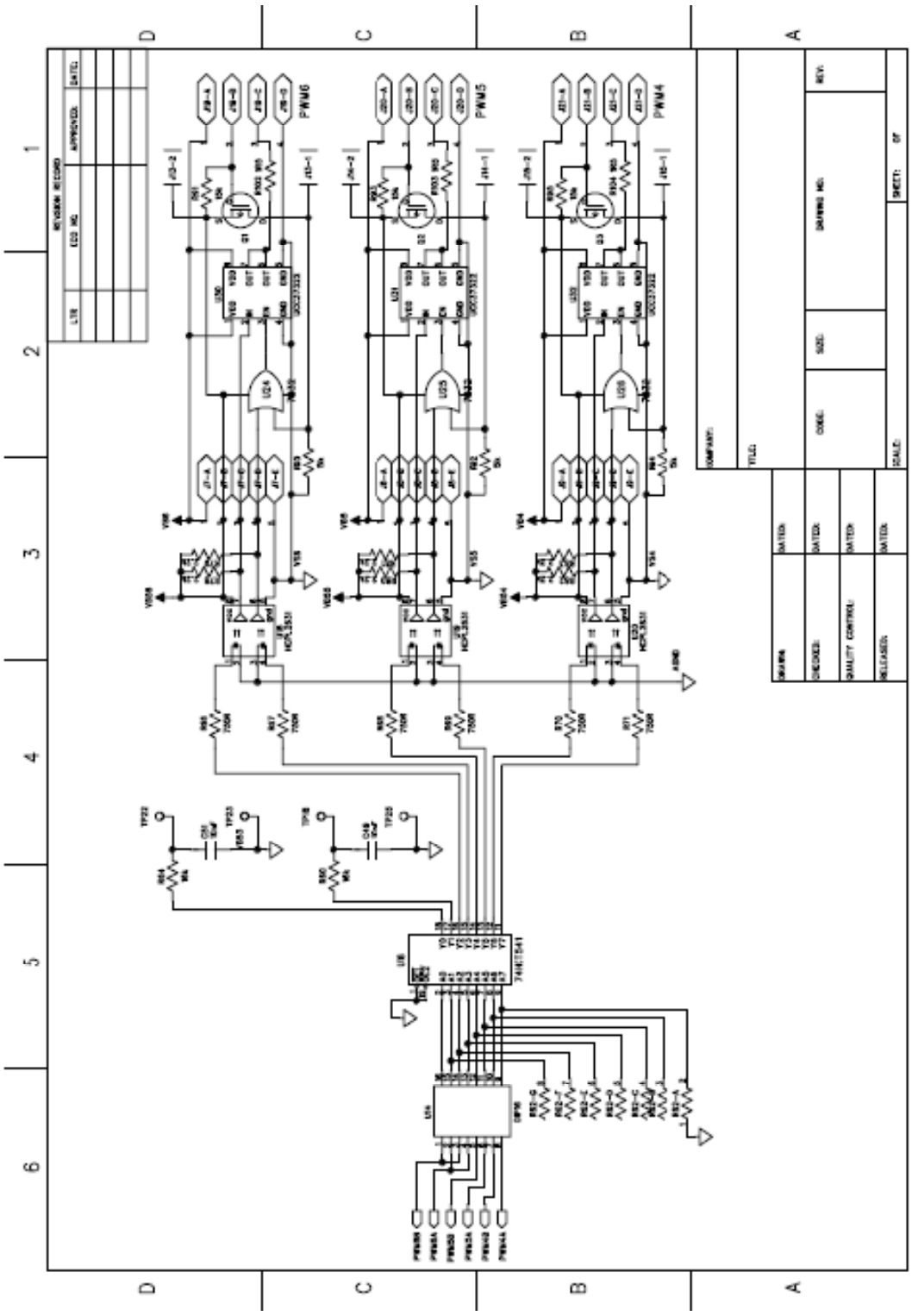

Figure A.13. PWM outputs with tranzistor drivers. Upper 3 channels with a zero voltage detection.

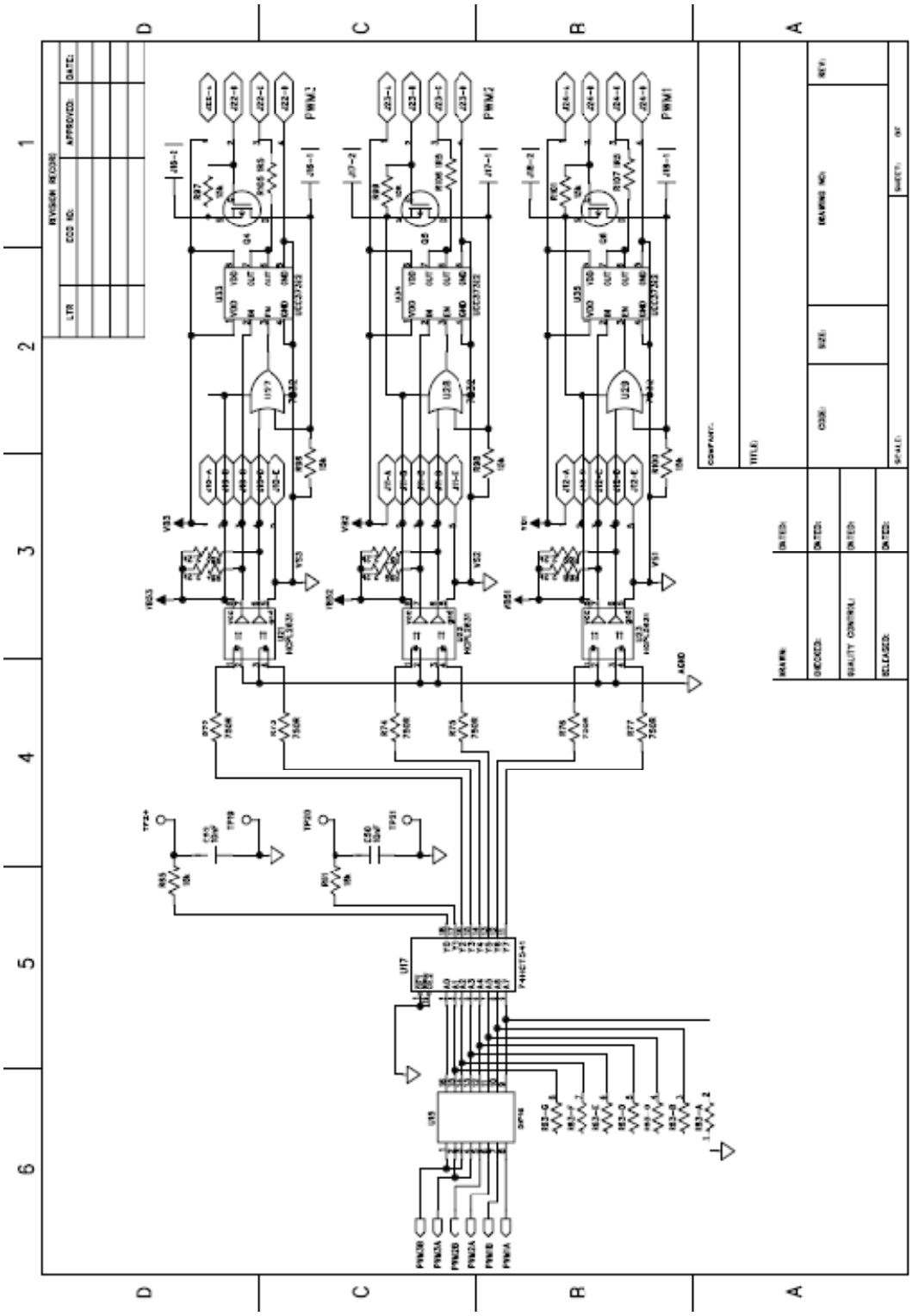

Figure A.14. PWM outputs with transistor drivers. Lower 3 channels with a zero voltage detection.

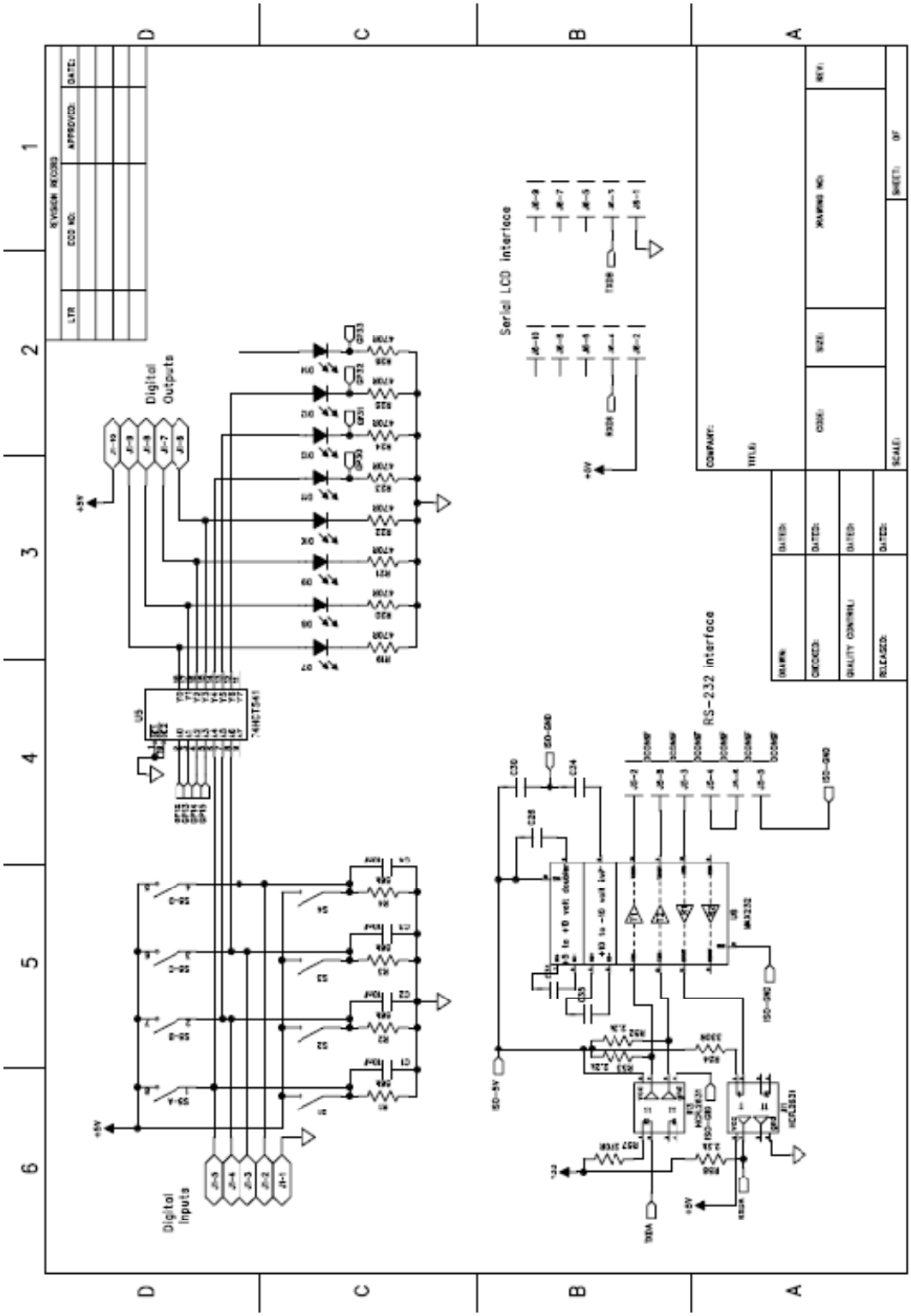

Figure A.15. Communication interfaces, digital I/O, LCD interface, signal diodes, keyboard.

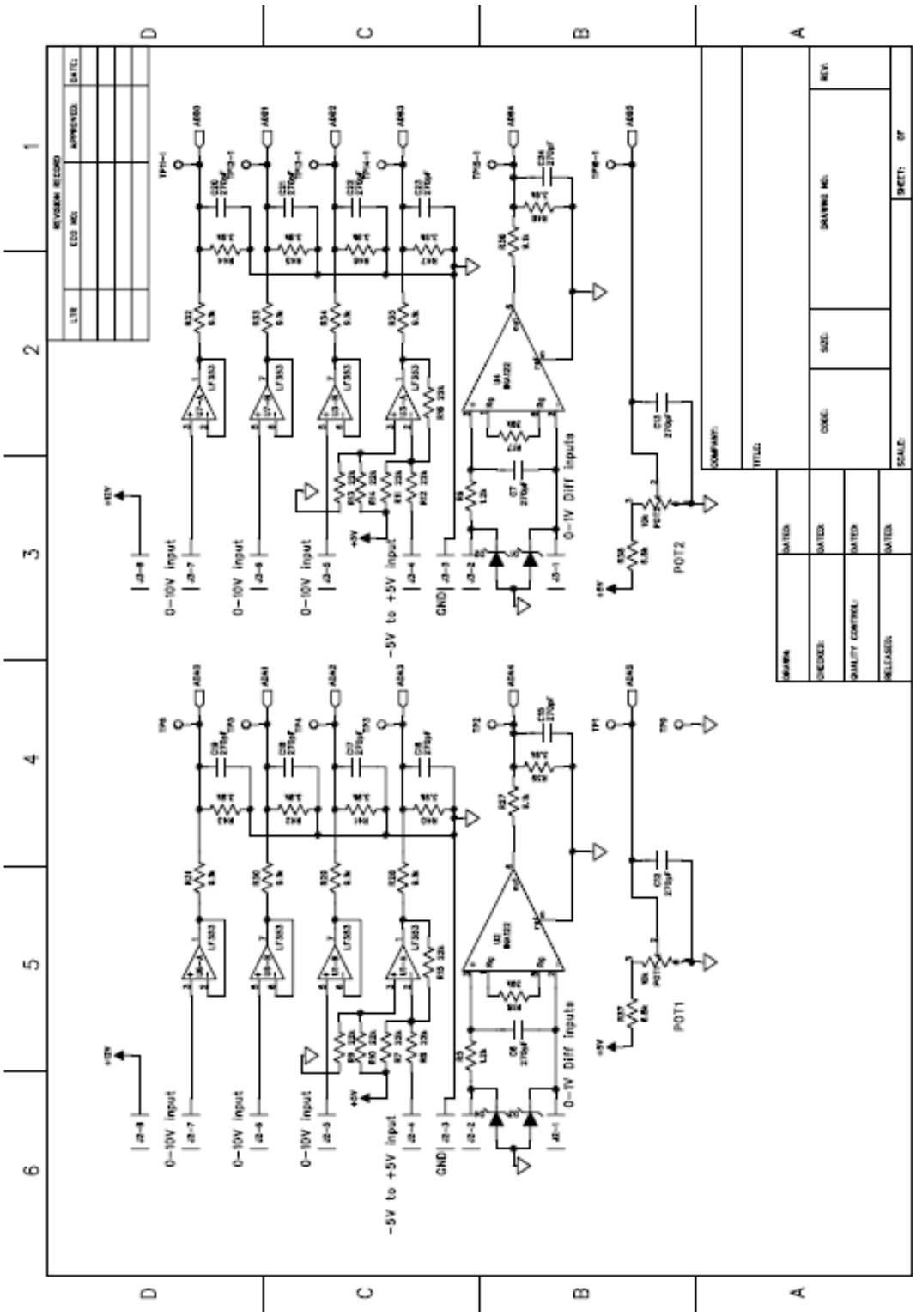

Figure A.16. Analog inputs: 6 voltage inputs, 2 voltage differential inputs, 2 high sensitivity current shunt inputs and 2 potentiometers.

Appendix B

Performance Factor

B.1. Steinmetz Parameters

The curves of anticipated power loss generated in a magnetic material are published in datasheets [72]-[80]; the curves are provided for specific conditions as constant frequency or constant flux density amplitude. The power loss generated at other frequencies and flux density amplitude than provided can be found by the Steinmetz equation [87]-[89]:

$$P_V = k\, f^m\, B_{ac}^n \tag{B.1}$$

where k, m, n are Steinmetz parameters. The power loss can be expressed either in gravimetric or volumetric units. The volumetric power loss in mW/cm^3 is the unit of choice for this work; however, it is easy to convert into W/kg just by dividing the volumetric power loss by the materials density. Steinmetz equation parameters are evaluated from the available datasheets for various materials at specified frequency and materials density. The parameters are provided in Table B.1 and continued in Table B.2. The parameters for powdered cores are selected from Mag. Inc. as a representative sample with an exception to the proprietary Crystal-X core from Arnold Magnetics. Note that parameters provided in Table B.1 and Table B.2 results in volumetric power loss in mW/cm^3 (kW/m^3) for frequency f given in kilohertz's and flux density amplitude B_{ac} in Tesla's.

Table B.1. Steinmetz equation parameters

Material	Density	Steinmetz Parameters for P_V in mW/cm^3					
2605SA1 Metglas	ρ_m = 7.18 g/cm^3	f	5 kHz	10 kHz	20 kHz	50 kHz	100 kHz
		k	56.617	112.391	35.133	28.523	25.686
		m	1.515	1.322	1.617	1.670	1.670
		n	1.827	1.934	1.813	1.834	1.796
2605S3A Metglas	ρ_m = 7.29 g/cm^3	f	10 kHz	25 kHz	50 kHz	100 kHz	250 kHz
		k	15.262	29.853	3.438	23.979	34.195
		m	1.588	1.415	1.907	1.513	1.513
		n	2.020	2.113	2.034	2.121	2.176
10JNHF600 JFE	ρ_m = 7.53 g/cm^3	f	10 kHz	20 kHz	30 kHz	50 kHz	100 kHz
		k	161.183	328.528	91.243	118.187	101.133
		m	1.515	1.309	1.675	1.585	1.585
		n	2.000	2.041	2.026	1.985	1.918
JFE Prototype JFE	ρ_m = 7.53 g/cm^3	f	10 kHz	20 kHz	30 kHz	50 kHz	100 kHz
		k	128.947	262.822	72.995	94.550	80.907
		m	1.515	1.309	1.675	1.585	1.585
		n	2.000	2.041	2.026	1.985	1.918
Vitroperm 500F VAC	ρ_m = 7.3 g/cm^3	f	20 kHz	50 kHz	100 kHz	150 kHz	200 kHz
		k	1.419	12.004	3.469	0.002348	0.0014535
		m	1.902	1.380	1.710	3.185	3.185
		n	1.918	2.096	2.096	2.111	2.086
3C93 Ferroxcube	ρ_m = 4.8 g/cm^3	f	25 kHz	100 kHz	200 kHz	500 kHz	-
		k	243.734	1.751	1.444	1.105	-
		m	1.322	2.263	2.137	2.137	-
		n	3.419	3.070	2.678	2.562	-
Mix -26 Micrometals	ρ_m = 7 g/cm^3	f	20 kHz	50 kHz	100 kHz	200 kHz	-
		k	6569.927	555.125	590.064	358.917	-
		m	0.756	1.492	1.492	1.572	-
		n	2.000	2.051	2.076	2.052	-
MPP 60 Magnetics	ρ_m = 8.2 g/cm^3	f	10 kHz	20 kHz	50 kHz	100 kHz	300 kHz
		k	46.225	261.654	48.787	109.756	111.611
		m	1.697	1.137	1.549	1.348	1.348
		n	2.224	2.247	2.219	2.168	2.175
High Flux 60 Magnetics	ρ_m = 7.7 g/cm^3	f	5 kHz	10 kHz	20 kHz	50 kHz	100 kHz
		k	1454.487	2851.516	1422.337	72.918	77.189
		m	1.218	0.909	1.120	1.870	1.870
		n	2.548	2.532	2.504	2.488	2.513

Table B.2. Steinmetz equation parameters

Material	Density	Steinmetz Parameters for P_V in mW/cm^3					
Kool Mu 60 Magnetics	ρ_m = 6.8 g/cm^3	f	20 kHz	50 kHz	100 kHz	200 kHz	300 kHz
		k	157.682	65.339	179.394	85.000	275.440
		m	1.322	1.585	1.354	1.485	1.261
		n	2.000	2.009	2.023	2.000	1.960
Xflux 60 Magnetics	ρ_m = 7.5 g/cm^3	f	10 kHz	20 kHz	30 kHz	50 kHz	100 kHz
		k	744.503	877.724	58.078	239.776	316.916
		m	1.031	1.000	1.659	1.475	1.475
		n	1.912	1.943	1.737	2.041	2.162
Crystal-X 60 Arnold	not available	f	10 kHz	25 kHz	50 kHz	100 kHz	200 kHz
		k	771.330	1004.470	1040.350	788.513	874.432
		m	1.176	1.120	1.102	1.155	1.155
		n	2.391	2.427	2.412	2.398	2.443

Appendix C

Area Product Analysis

In this section the procedure presented in Chapter 0 is used to analyse an inductor area product vs. current ripple for 1 kW and 10 kW boost converters and 20 to 150 kHz. The following materials presented in Table 3.1 are investigated: 2605SA1, 10JNHF600, JFE Prototype, Vitroperm 500F, 3C93, MPP 60, High Flux 60, KoolMu 60 and Xflux 60. The following are the electrical specifications for a boost converter: V_{in}/V_{out} = 200/400 V/V, P = 1 kW and 10 kW, inductor efficiency 99 %. The switching frequency is increased from 20 to 150 kHz in the following steps: 20, 50, 100 and 150 kHz. The ambient or cold-plate temperature is set at 70 °C. The maximum temperature rise allowed for each material is dependent on the continuous operating temperature of the material shown in Table 3.1.

The CC core is assumed. The core profile ratio, r_c, is allowed to change in the range between 0.5 and 2, the core window ratio, r_w, is allowed to vary between 0.5 and 2. The air gap is limited to 3 mm per leg. The permeability of powder materials is allowed to decrease down to 50 % of its initial value but, designs show that effective permeability roll-off is about 30 %. The winding interlayer insulation is assumed as 0.1 mm and the distance between the core and winding tips is set to 4 mm, while the distance between windings is 2.4 mm.

C.1. 1 kW Area Product vs. Current Ripple

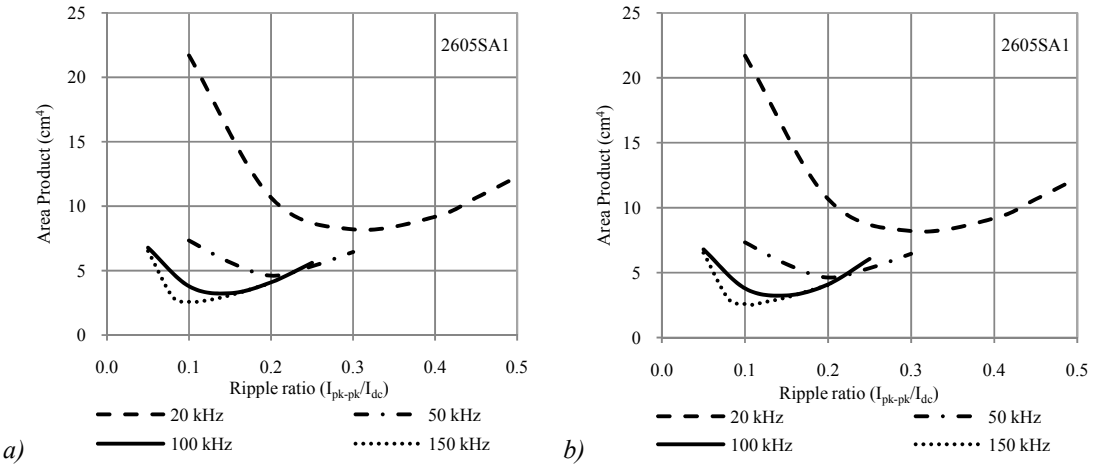

Figure C.1. *AP* vs. current ripple with frequency as a parameter for 2605SA1 1 kW gapped inductor design: *(a)* natural convection-cooling, *(b)* cold-plate conduction-cooling.

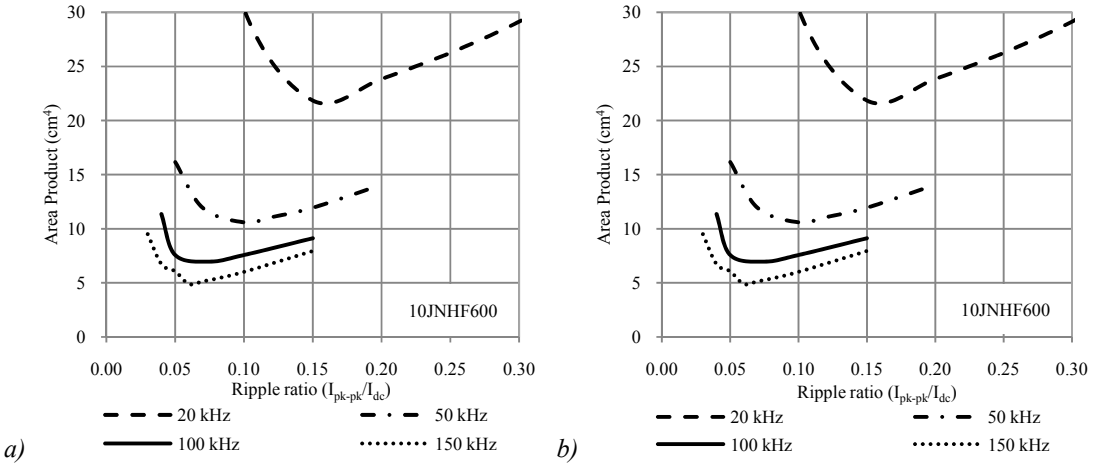

Figure C.2. *AP* vs. current ripple with frequency as a parameter for 10JNHF600 1 kW gapped inductor design: *(a)* natural convection-cooling, *(b)* cold-plate conduction-cooling.

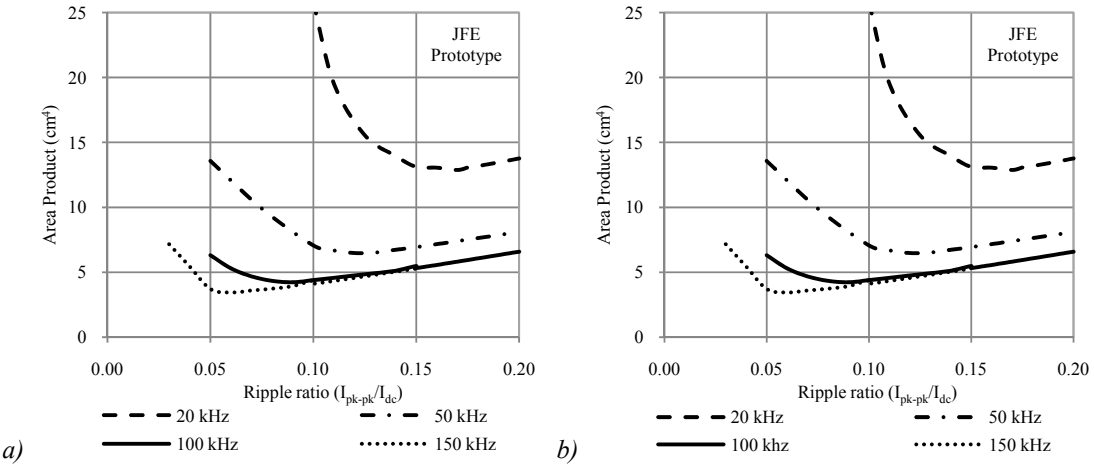

Figure C.3. *AP* vs. current ripple with frequency as a parameter for JFE Prototype 1 kW gapped inductor design: *(a)* natural convection-cooling, *(b)* cold-plate conduction-cooling.

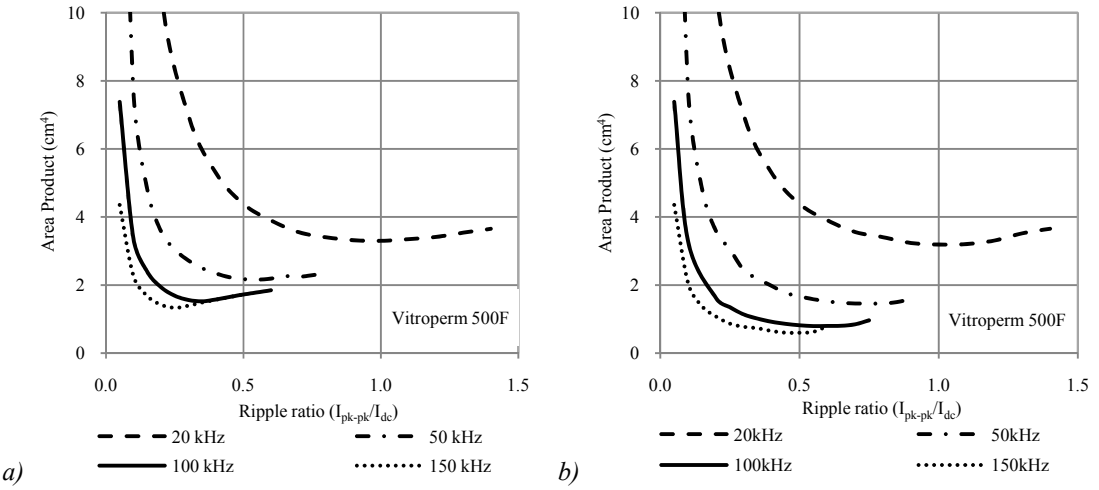

Figure C.4. *AP* vs. current ripple with frequency as a parameter for Vitroperm 500F 1 kW gapped inductor design: *(a)* natural convection-cooling, *(b)* cold-plate conduction-cooling.

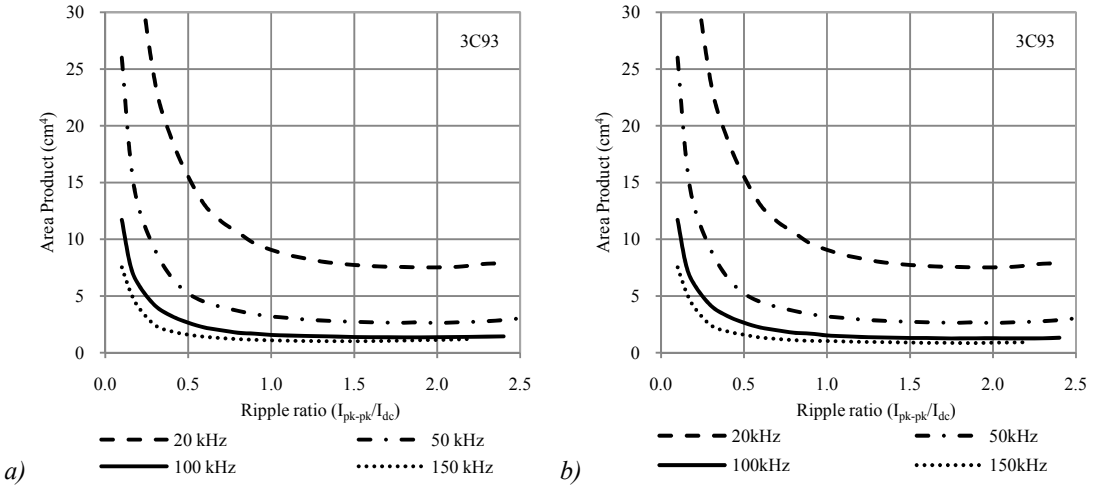

Figure C.5. *AP* vs. current ripple with frequency as a parameter for 3C93 1 kW gapped inductor design: *(a)* natural convection-cooling, *(b)* cold-plate conduction-cooling.

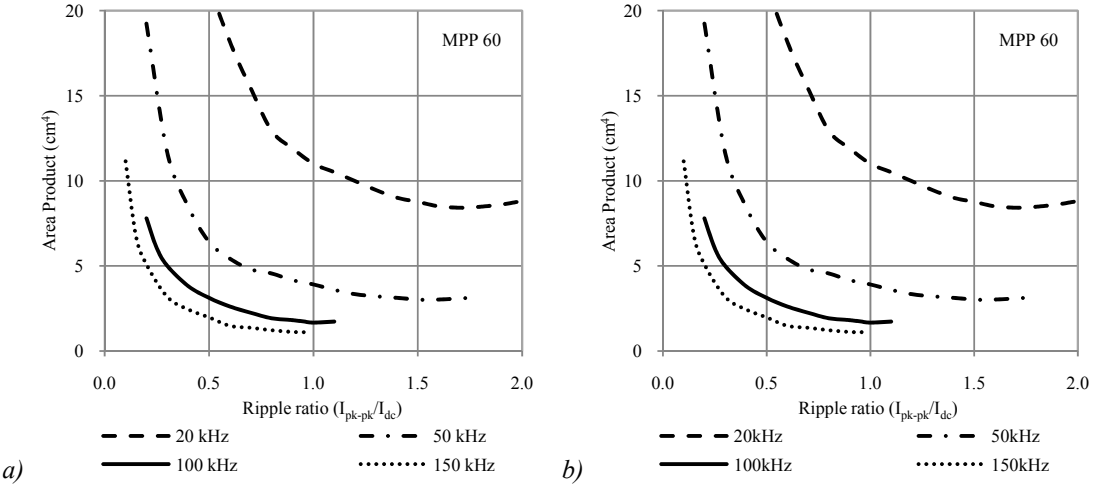

Figure C.6. *AP* vs. current ripple with frequency as a parameter for MPP 60 1 kW gapless inductor design: *(a)* natural convection-cooling, *(b)* cold-plate conduction-cooling.

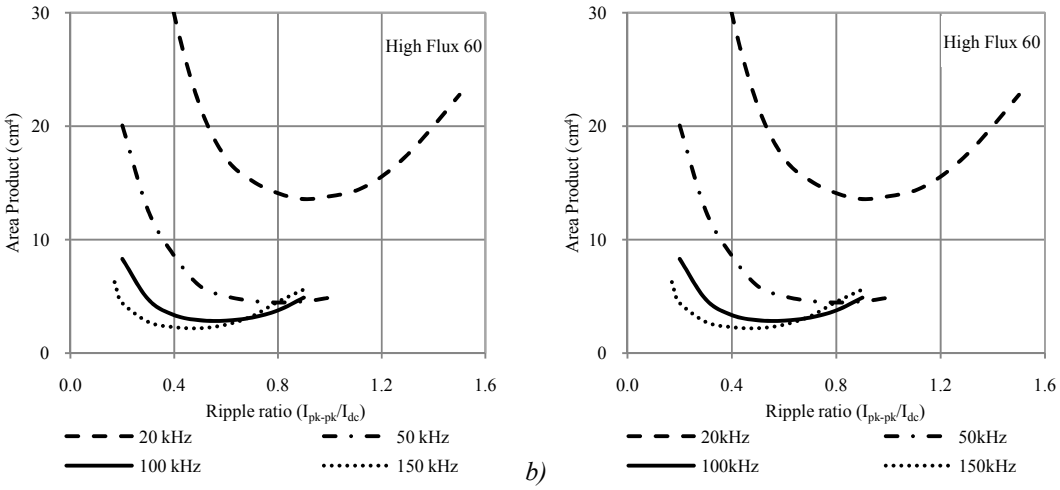

Figure C.7. *AP* vs. current ripple with frequency as a parameter for High Flux 60 1 kW gapless inductor design: *(a)* natural convection-cooling, *(b)* cold-plate conduction-cooling.

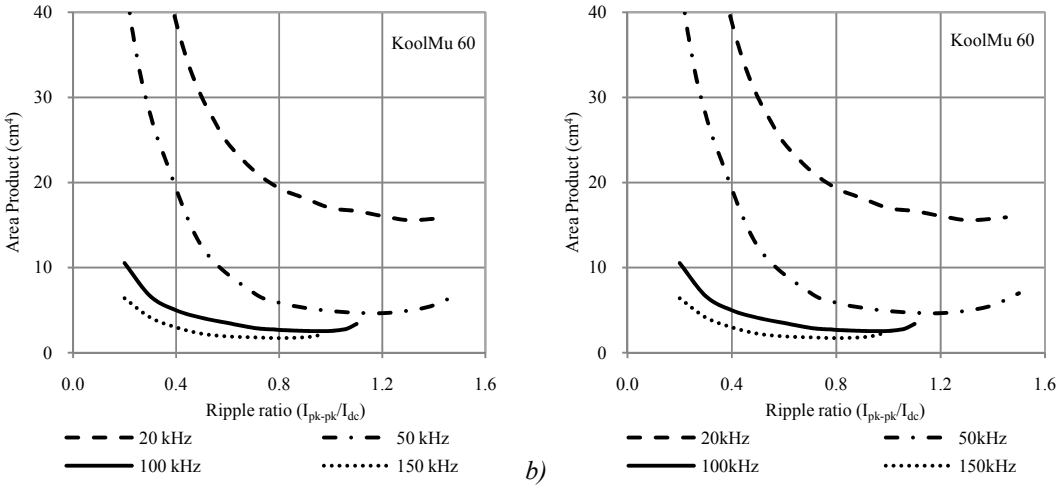

Figure C.8. *AP* vs. current ripple with frequency as a parameter for KoolMu 60 1 kW gapless inductor design: *(a)* natural convection-cooling, *(b)* cold-plate conduction-cooling.

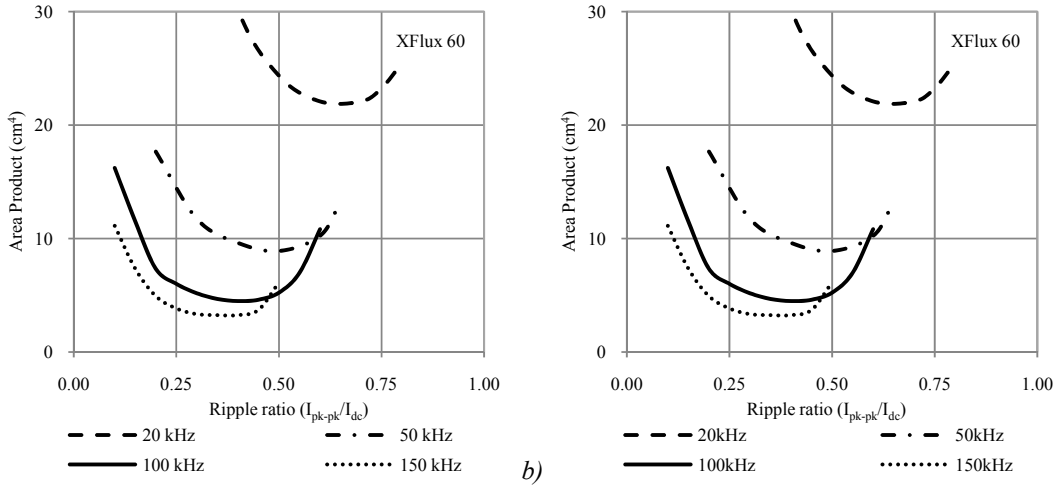

Figure C.9. *AP* vs. current ripple with frequency as a parameter for XFlux 60 1 kW gapless inductor design: *(a)* natural convection-cooling, *(b)* cold-plate conduction-cooling.

C.2. 10 kW Area Product vs. Current Ripple

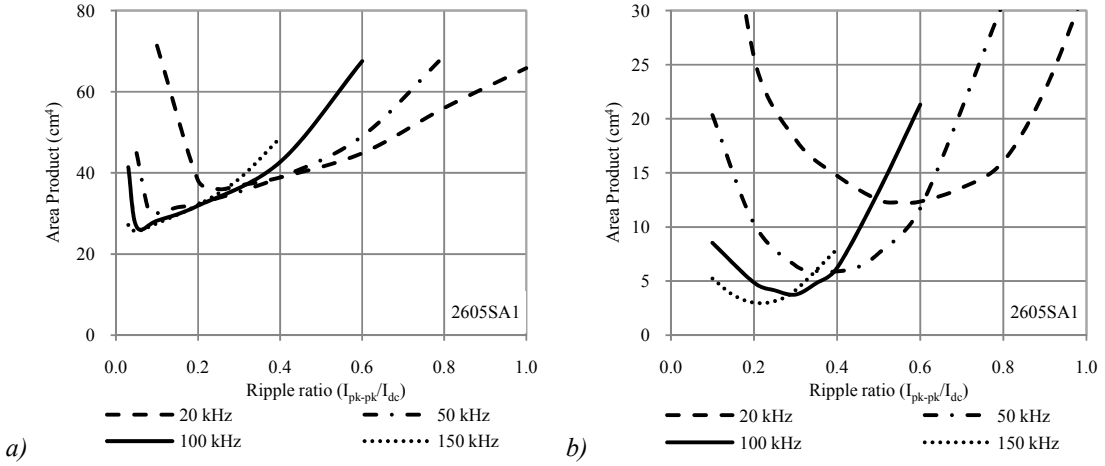

Figure C.10. *AP* vs. current ripple with frequency as a parameter for 2605SA1 10 kW gapped inductor design: *(a)* natural convection-cooling, *(b)* cold-plate conduction-cooling.

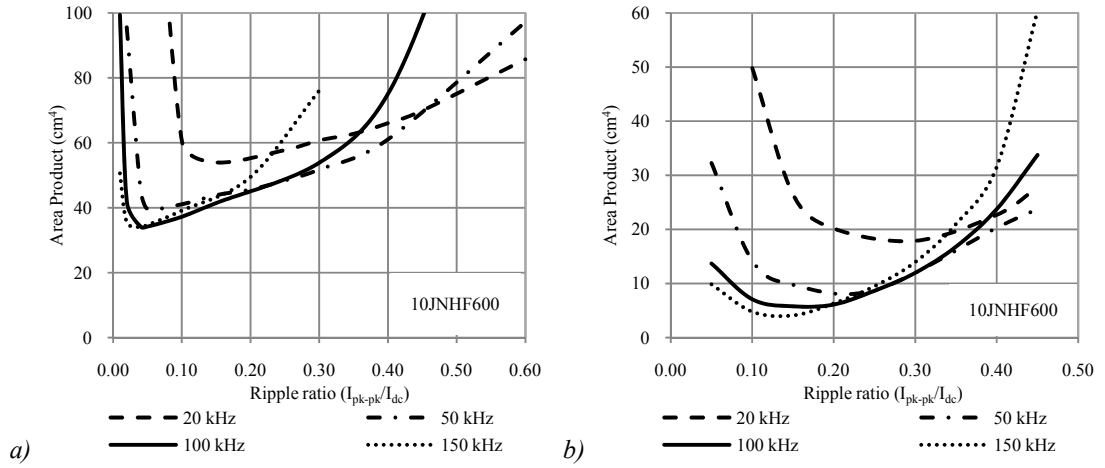

Figure C.11. *AP* vs. current ripple with frequency as a parameter for 10JNHF600 10 kW gapped inductor design: *(a)* natural convection-cooling, *(b)* cold-plate conduction-cooling.

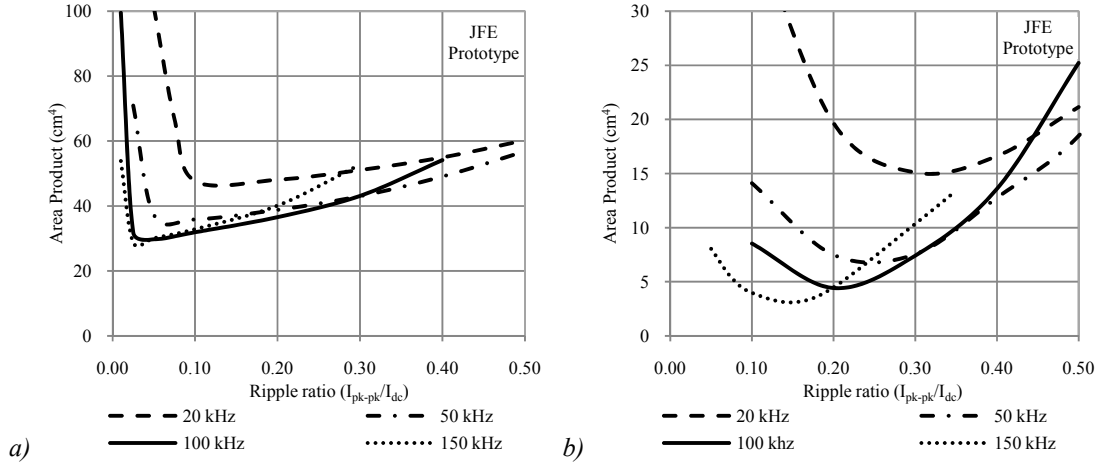

Figure C.12. *AP* vs. current ripple with frequency as a parameter for JFE Prototype 10 kW gapped inductor design: *(a)* natural convection-cooling, *(b)* cold-plate conduction-cooling.

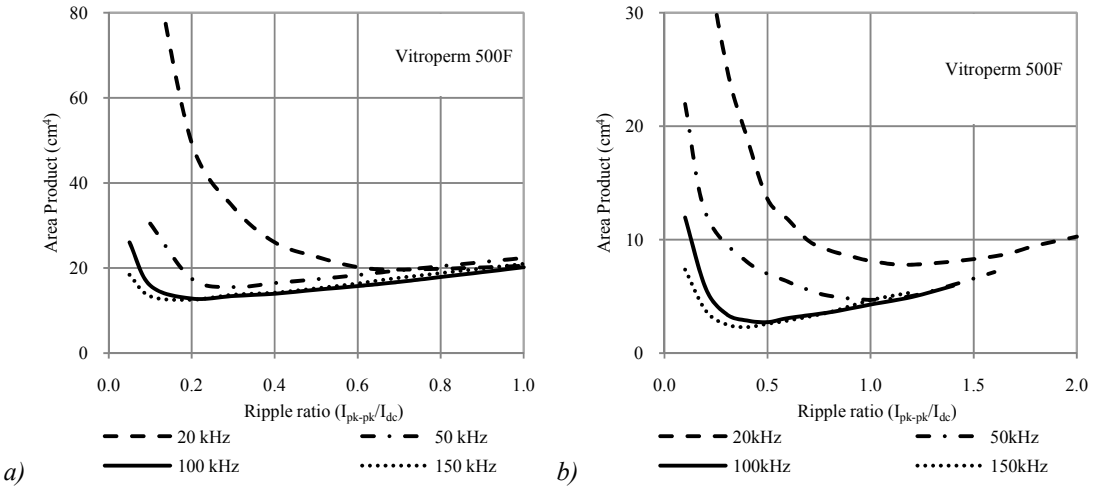

Figure C.13. *AP* vs. current ripple with frequency as a parameter for Vitroperm 500F 10 kW gapped inductor design: *(a)* natural convection-cooling, *(b)* cold-plate conduction-cooling.

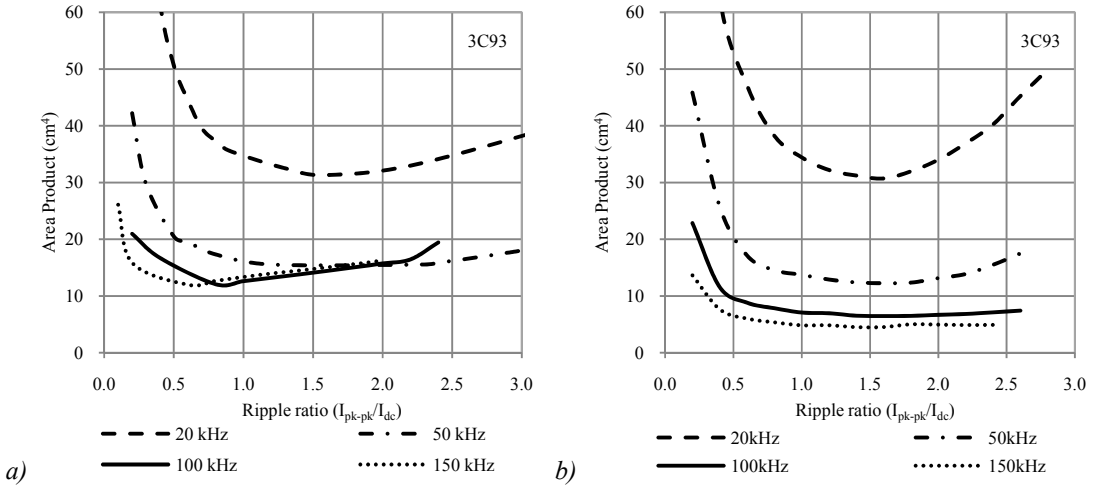

Figure C.14. *AP* vs. current ripple with frequency as a parameter for 3C93 10 kW gapped inductor design: *(a)* natural convection-cooling, *(b)* cold-plate conduction-cooling.

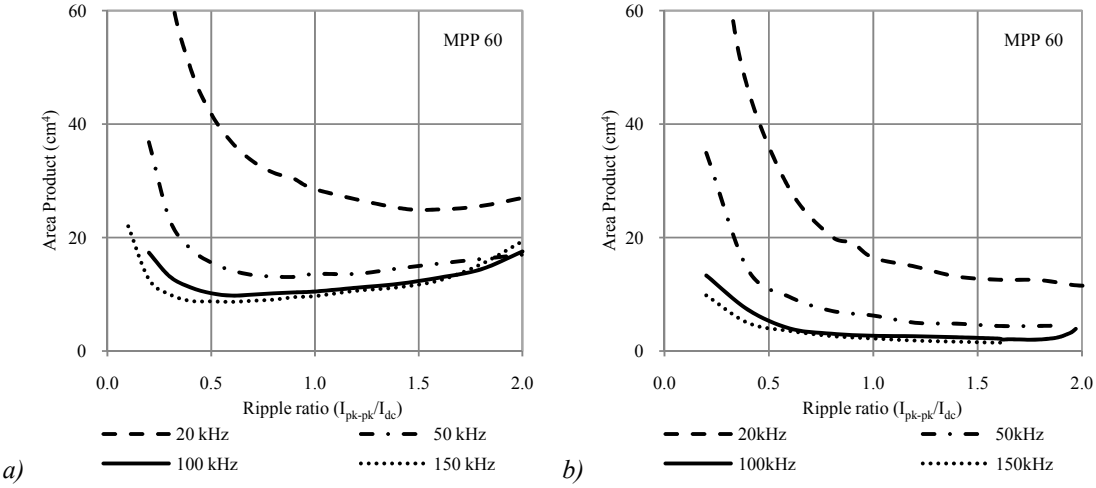

Figure C.15. *AP* vs. current ripple with frequency as a parameter for MPP 60 10 kW gapless inductor design: *(a)* natural convection-cooling, *(b)* cold-plate conduction-cooling.

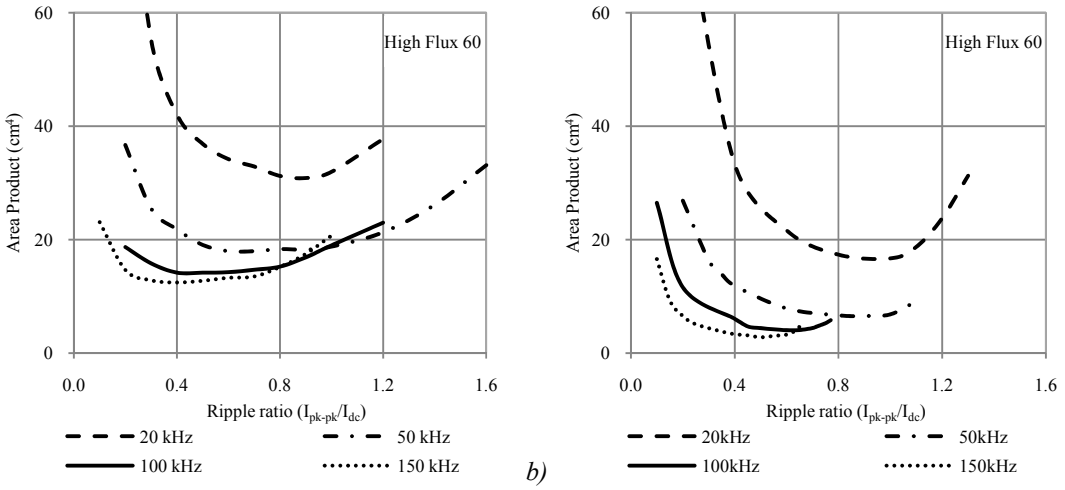

Figure C.16. *AP* vs. current ripple with frequency as a parameter for High Flux 60 10 kW gapless inductor design: *(a)* natural convection-cooling, *(b)* cold-plate conduction-cooling.

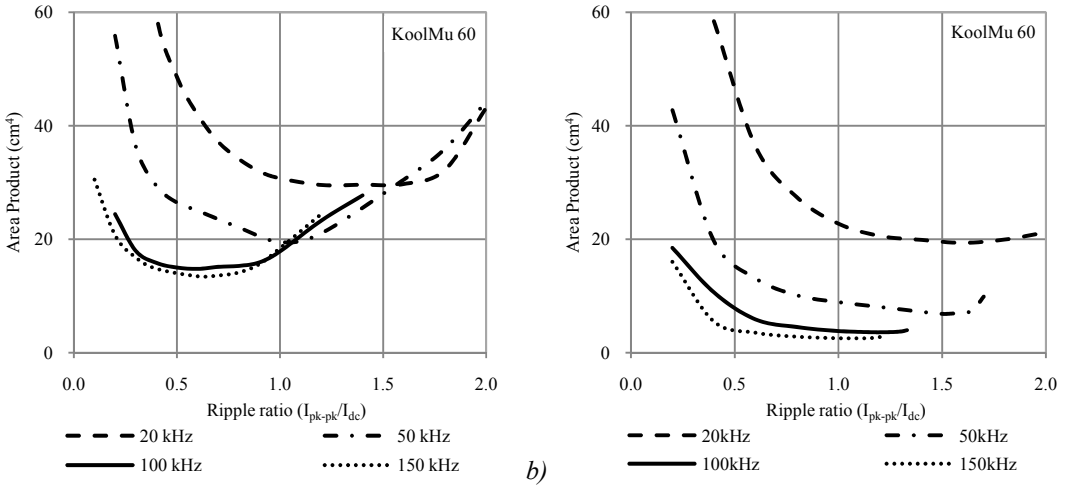

Figure C.17. *AP* vs. current ripple with frequency as a parameter for KoolMu 60 10 kW gapless inductor design: *(a)* natural convection-cooling, *(b)* cold-plate conduction-cooling.

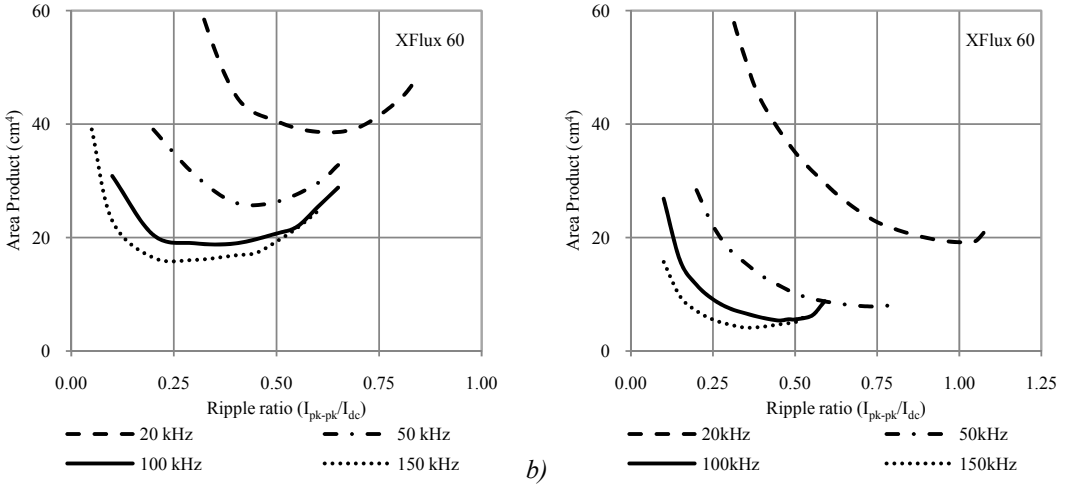

Figure C.18. *AP* vs. current ripple with frequency as a parameter for XFlux 60 10 kW gapless inductor design: *(a)* natural convection-cooling, *(b)* cold-plate conduction-cooling.

C.3. Minimum Area Product Analysis

Table C.1. Minimum *AP* vs. frequency for gapped materials (1 kW, 99% efficient), convection-cooling and conduction-cooling

Material	*f*	20 kHz		50 kHz		100 kHz		150 kHz	
		conv	cond	conv	cond	conv	cond	conv	cond
2605SA1	$I_{pk\text{-}pk}/I_{dc}$	0.3	0.3	0.2	0.2	0.15	0.15	0.1	0.1
	AP_{min} (cm^4)	8.2	8.2	4.6	4.6	3.3	3.3	2.6	2.6
10JNHF600	$I_{pk\text{-}pk}/I_{dc}$	0.15	0.15	0.1	0.1	0.075	0.075	0.06	0.06
	AP_{min} (cm^4)	21.8	21.8	10.6	10.6	7.0	7.0	4.9	4.9
JFE Prototype	$I_{pk\text{-}pk}/I_{dc}$	0.17	0.17	0.12	0.12	0.09	0.09	0.06	0.06
	AP_{min} (cm^4)	12.9	12.9	6.5	6.5	4.2	4.2	3.4	3.4
Vitroperm 500F	$I_{pk\text{-}pk}/I_{dc}$	1	1	0.55	0.7	0.35	0.55	0.25	0.45
	AP_{min} (cm^4)	3.3	3.2	2.2	1.5	1.5	0.8	1.3	0.6
3C93	$I_{pk\text{-}pk}/I_{dc}$	1.9	1.9	1.8	2	1.9	1.8	1.4	1.9
	AP_{min} (cm^4)	7.5	7.5	2.6	2.6	1.4	1.3	1.0	0.9

Table C.2. Minimum *AP* vs. frequency for gapped materials (10 kW, 99% efficient), convection-cooling and conduction-cooling

Material	*f*	20 kHz		50 kHz		100 kHz		150 kHz	
		conv	cond	conv	cond	conv	cond	conv	cond
2605SA1	$I_{pk\text{-}pk}/I_{dc}$	0.25	0.55	0.1	0.4	0.05	0.3	0.05	0.2
	AP_{min} (cm^4)	36.0	12.3	30.1	5.9	26.8	3.8	25.6	3.0
10JNHF600	$I_{pk\text{-}pk}/I_{dc}$	0.15	0.3	0.05	0.25	0.05	0.15	0.04	0.15
	AP_{min} (cm^4)	54.0	17.9	39.7	8.8	34.2	5.8	34.1	4.1
JFE Prototype	$I_{pk\text{-}pk}/I_{dc}$	0.1	0.3	0.1	0.2	0.05	0.2	0.025	0.15
	AP_{min} (cm^4)	47.7	15.1	35.9	7.5	29.8	4.4	28.8	3.1
Vitroperm 500F	$I_{pk\text{-}pk}/I_{dc}$	0.7	1.2	0.3	1	0.2	0.5	0.2	0.4
	AP_{min} (cm^4)	19.6	7.8	15.6	4.7	12.8	2.7	12.6	2.3
3C93	$I_{pk\text{-}pk}/I_{dc}$	1.6	1.6	2.3	1.6	0.8	1.6	0.6	1.4
	AP_{min} (cm^4)	31.3	30.7	15.5	12.2	12.1	6.5	12.0	4.5

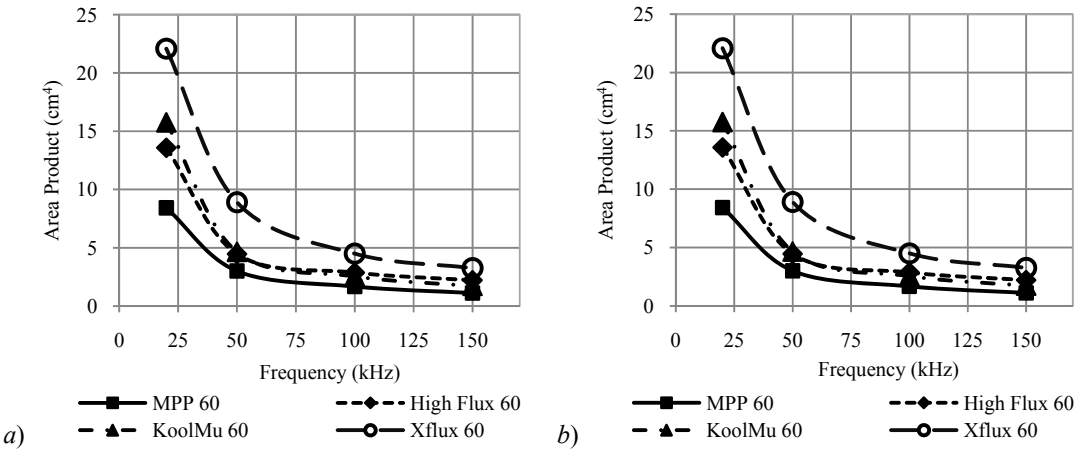

Figure C.19. Minimum *AP* vs. frequency for gapless materials (1 kW, 99% efficient): *(a)* convection-cooling and *(b)* conduction-cooling.

Table C.3. Minimum *AP* vs. frequency for gapless materials (1 kW, 99% efficient), convection-cooling and conduction-cooling

Material	*f*	20 kHz		50 kHz		100 kHz		150 kHz	
		conv	cond	conv	cond	conv	cond	conv	cond
MPP 60	$I_{pk\text{-}pk}/I_{dc}$	1.7	1.7	1.55	1.55	1	1	0.95	0.95
	AP_{min} (cm^4)	8.4	8.4	3.0	3.0	1.7	1.7	1.1	1.1
High Flux 60	$I_{pk\text{-}pk}/I_{dc}$	0.9	0.9	0.8	0.8	0.6	0.6	0.5	0.5
	AP_{min} (cm^4)	13.6	13.6	4.5	4.5	2.9	2.9	2.2	2.2
KoolMu 60	$I_{pk\text{-}pk}/I_{dc}$	1.4	1.4	1.2	1.2	0.95	0.95	0.8	0.8
	AP_{min} (cm^4)	15.7	15.7	4.6	4.6	2.5	2.5	1.7	1.7
XFlux 60	$I_{pk\text{-}pk}/I_{dc}$	0.7	0.7	0.5	0.5	0.4	0.4	0.35	0.35
	AP_{min} (cm^4)	22.1	22.1	8.9	8.9	4.5	4.5	3.3	3.3

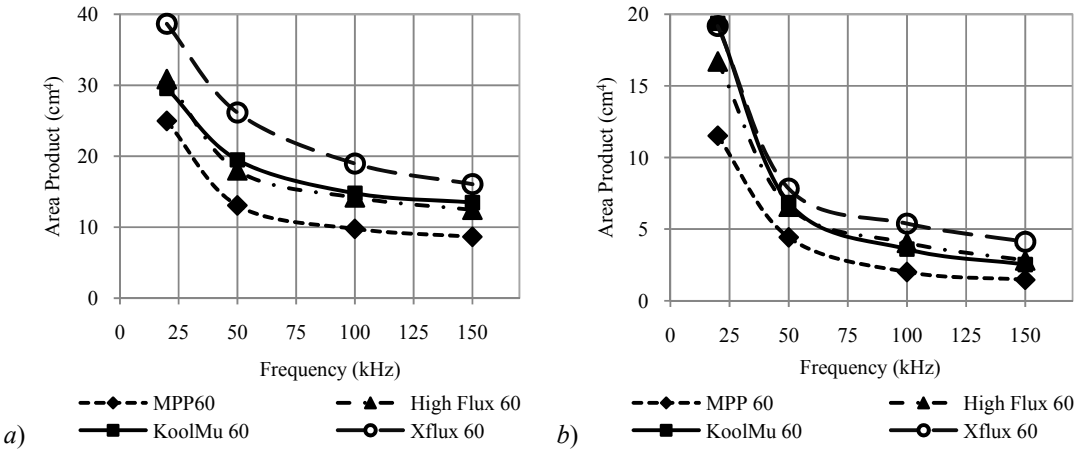

Figure C.20. Minimum *AP* vs. frequency for gapless materials (10 kW, 99% efficient): *(a)* convection-cooling and *(b)* conduction-cooling.

Table C.4. Minimum *AP* vs. frequency for gapless materials (10 kW, 99% efficient), convection-cooling and conduction-cooling

Material	*f*	20 kHz		50 kHz		100 kHz		150 kHz	
		conv	cond	conv	cond	conv	cond	conv	cond
MPP 60	$I_{pk\text{-}pk}/I_{dc}$	1.6	2	0.9	1.6	0.6	1.75	0.6	1.6
	AP_{min} (cm^4)	25.0	11.5	13.1	4.4	9.8	2.0	8.7	1.5
High Flux 60	$I_{pk\text{-}pk}/I_{dc}$	0.9	1	0.7	0.9	0.5	0.6	0.4	0.5
	AP_{min} (cm^4)	30.9	16.7	18.0	6.6	14.2	4.1	12.5	2.8
KoolMu 60	$I_{pk\text{-}pk}/I_{dc}$	1.2	1.6	1	1.5	0.6	1.19	0.6	1.1
	AP_{min} (cm^4)	29.6	19.4	19.5	6.9	14.8	3.6	13.5	2.5
XFlux 60	$I_{pk\text{-}pk}/I_{dc}$	0.6	1	0.4	0.75	0.4	0.45	0.3	0.35
	AP_{min} (cm^4)	38.7	19.2	26.2	7.8	19.0	5.4	16.1	4.1

C.4. Efficiency Effect on the Inductor Size

Table C.5. *AP* for 100 μH gapped inductor with and without efficiency restriction

Material	*f*	20 kHz		50 kHz		100 kHz		150 kHz	
		conv	cond	conv	cond	conv	cond	conv	cond
2605SA1	AP (cm^4)	53.3	7.1	39.1	4.6	32	3.7	29.1	3.5
	AP_{lim} (cm^4)	68.4	38.6	39.1	15.5	32	5.4	29.1	4.5
10JNHF600	AP (cm^4)	76.9	6.7	51.3	3.8	41.4	2.7	36.8	2.6
	AP_{lim} (cm^4)	-	19@50 kHz	62.0	10@75 kHz	43.6	6.4	37.5	3.8
JFE Prototype	AP (cm^4)	67.1	5.8	44.4	3.5	35.9	2.7	34.8	2.6
	AP_{lim} (cm^4)	199.5	24@30 kHz	49.7	12.3	36.8	4.2	35.0	3.1
Vitroperm 500F	AP (cm^4)	20.7	8.9	16.6	6.2	12.5	5.6	11.4	5.5
	AP_{lim} (cm^4)	20.7	8.9	16.6	6.3	12.5	5.6	11.4	5.5
3C93	AP (cm^4)	31.4	31.1	23.7	21.4	21.6	18.8	20.7	18.0
	AP_{lim} (cm^4)	34.7	35.0	26.5	25.1	23.0	20.6	22.1	19.2

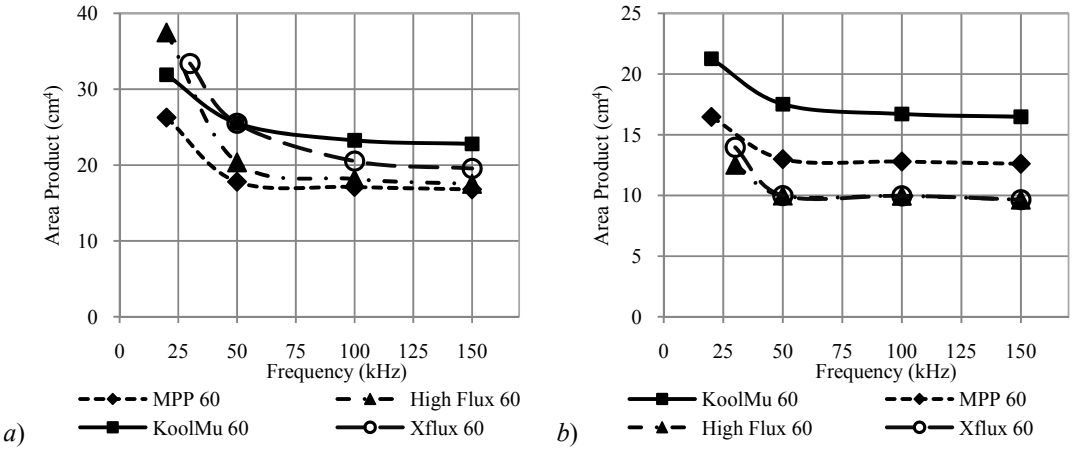

Figure C.21. *AP* vs. frequency for a 100 μH gapless inductor (10 kW, 99% efficient): *(a)* convection-cooling and *(b)* conduction-cooling.

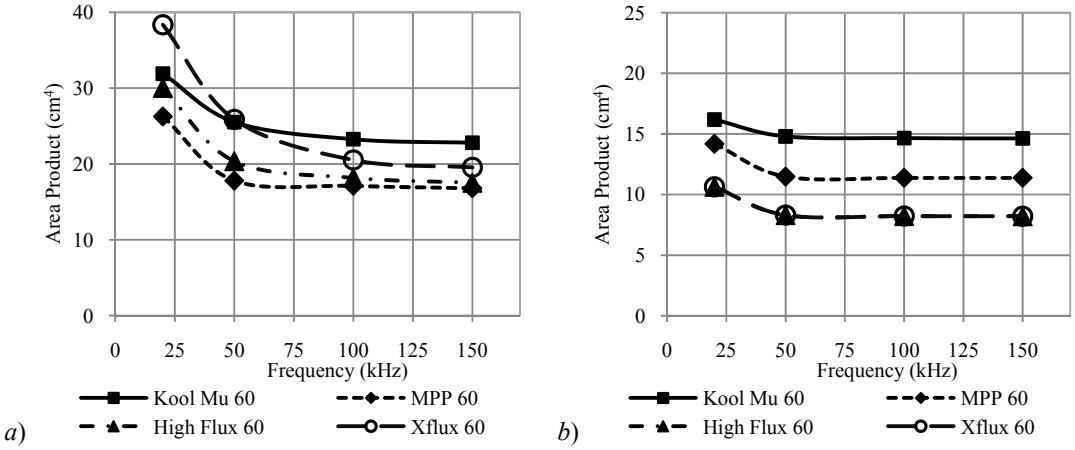

Figure C.22. *AP* vs. frequency for a 100 μH gapless inductor (10 kW, no efficiency restriction): *(a)* convection-cooling and *(b)* conduction-cooling.

Table C.6. *AP* for 100 μH gapless inductor with and without efficiency restriction 10 kW.

Material	*f*	20 kHz		50 kHz		100 kHz		150 kHz	
		conv	cond	conv	cond	conv	cond	conv	cond
MPP 60	AP (cm^4)	31.9	16.2	25.5	14.8	23.3	14.7	22.8	14.6
	AP_{lim} (cm^4)	31.9	21.3	25.5	17.5	23.3	16.7	22.8	16.5
High Flux 60	AP (cm^4)	26.3	14.2	17.8	11.5	17.1	11.4	16.8	11.4
	AP_{lim} (cm^4)	26.3	16.5	17.8	13.0	17.1	12.8	16.8	12.6
KoolMu 60	AP (cm^4)	30.0	10.6	20.4	8.3	18.2	8.2	17.5	8.2
	AP_{lim} (cm^4)	37.5	23.1	20.4	10.0	18.2	10.0	17.5	9.6
XFlux 60	AP (cm^4)	38.3	10.6	25.5	8.3	20.5	8.2	19.6	8.2
	AP_{lim} (cm^4)	33@30 kHz	41.3	25.9	10.0	20.5	10.0	19.6	9.6

Appendix D

Experimental Analysis

The following appendix presents tabulated experimental results for Chapter 5.

D.1. Frequency Effect Analysis

Table D.1. Experimental data for a low to medium frequency effect analysis

Material	2605SA1				10JNHF600				Mega Flux 60			
f (kHz)	15	20	25	30	15	20	25	30	15	20	25	30
V_{in} (V)	63.4	63.4	64.6	63.7	126.3	125.3	124.9	122.4	125.3	123.3	121.0	119.1
V_o (V)	126.4	127.2	130.2	128.8	254.6	254.1	255.2	251.9	252.3	249.7	246.8	243.6
I_{in} (A)	19.59	19.82	20.43	20.45	19.66	19.81	20.14	20.19	19.82	19.83	19.82	19.82
I_o (A)	9.43	9.47	9.68	9.59	9.37	9.36	9.40	9.29	9.45	9.37	9.27	9.20
P_{in} (kW)	1.24	1.26	1.32	1.30	2.48	2.48	2.51	2.47	2.48	2.44	2.40	2.35
P_o (kW)	1.19	1.20	1.26	1.24	2.39	2.38	2.40	2.34	2.38	2.34	2.29	2.23
η	0.96	0.96	0.95	0.95	0.96	0.96	0.96	0.95	0.96	0.96	0.95	0.95
$\Delta I_{p\text{-}p}$ (A)	38.8	28.4	24	20	32.4	25.2	20.4	16.4	30.4	22.6	18.2	15.6
N (turns)	16	16	16	16	22	22	22	22	28	28	28	28
L (μH)	54.3	56.0	54.3	53.7	131.0	126.0	125.0	127.9	138.3	138.1	135.6	130.1
$\Delta B_{p\text{-}p}$ (T)	0.42	0.32	0.26	0.22	0.43	0.32	0.26	0.21	0.33	0.25	0.20	0.16
ΔT_{exp} (K)	61	52	47	44	122	110	102	95	131	107	92	80

Table D.2. Experimental data for a low to medium frequency effect analysis on single- and multi-cut amorphous metal core

Material	2605SA1 single-cut				2605SA1 multi-cut			
f (kHz)	15	20	25	30	15	20	25	30
V_{in} (V)	63.4	63.4	64.6	63.7	125.6	125.5	124.6	123.5
V_o (V)	126.4	127.2	130.2	128.8	253.3	254.6	254.9	254.5
I_{in} (A)	19.59	19.82	20.43	20.45	19.59	19.79	20.11	20.31
I_o (A)	9.43	9.47	9.68	9.59	9.33	9.38	9.39	9.38
P_{in} (kW)	1.24	1.26	1.32	1.30	2.45	2.48	2.51	2.51
P_o (kW)	1.19	1.20	1.26	1.24	2.36	2.39	2.39	2.39
η	0.96	0.96	0.95	0.95	0.96	0.96	0.95	0.95
$\Delta I_{p\text{-}p}$ (A)	38.8	28.4	24	20	34.5	26	21.2	17.6
N (turns)	16	16	16	16	22	22	22	22
L (μH)	54.3	56.0	54.3	53.7	122.4	122.4	120.2	120.4
$\Delta B_{p\text{-}p}$ (T)	0.42	0.32	0.26	0.22	0.46	0.35	0.28	0.23
ΔT_{exp} (K)	61	52	47	44	113	100	89	80

Table D.3. Experimental data for a medium to high frequency effect analysis

Material	2605SA1			10JNHF600			JFE prototype		
f (kHz)	50	100	150	50	100	150	15	20	25
V_{in} (V)	125.1	125.1	125.3	125.4	125.4	125.3	125.5	125.4	125.6
V_o (V)	250.9	250.4	252.7	252.9	249.8	251.0	252.5	252.9	250.7
I_{in} (A)	10.02	10.03	10.02	10.00	10.03	9.93	9.87	9.95	9.94
I_o (A)	4.79	4.89	4.78	4.74	4.85	4.73	4.62	4.69	4.71
P_{in} (W)	1251	1248	1253	1247	1252	1250	1238	1243	1248
P_o (W)	1194	1201	1201	1175	1189	1183	1166	1182	1182
η	0.955	0.962	0.959	0.942	0.950	0.946	0.942	0.951	0.947
$\Delta I_{p\text{-}p}$ (A)	14.18	6.94	4.66	18.2	8.9	5.94	19.2	9.56	6.2
N (turns)	16	16	16	16	16	16	16	16	16
L (μH)	88.5	90.2	90.4	69.5	70.2	70.4	65.8	66.1	67.4
$\Delta B_{p\text{-}p}$ (T)	0.25	0.13	0.08	0.23	0.12	0.08	0.21	0.11	0.07
ΔT_{exp} (K)	93	64	57	128	99	88	105	80	71

Table D.4. Experimental data for a medium to high frequency effect analysis on single- and multi-cut amorphous metal core

Material	2605SA1 single-cut			2605SA1 multi-cut		
f (kHz)	50	100	150	50	100	150
V_{in} (V)	125.1	125.1	125.3	125.0	125.3	125.5
V_o (V)	250.9	250.4	252.7	252.6	252.4	248.7
I_{in} (A)	10.02	10.03	10.02	9.95	9.95	9.94
I_o (A)	4.79	4.89	4.78	4.65	4.75	4.78
P_{in} (W)	1251	1248	1253	1242	1241	1245
P_o (W)	1194	1201	1201	1168	1175	1182
η	0.955	0.962	0.959	0.940	0.947	0.949
$\Delta I_{p\text{-}p}$ (A)	14.18	6.94	4.66	10.72	5.61	3.8
N (turns)	16	16	16	12	12	12
L (μH)	88.5	90.2	90.4	117.8	112.5	109.1
$\Delta B_{p\text{-}p}$ (T)	0.25	0.13	0.08	0.25	0.13	0.08
ΔT_{exp} (K)	93	64	57	143	109	89

D.2. DC-Bias Effect on the Core Power Loss

Table D.5. Experimental data for dc-bias analysis

Material	2605SA1				10JNHF600					JFE Prototype				
V_{in} (V)	126	126	125	126	126	126	126	125	125	125	125	125	125	126
V_o (V)	251	250	250	251	250	250	250	250	250	250	250	250	250	250
I_{in} (A)	0.62	3.11	7.10	9.99	0.41	1.53	2.99	6.00	9.92	0.39	1.49	2.94	6.12	9.96
I_o (A)	0.29	1.49	3.41	4.81	0.19	0.72	1.42	2.84	4.70	0.19	0.71	1.40	2.92	4.75
t_{on} (μs)	4.90	4.99	5.07	5.07	4.99	5.00	4.99	5.01	5.06	5.00	4.99	5.07	5.01	5.00
P_{in} (W)	77.9	391	890	1254	51.5	192	376	752	1243	49	187	368	768	1250
P_o (W)	72.8	373	853	1206	48.6	182	355	711	1175	47	178	350	730	1188
$\Delta I_{p\text{-}p}$ (A)	0.315	0.684	1.42	2.45	0.22	0.25	0.36	0.59	0.96	0.18	0.26	0.38	0.69	1.24
N (turns)	30	30	30	30	50	50	50	50	50	50	50	50	50	50
L (μH)	1955	917	448	251	2873	2511	1738	1068	652	3583	2453	1655	910	504
H_0 (kA/m)	0.115	0.546	1.249	1.759	0.120	0.455	0.886	1.771	2.908	0.115	0.436	0.859	1.795	2.920
B_0 (T)	0.54	1.15	1.41	1.50	0.47	0.97	1.19	1.36	1.46	0.46	0.95	1.18	1.36	1.46
$\Delta B_{p\text{-}p}$ (T)	0.066	0.067	0.068	0.068	0.037	0.037	0.037	0.037	0.037	0.037	0.037	0.038	0.037	0.037
ΔT_{exp} (K)	24.5	27	41.6	51.5	8.7	10.2	13.8	20.3	24.9	5.3	7.4	10	16.8	22

D.3. Duty Cycle Effect on the Core Power Loss

D.3.1. Modified Steinmetz Equation

It is reported in [88][97][101] and [102] that ferrite power loss for triangular remagnetisation depends on the duty cycle. The symmetrical waveforms of duty cycle 0.5 displays similar power loss to the sinusoidal remagnetisation. However, the extreme duty cycles below 0.3 and above 0.7 produce elevated power loss. Thus, a modified Steinmetz equation is introduced in order to facilitate the power loss increase at extreme duty cycles.

Presented calculation is based on [97] where the Steinmetz parameters are only used without employment of any other parameters. The procedure presented in [97] assumes the averaging of the induction change rate *dB/dt* over a complete remagnetisation cycle *T*, thus from maximum induction B_{max} down to its minimum B_{min} and back

$$\dot{B} = \frac{1}{\Delta B}\oint \frac{dB}{dt} dB\,, \qquad \Delta B = B_{\max} - B_{\min} \tag{D.1}$$

The integral (D.1) can be transformed

$$\dot{B} = \frac{1}{\Delta B}\int_0^T \left(\frac{dB}{dt}\right)^2 dt \tag{D.2}$$

The following step is to find the relationship between the remagnetisation frequency *f* and the averaged remagnetisation rate $\dot{B}$. The equation (D.2) can be normalized with respect to a sinusoidal case. From the averaged remagnetisation rate an equivalent frequency f_{eq} can be calculated using the normalization constant $2/(\Delta B\, \pi^2)$

$$f_{eq} = \frac{2}{\Delta B^2 \pi^2}\int_0^T \left(\frac{dB}{dt}\right)^2 dt \tag{D.3}$$

Similar to the empirical formula of Steinmetz the specific energy loss w_V of every remagnetisation cycle can be determined using this equivalent frequency

$$w_V = k\, f_{eq}^{m-1}\, B_{ac}^{n} \tag{D.4}$$

where B_{ac} is the remagnetisation amplitude, $B_{ac} = \Delta B/2$. If the demagnetization is repeated with the period $T_r = 1/f_r$, the power losses are

$$P_V = \left(k\, f_{eq}^{m-1}\, B_{ac}^{n}\right) f_r \tag{D.5}$$

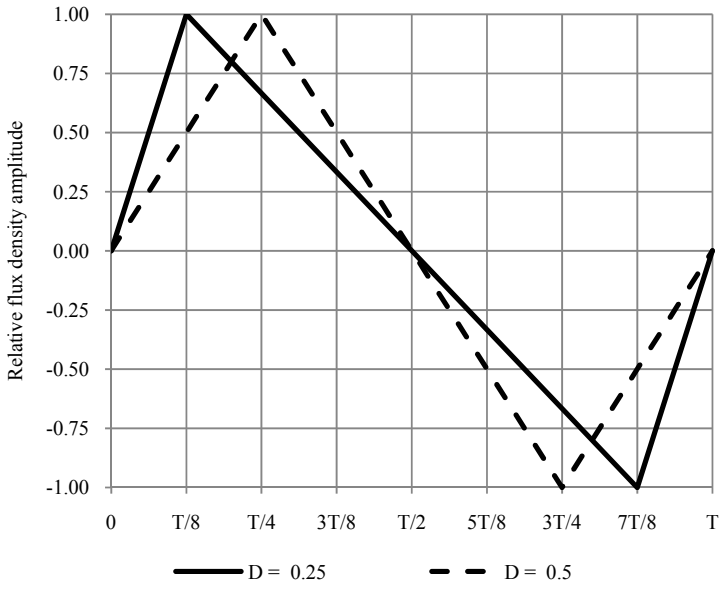

Figure D.1. Triangular remagnetisation with varying duty cycle.

The triangular remagnetisation waveform, normalized to its amplitude, for two duty cycles 0.25 and 0.5 is presented in Figure D.1. Where the duty cycle D is a ratio of rise time and period T_r of the base waveform. A waveform for duty cycle 0.5 is symmetrical where falling and rising edge has the same rate of change. The asymmetrical waveform is produced for other duty cycles as shown for duty cycle 0.25. The rising edge rate of change is three times of the falling edge.

The waveform asymmetry causes the equivalent frequency to differ for rising and falling remagnetisation components. The equivalent remagnetisation waveforms for normalized induction rise and fall are presented in Figure D.2 and Figure D.3, respectively. In this case, the induction rise equivalent frequency is two times higher than base waveform frequency while induction fall frequency is 1.5 times lower.

The equivalent magnetization waveforms are triangular and symmetrical with respective frequencies for rise and fall and they can be written as

$$B(t) = \frac{\Delta B}{D T_r} t\,, \qquad B(t) = \frac{\Delta B}{(1-D) T_r} t \tag{D.6}$$

Hence, differencing (D.6) and substituting into (D.3) the equivalent frequency for triangular waveform rise and fall is found:

$$f_{eq} = \frac{2}{\pi^2} \frac{1}{D^2\, 2\, D\, T_r}, \qquad f_{eq} = \frac{2}{\pi^2} \frac{1}{(1-D)^2\, 2(1-D) T_r} \tag{D.7}$$

Finally, the power loss generated in the magnetic material due to asymmetric triangular

waveform can be calculated from (D.5) as:

$$P_V = \left(0.5\,k_r\, f_{eqr}^{mr-1}\, B_{ac}^{nr} + 0.5\,k_f\, f_{eqr}^{mf-1}\, B_{ac}^{nf}\right) f_r \tag{D.8}$$

The equation above has two components whose are corresponding to the rise and fall part of the waveform.

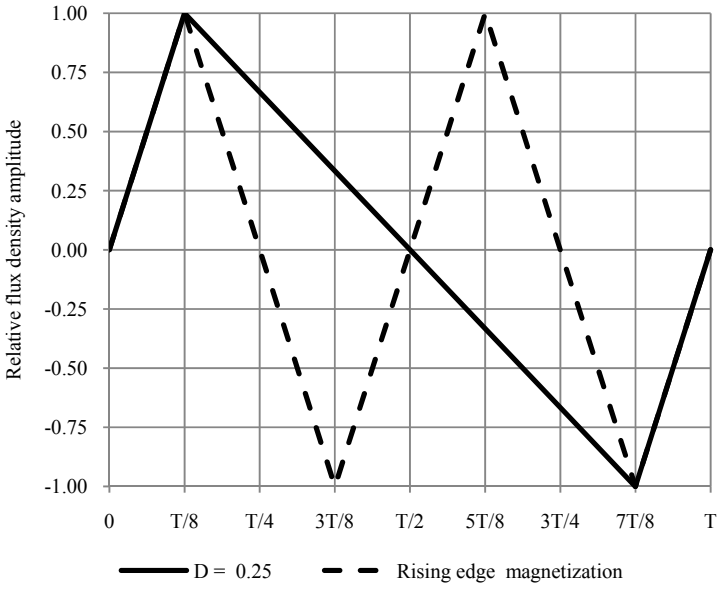

Figure D.2. Rising edge equivalent demagnetization waveform.

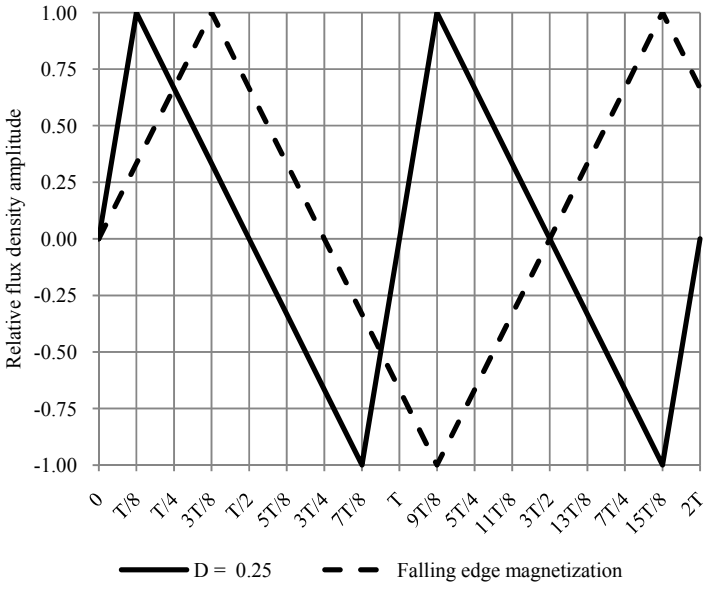

Figure D.3. Falling edge equivalent demagnetization waveform.

D.3.2. Experimental Results

Table D.6. Experimental data for duty cycle effect on the core power loss

Material	2605SA1				10JNHF600				Mega Flux 60			
V_{in} (V)	82	55	42	39	87	57	42	35	203	135	98	81
V_o (V)	102	77	68	64	107	81	69	68	253	193	163	160
I_{in} (A)	19.8	19.8	19.8	19.8	19.8	19.8	19.8	19.8	19.8	19.8	19.8	19.8
I_o (A)	15.6	13.6	11.7	9.7	15.6	13.6	11.6	9.6	15.5	13.5	11.6	9.6
t_{on} (μs)	20	30	40	50	20.4	30.0	40	50.4	20.4	30.4	40.4	50
D	0.2	0.3	0.4	0.5	0.2	0.3	0.4	0.5	0.2	0.3	0.4	0.5
P_{in} (W)	1628	1080	830	652	1717	1135	840	694	4010	2687	1948	1599
P_o (W)	1586	1043	794	617	1669	1094	801	655	3926	2617	1884	1535
$\Delta I_{p\text{-}p}$ (A)	26.6	26.2	26.2	26.2	30.0	27.8	27.8	29.0	31.2	31.0	30.0	30.4
N (turns)	16	16	16	16	16	16	16	16	28	28	28	28
L (μH)	60	60	61	59	57.5	59.6	58.7	57.3	131.1	130.9	129.6	130.4
$\Delta B_{p\text{-}p}$ (T)	0.274	0.272	0.279	0.274	0.294	0.286	0.285	0.294	0.328	0.327	0.315	0.323
ΔT_{exp} (K)	26.5	22.6	21.9	20	38.5	32.4	28.7	30	93	90	84	83

D.4. Air Gap Effect

Table D.7. Experimental data for air gap effect on the core

Material	2605SA1 Shielded				2506SA1 Unshielded			
l_g (mm)	0.5	1	1.5	2	0.5	1	1.5	2
V_{in} (V)	93.5	93.6	93.5	93.5	93.3	93.3	93.3	93.6
V_o (V)	186	186	185	185.7	186	185	185	185
I_{in} (A)	0.74	0.90	1.08	1.27	0.69	0.78	0.88	0.96
I_o (A)	0.13	0.1	0.1	0.14	0.1	0.1	0.1	0.1
t_{on} (μs)	10	10	10	10	10	10	10	10
P_{in} (W)	69	84	101	118.6	63	69	78	86
P_o (W)	25	25	24	25.30	24	24	25	25
$\Delta I_{p\text{-}p}$ (A)	24.5	38.2	47.3	60.45	17.1	25.8	32.3	38.8
N (turns)	10	10	10	10	10	10	10	10
L (μH)	37.0	24.0	19.3	15.5	54.5	36.2	28.9	24.2
$\Delta B_{p\text{-}p}$ (T)	0.300	0.300	0.300	0.300	0.300	0.300	0.300	0.300
ΔT_{exp} (K)	100.4	102.0	102.5	106.0	98.2	96.8	98.7	102.8

Table D.8. Experimental data for air gap effect on the winding

Material	2605SA1			10JNHF600		
f (kHz)	30	30	30	30	30	30
No. of gaps	1	2	3	1	2	3
l_g (mm)	1 x 3	1 x 1.625, 1 x 1	2 x 1, 1 x 0.625	1 x 3	1 x 1.625, 1 x 1	2 x 1, 1 x 0.625
V_{in} (V)	123.4	123.7	124.1	123.1	123.5	123.8
V_o (V)	252.7	253.3	254.0	252.1	252.8	253.3
I_{in} (A)	20.27	20.26	20.26	20.26	20.26	20.22
I_o (A)	9.31	9.32	9.34	9.30	9.31	9.29
P_{in} (kW)	2.502	2.508	2.511	2.495	2.495	2.501
P_o (kW)	2.355	2.362	2.371	2.345	2.353	2.353
η	94.13	94.18	94.43	93.98	94.31	94.08
$\Delta I_{p\text{-}p}$ (A)	38.8	40.4	40.4	38.8	38.8	40
N (turns)	22	22	22	22	22	22
L (μH)	53.0	51.0	51.2	52.9	53.0	51.6
ΔT_{core} (K)	91	81	76	90	84	83
$\Delta T_{winding}$ (K)	80	70	63	78	70	60

D.5. Thermal Configuration

Table D.9. Experimental data for thermal configuration analysis

Material	2605SA1			10JNHF600			Mega Flux 60		
f (kHz)	30	30	30	30	30	30	30	30	30
Direction	*x*	*y*	*xy*	*x*	*y*	*xy*	*x*	*y*	*xy*
V_{in} (V)	123.6	123.6	123.2	123.2	129.2	123.2	119.9	118.8	119.8
V_o (V)	253.6	253.4	252.6	252.4	252.4	252.7	246.0	243.8	245.8
I_{in} (A)	20.29	20.28	20.30	20.30	20.30	20.30	19.83	19.83	19.83
I_o (A)	9.34	9.34	9.31	9.32	9.32	9.32	9.18	9.18	9.18
P_{in} (kW)	2.514	2.507	2.500	2.500	2.502	2.501	2.377	2.356	2.374
P_o (kW)	2.369	2.367	2.351	2.353	2.354	2.354	2.259	2.239	2.255
η	94.23	94.42	94.04	94.05	94.09	94.12	95.04	95.03	94.99
$\Delta I_{p\text{-}p}$ (A)	33.6	33.6	33.2	36.8	36	34.8	16.8	18	16.8
N (turns)	22	22	22	22	22	22	28	28	28
L (μH)	61.3	61.3	61.9	55.8	57.0	59.0	119.9	110.0	118.8
ΔT_{core} (K)	38	32	29	21	42	16	45	44	40